Study of a low Re airfoil considering laminar separation bubbles in static and pitching motion

by

Faegheh Ghorbanishohrat

A thesis
presented to the University of Waterloo
in fulfillment of the
thesis requirement for the degree of
Doctor of Philosophy
in
Mechanical and Mechatronics Engineering

Waterloo, Ontario, Canada, 2019

© Faegheh Ghorbanishohrat 2019

Examining Committee Membership

The following served on the Examining Committee for this thesis. The decision of the Examining Committee is by majority vote.

External Examiner	Pierre Sullivan Professor, Dept. of Mechanical & Industrial Engineering, University of Toronto
Supervisor	David Johnson Professor, Dept. of Mechanical & Mechatronics Engineering, University of Waterloo
Internal Member	Carolyn Ren Professor, Dept. of Mechanical & Mechatronics Engineering, University of Waterloo
Internal Member	Xianguo Li Professor, Dept. of Mechanical & Mechatronics Engineering, University of Waterloo
Internal-external Member	Ali Elkamel Professor, Dept. of Chemical Engineering, University of Waterloo

I hereby declare that I am the sole author of this thesis. This is a true copy of the thesis, including any required final revisions, as accepted by my examiners.

I understand that my thesis may be made electronically available to the public.

Abstract

Performance of low Reynolds number (Re) devices is highly dependent on their airfoil design. Small wind turbines that usually work in areas with poor wind resources with a vast application from remote to busy urban regions are no exception. The unsteady flow field around the turbine blade results in an unsteady boundary layer that makes aerodynamics of these turbines complex and interesting. But due to the complexity of unsteady low Reynolds flow, and the small scale of boundary layer flow there are still unanswered questions in this area. Therefore, this study is arranged to fully investigate low Reynolds number boundary layer flow in steady and unsteady flow using small scale experiments.

For this goal, three non-intrusive experimental techniques used to study low Re flow behavior over a miniature SD7037 airfoil including surface oil flow visualization (SOFV), IR-Thermography (IT), and particle image velocimetry (PIV) at $14000 \leq Re \leq 48000$ have been developed and utilized. To model unsteady flow a pitch oscillation about the static stall angle of attack with amplitude 9° was considered. The quality of acquired results from all the experimental methods confirms the possibility of downscaling of low Reynolds flow experiments. Flow parameters such as the separation and reattachment points were quantitatively determined from SOFV and IT. The high-resolution PIV measurements provided an accurate velocity field so that surface pressure distribution and estimation of skin friction coefficient were determined from the velocity fields in both the steady and unsteady flow where due to the scale of the experiment and low magnitude of shear stress other measurement techniques would be intrusive or cannot be used. Estimated surface pressure coefficient (Cp) from PIV data revealed vortical structure effects as low-pressure waves that cannot be captured with coarse resolution methods. Integral boundary layer parameters are calculated in steady and unsteady conditions that provide in-depth information regarding low Re boundary layer flow behavior and laminar separation bubble characteristics. Boundary layer flow and reversed flow under the separated bubble were captured precisely while the Field of View covers the whole airfoil and results were confirmed by acquired data using finer spatial resolution. The measured aerodynamic force shows the effect of the height of the bubble on increasing the drag and the proper orthogonal decomposition method provided more information regarding the time-dependent behavior of vortices.

Acknowledgements

The beginning of my Ph.D. program was associated with a significant change in my life as starting to live in a new country, far from my family and friends. From that day many people helped me during this journey that without them this would not have been possible.

First and foremost, I would like to thank and express my special appreciation to my supervisor, Professor David Johnson who made this work possible. I would like to thank him for giving me the opportunity to work on this fascinating project and so selflessly and passionately mentored and guided me throughout my Ph.D. studies and shared his immense knowledge with me. He has been a tremendous mentor for me who helped me to overcome the difficult times and to stay positive in my work and my personal life.

I would also like to say special thanks to my Ph.D. committee members, Professors Pierre Sullivan, Carolyn Ren, Ali Elkamel, and Xianguo Li for their support and guidance.

I would also like to thank University of Waterloo faculty members, staff, and technicians especially Jason Benninger who helped with all the lab related challenges and Martha Morales.

During my studies, I met wonderful colleagues and friends who without them life would not have been as lovely. So many thanks to Nicholas Tam, Kobra Gharali, Nigel Swytink-Binnema, Farid Samara, Alison Zilstra, Micheal McKinnon, Michel Gaetan, Rifki Nugroho, and Mehrdad Bakhtiari for their help and support. I would also like to thank all our co-op students.

Finally, I want to show my deepest love to my amazing family; my parents Azar and Mohsen, my siblings and in-laws Fakhteh, Adele, and Fariborz who supported me during the hardest times of my life and gave me hope, joy, and courage to complete my studies. My nephew, Farbod who his smile warms my heart. And Nima, for his love and support. He never let me feel alone and encouraged me to pass all obstacles and appreciate every day of my life as an opportunity to learn.

Dedication

To my amazing family

Table of Contents

List of Tables

List of Figures

Nomenclature

A	Axial Force [N].
A_{span}	Span area of airfoil [m^2].
b	Span length[m].
c	Chord length [m].
C_D	Drag coefficient.
C_L	Lift coefficient.
C_p	Pressure coefficient.
D	Drag Force [N].
f	Frequency of Oscillation [Hz].
f_v	Frequency of Vortex shedding [Hz].
H	Boundary layer shape factor.
h_b	Bubble Height[m].
k	Reduced Frequency.
L	Lift Force [N].
l_b	Bubble length[m].
N	Direction Normal to the Surface.
n	Number of Refinement Steps.
p	Precision uncertainty.
P_{atm}	Atmospheric pressure [Pa].
Re	Strouhal number.
St	Reynolds number.
U_e	Streamwise velocity at the edge of the boundary layer[m/s].
U_∞	Free Speed Velocity [m/s].
u_{tot}	Total uncertainty.
x_R, R	Reattachment point[m].
x_s, S	Separation point[m].
x_t, tr	Transition point[m].

α	Angle of attack [°].
α_{amp}	Pitch Oscillation Amplitude [°].
α_{mean}	Mean angle of attack [°].
δ	Boundary Layer thickness[m].
δ^*	Displacement thickness[m].
μ	Dynamic Viscosity [kg/m s].
ν	Kinematic Viscosity [m^2/s].
λ	Wave Length[m].
ρ	Density [kg/m^3].
τ	Shear Stress [Pa].
τ_w	Wall Shear Stress [Pa].
σ	Standard deviation.
θ	Momentum thickness[m].

$2D$	Two Dimensional.
$3D$	Three Dimensional.
AOA	Angle of Attack.
CFD	Computational Fluid Dynamics.
DAQ	Data Acquisition.
DOF	Degree of Freedom.
FOV	Field of View.
$HAWT$	Horizontal Axis Wind Turbine.
LE	Leading Edge.
MAV	Micro Air Vehicle.
NI	National Instruments.
SWT	Small Wind Turbine.
TI	Turbulent Intensity.
TE	Trailing Edge.
UAV	Unmanned Aerial Vehicle.
UW	University of Waterloo.
WT	Wind Turbine.

Chapter 1

Introduction

Aerodynamic efficiency increases dramatically in the transitional Reynolds number(Re) region (10^4-10^6)[86, 109]. Figure 1.1 shows the trend of aerodynamic efficiency versus Re. Applications such as Micro Air Vehicles (MAV), Unmanned Aerial Vehicles (UAV), and Small Horizontal Axis Wind Turbines (SWT) typically operate in this low Re regime. Due to significant progress in technology, an increase in their performance and efficiency is considered much more than before.

SWTs are one of the sources of green energy that can be used from the most populated cities to totally remote regions that makes them one of the areas of interest in research. SWTs are designed to operate individually at lower local wind speeds, and then their efficiency becomes relatively more important compared to large commercial wind turbines. One of the most important components of a wind turbine which has a great effect on the efficiency is the blade. Therefore, the design of the blade becomes a crucial part of the strategy to maximize the efficiency of wind turbines especially for SWTs. However, wind turbine aerodynamics are complex due to many reasons including unsteadiness. For this reason unsteady blade air loads, blade performance, aeroelastic response of the blade, and environmental effects such as ground boundary layer effects should be considered all together[71]. The unsteady flow field around the turbine blade can cause an unsteady boundary layer (BL) which is affected by parameters such as environmental conditions, size of the blade (i.e., aeroelastic effect), and wind velocity.

Other low Re devices such as UAVs, MAVs, and low-pressure turbine blades operate under similar conditions. Poor aerodynamic performance for MAVs working at Re less than 70,000 was reported to be partly due to airfoil performance[112]. At low Re, a thick boundary layer increases the viscous drag [112] and formation of a laminar separation

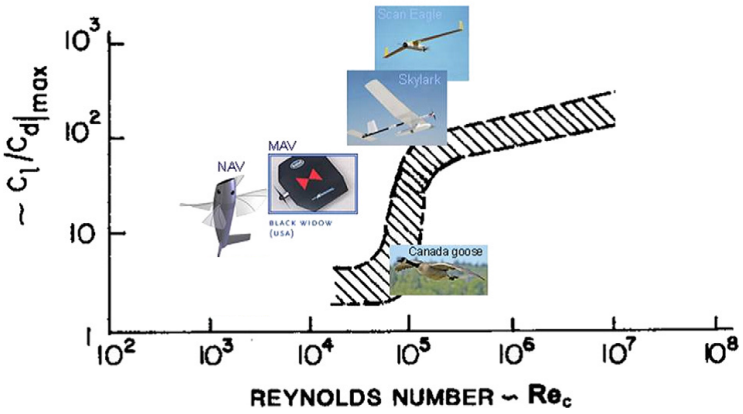

Figure 1.1: Aerodynamic efficiency vs. chord Re[109, 86]

bubble on the suction side of the airfoil increases the pressure drag [132] that results in a considerable drop in performance.

In summary, in low Re flows transition occurs and can include a laminar separation bubble (LSB). Formation of the LSB over the airfoil and sensitivity of this phenomenon to parameters such as the angle of attack (AOA), turbulence intensity (TI), and Re could cause unexpected behavior in aerodynamic forces followed by undesired changes in airfoil performance. In order to design an optimum airfoil and achieve better performance in low Re applications, further understanding of flow behavior and especially the laminar separation bubble on a low Re airfoil in different static and dynamic conditions is necessary and will be the subject of this study.

1.1 Low Re applications and small-scale experiments

Small Horizontal Axis Wind Turbines Wind turbines are devices which convert kinetic energy from the wind usually into electrical power. SWTs are used for many different applications such as remote off-grid residences and farms, telecommunication towers, offshore platforms and boats to name a few and are designed to operate at lower wind speeds. Therefore, regarding the increased concern about the use of green energy in the world, SWTs can potentially be one the major sources of energy for urban and rural life.

SWTs can include micro turbines rated less than 5kW, residential applications, 1kW to 10kW, and farm or institutional uses more than 10kW up to 300kW with a typical total

Flow field	Periodic	• Wind speed • Inflow • Yaw • Tower shadow
	Aperiodic	• Wind turbulence • Wake dynamics • Blade/Wake interactions

Figure 1.2: Aerodynamic sources affecting wind turbine airloads

height for a small horizontal wind turbine rated at 250kW is about 75m[105]. Loads on SWTs are typically controlled through stall-regulation, meaning that with an increasing wind velocity higher than a certain value, the blade surface area covered by separated flow increases, and eventually, the wind turbine captures less energy than before. This passive control method decreases the cost of small wind turbines but makes these turbines highly dependant on the aerodynamic design of the blade. Wind turbines usually operate under dusty weather conditions; therefore, the turbine blade erodes with undesirable roughness. Due to the cold weather in some parts of Canada, ice can develop on the leading edge (LE) of the blade which changes the effective shape of the LE and surface roughness. Roughness variation due to the conditions such as ice-covering of the blade can make changes occur in the airfoil laminar separation and turbulent transition phenomena[121] which can cause a reduction in the airfoil performance and captured energy. Therefore, sensitivity to roughness should be reduced[105, 118]. Wind turbines, due to the working environment, experience unsteady conditions. Figure 1.2, shows a summary of aerodynamic sources presented by Leishman[71] that can affect wind turbine blade loads.

Some prior scaled wind turbine experiments have Re in the order of 10^3 to 10^4, based on tip section of the blade[87]. For small wind turbines increasing the performance also depends to the response of SWTs to low startup wind speeds that could be about 3-8m/s[125].

Micro Air Vehicles MAVs are getting more attention in the market and typical airfoils for these applications are in the Re range from 10^3 to 10^5. Thin airfoils with camber up to 8% that provide higher performance in lower Re are reported for these application[112].

This study covers the Re range of 1.5×10^4 to 5×10^4 to study boundary layer flow in static and pitching motion over a low Re airfoil . The next section provides a short theory of boundary layer and laminar-turbulent transition.

1.2 Theory

1.2.1 Boundary-Layer

An object in a flow is subjected to two types of forces, normal and tangential forces. One tangential force, the friction force (friction drag) is related to the fluid viscosity, where the viscosity highly depends on the fluid temperature. The effects of viscosity are considerable in a narrow region in the vicinity of a wall, as the velocity grows from zero on the wall to the free stream velocity and this region is called the Boundary Layer. Apart from this region, the flow may treated as inviscid. Although the boundary between these two regions is not clear, particularly in laminar flows, where the velocity reaches the 99% of free stream velocity is considered to be the boundary. Regarding equation 1.1 shear stress and its resulting friction drag have an inverse relation with boundary layer thickness[111]. Laminar wall shear stress τ_w is typically written as:

$$\tau_w(x) = \mu(\frac{\partial u}{\partial y})_w \tag{1.1}$$

where μ is the viscosity, y is the direction perpendicular to the surface and u is the velocity. In inviscid flow, the outer region, the pressure distribution changes along the surface geometry and this pressure imposes onto the limit of the BL. In the narrow BL region, the pressure is constant perpendicular to the wall. Simplistically, while particles in both regions are under the same pressure distribution, in the BL due to the friction force particles lose kinetic energy and may flow toward a higher pressure and as a result may divert to the main flow leading to flow separation from the surface and a separated shear layer[63, 92]. Accordingly, the separation point is the junction of forward flow and reverse flow. The slope of the velocity profile at the separation point at the wall is zero ($\frac{\partial u}{\partial y} = 0$ at $y = 0$). Representative velocity profiles are shown in Figure 1.3.

Before the separation point, there is an accelerated BL flow with a favorable pressure gradient ($\frac{dp}{dx} < 0$). Simplifying the boundary layer equation 1.2 (simplified Navier-Stokes momentum equation in the boundary layer) on the wall ($(u, v)_w = (0, 0)$) reveals $(\frac{\partial^2 u}{\partial y^2}) < 0$ in the viscous layer before separation.

$$u\frac{\partial u}{\partial x} + v\frac{\partial u}{\partial y} = -\frac{1}{\rho}\frac{dp}{dx} + \nu\frac{\partial^2 u}{\partial y^2} \tag{1.2}$$

After the separation point, the flow has an adverse pressure gradient ($\frac{dp}{dx} > 0$) that means $(\frac{\partial^2 u}{\partial y^2})_w > 0$. Further along the BL far from the separated shear layer, $(\frac{\partial^2 u}{\partial y^2}) < 0$,

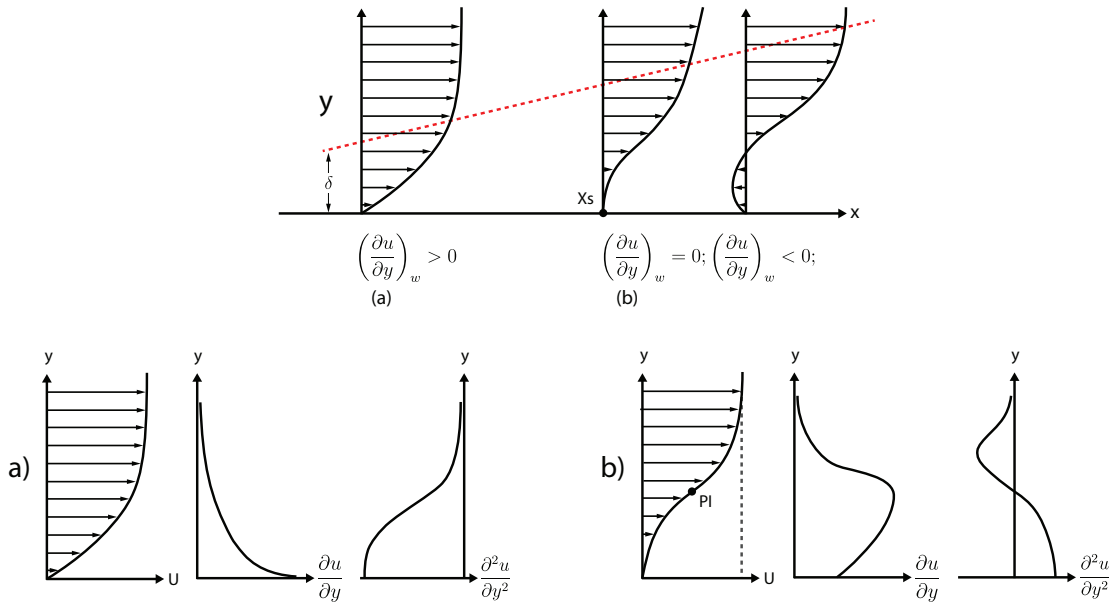

Figure 1.3: Velocity distribution in the BL a) favorable pressure gradient b) adverse pressure gradient

therefore somewhere in the middle $(\frac{\partial^2 u}{\partial y^2}) = 0$. This point is the point of inflection (PI) of the velocity profile[111]. This is a sufficient condition for amplified disturbances to develop inviscid flow instability(Kelvin- Helmholtz)[12, 25]. Figure 1.3 shows a velocity profile in the BL with its first and second derivatives profiles.

1.2.2 Instability and Transition

BL flows can be laminar if flow particles move in layers without strong exchange between layers, or it can be turbulent if particles move in irregular and random behaviour in both time and space which causes significant particle transfer between layers. In turbulent flow, effects of viscosity are limited in a narrow layer on the wall that is called the viscous or laminar sublayer where the velocity gradient is very large. Laminar flow transitions to turbulent flow with random fluctuating motions. It occurs when small 2D perturbations, Tollmien-Schlichting (T-S) waves caused by wall roughness or outer flow irregularities appear in laminar BL flow, and the viscosity is not enough to dampen them. These disturbances grow and intensify to a 3D disturbance that characterizes turbulent flow. For lower Re flows even small perturbations can destabilize the BL while with increasing Re the laminar BL is more stable [111]. Figure 1.4 is a schematic of the transition process in a laminar BL

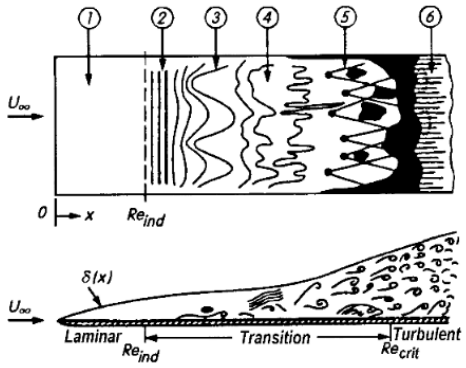

Figure 1.4: BL flow behavior on flat plate at zero incidence.[111, 134]

flow on a flat plate. As shown, following stable laminar flow (1) the transition region begins with initiating unstable 2D Tollmien-Schlichting (T-S) waves(2) moving downstream, and they become elongated to span-wise vortices and form a Λ structure vortex (3), following by 3D vortex breakdown(4) and a turbulent flow region(5)[35, 111].

When transition phenomenon occurs in the separated shear layer, disturbances due to T-S instabilities roll up into vortices along the span. Downstream, merging and break down of these vortices causes mixing of the layers and increases the flow momentum. If the energy of the flow is large enough, the separated shear layer reattaches to the surface as turbulent flow and forms a Laminar Separation bubble (LSB)[35, 63, 108]. Although the creation of a LSB may prevent the airfoil from stalling, vortices formed along with the LSB can increase the noise level and/or fluctuating load on the airfoil[63].

Although the BL region is a narrow area, its impact on airfoil performance is significant so that forces acting on the body are highly dependent on the type of BL[111]. Therefore, more understanding of laminar BL transition and its affecting parameters such as vortices could help in developing low-Re applications.

1.2.3 Laminar Separation Bubble (LSB)

In many applications that deal with low Reynolds number flows (1×10^4 to 50×10^4)[53], such as turbomachinery, unmanned aerial vehicles, micro air vehicles, and wind turbines, smooth transition[1] occurs with the existence of a LSB. For example, SWTs usually work in areas with a poor wind resource and they face continuous changes in wind speed and

[1]Transition from laminar (smooth) flow.

direction. Therefore, a large part of the SWTs' blade operates under laminar or transitional flow [79]. Shear stress and heat transfer rate increases in transition which both can have effects on the drag force[28], the rate of increase or decrease of these features can be used to define or aid in interpretation of experiments. Therefore, identifying the dependency of the LSB and critical location and condition which cause the SWT to lose power can help to improve SWTs performance.

In low Re flows the flow is laminar and there are no/negligible interactions between different layers. Because of the existence of velocity shear in the boundary layer, with small external flow fluctuations, Kelvin-Helmholtz (K-H) instabilities can occur. When separation occurs, a laminar BL is very unstable and due to the strengthening of K-H instabilities fluctuations increase creating unsteady vortex structures[53, 93]. Therefore fluid particles are no longer aligned in parallel layers and energy transfer in different layers is called laminar-turbulent transition flow. To give an estimate, it should be noted that transition can happen when the local Re is less than 3×10^6[34]. Also transition causes an increase in the boundary layer thickness and shear stress and due to the K-H instabilities, energy and momentum of the fluid increase. However, if the energy is high enough, it overcomes the adverse pressure gradient and the flow reattaches to the surface otherwise the flow remains separated until it passes the airfoil chord length. In reattached flow, velocity, position, pressure, and temperature of fluid particles change permanently, and this flow is called turbulent. In turbulent flow due to the existence of vortices (eddies), energy and momentum transfer is larger-scale than laminar flow. As mentioned, the process of separation, transition, and reattachment forms a bubble shape on the airfoil's surface that is called LSB[108]. The following section explains the LSB in detail.

Geometric Properties Figure 1.5, shows a schematic of a LSB developed over the airfoil and the details of flow behavior around this bubble is explained in the picture on the top right from Horton[50].

Studies that have been done until now show that shape, size, and location of the LSB could be affected by the airfoil shape, roughness, angle of attack (AOA), turbulence intensity of the flow,TI ($TI = \sqrt{(\frac{1}{3}(\overline{u'^2} + \overline{v'^2} + \overline{w'^2}))}/U$, where U is the free stream velocity and $\overline{u'^2}$, $\overline{v'^2}$, $\overline{w'^2}$[111] are time averaged velocity fluctuations), and Re.

The transition can affect BL behavior after the flow separation and aerodynamic forces consequently[48]. Obtained results by Hu and Yang [53] showed that after creation of the LSB, with further increase in the AOA, drag increases intensely while the rate of increase in lift decreases. Then due to the bubble bursting, stall occurs and lift (drag) significantly drops (increases)[53]. Losing lift and increasing drag results in the loss of the blade's

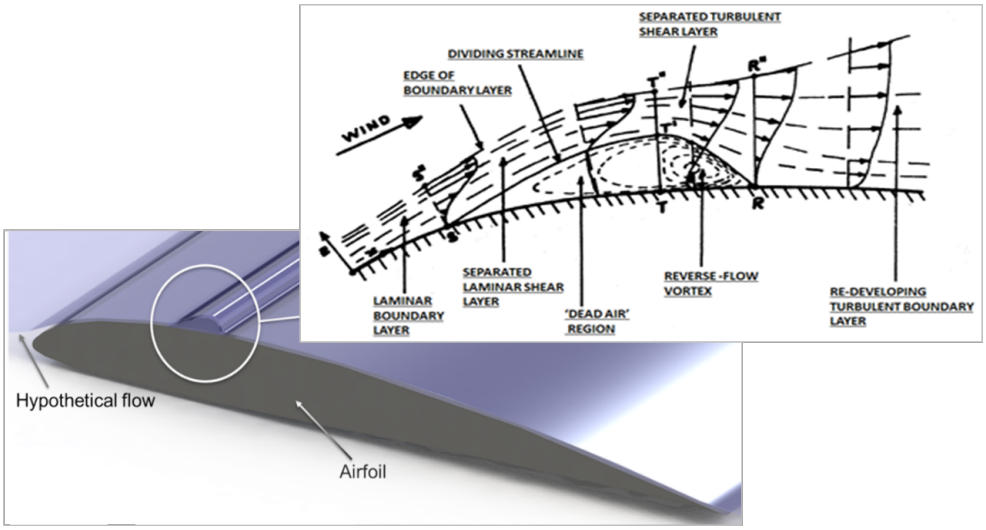

Figure 1.5: Schematic of laminar separation bubble created over an airfoil and profile of it in detail[50]

performance. In general, LSB decreases the suction peak so increases the pressure over the LE. Due to this increase, the pressure drag increases significantly that decreases lift/drag (L/D) or in other words, the airfoil's performance [4]. From previous reviews [83], the Re range of 10^4 to 10^6 can be considered as the critical range[2] for most airfoils, although the geometry of the airfoil can slightly change the range. An experimental study has been done for over 60 airfoils from 1986 to 1989 by Selig *et al.*[114]. Their results show that for a Re higher than 10^5 the general form of the drag polar stays the same so that for a wide range of lift coefficients the drag coefficients stay low. While for lower Re, unusual behavior occurs that the drag coefficients unexpectedly increase for a limited range of lift coefficients.

Another important point presented by McArthur[83] comes from comparing the drag polar data for a E387 airfoil acquired from different facilities, and shows that the drag polar for the lowest Re (6×10^4) are less repeatable than higher Re (10^5- 3×10^5). They stated that the difference can be due to: 1) high relative uncertainty of measurement because aerodynamic forces are smaller in lower Re or 2) Higher sensitivity of aerodynamic forces to the turbulent intensity at lower Re. Along with these data, McMasters and Henderson [83, 86] presented an empirical survey as a plot of Cl/Cd changes vs. change of Re. It shows that below the critical Re (10^5), roughness increases L/D that is beneficial but above this Re, smooth airfoils have better L/D. It was shown that by approaching the critical Re, the effect of the transition region increases due to the increasing of the transitional region

[2]Under this range flow is totally laminar.

length relative to the airfoil chord length. It is a good explanation for higher sensitivity to the turbulent intensity in lower Re flows[83].

While increasing the drag coefficient with the existence of the LSB is expected, McArthur [83] compares the results of Ol *et al.* [97] with the results of Selig *et al.* [80, 117] that regarding the Ol experiments at Re=6×10^4 and AOA=4°, the existence of a LSB on a SD7003 airfoil was confirmed. Based on the Selig results, no abrupt increase in drag occurred for the SD7003 airfoil at this Re and conclude that the separation bubble may have little effect on the drag polar and does not seem to be the reason for an abrupt drag increase in E387. But here, considering the difference between the increased amount of the drag for SD7037(C), E387(C), and SD7003, it is possible that shape or location of the bubble has a significant effect on aerodynamic forces.

Aholt and Finaish[4] computationally estimate that by removing the LSB, an airfoil's aerodynamic efficiency can improve by 60% that makes it comparable with the aerodynamic efficiency of the same airfoil at high Re where no LSB occurs. Therefore elimination or controlling the LSB would be a highly interesting task in flows with low Re.

1.2.4 Basic concepts and definitions

The definitions of some important aerodynamic parameters that have been used in this document are presented in this section. First, one of the most common non-dimensional parameters in fluid dynamics is the airfoil Reynolds number (Re) and is as defined as

$$Re = uc/\nu \tag{1.3}$$

where, u is freestream flow velocity, c is the chord length of the airfoil, and ν is the kinematic viscosity. If Re of two flows are equal then mechanical similarity exists that means flow behaves similarly on similar geometries [111]. In fact, Re is the ratio of inertial forces to the viscous forces and appears as the only non-linear term of the non-dimensional incompressible, Navier-Stokes equation[83].

For $Re > 10^6$ the boundary layer is turbulent and for $Re < 10^3$ the viscosity is too high that flow will not transition to turbulence for regular airfoils. Then the range of Re between 10^3 and 10^6 is a transitional region, and study of the flow behavior in this region is one of the most challenging issues in blade aerodynamics[83]. Second, the Mach number that is defined as

$$M = \frac{u}{C} \tag{1.4}$$

where C is the speed of sound.

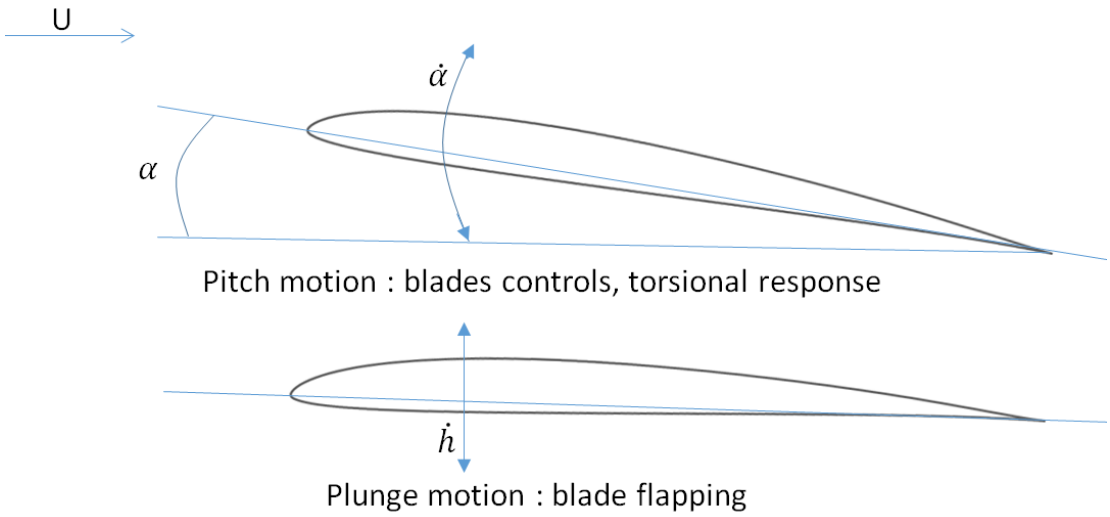

Figure 1.6: Airfoil unsteady aerodynamic models (pitch and plunge)

The third important non-dimensional parameter that will be used represents the unsteadiness, represented in this thesis as a pitching motion. As stated by Leishman, "Wind turbines operate in an adverse, unsteady aerodynamic environment that is hard to define using mathematics models"[71]. All the effects that come from sources of unsteadiness can be considered due to AOA and velocity perturbations that are summarized and presented by Leishman[72].

That according to Figure 1.6, part of the aerodynamic unsteadiness over a wind turbine blade airfoil can be modeled by pitch oscillation[72]. This motion can be simulated by sinusoidal motion about the quarter chord of the airfoil. Pitch oscillation can be defined by equation 1.5,

$$\alpha = \alpha_{mean} + \alpha_{amp} \sin(2\pi f t) \tag{1.5}$$

where α_{mean} is the mean angle of attack, α_{amp} represents the pitch oscillation amplitude, and f is the oscillation frequency. Therefore, for unsteady motion α_{mean} usually is chosen to be close to the static separation angle of attack where dynamic stall can occur. The fifth group, the dimensionless frequency, is defined by a non-dimensional parameter called the reduced frequency, k, which is defined as;

$$k = \frac{\pi f c}{u} \tag{1.6}$$

where f is frequency of oscillation (Hz), and u is the freestream velocity (m/s). The flow condition based on k is divided into;

- Steady-State: k=0,
- Quasi-Steady:$0 \geq k \leq 0.05$
- Unsteady: $k > 0.05$, and Fully Unsteady: $k > 0.2$[72].

Finally Strouhal number (St) that is a non-dimensional parameter used in oscillating flow motions like vortex shedding. Usually, it determined from equation 1.7:

$$St = \frac{f_v l}{U_\infty} \tag{1.7}$$

Where f_v is the frequency of vortex shedding, U_∞ is the flow velocity, and l is the characteristic length that differs based on the study case. Faure *et al.*[30] studied the dynamic vortex result of two airfoils' interaction with the PIV method. They used the Taylor Hypothesis [3] to determine the vortex shedding frequency from equation 1.8

$$f_v = \frac{1}{T} = \frac{U_\infty}{\delta_x} \tag{1.8}$$

where T is the shedding period, U_∞ is the upstream flow velocity and δ_x is the space between two successive detached vortices. Then St is estimated based on the calculated shedding frequency, 1.9[30].

$$St = \frac{f_v c}{U_\infty} = \frac{c}{\delta_x} \tag{1.9}$$

Burgman *et al.* [95] used the momentum thickness (θ_s) as a characteristic length, and boundary layer velocity at the separation point (U_s) instead of free stream velocity to calculate St for Kelvin-Helmholtz instabilities ($St_{KH} = f_v \theta_s / U_s$) in the shear layer. For these range of Re flows, the range of St_{KH} was from 0.006 to 0.012 approximately.

Because of the expected key role of the LSB on the performance of low Re flow applications many studies have been done on this subject in static cases. Despite the large number of studies, a brief review is presented, to draw attention to those works that are most relevant to the lower Re and utilize advanced techniques.

[3] When $u^{'}/U << 1$ Or in other words, the spatial acceleration $u.\nabla u$ exceeds the temporal acceleration $\partial u/\partial t$, the advection of the vortices can be considered due to the upstream flow velocity

1.3 Previous Works

1.3.1 Laminar Separation Bubble

It seems that the first study on LSB has been done by Jones about 1933[72, 83]. In addition to this paper, one of the other first literature reviews on LSB distribution and its effects on airfoil stall has been done by Tani[129]. This work approximately covers flows with Reynolds numbers between 2 to 6 million on NACA airfoils. Pressure distribution and liquid film methods were used in these experiments. It was concluded that transition occurs in separated flow, and the length of the bubble increases with increasing Re or decreasing the AOA; however, they could not find a clear relation between a critical value such as the boundary layer Re and the pressure at the reattachment point after bubble breakdown. Gaster[32] organized an experimental study on LSB. In this experimental study, both Pitot tube and hot wire techniques were used. The study states that the subsequent structure of the bubble depends on pressure gradient and separation Re, however, the behavior of the bubble is not a function of only these two variables and it is not clear what parameters play an important role in bursting the bubble to consider them in analytical approaches. Gaster[124] has played a significant role in understanding of bubble structure and behavior. A semi-empirical theory based on Horton's method along with experimental correlation has been provided to estimate the development and bursting of the LSB. Predicted results compared to the experimental data for a $NACA\ 66_3 - 018$ airfoil was acceptable, but the author mentioned that the results were highly dependent on the pressure or velocity distributions and the type of BL. Therefore, more experimental data are needed to verify the results, and to ensure that the empirical coefficients are correct.

Laser velocimetry (LV) was used to investigate LSB characteristics in the concave region of an airfoil model at Re=2.1×10^6 [81]. The location of the LSB was determined by comparing results acquired from histograms of particle velocity in the stream-wise and normal direction, velocity profiles in the boundary layer, and turbulence intensity. The velocity and intensity profiles were simultaneously used to determine the position of the separation point at 0.19c, and reattachment point at 0.23c. It was mentioned that the "largest fluctuations in turbulence intensity indicating the end of transition at 0.225c and a fully turbulent profile is observed at 0.25c" which confirms the results of previous papers about the difference between the type of turbulent boundary layer in the reattachment point and the rest of the boundary layer. Results of this paper confirmed that laser velocimetry is an effective method to be used in this area [81].

A study of the creation of a LSB in gas turbine engines shows that long bubbles cause a significant reduction in performance and major change in flow direction which is not

desired. Therefore, preventing long bubble formation should be considered in engine designs. However short bubbles generate turbulent flows on the surface of the blade which can be used to control the airfoil's performance [82].

As mentioned in section 1.2.3, Ol *et al.* [97] report research on the characteristics of LSB over a SD7003 airfoil with different facilities including a wind and water tunnel which take advantage of PIV methods. They mentioned seeing the LSB separation point and the following vortex in instantaneous images, however due to low spatial resolution in PIV; it was not fully clear in the averaged result. All the experiments have been done for an SD7003 airfoil model of chord length of 201-203mm at Re=6×10^4. It is claimed that characterizing the LSB is possible using 2D PIV. The general information regarding the bubble shape and the velocity field is the same in different facilities' results, even though there are some differences in the location and the flow structure of the bubble. In addition, the experiment results are close to results modeled with X-FOIL[4]. Also Zhang *et al.* [140] report a quasi-3D PIV experiment on the same airfoil using scanning PIV. Their main focus is dynamic vortex behavior of the LSB at Re=60,000 and 20,000 and AOA=4°. In this experiment a water tunnel with a free stream speed of 0.3 m/s was used; this gave an opportunity to use a transparent airfoil which has no or negligible reflection in water. Length of field of view (FOV) can be small enough, for example 0.3 chord length, which provides high resolution in a small area. In this paper, it is claimed that with decreasing the Re, a longer region of reverse flow includes a large vortical structure.

Hu and Yang [53] take advantage of both the pressure methods and the PIV method to study LSB in $Re_c = 70,000$ on NASA GA (W)-1 airfoil model; which is stated that the airfoil is a low speed one. For the pressure distribution experiment, the location of LSB including separation, transition, and reattachment points were determined by a model known as Russell theory [110, 83], Figure 1.7. Russell theory, suggested by Russell [110] so that the starting point of constant pressure is the separation point, transition of laminar BL to turbulent BL is accompanied by rapid pressure rise then the end point of the constant pressure line is the transition point, and at reattachment region the pressure equals inviscid pressure therefore the point where this graph meet inviscid surface pressure graph is the reattachment point. In figure 1.7, there are two parts for the LSB; the laminar part of LSB where the upper surface pressure distribution is flat and the region with high gradient in the pressure distribution curve that represents the turbulent part of the LSB [53, 50]. They found that the length of the LSB remains almost constant, 20% of chord length, by increasing the AOA from 8° to 12°. However, with increasing AOA, the length of the turbulent part of the LSB becomes a little shorter; therefore, the length of the laminar part increases with increasing AOA. In this figure, consider S as a separation point, T as a

[4]Refer to 4.3 XFoil program.

transition point, and R as a reattachment point.

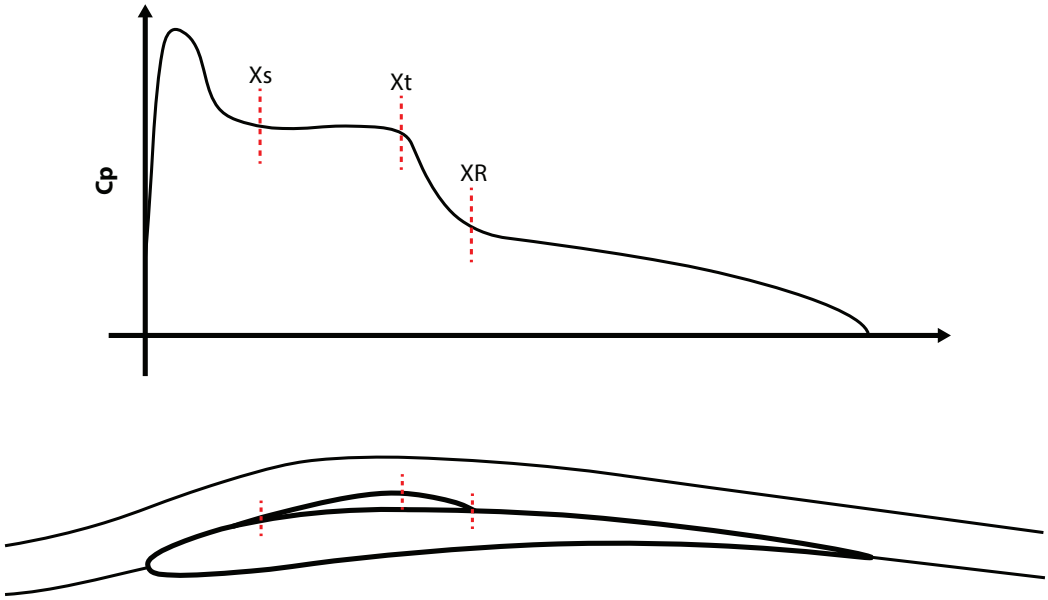

Figure 1.7: Surface pressure distribution in existence of LSB

However, Hu and Yang [53] obtained valuable quantitative data about the pressure distribution but because of limitations in the numbers of pressure transducers, the PIV method had been chosen to measure the flow field features. To achieve complete understanding of the steps involved in the creation of LSB, three FOVs were applied which are named coarse level, refined level, and superfine level. These FOVs together can cover the entire airfoil area, near the LE until about half of the chord length, and the transition and the reattachment areas correspondingly. Their results reveal that for a desired airfoil, a LSB with a height of about 1% of chord length is generated when the AOA is higher than 8°. By increasing the AOA to 12°, the vortices created due to Kelvin- Helmholtz instabilities in the transient flow are not strong enough to overcome the adverse pressure gradient. The result is bursting of the LSB which leads to the airfoil's stall. In the PIV method, the separation and the reattachment points were determined by following the streamlines of flow, in addition to the velocity and the span-wise vorticity fields. Also 2D turbulent kinetic energy ($TKE = 0.5 \times \frac{\overline{u'^2} + \overline{v'^2}}{U_\infty^2}$) was used to locate the reattachment point. The transition point was determined by using the critical number of normalized Reynolds shear stress, $-\overline{u'v'}/U_\infty^2$, which is 0.001 as in previous works [13, 97]. Kim *et al.* [62] stated that transition causes an increase in both u' and v' and creates a virtual value

that is also can be seen in velocity fluctuation profiles.

Genc *et al.*[35] have studied the performance of a NACA2415 airfoil at low Re flows (0.5×10^5 to 3×10^5) for a wide range of AOAs ($12^\circ \leq \alpha \leq 20^\circ$) using experimental force measurements using an external three-component load-cell system. Additionally, they experimentally investigated the location of the separation, transition and reattachment points as a result of a laminar separation bubble by performing surface pressure and velocity measurements and applying the SOFV method. They stated that following laminar separation, transition occurred immediately after the highest point of the pressure coefficient (Cp) curve. Moreover, similar to Tani[129] results, they reported that by decreasing the Re, the intensity of the abrupt stall increases. SOFV for the SD7037 airfoil, a low Re airfoil, is reported by McGranahan and Selig[85] at three different Re of 2×10^5, 3×10^5, and 5×10^5. For this particular airfoil even at the highest Re (Re=5×10^5) transition occurs in the presence of a LSB and this bubble remains for all angles of attack until the airfoil stalls. It is mentioned that at the point that the oil has accumulated, exactly after untouched oil coating can be seen, is not a reattachment point rather this line is where there is a balance between surface tension and oil adhesion close to the reattachment point. By comparing some results they believed that there is a difference between the oil accumulation line positions due to using different types of oil but this difference is negligible. They also declare that for airfoils such as SD7037 that has high performance in low Re flows there is a small distance between the accumulation line and the reattachment line.

In addition to the experimental studies, some numerical studies have been done to predict the LSB characteristics. Since LSB is associated with transitional flow then numerical simulation is substantially more challenging. Singh and Sarkar [124] simulated a flow environment that a gas turbine blade is facing during its operation. They used direct numerical simulation (DNS) to investigate the process of separation, transition and reattachment during formation of a LSB. According to their results, after the separation point until 27% of bubble length, no growth of fluctuations is observed (in dead air region, look at Figure 1.5). But after this length, 3D behavior and non-linear interaction occurs which leads to the breakdown of long and narrow streaks to short and irregular streaks (transition and turbulent zone). They used the skin friction coefficient (C_f) to determine the locations of the separation and reattachment points.

So that, the separation and the reattachment points can be determined by the zero crossing of the skin friction plot and the flat section after the separation point indicates the dead air zone. They suggest the sharp negative increase in the skin friction coefficient just after the flat section was caused by a reverse flow vortex. Richez *et al.*[107] applied large eddy simulation (LES) to model the transition process due to the creation of a LSB for Re=1.8×10^6, and the phenomenon downstream of the LSB on an airfoil model at a

high angle of attack. Then they used those acquired transitional data for RANS turbulence models. Finally, they stated that turbulent flow characteristics do not exist exactly after the reattachment point because the adverse pressure gradient is still strong and it takes a little more distance to reach an equilibrium turbulent region. It is clearly shown on Figure 1.8, streak lines (red lines) are long and stretched in the equilibrium turbulent region while they are short and they do not exactly follow the stream-wise direction about the reattachment point[107].

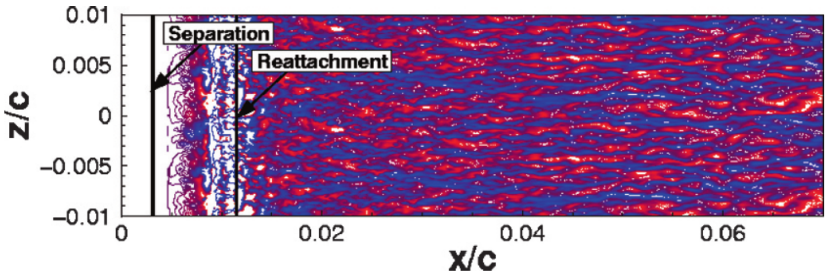

Figure 1.8: CFD result of streamwise velocity fluctuations over 2D OA209 helicopter fan blade at $Re = 1.8 \times 10^6$ (blue is positive and red is negative)[107]

As has been understood from numerical and experimental studies, the effects of a laminar separation bubble on aerodynamic forces depend on the position and physical dimensions of the bubble. The distance between the separation point and the transition point is called the transition length. Singh *et al.* [124] define the transition length as a distance between separation point and the point of minimum skin friction. Another method of measuring transition length is the distance between separation point and the maximum height of the bubble[48]. Also, bubble length is usually defined as a distance between the separation point and the reattachment point. The height of the bubble is defined as a maximum distance between the dividing streamline and the surface of the airfoil. The initial position of the bubble is determined by the location of the separation point. These characteristics vary with Re, angle of attack (AOA), external disturbance[120, 56], and unsteadiness of the flow[37]. A review paper on LSB was provided by Jahanmiri[56] which covers most areas related to the LSBs until 2011.

The experimental results obtained by O'Meara and Mueller[98] for NACA $66_3 - 018$ airfoil at AOA $8° - 12°$. These results give a good view for a better understanding of this phenomenon as well. They results show that the length of the bubble is less sensitive to changes in Re. It can be concluded that there is a critical range of Re for each thin airfoil which the length of the laminar separation bubble increases dramatically in that range. Identifying this domain is very important to avoid applying the airfoil in that working range.

Their results also show that the height of the bubble is very small compared with its length. More analysis shows that the rate of increase in the length of the bubble is much smaller than the rate of increase in its height. When it comes to designing the airfoil, depending on the importance of the amount of lift or drag this point can be crucial. Lissaman [77] also mentioned that the features of the bubble, i.e. the length of the bubble, may vary with changes in Re, and airfoil angle of attack.

Momentum thickness at the separation point is one of the characteristics of LSB; from some literature, it is found that the momentum thickness (θ) up to the transition point can be assumed as a sort of constant value[48] where θ is defined as,

$$\theta = \int_0^\infty \frac{u_y}{u_e}(1 - \frac{u_y}{u_e})\,\mathrm{d}y \tag{1.10}$$

where u_e is the velocity of the flow at the edge of the boundary layer and y is the vertical dimension from airfoil surface.

A separation bubble on an SD7003 airfoil model was studied by Burgmann and Schroder with time-resolved (TR)-PIV and Scanning PIV at three Re=20,000, 40,000, 60,000 using multiple light sheets and combined FOVs to cover flow field about the airfoil[13, 14, 15, 16, 95]. Their results show typical 'cat-eye' shape in vortices that is a feature of Kelvin-Helmholtz instabilities, Figure 1.9. Their results show that effects of AOA on separation, transition and reattachment points are stronger than Re. Also, they confirm the dependency of LSB geometry to flow conditions.

Zhou and Wang studied the leading edge instabilities at $Re = 10^4 - 10^5$ over an SD7003 airfoil numerically[141] for four Re, 30,000-60,000-90,000-120,000. Their results show that the scale of shedding vortices and separated flow area are quite different for these Re.

Numerical and experimental results for an Eppler 387 airfoil at Re=60,000 and 200,000 presented by Lin and Pauley [76] shows the transition ramp above the bubble at AOA=4°. The curve of the transition ramp is changed depending on the height of the LSB. The existence of a strong recirculation region (in their case close to the TE) correspond to a strong gradient in surface pressure distribution.

Lang *et al.* [64] used LDA and PIV to investigate controlled transition in a LSB. Their results show the possibility of measuring unsteady phenomena using PIV and decreasing the time compared with adequate LDA measurements.

Lengani *et al.* [73] studied coherent structures in the BL of a low pressure turbine blade at Re=70,000 using 2D PIV for flows with different turbulence intensities. PIV measurements performed in two planes, parallel and perpendicular to the blades. The results in the

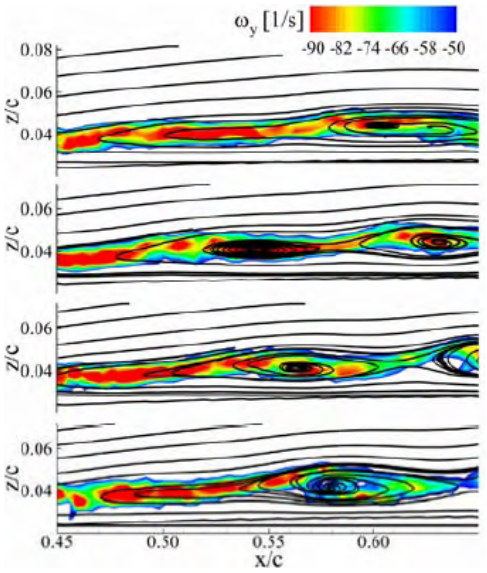

Figure 1.9: Cat-eye pattern in Kelvin-Helmholtz instabilities with vorticity contours and streamlines over an SD7003 airfoil[95]

perpendicular plane have been used to study the propagation of these structures that generate shear stress in the BL. Parallel plane results have been used to analyze the rear part of a LSB. POD has been used to reconstruct data within Kelvin-Helmholtz vortex shedding period. They also used POD to study a LSB over a flat plate at Re=70,000[74]. Their results show the first two POD modes of normal velocity components are coupled that is the result of Kelvin-Helmholtz instabilities. Istvan *et al.* [55] studied the effects of turbulence intensity on pressure distribution over NACA0018 at Re=100,000 and 200,000. It is mentioned that the effects of free stream turbulence intensity on the LSB are increases as Re decreased.

Aholt and Finaish[4] computationally investigated effects of localized body force on the LSB. They studied effects of size and strength of a plasma actuator, a body force generation system, on LSB features and consequently the airfoil's aerodynamic performance. Also some passive control methods that accelerate transition to turbulent flow, such as locating some tiny rough obstacles before the separation point have been used by other researchers. Aholt and Finaish investigate for an elliptical airfoil at 10° at Re=10^4. They found that removing the LSB or even shrinking it results in higher aerodynamic efficiency so that the efficiency of the airfoil after using an actuator can be comparable with its efficiency in high Re flows. But the location of the actuator is very important so that, if it is located too far after the separation point, it will cause flow instability due to generating small vortices

before the LSB[4].

The next section focuses on the importance of the LSB in pitching motion.

1.3.2 Laminar Separation Bubble in Unsteady Flows

There are several works at high Re flows which study effects of unsteady motion such as pitch and plunge motion. As a result of changes in the aerospace and wind energy industries, small devices like UAVs, MAVs, and SWTs get more attention than before. These devices face unsteady low Re flows because of their physical size and working conditions. Only a few studies that investigate this type of flow are known to the author. In fact, the transition and reattachment caused by the LSB strongly depends on Tollmien-Schlichting waves' strength that occur before flow separation[93]. Based on previous works, pitch and plunge oscillations affect flow separation. Therefore, they can affect LSB characteristics.

Lou and Hourmouziadis[79] simulated the blade's BL in a low speed wind tunnel to study the development of the LSB under steady and periodic-unsteady main flow conditions. Periodic-unsteady flow was produced by mounting a rotating flap which can increase the frequency of oscillation flow up to 100 Hz downstream of the test section. The experiments cover a wide range of Re from 100,000 to 2,000,000 with Strouhal number ($St = fL/v$ where f is the frequency of vortex shedding, L is the characteristic length and v is the flow velocity) from 0 to 3 to model turbomachinery conditions without considering the compressibility effects over a flat and smooth plate with enforced pressure distribution. In steady tests, hot-wire and laser sheet flow visualization, and in unsteady ones, pressure taps in addition to the flow visualization were used. The authors summarized the development of a LSB in 4 steps: at the maximum vorticity of the velocity profile, free shear layer instability initiation that transfers the energy from shear layer to the instability waves; the instability waves are magnified in the stream-wise direction that cause transition; the momentum transfer across the shear layer intensify because of the existence of turbulent fluctuation in the transient flow; transition to turbulence happens in a very small distance. Ultimately, they have concluded that the overall structure of laminar separation, transition, and reattachment is the same for steady and unsteady flows. For steady flow, momentum thickness behavior after the attachment remains the same and may be used to describe the bubble. In unsteady flow, separation remains the same, but there is a strong relation between the transition and reattachment points with the oscillatory flow parameters.

Pascazio *et al.*[100] used the Embedded Laser Velocimetry(ELV) measurement method with a Re of 10^5 to determine the instantaneous 2D velocity components with respect to local surface of the *NACA0012* airfoil under sinusoidal pitching motion. The boundary-layer

dynamic development and the local unsteady flow features such as the laminar to turbulent flow transition and laminar separation were investigated. Additionally, the obtained results in this paper show that as reduced frequency (k) increases the core unsteady feature produced by the sinusoidal pitching motion leads to a time delay on the laminar, transitional, turbulent and turbulent-separated boundary-layer behaviour. Similar to Pascazio *et al.*[100], Lee and Basu[65] also investigated the unsteady boundary-layer development with a Re of 169,000 on an NACA0012 airfoil. The measurement method used in this experiment was multiple hot-film sensors (MHFS). The results of the measurements showed that compared to the steady case the laminar separation and transition to turbulent flow were delayed with increasing AOA. Additionally, the results also showed that the reattachment point moves rearward with decreasing AOA. The sinusoidal pitching motion also helped keep the boundary layer attached at higher AOAs.

Furthermore, Lee *et al.*[67] investigated the boundary-layer transition, separation, and reattachment of a NACA0012 airfoil going through a sinusoidal pitching motion with Re of 195,000 using multiple hot-film sensors. In the results of these measurements, the boundary-layer transition and separation were delayed with increasing k. Also, the dynamic stall process was originated with a turbulent LE. These results support the previous results in Lee and Basu[65]. Lee and Gerontakos [66] in study of NACA0012 airfoil at $Re = 1.35 \times 10^5$ found that LE dynamic stall did not originate with the bursting of LSB but with sudden turbulent breakdown slightly downstream of LE. Tanaka [128] has studied the quasi-periodic behaviors of a LSB on a NACA 0012 airfoil near its stall angle of attack, 11.5°(11°-12°), at Re=1.3×10^5 experimentally. Smoke flow visualization, and PIV measurements were used. Results show an increase in the length of the bubble with flow oscillation. Analysis of the instantaneous velocity field near the LE shows flow fluctuation near the stall angle (11.3°-12°), but quasi-periodic behavior for fluctuation at 11.5° with a little change in frequency over time. Increasing AOA increases fluctuation frequency. Switching flow from separated to attached produces a vortex near the LE which deforms the shear layer on the airfoil.

Following these works, Radespiel *et al.*[102] used RANS simulations, and experimental 2D phased-locked PIV measurements on a SD7003 airfoil model at Re=6×10^4. The experiment was performed in wind and water tunnels for steady-state condition. Also, the water tunnel was used for the unsteady case with a plunge motion of k=0.52. Numerical results were in good agreement with experimental results; therefore, this shows the strong effects of unsteadiness on the LSB, and consequently, the flow behaviour including the transition and the turbulent features in flow. They claimed that based on comparison of numerical and experimental results, the unsteady transition model is an appropriate method. In addition, results reveal that the effect of transition and turbulence in the

unsteady aerodynamics of airfoils at low Re flows should be considered as an important parameter in the design and optimization of an airfoil shape.

The most recent work in this field has been done by Nati *et al.*[93]. They used planar time-resolved PIV for investigating the quantitative characteristics of the LSB over the SD7003 airfoil in flow with Re=3×10^4 while having a pitching oscillation motion. In addition, tomographic PIV was used for qualitative measurements for the same case study. Unsteady motion was modeled with a sinusoidal equation with mean of 6° and amplitude of 2° at k=0.2.

They state that the separation point was only found visually from raw images. The reattachment point was established from streamlines structures in time-averaged post-processed results. Similar to other papers, the transition point was measured as previous works by using Transition Exponential Method (TEM) where an exponential increase in Reynolds stresses occurs and the Transition Threshold Method (TTM) where Reynolds stresses:

$$\frac{\overline{u'v'}}{U_\infty^2} \leq -0.001 \tag{1.11}$$

The vortex roll-up location and the vortex shedding frequency were determined by wavelet analysis. Drift velocity or the movement of the vortex core with time was calculated manually to be used in drawing streamlines. They conclude that separation, vortex roll up, transition, and reattachment points have a hysteresis behavior during pitch up and down motion. In comparison to the steady case pitch up motion promote instabilities and pitch down motion delays them. The vortex shedding frequency increases in pitch up motion and decreases in pitch down motion showing a hysteresis behavior about the steady case. The structure of the transition and the reattachment phenomena from formation of the vortex rollers to breaking them to hairpin structures was visualized with tomographic PIV. Also results that structures of the shedding vortex are not affected by the pitching motion[93].

Experimental studies by Kim and Chang [59, 60, 61] have been completed on a NACA0012 airfoil in sinusoidal pitch motion with a fixed k=0.1 while the AOA changes from $-6°$ to 6° at Re=$23,000$, Re=$33,000$, and Re=$48,000$ by surface mounted probes and smoke-wire visualization. Their results show the sensitivity of unsteady BL to Re in low Re flow. Lift and drag are estimated by measuring unsteady pressure. The results show the variation of lift and drag coefficients hysteresis loops with Re.

Ol[96] presents a report which covers aerodynamics of the SD7003 in steady and unsteady low Re flows that is based on conference and journal articles from 2002 to 2010. Part of this report is allocated to the LSB in steady flow. In this study the airfoil model was tested

in 3 different facilities: a water tow tank, a wind tunnel, and a horizontal surface-free water tunnel. The main focus at steady flows condition is the transition between the laminar and turbulent flows in addition to the effects of Re, flow field conditions, and model geometry on the laminar separation and possible turbulent reattachment. Furthermore, the variations of the pitch-plunge parameter were studied in the unsteady flow. The goal of this work was to show which unsteady flow with low Re has an aerodynamics of a quasi-steady flow and the importance of laminar to turbulent transition in unsteady problems.

Gharali and Johnson[37] studied the effects of reduced frequency on an LSB and aerodynamic forces over SD7037 airfoil at Re=40,000 in pitching motion at AOA 9 to 14. Their results show with lowering k the LSB disappears faster. Also with increasing, either k or AOA transition point moves upstream. The height of the bubble increased (decreased) with increasing AOA (k).

The behavior of the BL on a NACA0012 airfoil in static and quasi-static pitch motion cases was studied by Rudmin *et al.*[109] at three transitional chord Re of 6.2×10^4 , 8.2×10^4, and 11.3×10^4 ($10^4 < Re < 10^6$). Pitch motion with k=0.025 was considered to produce AOAs of less than 6°. Results show aeroelastic oscillation in the transitional Re regime where the authors mentioned that "there are not many published studies". Similar to the static case, the characteristics of the generated LSB depend on Re and angle of attack so that with increasing each Re and/or AOA, the size of the bubble shrinks. They suggested that by studying a LSB in dynamic cases, it may be possible to change the flow in a way that prevents such oscillations.

Recently a CFD simulation on different NACA series airfoils at Re=200,000 at static and dynamic conditions has been done by Sharma and Visbal[119]. Figure 1.10 shows their surface pressure results over a NACA-0015. In this figure the transition region corresponds to Cp instabilities.

Also a LES simulation and smoke visualization has been done on a bionic airfoil by Ge [33]. Downstream of the shear layer roll-up, large scale vortex are observed that detaches from the bubble and moves downstream. Figure 1.11 shows velocity vector and static pressure field about the airfoil (top), with lower and upper surface pressure distribution (bottom). It is explained that at upper surface Cp, the flat region after the first pressure peak corresponds to the recirculation region ($x/c = 0.2 \sim 0.5$). The second peak shows the rolling up of the vortex at the end of the bubble. Following, the sharp pressure recovery presents the turbulent reattachment of the free shear layer. The highest pressure peak at the end confirms the large scale separated vortex. It is noted that the large scale vortex is responsible for the generated noise.

CFD can solve the flow with high resolution in time and space although as Zhang *et al.*[140] mentioned computational methods are useful in simplifying flow physics to simulate

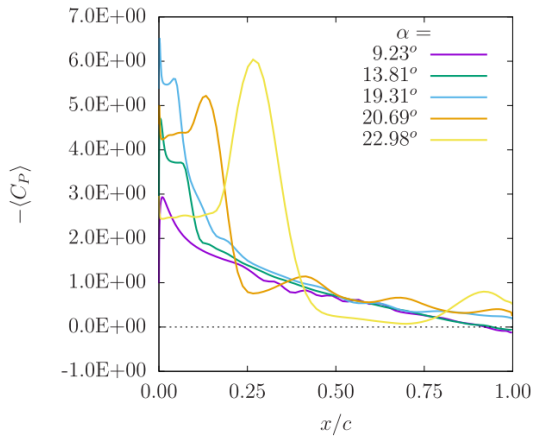

Figure 1.10: Span averaged pressure coefficient distribution over NACA-0015 at Re=200,000 at pitch up motion[119]

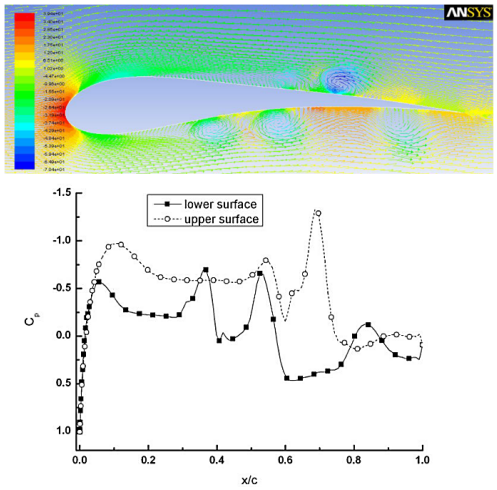

Figure 1.11: Surface pressure distribution over a bionic airfoil at $Re < 2 \times 10^5$, AOA=0° [33]

flow behavior, complexity of the flow structure around the LSB causes unknown conditions where simplifying the conditions in this area may not work properly. Therefore, providing an experimental data base for a thin airfoil family can help in understanding the flow and in developing computational methods[140]. Most experimental methods are limited in either time or space to identify coherent structures characteristics. Some techniques such as LDA, hot wire or fast transducers can collect temporal data at points. Others like PIV are limited in time resolution but provide high spatial resolution[68]. Time-resolved PIV can collect data with high temporal and spatial resolution. However, it is limited in measurement duration due to memory capacity, energy or frequency of the laser except for highly costly equipment[68].

1.4 Motivation and Objective

This study begins regarding boundary layer flow behavior at low Re flows. Although this is a long-studied subject, the scale of BL flow and laminar separation bubble phenomenon limits the experimental studies. Previous experimental works usually used large-scale models in visualization methods that demand large experimental facilities and equipment. In the case of PIV methods, a large FOV is usually divided into a few smaller ones to achieve enough spatial resolution and cover the whole model to study BL flow. Therefore, in addition to the cost of PIV facilities, the required time for experiments and data processing, and the size of the acquired images that need to be stored limits the experiments. These problems became even more considerable in the cases of 3D PIV, and TR-PIV. Therefore most available data are limited in case studies or FOV. Also, a lack of data is more noticeable for cambered airfoils that are mostly designed for low Re applications. On the other hand, BL flow is highly sensitive to the turbulence intensity of the flow and surface roughness of the model. Therefore, it is necessary to provide exact test conditions in case of combining the results. Larger facilities also could limit the minimum achievable Re that results in fewer data in low Re flows. Available previous data in dynamic flow usually used hot film, hot wire, pressure transducer, or LDV such that their configuration or physics does not allow capture of the whole flow field at once. Therefore those BL results are based on discrete point information and cannot be generalized on flow behavior or they are limited to a few case studies mainly because of added variables such as type and frequency of the motion. Therefore a review of prior research indicated that some knowledge gaps exist and motivated this study to attempt to answer some of the following questions:

Would it be possible to apply accurate low Re flow experiments using miniature models?

Would it be possible to study boundary layer flow over a miniature scale experiment?

How would it be practical to measure surface pressure (aerodynamic forces) on a small model?

Would it be possible to acquire surface pressure and BL behavior with PIV at the same time?

Would it be possible to measure skin friction in small scale experiments (with low values)?

How will the pressure field be affected by small vortical structures in the turbulent region after the reattachment point?

How does unsteady motion affect boundary layer parameters and LSB characteristics?

How do small vortical structures change with unsteadiness?

Do the effects of unsteadiness stay the same with changing Re?

Does the shape of the airfoil affect BL behavior?

How could the design of low Re airfoils be improved?

Therefore, due to an increased demand in the performance of low Re airfoils in applications the **objective of this research** was set to investigate accurate miniature scale low Re experiments unlike previous works and compare and validate these experimental methods to study low Re flow behavior in general and specifically laminar separation bubble characteristics over a cambered airfoil in steady and pitching motion. Also, to develop an estimation of the surface pressure coefficient and skin friction coefficient in a small scale experiment without using intrusive methods while studying BL flow was a goal of the study. To also provide experimental data for a wide range of case studies in pitching motion over a cambered airfoil where information is currently lacking. This research helped to answer the above questions although more studies will be required to answer the last question regarding the design of an optimum airfoil.

1.5 Outline of thesis

To follow the main subject of this study a summary of the thesis is provided here:

An overview of previous works, methods and available data on laminar separation bubbles in steady and unsteady flows have been presented in Chapter 2. Following this

chapter, three independent non-intrusive measurement techniques and results of their use are provided in chapters 3 to 6 in the following manner:

Surface Oil Flow Visualization (SOFV) and its application in steady flow In this part, whether surface oil flow visualization can be used over a miniature model of a SD7037 airfoil at low Re flow to characterize a LSB has been investigated. Experiments have been performed at four Re=32000,38000,41000, and 48000. Many attempts have been made to find a proper mixture for the experiment in this size to visualize the flow accurately. Applying a proper coating combination on a small size airfoil model decreased the required run time for each test noticeably. Low required runtime provided excellent visualization results so that flow regions are clearly recognizable and confirm the possibility of using this method at flows with Re lower than 30,000. The experimental method and set up are in Chapter 3 and the results presented in Chapter 5.

This method and a portion of the results are presented and published in "25th CANCAM Conference"[42], "1000 Island Energy Research Forum"[41], and "Journal of Physics: Conf. Series" [40].

IR-Thermography and its application in steady and unsteady flow The goal of this part was developing an IR thermography method on a miniature airfoil to study the LSB characteristics. Numerous approaches were utilized to create a temperature difference on the airfoil and obtain IR images for this study. Three successful heating methods established using aluminum and 3D printed airfoil models, but reflection effects and small temperature ranges were two significant challenges in developing this experiment. Techniques for post-processing the IR temperature data both temporally and spatially revealed several innovative approaches that provide details of the BL flow. Evaluating the entire airfoil allows the opportunity to obtain a comprehensive understanding of the LSB in chordwise and spanwise directions. The author is not aware of any other published research regarding IR-thermography on miniature airfoil models in low Re flow. The Experimental method and setup presented in Chapter 3 and the static results are provided in Chapter 5.

This method and the results have been presented and published in "Journal of Physics: Conf. Series" [40], and "18th International Symposium on the Application of Laser and Imaging Techniques to Fluid Mechanics" [44].

Particle Image Velocimetry and its application in steady and unsteady boundary layer flow In the following sections, whether a 2D PIV technique over a miniature

airfoil can be used to study boundary layer flow and laminar separation bubble characteristics are investigated. Many challenges including surface reflection and airfoil vibration have been solved throughout the experimental setup (Chapter 3) and post-processing of data (Chapter 4). The high quality of the PIV images provided the possibility of detecting LSB characteristics (separation point, reattachment point and height of the bubble) from raw images. But to gain in-depth information regarding BL flow and LSB, different image processing methods with their advantages and disadvantages are presented in Chapter 4. The theory of different approaches to extract data from the measured velocity field from PIV, such as calculating the surface pressure coefficient, skin friction coefficient, integral boundary layer parameters and proper orthogonal decomposition are discussed in Chapter 4. Sample measured results are provided to support each method to estimate the ability of the method in the study of LSB characteristics. Because there is no literature regarding surface pressure distribution and BL flow information on the SD7037 airfoil, XFoil has been used to examine the results in some cases. Various approaches have been used in investigating the effects of Re and AOA on a steady BL flow and LSB that are presented in Chapter 5. Also, unsteady BL flow was examined using different post-processing methods and the effects of reduced frequency, AOA and Re are studied. Airfoil dynamic results for many cases are summarized in Chapter 6. There is no other publication that the author is aware of that studies effects of reduced frequencies on integral BL parameters, skin friction and surface pressure distribution using PIV on SD7037 airfoil. Also aerodynamic forces in static and dynamic flows are calculated from the velocity field through a volume control method to investigate the effects of LSB on aerodynamic forces.

This method and parts of the results were presented and published in "18th International Symposium on the Application of Laser and Imaging Techniques to Fluid Mechanics" [44] and "19th International Symposium on the Application of Laser and Imaging Techniques to Fluid Mechanics" [43].

A summary of the conclusions are highlighted in Chapter 7.

Chapter 2

Methods and Experimental Setup

The first step in doing an experiment is to consider important and influential relevant variables to establish similarity between the experiment conditions with the original model. This similarity includes three subsets; geometric similarity, kinematic similarity, and dynamic similarity. As it is clear from geometric similarity's name, the model and prototype should be similar in shape so that all lengths scale with one scale factor from prototype to model. In kinematic similarity, in addition to the geometric similarity, there should be similarity in motion, a time scale factor. Dynamic similarity requires both first similarities in addition to constant force scale factor for all forces in model and prototype. In this experiment which is considered an incompressible flow (since $M < 0.1$), to meet dynamic similarity, geometric similarity plus similar Reynolds numbers are required therefore the planned experiments are designed to simulate the real conditions for low Re applications.

In the following sections all facilities and experimental setups are explained in detail.

2.0.1 Wind tunnel

All experiments have been done in a closed circuit subsonic wind tunnel belonging to the wind energy group at the University of Waterloo. This tunnel was built by Sperandei[127] to be used with optical measurement techniques such as PIV and LDA and is located in the Turbulent flow lab. The dimensions of the test section are $152.4mm \times 152.4mm \times 450mm$. Due to a need for optical access the test section was modified and constructed of float glass with 2mm thickness. Float glass has been used because it has uniform thickness with a high degree of light transmission[8]. A tube axial fan produced the required air flow with a maximum rotation rate of 3450 rpm. The fan is controlled by a variable frequency drive

with input frequency of 0 to 60 Hz that can change the tunnel velocity from 0 to 36m/s in the test section [99, 127]. It is a low speed wind tunnel so the turbulence intensity (TI) plays a critical role in simulating the conditions in the real world. Orlando [99] modified wire mesh screens with ones with a porosity of 65% and mesh length of 0.85mm to reduce TI of the tunnel. Measured turbulence intensity for this tunnel is less than 1%.

Figure 2.1 shows the wind tunnel schematic. Calibration of the wind tunnel has been performed before and after running the experiments by the wind energy group of the University of Waterloo using manometer, pitot tube and PIV at the mid plane of the test section. The results of wind tunnel calibration are presented in Figure 2.2. Temperature of the tunnel also measured during the calibration process and experiments.

The next step is manufacturing an airfoil model. Determination of the model size is one of the most important steps in preparing the test equipment. It is described in the following section in more detail.

2.0.2 Airfoil model

As explained in the small wind turbine section, small wind turbines use stall regulation as a passive control and they are highly dependent on aerodynamic design. Stall regulated turbine airfoils should be insensitive to the undesired roughness at Cl_{max} to decrease the power lost and make performance more predictable. The SD7037 airfoil, designed by Selig and Donovan in 1987, is one of the airfoils that its Cl_{max} is not sensitive to roughness[45] and reported an applicable airfoil for stall regulated small horizontal axis wind turbines[36, 45, 46]. It is a low Re airfoil with maximum thickness of 9.2% at 26.1% chord. Thin airfoils have a lower adverse pressure gradient than thick ones because it decreases the pressure peak at the LE of the airfoil[125]. The maximum camber of this airfoil is 2.5% at 44.7% chord. In comparison to the NACA0012 airfoil, this airfoil has a larger camber and less thickness, shown in Figure 2.3. The combination of all these features can increase the possibility of creating a stable LSB in most airfoil operating conditions so that the existence of a LSB for this airfoil is reported even at Re=500,000[85]. Increasing Re from 60,000 to 300,000 does not change the lift coefficient at AOAs 0° to 10° although unusual behavior has been seen in the drag polar graphs at lower Re (Re=60,000 and Re=100,000) that is presented by Selig *et al.*[118]. This might be due to the dramatic changes of drag coefficient with Re. The hypothesis is that, increasing the drag force at lower Re could be related to the existence of LSB. The smoothed coordinates for SD7037 airfoil that is called SD7037(c) and used in previous experiments[36, 118] has been used in this study as well.

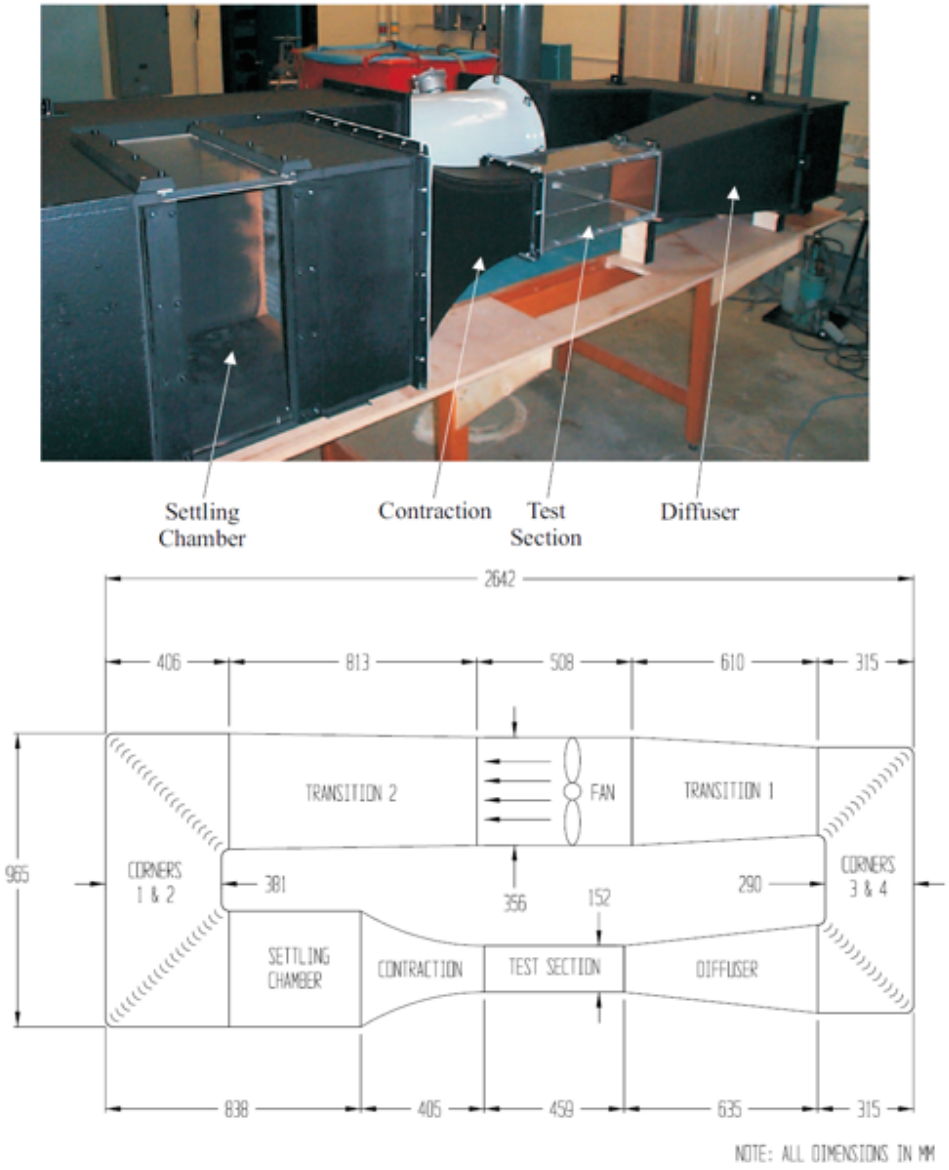

Figure 2.1: Test section side view and schematic of wind tunnel in detail[127]

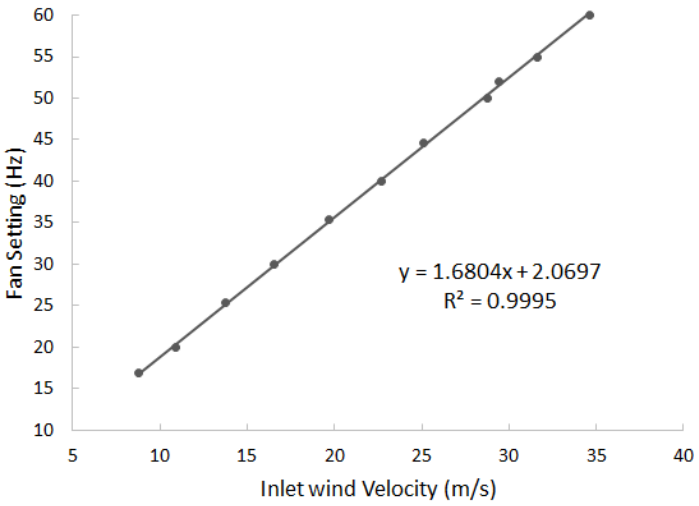

Figure 2.2: Inlet wind velocity and temperature versus VFD fan setting (Hz)

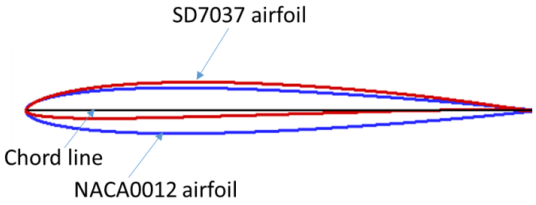

Figure 2.3: Schematic of the SD7037 airfoil compared with NACA0012.

Regarding the selected wind tunnel, there are three limitations for the size of the model. First; the blockage ratio of the tunnel, second; providing the required Re for the test based on the available wind tunnel fan speed, and third; the span of the model.

Solid blockage is defined as[9],

$$BlockageRatio = \frac{Object\ frontal\ area}{stream\ cross\ sectional\ area} \tag{2.1}$$

This ratio has an effect on the approaching flow speed and consequently on dynamic pressure. To assume no change in surface stress in wind tunnel tests, an acceptable blockage ratio range is considered to be from 1% to 10%, and usually it is chosen to be less than 5% [9]. It means that there is a limitation for the model in reference to the cross section of the wind tunnel. Both the size of the airfoil model and the airfoil angle of attack has an

Figure 2.4: Manufactured SD7037 airfoil model.

effect on this. Regarding the limitation, in this experimental test plan, angles of attack are considered to be less than 17°.

The desired Re based on provided information in section 1 are selected to be about 2×10^4 - 5×10^4 which means the chord length can be around 25 mm. The last limitation is the span of the airfoil, since the experiment was assumed to be two dimensional (2D). The span length was considered to be same as the width of the test section. In examining the 2D tests, OFV has been done and 3D behavior has negligible effects at wall boundaries, since the measurement is performed at the middle of the test section then the assumption of 2D flow is allowable and confirms results of the previous experiments that are performed in the tunnel[99].

Regarding all described limitations, the chord length for the airfoil model can be about 24 mm to 27mm. For manufacturing the airfoil, aluminium was selected which Sciacchitano and Scarano [113] mentioned based on Kahler's work [58] a polished aluminum surface has a minimum diffuse reflectivity compared with other materials such as steel, plastic, glass, and PMMA. The airfoil is machined using a three axis CNC mill which has a 0.025 mm tolerance (In the Appendix A there is a mechanical drawing of the airfoil). Then it was anodized and painted black to decrease the reflection from the surface as much as possible. It is attached to the rotation shaft at a quarter of the chord that makes it possible to mount the airfoil at the tunnel and attach it to a brushless servo motor for changing the angle of attack and test conditions. The chord length of the airfoil after manufacturing is 25.8mm. This chord length, 25.8mm, covers the desired Re ranges and keeps the blockage ratio in an acceptable range, Figures 2.4 and 2.5. To adjust the airfoil to a zero angle of attack an angular adjustment device used by Gharali[36] and a new fabricated one that is shown in section 2.3.2 was utilized.

2.0.3 Dynamic motion control

To adjust the airfoil to a determined angle and also for simulating the pitching part of the airfoil's dynamic motion, a brushless servo motor *T0603-A0-N-CG-N-F-A-A Cleveland Motion Controls MDM-5000* was used. This servo motor was selected by Gharali [36] based

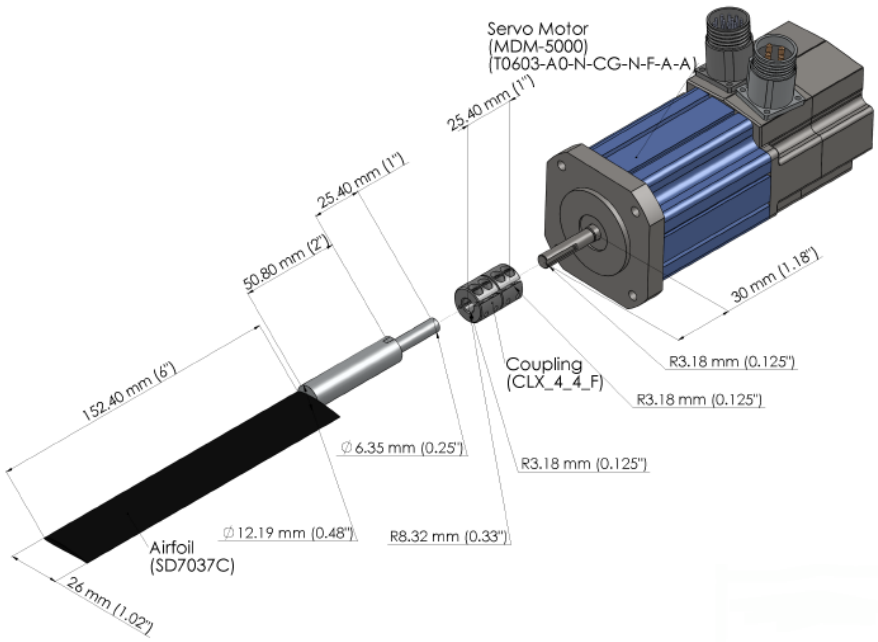

Figure 2.5: Servomotor in addition to the coupling and model [36]

on the anticipated loads and required RPM. In this servo motor each degree of rotation represents 22 steps which create high precision motion in high frequency movements. In addition, this series of servo motors have low rotor inertia that makes it suitable for simulating fast sinusoidal movements[36]. With an Input power of 24VDC/12A which is provided by power supply (PSR-12-24), the maximum speed will be 508RPM/60 Hz for 360 degree in continuous rotation. A PID controller was used to trigger the motor and PIV system. It locates the airfoil at the desired angle of attack according to the defined motion, Equation 1.5. Figure 2.5 shows the motion setup in addition to the airfoil model [36].

2.1 Oil Flow Visualization

As explained in previous sections, one of the methods which can be used to determine LSB characteristics is SOFV. In this method, the upper surface of the airfoil can be painted with a light pigmented oil mixture. The process requires placing the airfoil in the running wind tunnel for a few minutes. The pigmented oil moves with the local flow in accordance with the skin friction of the BL and surface tension of the oil[116] so the flow pattern and shape of the streak-lines on the surface are stabilized and observable after a specific time. Required

time of running the wind tunnel is dependent on the mixture of oil, freestream velocity, and size of the model. When the oil mixture has dried, the model can be taken out for photographing. With this method the different region of flows and LSB are determinable.

Figure 2.6 shows the applied OFV experiment set up. This setup includes the closed subsonic wind tunnel, SD7037 airfoil model (c=26mm), and the servo motor that are explained above in addition to a Nikon D70 camera with a Nikkor 50 mm F/1.8 lens that has been used to take pictures. Using a proper oil mixture depends on the flow velocity and the surface roughness. Based on literature review, many different oil mixtures were evaluated during the development of this study to identify different flow regions on a miniature airfoil. The final oil mixture used in this study contained mineral oil, (Monarch Oil #70 with a density of 0.842 to 0.8639 kg/L at 15°C), titanium dioxide and a very small amount of linseed oil (the ratio of mineral oil to titanium dioxide to linseed oil was 15:15:4). Then for every freestream velocity and angle of attack, it was painted on the surface of the airfoil with a thin and smooth paintbrush, Figure 2.7.

It should be noted that to reduce the oil viscosity, for each 8 m/s velocity decrement, 1 droplet of linseed oil was added to the mixture. In this study after 5 to 10 minutes of running the wind tunnel, the oil mixture had dried and the model was taken out for photographs. The camera with a Nikkor 50 mm F/1.8 lens has the resolution of 3008×2000 pixels. The field of view for all the images was fixed at 422mm×277mm[42]. In the results, tests were completed for different low Re, with the angle of attack changed from 1° to 11°.

2.2 Infrared Thermography (IT)

In the past, many experimental methods and visualization techniques have been used to facilitate the investigation of the boundary layer flow such as pressure tabs, hot films, pressure sensitive paints, particle image velocimetry, SOFV and IT [7, 19, 42, 44, 103, 106]. Most of these methods are more challenging when dealing with small or complex model sizes, and low Re flows [47]. For example, placing pressure tabs in complex or small geometries would not be practical. With advancing technology in infrared cameras, IT provides high resolution visualized data. Heat flux between the surface and flow is different for laminar and turbulent flows. As mentioned, in low Re flows, LSB forms due to the laminar flow separation and turbulent flow reattachment therefore detecting these areas utilizing IT allows the opportunity of detecting LSB characteristics on the surface of the airfoil [20]. A useful study related to separation detection using IT was reported [23] where the flow about a cylinder was studied and also investigated the separated flow area in deep stall condition over an airfoil using thermographic imaging, and temperature fluctuation to

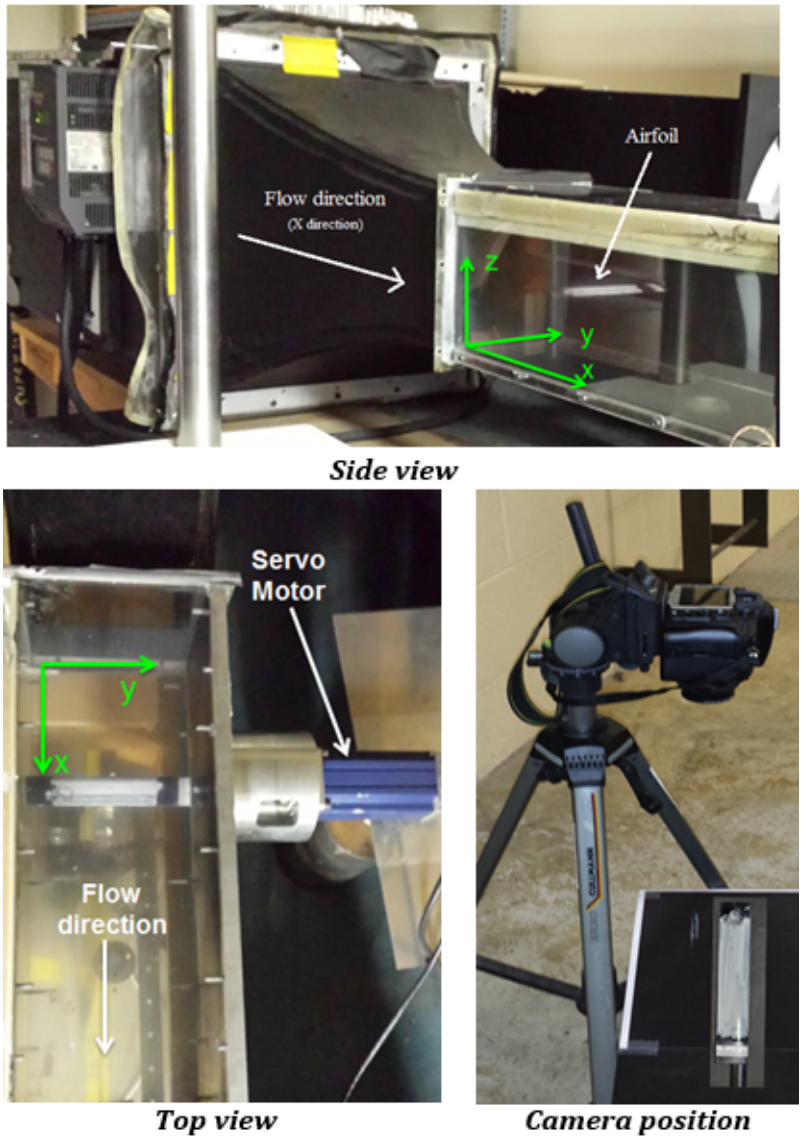

Figure 2.6: Oil flow visualization setup

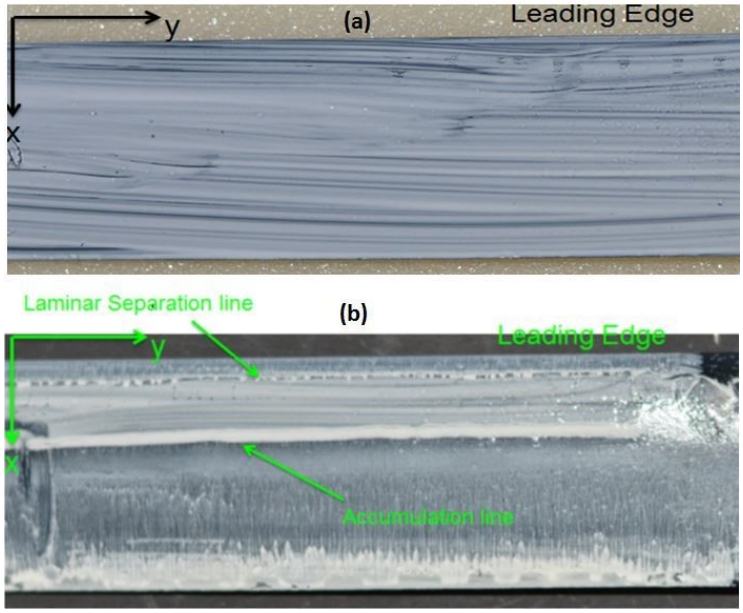

Figure 2.7: Sample pictures from the surface of the painted airfoil a) before turning on the wind tunnel b) after turning on the wind tunnel

detect the separated flow. Simon *et al.* [122] studied the laminar-turbulent transition on a flat plate using several heating methods and stated that overall internal heating was more suitable than others. As expected, the heating method and post-processing techniques are more crucial in unsteady cases where the temperature changes due to irregular unsteady structures. In this regard, here different heating methods and post-processing techniques were investigated in the steady case to evaluate the possibility and accuracy of using them for unsteady cases of complex flow about wind turbines in subsequent experiments.

For this part, three airfoil models of SD7037 airfoil with $25.8mm$ chord spanning the entire tunnel width were used, one precision machined from aluminum (details are in section 2.0.2) and the other two 3D printed from polycarbonate material with enhanced resolution using the same coordinates that were used for the aluminum model. Although using a small model is a very challenging task when working in the vicinity of the surface using thermography it does allow a high resolution of the local flow. In the results, tests were completed for constant Re = 48000, with the angle of attack changed from 0° to 13°. The IR camera used in the infrared thermography experiments is a T650sc FLIR camera with an array of 640×480 pixels while the thermal sensitivity is $< 20mK@+30°C$. Minimum focus distance is $0.15m$, and the image acquisition frequency is $30Hz$ at the full array. The detector type is Focal Plane Array (FPA), uncooled micro bolometer with a spectral range

between 7.5 and 14μm. Figure 2.8 shows a schematic of the experimental setup. The walls of the wind section have been shown as clear material, but in the experiment, clear glass walls of the wind tunnel were replaced by less reflective walls to prevent inappropriate reflections.

In these experiments, airfoil heating was accomplished by using three different methods including two active and one passive approach.

First, Joule heating was implemented with a resistive heating wire mesh on the pressure side of the aluminum airfoil. For the mesh, the heating wire is bent in a zig-zag formation to heat the airfoil evenly along its span and chord and to have the least amount of effect of the flow around the airfoil, a thin heating wire with a diameter of 0.25 mm is chosen. A thin layer of Kapton tape is placed between the airfoil and the heating wire due to the conductivity of the airfoil. Another layer of Kapton tape is placed on top of the heating wire mesh to prevent direct thermal contact with airflow while keeping it attached to the airfoil's surface, see Figure 2.9. Although using regular heating pads are more common and available, size constraints prevented their use. Therefore, design and custom fabrication of the tools to heat the airfoil uniformly was necessary.

Second, the suction side of the 3D printed airfoil was uniformly coated with electrically conductive paint. This method could eliminate the errors caused by the non-uniformity of heating distribution on the surface. Also, there are no considerable temperature changes in flow in the vicinity of the airfoil surface because there is no need to heat up the entire airfoil, just the suction side. Figure 2.9 shows prepared airfoils for the first and second methods.

In the ***third*** method an air heater was used to heat the airfoil surface (both aluminum and 3D printed models) to the desired temperature then the wind tunnel was turned on, and temperature changes were recorded. After a few seconds, constant behaviour was seen for awhile before the airfoil cooled down completely. The printed airfoil was a better option than aluminum because of its heat transfer characteristics. However, post-processing of data from passive methods is more challenging than active methods and data should be observed precisely to find the desired time and extract the proper data.

Reflection effects and small temperature ranges are a significant matter in low Re flows with the existence of LSB, because of a slight temperature difference after the turbulent reattachment point that can be due to the irregular movement of existing small vortices or possibly a reflection error. Therefore solving reflection problems is one of the priorities in thermography experiments[40].

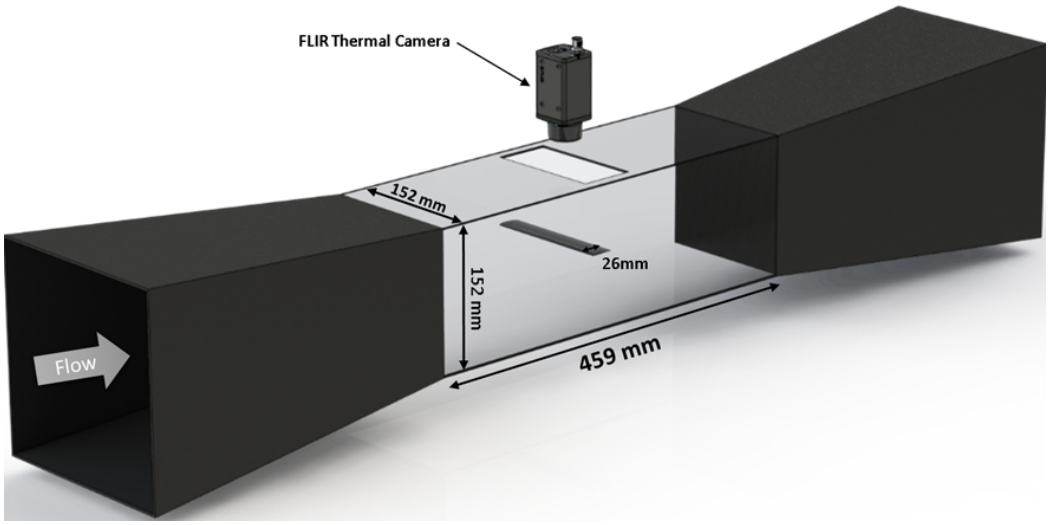

Figure 2.8: Schematic of wind tunnel and IT thermal camera experimental setup.

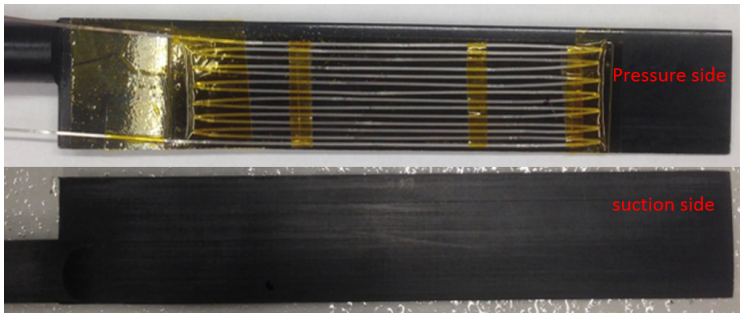

Figure 2.9: Resistive heating wire mesh on the pressure side of the aluminium airfoil (top) the suction side of the 3D printed airfoil coated with electrically conductive black paint (bottom)

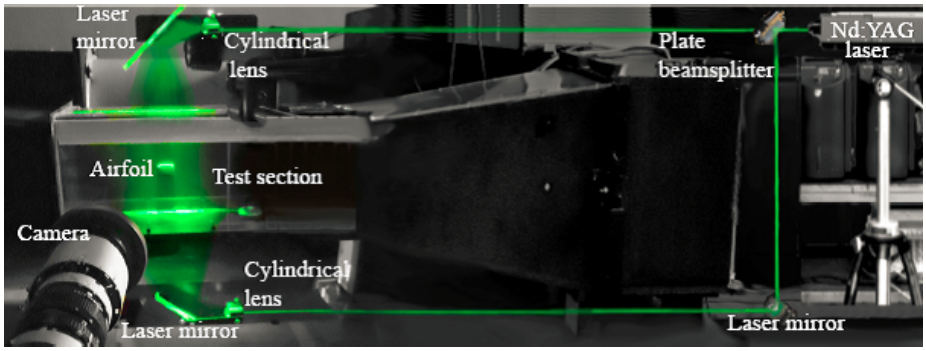

Figure 2.10: A schematic of the PIV experimental setup[36]

2.3 PIV Technique

The objective of the third part of the experiments was visualizing the LSB on the desired airfoil using PIV. The first step used oil flow visualization to show the existence of LSB in selected flow conditions with high accuracy. Since OFV is a qualitative method, then the next step was confirming the results using thermography and PIV. PIV also gives the opportunity to calculate the performance of the airfoil through calculating aerodynamic forces, in each test condition. Therefore, 2D PIV was used to obtain two components of velocity. Figure 2.10 shows the PIV experiment set up. More details of the dimensions are presented in Figure 2.11. As can be seen the experiment facilities include a dual head laser, wind tunnel, motion control system, camera, and optical instruments, in addition to the airfoil model.

2.3.1 PIV setup

Particle image velocimetry (PIV) is an experimental method for visualizing the instantaneous fluid flow by determining vector velocities through visualizing tracer particles. This method first was presented in 1983 by Meynart[11, 88]. PIV was improved from 1983 by developing the involved technologies such as computers, and lasers, etc.[11]. Figure 2.12 briefly shows the whole process of the PIV technique.

The following section explains PIV technique requirements which are used in the desired experiments in detail.

Flow seeding, The principle of flow visualization by PIV is seeding the flow with tracer particles and taking image pairs with a determined time interval, *dt*. The time interval

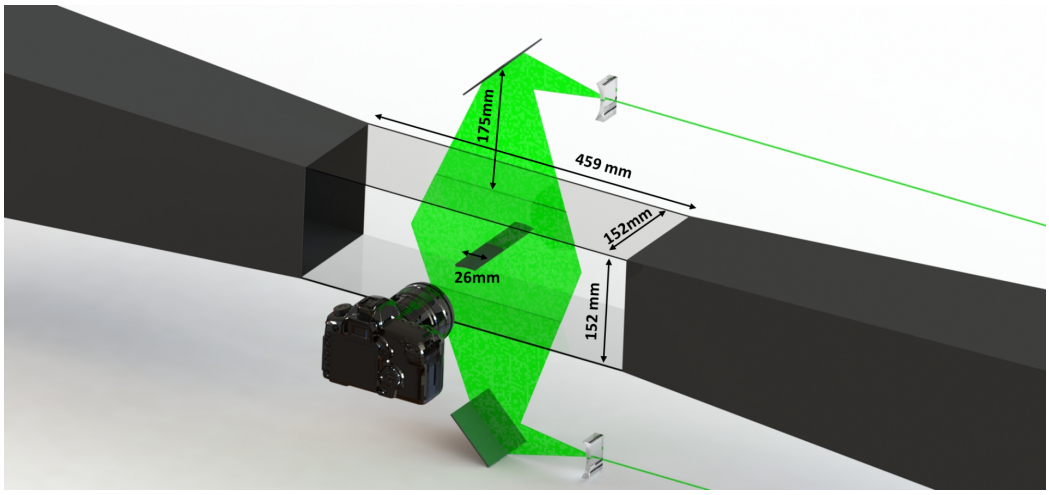

Figure 2.11: Experimental setup with size details

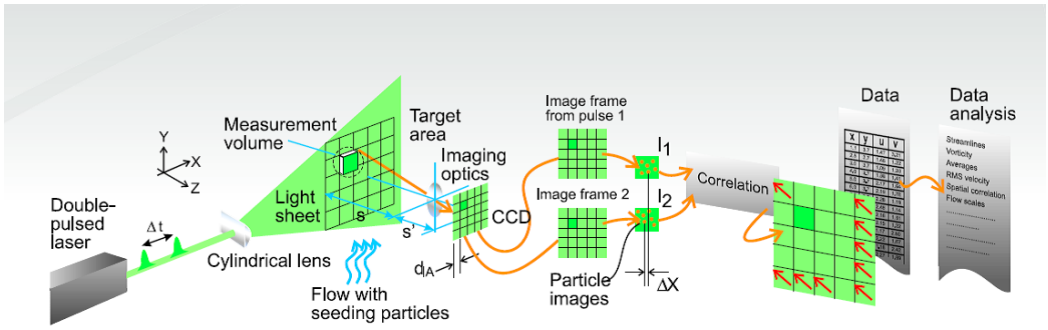

Figure 2.12: PIV technique[5]

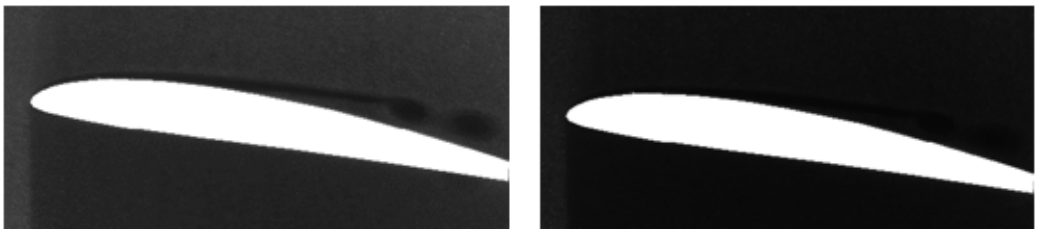

Figure 2.13: The effect of different power in dual pulse laser ($9° - 25$ Hz with white mask)

depends on some parameters such as the velocity of the fluid and interrogation area (IA) size. The velocity field calculation is based on linear behavior, $v = \frac{dx}{dt}$where dx is the traveled distance by a tracer particle in time interval of dt. Two features are necessary in choosing tracer particles; they should be large enough to scatter light properly, their size is in order of $0.1 - 50\mu m$ [1] and the weight ratio of the particle compared with the fluid should be such that particles follow the flow. If particles are heavy, they will not follow the flow, and if they are too light they cannot overcome buoyancy forces. In ideal conditions the density of particles should be same as the density of fluid[1, 127]. If flow seeding is more uniform, higher quality images will be obtained. In this setup a smoke generator (Antari-Zseries 1200II) with water based (UVG) fog liquid has been used.

Light sheet Optics, As can be seen in Figures 2.10 and 2.11 experimental setup in detail, the optical configuration including a beam splitter, mirrors, and cylindrical lenses were used to create two light sheets which come exactly at the mid plane of the test section from the top and bottom. Having two light sheets provide the possibility to cover the whole area around the airfoil. The first mirror that changes the direction of the beam from vertical to horizontal is a Line mirror (Edmond Optics) which can reflect more than 99 percent of the beam to ensure creating even beams[36].

Lasers, The laser used in these experiments is a Nd: YAG laser (New Wave Research Gemini PIV/15Hz). It's a dual-cavity laser which has the ability to produce two pulses of 5ns duration and 532nm wavelength with a micro second time difference[11, 36, 94].

Figure 2.13 shows the importance of aligning the two laser beam at the mid plane while working with shallow depth of field. In this pair of images, the first laser beam precisely aligned with the mid plane (left picture) while the second beam is slightly misaligned (right picture). As can be seen the second frame is totally dark makes following the particles impossible or adds unacceptable errors. In addition to the beams alignment, the quality and power of the beams are different that should be considered while setting up each beam.

The time interval is chosen carefully regarding the tunnel velocity, and IAs sizes. Also some experiments in an empty tunnel have been done using different time intervals to make sure that the calculated velocity from the PIV images are correct. Looking at the image pairs is a practical method to estimate the number of pixels for a displaced particle from frame 1 to 2. It gives an estimation to compare the time interval with the calculated time interval, dt, from equation 2.2.

$$dt(s) = \frac{pixel\ motion(pixel) \times \frac{size\ of\ field\ of\ view(m)}{Resolution\ of\ images(pixel)}}{Inlet\ test\ section's\ tunnel\ velocity(\frac{m}{s})} \tag{2.2}$$

where *pixel motion* is the number of pixels that the particles move in an image pair and usually can be around 3-10 pixels. This formula has been used in the wind energy group of the University of Waterloo for years. The calculated time interval is validated by the size of the IA and estimated velocity of the particles at minimum IA using equation 2.3. In these experiments time interval was set around $2 \sim 18\mu s$ based on different conditions.

$$\frac{\frac{size\ of\ field\ of\ view(m)}{Resolution\ of\ images(pixel)}|\triangle u|_{IA}dt}{size\ of\ IA(pixel)} < 5\% \tag{2.3}$$

Camera, The camera that is used is a Flow Sense EO 4M camera with 60mm/105mm f/2.8, and Nikkor lens. 20.4 fps at full resolution, 2048px×2048px. Three different fields of view were selected to provide accurate information regarding the flow field about the airfoil, the laminar separation bubble (LSB), separation, reattachment and vortices. These three FOVs together provide high resolution data to fully study the flow field behavior about the airfoil. The first FOV (coarse level) is about 2.5C to cover whole flow field about the airfoil. This FOV can be used to measure aerodynamic forces about the airfoil and cover existing phenomenon downstream of the airfoil's TE. Since the airfoil dimension is less than 30 mm, this experiment does not require an extra camera or stronger laser to cover the field which is a huge benefit in saving time in both acquiring and analyzing the data, in addition to avoiding the errors associated with using multiple equipment[36].

The second FOV (fine level) is about the length of the chord (∼26 mm). Mostly acquired data from this FOV has been used to characterize the LSB features in detail. Then the last FOV (superfine level) is about 0.6C and has been chosen based on the location of the transition point that is determined from the second FOV. This level is mostly used to study the phenomena after the transition point and close to the reattachment point (turbulent flow) that are associated with the existence of the LSB. Therefore, the focus of this part is mainly on after bubble vortices behavior using POD post processing.

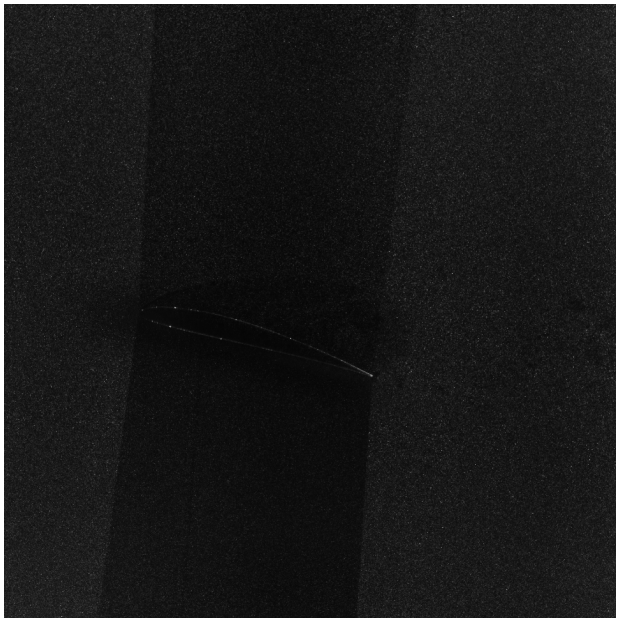

Figure 2.14: Sample PIV image

A calibration object is placed in the middle of the test section with calibration marker points in both vertical and horizontal directions. Comparing the distance of marker points in images and real objects determine that the camera is mounted precisely perpendicular to the laser sheet or if there are some offsets. Also, comparing these distances gives the image aspect ratio to calculate the velocity vectors.

For each experiment(case) between 300 to 1000 pairs of images have been acquired. Figure 2.14 shows a sample PIV image taken for pitching motion case. Figure 2.15 shows an enhanced and brightened sample to illustrate different FOVs. The test section and airfoil surface were cleaned regularly during the tests to avoid any smoke accumulation on the walls.

2.3.2 Experimental setup improvements

After each step of the experiment based on the acquired results it was possible to improve the experimental facilities or setup to improve the quality of later results. Here are some adjustments that are considered during the current experiments.

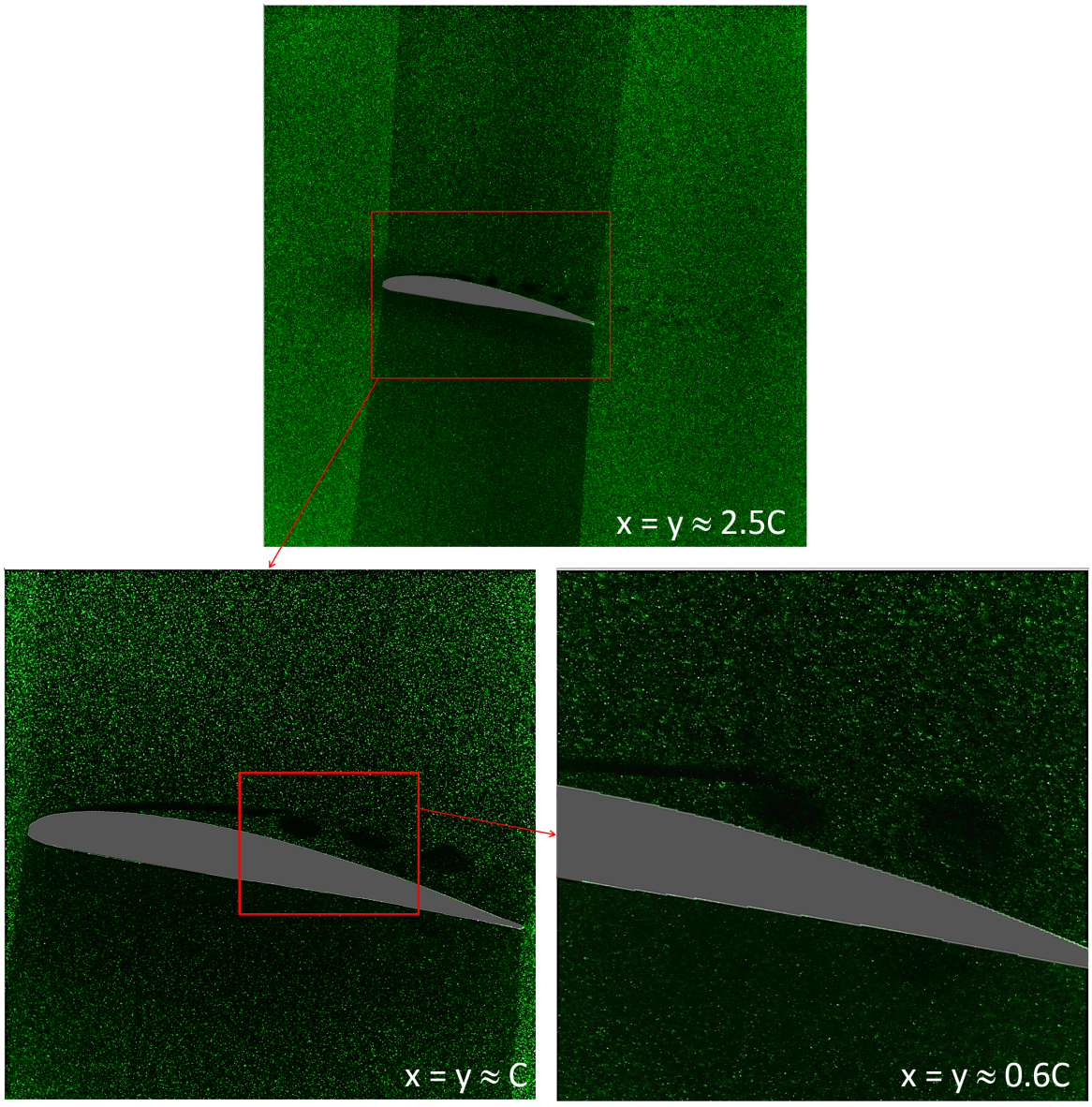

Figure 2.15: PIV images FOVs

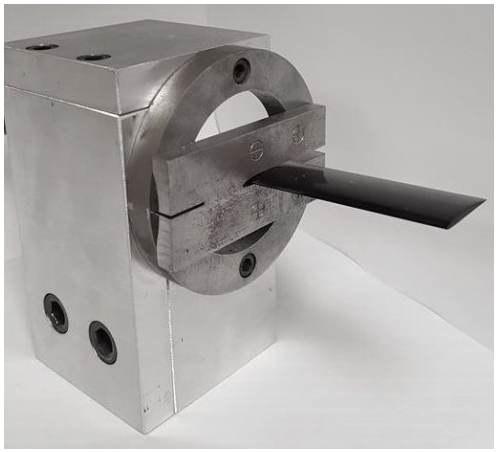

Figure 2.16: Adjusted calibration device.

Angular calibration device, After taking PIV images and analysing the data, it was shown that there are some errors in the accuracy of the angle of attack. Therefore an angular calibrator was designed and manufactured that can be adjusted to the airfoil from the LE and shows the angles of attack before starting every set of tests and after finishing it. If there were non-negligible errors they would be determined and solved. Also, this calibrator is designed so that its width is half of the test section width with four circles on its surface. Therefore it is used as a calibration tool to make sure the camera is located in the right position and the correct angles, Figure 2.16.

Sift PIV images through in-house program, This is a handy program to be applied to compare the original airfoil coordinate and the desired AOA by the position of the airfoil in PIV images to give an exact angle of attack. This useful program has the option to open all 400 images together then it is possible to calculate how much the airfoil moves during every set of experiments and eliminate data with a high error in AOA. Measuring the amount of vibration or movement would help because small changes in the AOA, even less than 0.5°, especially in the trailing edge area have a large effect on following the created vortices. In consequence, it changes the LSB features. This will be explained in more detail later. Figure 2.17 presents a screenshot of this program and its application.

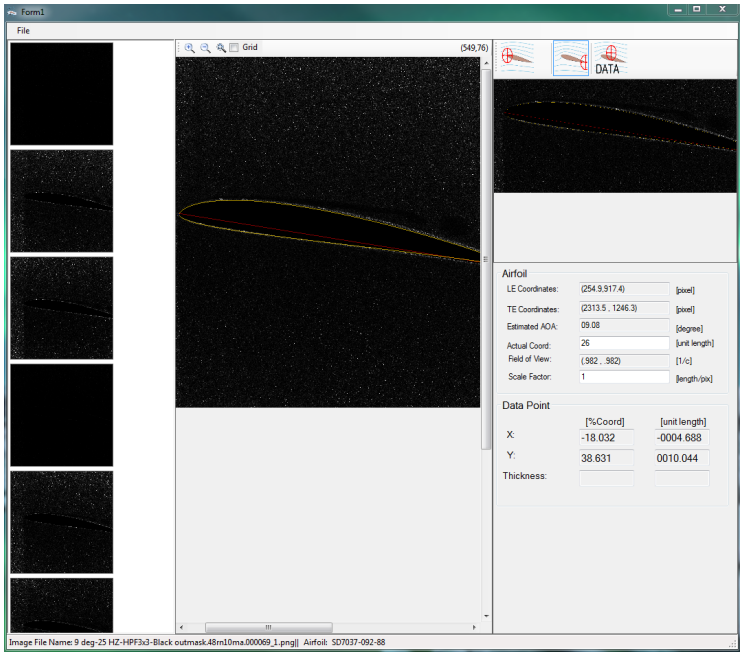

Figure 2.17: Example of program application

2.4 XFoil program

XFoil [27] is a user friendly program that is written in FORTAN to analyze viscous/inviscid subsonic airfoils. This program can be used for design/redesign of low-Re airfoils with LSB. XFoil using inviscid linear-vorticity panel method computes potential flow about the airfoil then uses a global Newton method to solve the BL equation along the airfoil[27, 83]. There is a critical N-value that is related to the point of transition to turbulence and usually considered as 9. Using the skin friction coefficient the location of separation and reattachment points and subsequently, the length of the bubble could be examined by XFoil. But Xfoil cannot modify the recirculating flow by velocity profiles to determine the height of the bubble. Ol *et al.*[97] compared the experimental results with calculated XFoil results for SD7003 airfoil in Re=6×10^4 then conclude that the location of separation and reattachment points at AOA=4° are in a good agreement for experimental and XFoil results. Also, McGranahan and Selig[85] compared experimental and XFoil results. They found that the results of XFoil for the reattachment line are more reliable than the results of the separation line[27].This program is released under the GNU General Public license[26].

2.5 Challenges

Like all experiments, this work faces many setup challenges. Although the size of the experimental equipment added a few more challenges to the setups including; airfoil vibration with increases in the aerodynamic loads on it during the PIV experiment. In this study the airfoil was supported from one end to give the opportunity of taking the stream-wise pictures without blockage. This vibration was more considerable in dynamic than static cases. A practical solution was supporting the airfoil from both ends of span without blocking the camera. The first solution was drilling a 0.5mm hole at the quarter chord of the airfoil and at the same location on the test section window to locate a pin and support the airfoil. This method solved the vibration problem but drilling the hole after building the airfoil increases the risk of drilling this tiny hole at a quarter chord of the airfoil and caused a slight twist at the airfoil span that affects the results. The second solution was attaching a hemisphere to the end of the span with a maximum diameter less than airfoil thickness with minimum possible friction to support the span on the test section glass without deforming the airfoil or blocking the FOV. The second method provides excellent results in supporting the airfoil and reducing the vibration.

The airfoil surface reflection in the PIV experiment is discussed in section 3.1. The BL thickness is very thin especially in laminar flow, and the surface reflection could affect the dominant region of interest. In dealing with this problem, the airfoil was anodized in black. Also, different setups for laser intensity and amount of released smoke in every test were examined to find the minimum reflection in the vicinity of the surface.

Another challenge was using the metal airfoil model in IR thermography. Heating the airfoil uniformly using a resistive heating wire mesh needed a custom-designed tool. The heating pads available in the market are very thick and mostly rougher than general airfoil surfaces that sometimes even need an extra layer of smoother material on top. In using large models, it may not dramatically affect the results but in this case, using a thick layer could change the effective surface shape of the airfoil. Therefore a very high resistive thin wire was wrapped in a Kapton tape to solve the problem due to the conductivity of the airfoil and prevent the direct contact of the wire with airflow.

Chapter 3

PIV Image Post Processing

Post processing is the next step after acquiring PIV images. In general, the velocity field can be calculated from PIV images with different methods. Using different analysis methods can produce different results because it can ignore or emphasize a particular piece of data. Dantec Dynamic Studio software[22] was used for the post processing of the PIV images.

3.1 Image Analysis

Cross Correlation

As explained before a velocity field is calculated from an image pair based on the distance traveled by the particle and the time difference between two images. The images are divided into smaller areas named interrogation areas (IAs). If N is a size of IA in pixels, the typical particle movement has to be less than N/4 in the area[127, 135]. Having two single-exposed images is necessary for cross-correlation. To determine the particle displacement, cross-correlation is applied for each pair of IA. The mean particle motion within the IA will be the peak location in the cross-correlation domain. By having a ratio of physical/pixel domain and time between two frames of an image pair, this particle motion of each IA can be converted to the velocity in the physical domain[21, 127].

Figure 3.1 shows the cross-correlation map for different areas of one sample image pair. A closer look reveals that under the black line which is like a separation line there were fewer particles for cross-correlation although there are enough particles that the peak is detectable.

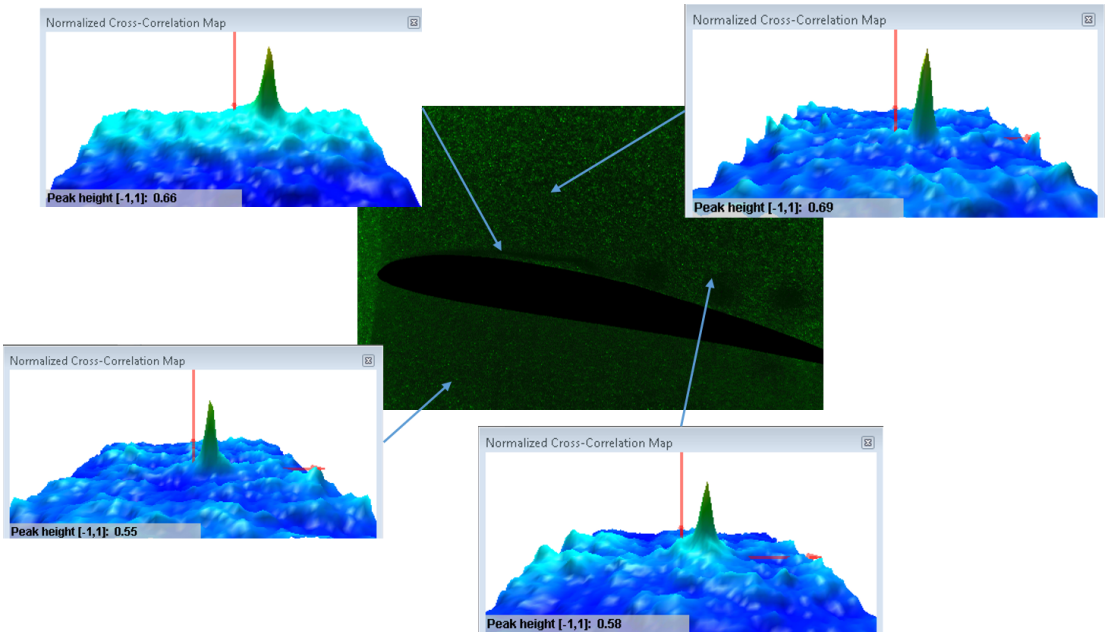

Figure 3.1: Illustration of the cross-correlation at different locations (sample image)

Adaptive Correlation

Adaptive correlation is a post processing method to calculate the velocity vectors. In this method, in addition to the final interrogation area, IA, n as a number of refinement steps, should be selected. For example consider a final IA=16 $\times$ 16 pixels and n=3, an initial IA would be 128 $\times$ 128. In this method intermediary results will be used as information for the next step of a smaller IA size. Overlap for neighboring IAs can be defined in both horizontal and vertical directions independently therefore it can increase the resolution of the velocity vectors, Figure 3.2.

The correlation method uses Fast Fourier Transform (FFT) for image correlation and processing. This method assumes a cyclic pattern for particles inside an IA and causes an error that can be decreased by selecting the proper IA size and considering a suitable time between the image pairs. Using a top hat window function, it is possible to remove 25% of an IA from each edge then post processing will be done on 50% of the IA. Using 50% of IA will decrease the signal strength; to solve this problem a large IA should be chosen that for a boundary layer calculation does not sound logical. Another option for adaptive correlation is using a high accuracy module and window deformation; for the high accuracy module regardless of fitting a correlation peak model, a sub pixel algorithm can be used.

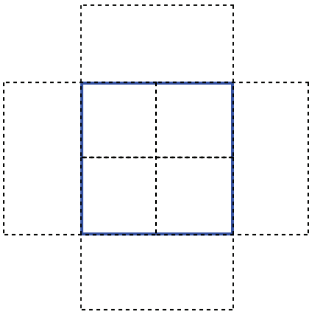

Figure 3.2: Interrogation area overlapping, blue line: IA, dashed black line: overlap with neighboring IA

By assuming adaptive windows, the effect of the flow velocity gradient will be considered in the shape and size of the IA.

Adaptive PIV

Adaptive PIV is an image processing method that automatically adjusts the shape and size of the IA based on the local seeding densities and flow gradients. The grid step size should be chosen as a number of pixels between the centers of two neighbors IAs. A smaller grid size means a greater number of IAs in the determined area. Grid step size can be selected in both horizontal and vertical directions independently as IAs sizes. Another adjusted point in Adaptive PIV is the size of the IA that will be determined by the program automatically. Two limits, maximum and minimum size of IA, should be defined in this module. Similar to adaptive correlation the processing starts with maximum IA size and iterates till a possible minimum IA based on valid particle density. Desired numbers of particles and the particle detection limit should be defined so that IA's size is adjusted by particle density. Limitations for the components of the velocity gradient vector can be defined to make sure that the velocity gradient is in the range while adjusting the shape of the IA. Adjusting the shape and offsets of IAs updates in each iteration and it is controlled by the effect of the previous iteration. Other restrictions such as convergence condition and maximum number of iterations can be defined for the adaptive PIV module.

High pass filter in image processing

In this experiment the desired area is a tiny layer in the vicinity of the airfoil surface. Due to laser light reflection in this area there is undesirable noise that can change the

correlation peaks. Except for the background part of a PIV image, there are two more parameters; scattering light of seeding particles, and undesired light contributions from surface light reflection[11, 113], this light reflection depends on: experimental setup material and color of models, and finally quality of the laser beam. Therefore modifying the image may improve the quality of the acquired post processed results. Based on Sciacchitano and Scarano[113] it is possible to separate these two light contributions by analysing the images in the frequency domain. The particle motion has high frequency contributions while the light reflection causes a low frequency contribution. Then reflection removal would be possible by removing low frequency content. This can be done using high pass filters (HPF). Image processing on an edge is not precise enough due to the noise caused by the surface reflection. Based on image processing documents, a high pass filter can be used for edge detection. Uzol et al[130] have done some PIV tests in the field of turbomachinery, they faced the problem of light saturation near the blade in some images. The reflection problem was solved by applying a maximum filter 3×3 mask and a median filter 11×11 to 21×21. Bremmer *et al.* [11] used a high pass filter to remove reflection using an algorithm which enhances reference images. Sciacchitano & Scarano [113] take advantage of a high pass filter, a third order Butterworth filter, to remove undesired reflection. Five types of high pass filters are predefined in Dantec software that can be used as an edge detection option. Obviously, there was some noise and undesired reflection in transferring between two different phases or in a surface area then a HPF can be used as an edge detection or reflection removal. Here is an example of this filter[22];

- N×N High-Pass filters (3×3 to 5×5) with following convolution kernels

3x3:

-1	-1	-1
-1	8	-1
-1	-1	-1

5x5:

-1	-1	-1	-1	-1
-1	-1	-1	-1	-1
-1	-1	24	-1	-1
-1	-1	-1	-1	-1
-1	-1	-1	-1	-1

To see how high pass filters can modify a PIV image a brief background is presented in this section. At the edge of two different phases or materials, the intensity of a received or an emitted signal in a desired area which is present as a digital number in each pixel of a captured image changes sharply. Therefore this small area about the edge has a high frequency characteristic. A high-pass filter highlights the location of edges by putting weight on high frequencies and reduces the error in cross-correlation caused by surface reflection.

Here filters consisting of 3×3 and 5×5 arrays of weighting factors were used[54] where was necessary.

x	x	x	x	x
x	x	x	x	x
x	x	y	x	x
x	x	x	x	x
x	x	x	x	x

so that $y + \sum_{n=1}^{N \times N-1} x = 0$ and $y > 0$

3.2 Validation, Errors, and Uncertainty

Similar to all other experiments, the PIV method is associated with two kinds of errors; Random errors and Bias errors that cause some uncertainty in PIV measurements. Here are some of these errors[21, 127] that have been considered in the experiment:

1. **Three-Dimensional effects,** as explained before the laser sheet has a small thickness and it is not two dimensional. Therefore in reality particles move in three-dimensions so that they can appear in just one frame of an image pair and cause complexity in finding the particle movement. Choosing a time difference between two frames so that the particles displacement be up to 0.25 laser sheet can decrease the uncertainty of results. If the thickness of the laser sheet is larger than the expected one, some unfocused particles which are not in the two dimensional sheet will be recognized as tracer particles and cause incorrected velocity vectors. This condition usually happens for smaller field of views where the distance between the camera and the laser sheet is small.

2. **Tracer particle number density,** increasing number of particles in each IA results in a more accurate cross-correlation process that consequently decreases the error/uncertainty of PIV measurements. Figure 3.3 shows particles in IAs with the same size in different locations of FOV. Therefore, the number of particles in all of IAs should be considered in the experiment.

3. **Tracer particle size,** since every pixel can register one intensity, if tracer particles are taking less than one pixel then determining the location can be difficult and impossible in some conditions, an optimum particle diameter should be larger than 2 pixels that is considered in the experiments.

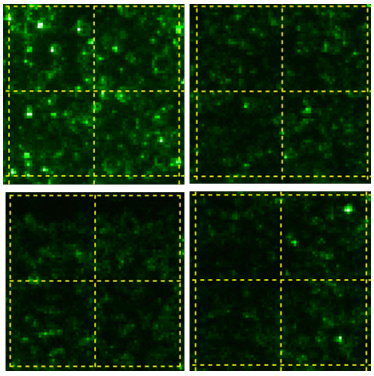

Figure 3.3: Sample IAs from different parts of an image

4. **Tracer particle error,** choosing neutrally buoyant tracer particles in flow so that they are not heavier/lighter than the fluid and are able to follow the flow exactly is necessary in PIV to avoid this error.

5. **Displacement Gradient error,** PIV with CMOS cameras is a suitable method for uniform flows. But in reality flows with velocity gradients are more complex and interested ones. Therefore to avoid having displacement gradient error choosing smaller IAs or higher particle density based on flow velocity is suggested. The effect of smaller IA has a larger effect than higher particle density.

The statistical uncertainty for the velocity field of the PIV method with FOV=c, 2.5c are estimated according to Benedict and Gould[10, 36] and presented in Table 3.1. n is the number of sample images that is 450 in this calculation.

Table 3.1: Statistical uncertainty for PIV method, Re=41000

uncertainty definition	$\varepsilon_u = \frac{\sigma_u}{\sqrt{n}}$	$\varepsilon_v = \frac{\sigma_v}{\sqrt{n}}$	$\varepsilon_{u'} = \frac{\sigma_u}{\sqrt{2n}}$	$\varepsilon_{v'} = \frac{\sigma_v}{\sqrt{2n}}$	$\varepsilon_{u'u'} = \frac{2{\sigma_u}^2}{\sqrt{2n}}$	$\varepsilon_{v'v'} = \frac{2{\sigma_v}^2}{\sqrt{2n}}$
FOV=c, % relative to U_∞	0.42	0.31	0.3	0.22	0.05	0.03
FOV=2.5c, % relative to U_∞	0.15	0.13	0.10	0.09	0.006	0.005

3.3 Post Processing of PIV data

Eventually, the APIV method from Dantec Dynamic Studio software with a minimum IA of 16×16 pixels and maximum 64/128 pixels has been selected to process the images.

Velocity vectors were validated by the universal outliers detection local neighborhood with the size of 3×3 pixels, and S/N ratio. It means if the ratio of correlation peak to noise level is above the selected level, they will be considered valid[22]. Figures 3.4 to 3.6 show samples of a time-averaged velocity vector map and contour of velocity magnitude of 450 sample images for the three FOVs. In the vector map figures a few data points in the x direction are skipped to present velocity profiles with higher magnitude that show a clear trend of velocity profiles close to the surface and in the BL flow.

The spatial resolution (SR) of each set of data is calculated with equation 3.1, therefore the spatial resolution is 0.25 mm, 0.10 mm, and 0.06 mm for largest FOV to smallest one respectively.

$$SR = \frac{Grid\ size\ (px)}{Image\ Resolution\ (px/mm)}\ (mm) \tag{3.1}$$

Using PIV technique and provide enough brightness, raw images might also be used as smoke flow visualization data. In this case, there should be enough light and smoke to make the phenomenon visible with the naked eye. Also, the FOV should cover the specific area (or the quality of the camera's lens should be high enough to allow zoom in the area after acquiring the images). Figure 3.7 shows a sample enhanced instantaneous PIV image with marked separation, transition and turbulent regions on it. As explained, due to the surface reflection, post-processing of the results very close to the surface is more complicated, and the BL thickness in laminar flow is very small that can be missed easily. Therefore, some of previous research used raw images solely to detect the separation point[93].

Although some flow features are recognizable through instantaneous PIV images, their measured velocity fields will provide further details of the fluid features and motion, especially in dealing with complex or unsteady flow fields. Here are some post-processing methods that have been used to identify flow features over the airfoil. Increasing the number of samples (N) from 300 to 1000 decreased the statistical errors and smoothed the results although it did not indicate any significant difference in BL flow structures either in the velocity field or post-processed results that were calculated from the velocity field such as integral BL features ((δ^*), θ) or surface pressure coefficient (Cp). Since the overall behavior of post-processed results stays the same and increasing samples only smoothed the graphs without changing the results specifically, and considering the processing time of raw PIV images to obtain the velocity field, N selected as 450 images pairs. All presented results in the following sections and results chapters are acquired from 450 samples image pairs.

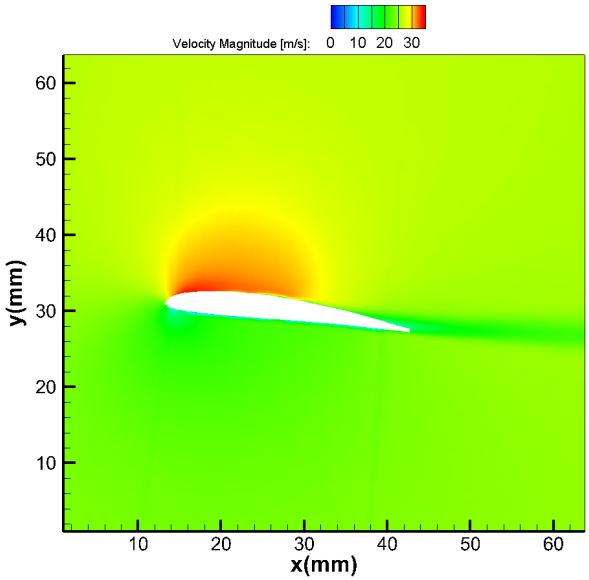

(a)

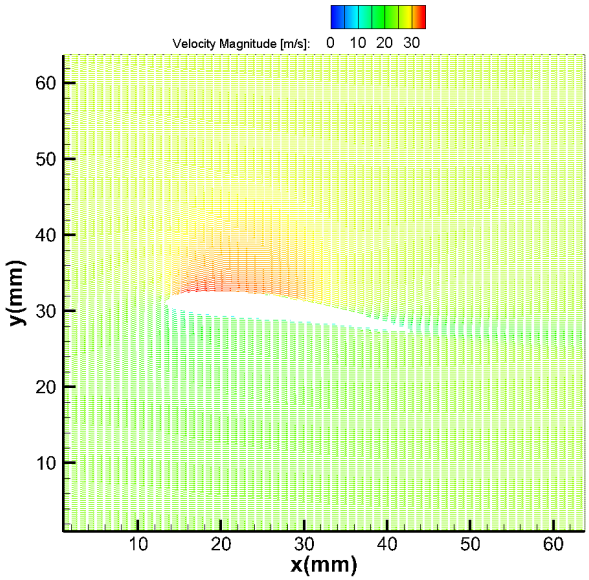

(b)

Figure 3.4: Sample PIV result of FOV=2.5c, case: Re=40,000, $AOA = 7°$ a) Average Velocity Magnitude contour b) Average Velocity vector map (every other six vectors shown for clarity)

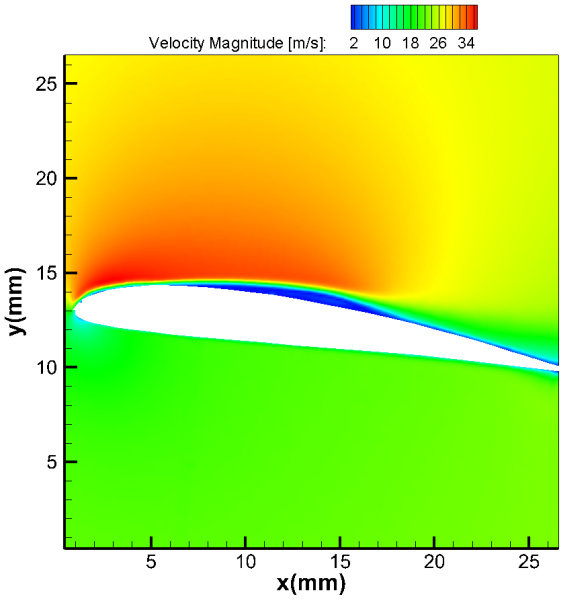

(a)

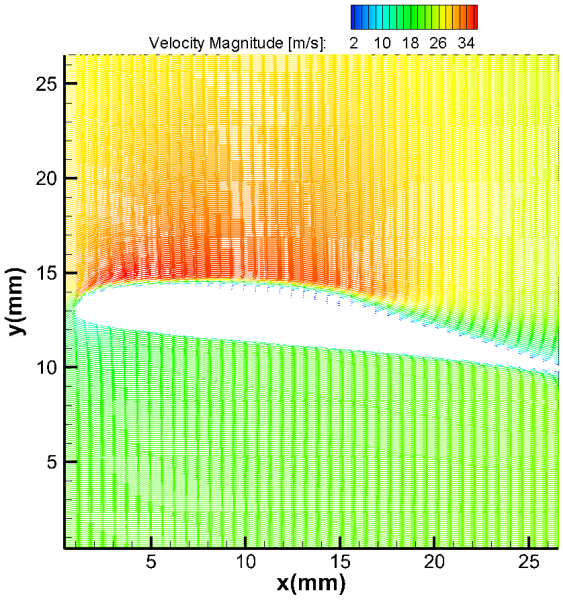

(b)

Figure 3.5: Sample PIV result of FOV=c- case Re=40,000, $AOA = 7°$, a) Average Velocity Magnitude contour b) Average Velocity vector map (every other six vectors shown for clarity)

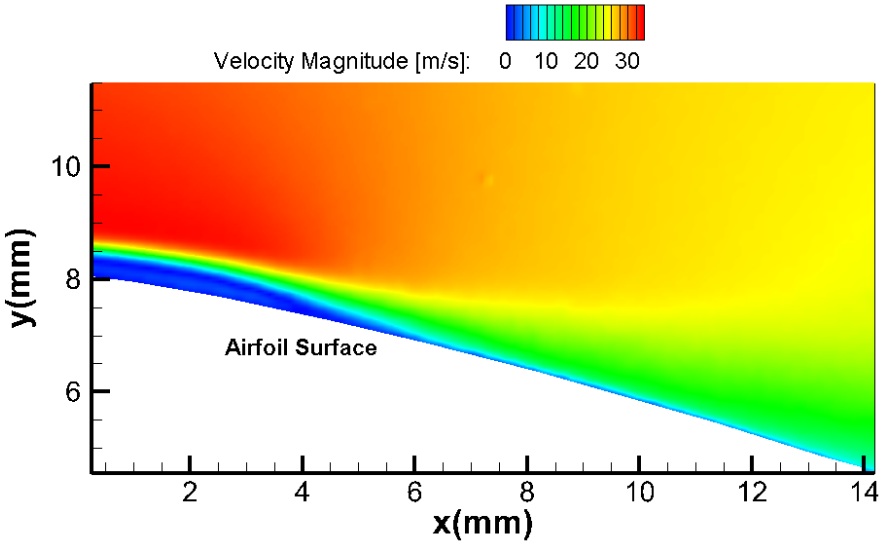

(a)

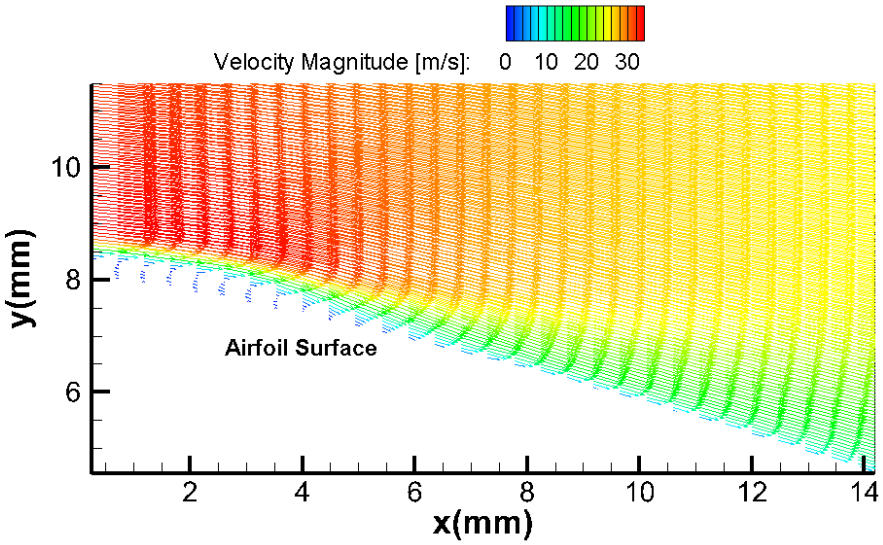

(b)

Figure 3.6: Sample PIV result of FOV=0.6c- case Re=40,000, $AOA = 7°$, a) Average Velocity Magnitude contour b) Average Velocity vector map (every other six vectors shown for clarity)

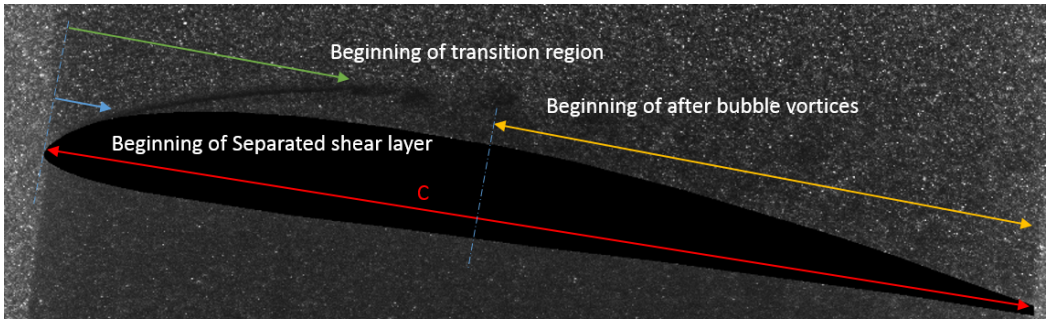

Figure 3.7: Sample Instantaneous PIV image, case: SD7037 airfoil, Re=40,000 and AOA 9°

3.3.1 Contour Lines of Streamwise Velocity Component

The separated shear layer could be identified through iso-contour lines of streamwise velocity[73]. Figure 3.8 shows the streamwise velocity component contours over the airfoil at Re=41000 and AOA 9° with iso-contour lines.

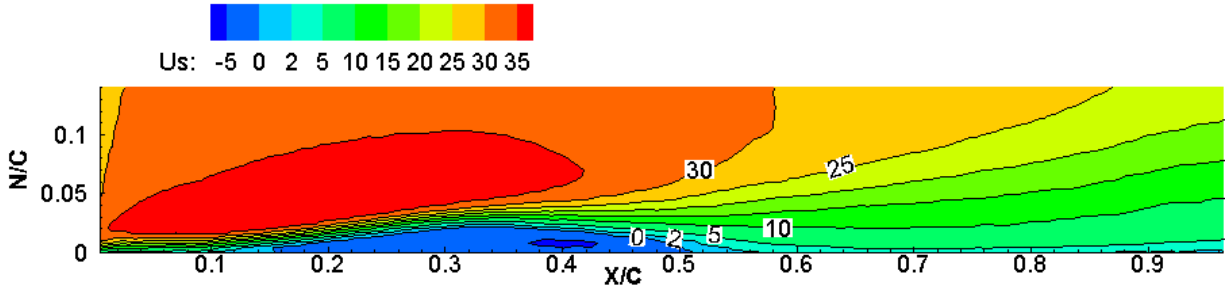

Figure 3.8: Mean streamwise velocity component(U_s), current experiment, SD7037 airfoil, Re=41,000, AOA 9°.

Figure 3.9 presents the same iso-contour but zoomed in at the separation region of the bubble. The BL separation is detectable at about $X/C = 0.11$ where velocity vector component U_s along the surface of airfoil and normal to the wall velocity gradient are almost zero[74]. The point is visible from either iso-contour lines of U_s or velocity profiles.

Also, from the separated shear layer the height of the bubble and its location can be determined. There are different definitions for the height of the the bubble, Nati *et al.* [93] defined this height, the maximum distance from the airfoil surface where the highest velocity in the boundary layer occurs. Burgmann *et al.* [14] used the distance of local maximum velocity profile from the airfoil surface at the transition point that either define

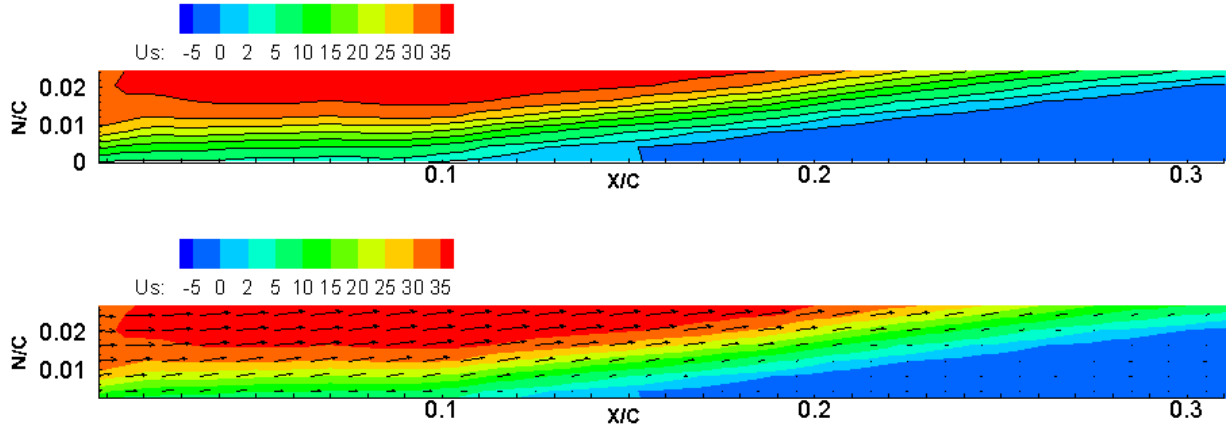

Figure 3.9: Mean streamwise velocity component(U_s) over SD7037 airfoil at Re=41000 and AOA 9°. a) Iso-contour lines, b) Velocity profiles

BL thickness or LSB thickness. Michelis *et al.* [90] used the maximum distance of dividing streamline from airfoil surface that is slightly upstream of their measured transition point. Simoni *et al.* [123] consider the bubble maximum displacement and its position the same as the maximum displacement thickness and its location whereas the maximum of shape factor corresponding to the transition point occurs just its upstream. The height of the bubble is about $0.033c$ at $x/c = 0.4$, transition point(x_{tr}). Similar to the separation point, the reattachment point can be identified through iso contour lines of U_s or velocity profiles. Here, it is about $x/c = 0.5$, Figure 3.10.

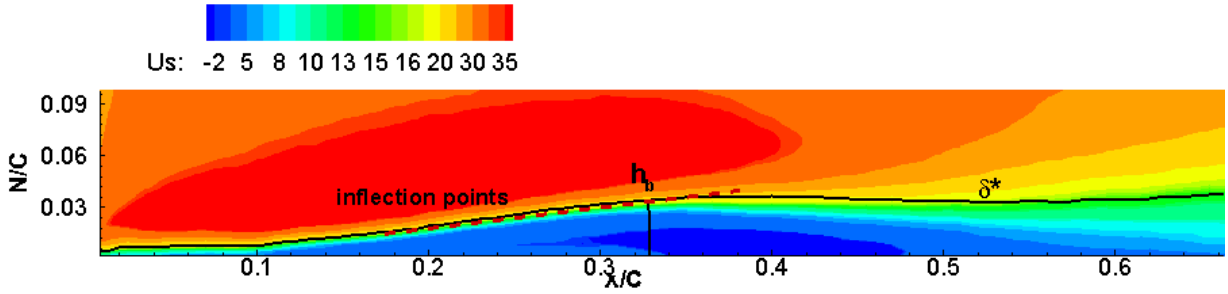

Figure 3.10: Mean streamwise velocity component(U_s) over SD7037 airfoil at Re=41000 and AOA 9°, δ^* (black solid line)

3.3.2 BL Thickness and BL Momentum

For an airfoil with a cambered surface and with the existence of a pressure gradient, the edge of the BL is found where the local velocity equals the free stream value U_e, Figure 3.11(b). In theory, this velocity can be calculated from irrotational flow and be used as the outer boundary condition[18]. Besides, as the shear stress and vorticity exponentially decay at the edge of the boundary layer[18], they can be used to characterize BL thickness over the surface, Figure 3.11(a). Although the transition from BL flow to outer flow is a continuous process, the concept of BL thickness is typically defined where $U = 0.99\,U_e$, ($\delta_{0.99}$). Another way to estimate BL thickness is using the vorticity domain(ω). In this method, integration of ω normal to the local wall will reach the constant value on the outside of the BL ($\nabla \times u = 0$). Therefore using the 0.99% criterion, the BL thickness can be identified. For these experiments, the BL thickness was calculated from both methods ($U = 0.99\,U_e$ or $\omega = 0.99\,\omega_e$) and the results are similar with excellent agreement.

Then, the BL displacement thickness (δ^*) that shows the displacement of the outer flow by the boundary layer, and momentum thickness (θ) can be determined by integrations presented in Equation 3.2 and Equations 3.3[139].

$$\delta^* = \int_0^{\delta} (1 - \frac{U}{U_e})dy \tag{3.2}$$

$$\theta = \int_0^{\delta} \frac{U}{U_e}(1 - \frac{U}{U_e})dy \tag{3.3}$$

Using these BL parameters, the BL shape factor H, Equation 3.4 and Re_θ, Equation 3.5 can be determined.

$$H = \frac{\delta^*}{\theta} \tag{3.4}$$

$$Re_\theta = \frac{U_e\theta}{\nu_e} \tag{3.5}$$

Previous work shows that due to changes in flow structures, δ^* considerably increases during flow separation and causes a rapid increase in the shape factor H while θ remains almost constant inside the LSB until the vicinity of the transition point[48]. The beginning of the increase in θ marks the beginning of the transition[64]. Figure 3.12 shows δ^* and θ calculated from sample PIV data for SD7037 airfoil. Burgmann and Schroder [15] measured

x_{tr} where the maximum H was observed as McAuliffe and Yaras [84]. Figure 3.13(a) shows a sample calculated shape factor from measured PIV data.

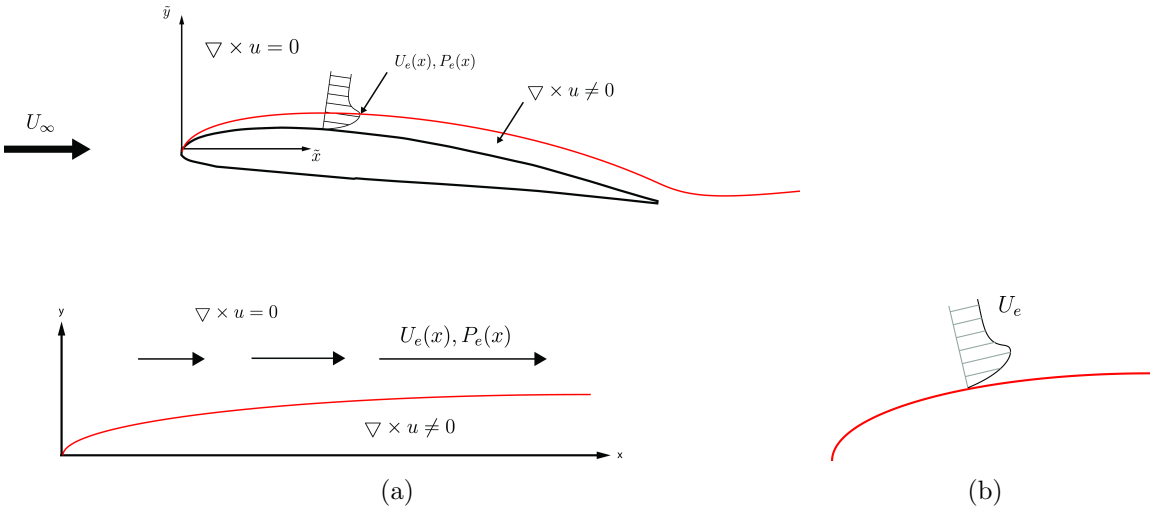

Figure 3.11: Detection of the BL Profile a)Vorticity over the airfoil's surface[18], b) No-slip flow near a curved solid surface[18]

3.3.3 Reynolds shear stress

Considering the criteria of 0.001 for Reynolds shear stress (equation 1.11) as the location of the transition point at the beginning of the transition region is not an absolute condition. Variation in Re and dynamic motion can affect this number significantly. The importance of this point in finding the transition point should be taken into consideration[93, 15]. Some works prefer to use the rate of Reynolds shear stress increase known as the transition exponential method (TEM) to define the transition point but there is not a unique way to define this point. Nati *et al.*[93], and Burgmann and Schroder[15] consider the transition point where a significant increase in Reynolds shear stress occurs. Lang *et al.*[64] used the same method but consider the transition point at the end of significant growth in the Reynolds shear stress. Lengani *et al.*[75] mentioned Reynolds normal and shear stress shows their highest values at the transition point where breakdown of large scale coherent structures to smaller scales sets transition in the separated shear layer[73]. Figure 3.13(b) shows maximum Reynolds shear stress along the chord of the airfoil. The dashed line shows the significant growth in Reynolds shear stress and the location of the end point of this line is in good agreement with the location where the maximum H occurs and is considered as the transition point.

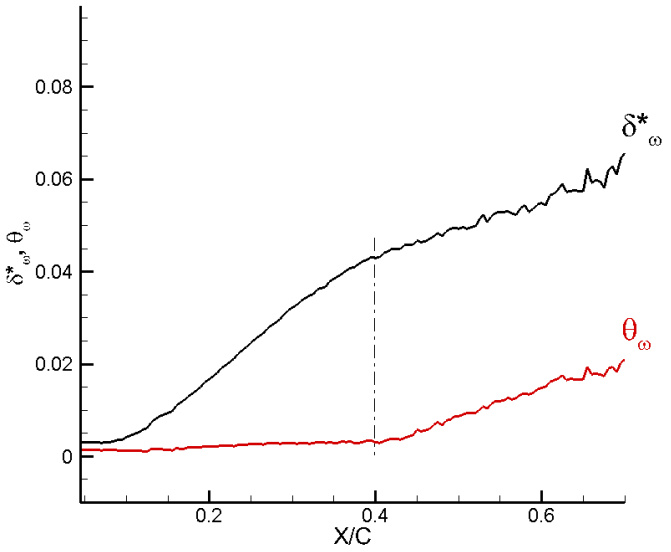

Figure 3.12: BL quantities in the existence of LSB, Sample δ^*, and θ measured from PIV data over SD7037 airfoil

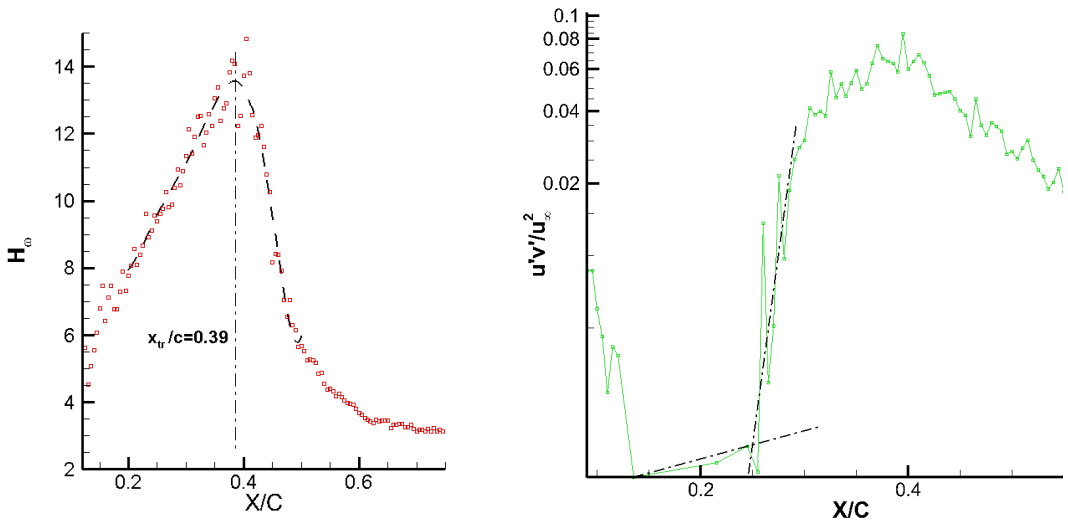

(a) (b)

Figure 3.13: Sample results of BL quantities in the existence of LSB over SD7037 airfoil a) Shape Factor, H b) Values of the Reynolds shear stresses on the line of maximum shear stress along the surface of the airfoil

3.3.4 Pressure coefficient

The pressure (Outer flow velocity) is almost constant over the laminar part of the bubble[51] and it falls linearly (with good approximation) between the transition and reattachment points while there is a discontinuity at the reattachment point that will change the slope of the pressure coefficient [51] or at the end of the enhanced rate of pressure recovery[24]. These points are displayed schematically in Figure 1.7. Surface pressure is usually measured with pressure transducers, but requires a fairly large airfoil model to set up this method. Alternatively, the pressure field can be calculated from the velocity field by solving the Navier-Stokes equations. To estimate the surface pressure distribution the Navier-Stokes momentum equations should be solved over the airfoil. There are many studies in this field that focus on the accuracy of this method. While this calculation is complicated and time-consuming, having the surface pressure coefficient provides sufficiently reliable data to identify bubble characteristics. For this purpose pressure derivatives are calculated from the 2D Navier-Stokes momentum equations for BL flows, Equation 3.6[111]. These equations are:

$$\begin{aligned}
\rho(\overline{u}\frac{\partial \overline{u}}{\partial x} + \overline{v}\frac{\partial \overline{u}}{\partial y}) &= -\frac{\partial \overline{p}}{\partial x} + \mu \triangle \overline{u} - \rho(\frac{\partial \overline{u'^2}}{\partial x} + \frac{\partial \overline{u'v'}}{\partial y}) \\
\rho(\overline{u}\frac{\partial \overline{v}}{\partial x} + \overline{v}\frac{\partial \overline{v}}{\partial y}) &= -\frac{\partial \overline{p}}{\partial y} + \mu \triangle \overline{v} - \rho(\frac{\partial \overline{u'v'}}{\partial x} + \frac{\partial \overline{v'^2}}{\partial y})
\end{aligned} \tag{3.6}$$

Then pressure derivatives are transferred to S-N coordinates. The static surface pressure can be calculated by integrating the derivative of pressure in a direction perpendicular to the surface if there are accurate boundary conditions. Since total pressure is a constant value on a streamline(P_t) then by selecting a start point of integration on a specific streamline dealing with a constant unknown value along the surface, $p_s = P_t - \frac{1}{2}\rho U^2$. This P_t can be removed from the Cp calculation considering $p_\infty = P_t - \frac{1}{2}\rho_\infty {U_\infty}^2$. Besides, the pressure coefficient reaches zero at the TE of the airfoil that can be used to calculate the constant unknown value. Consequently, the surface pressure coefficient can be calculated from equation 3.7. Figure 3.14 shows a sample of the estimated surface pressure coefficient from PIV data in comparison with XFoil results. As can be seen, the separation point is the same, the beginning of the constant pressure region. Also, the transition at the end of the constant pressure region represents the transition point. The reattachment point is marked where there is a significant change in the slope of Cp. It should be mentioned that reattachment points move along the vortex shedding region of the separated shear layer and the instantaneous data is quite different compared with the time-averaged value and this will be explained in detail in chapter 4.

$$Cp = \frac{p - p_\infty}{\frac{1}{2}\rho_\infty {U_\infty}^2} \tag{3.7}$$

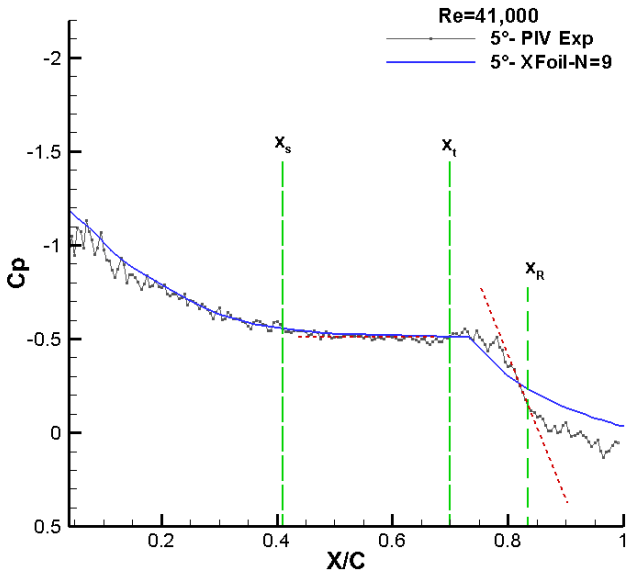

Figure 3.14: Surface pressure coefficient over SD7037airfoil, case Re=41,000 and AOA 5°

3.3.5 Skin friction coefficient

The measured skin friction distribution ($C_f = \frac{\tau_w(x)}{\frac{\rho}{2}U^2}$) on the surface also has been used to recognize laminar, and turbulent flows along with separation, and reattachment points. These points can be found through the C_f zero line crossing on the skin friction plot [124]. Skin friction has been measured using the velocity gradient near the wall (equation 1.1) or a force balance. Each method has its limitation. In this experiment the size of the airfoil does not allow the use of a force balance but the shear stress is calculated through velocity field data. In calculating wall shear stress, the distance from the wall has a considerable impact on the wall shear stress. In turbulent flows, shear stress should be calculated in the viscous sublayer. Based on a literature review it should be calculated where $y^+ \leqslant 5$ [6], So that $y^+ = \frac{yu_\tau}{\nu}$ where y is the distance normal to the surface, ν is the kinematic viscosity and u_τ is the friction velocity. For these results, velocity data with the spacing of $8 \times 8\, pixels (\approx 0.1mm)$ and $4 \times 4\, pixels (\approx 0.05mm)$ close to the wall are

considered. As the results are similar for both grid sizes therefore to decrease processing time the larger grid was chosen. Based on this method, the separation point is where the friction coefficient (on the wall) reaches zero. In other words, it is a boundary between forward and back-flow in the closest layer to the wall[111]. In the skin friction graph, the flat part after the separation point shows the length of the dead air region under the LSB [124]. As reverse flow velocity under the bubble is very small, skin friction would be minimal too. Rewriting the momentum equation results $\frac{d\theta}{dx} = 0$ or in the other words $\theta_T = \theta_s$[51]. Using this method the transition point can be identified as explained in section 3.3.2.

Figure 3.15 presents the skin friction coefficient along the surface of the airfoil at Re=41,000 and AOA=7° and 9°. At 9°, the separation point is at $x_s = 0.12$ that is a bit farther downstream of the LE in comparison with the separation point from the surface pressure coefficient method where $x_s = 0.09$ and SOFV results. This difference in the separation point location in the methods is less than $1mm$, and it is likely due to the thickness of the laminar boundary layer. The results show the location of 0.4C as the oil accumulation line (where minimum C_f occurs), and it is in excellent agreement with SOFV results.

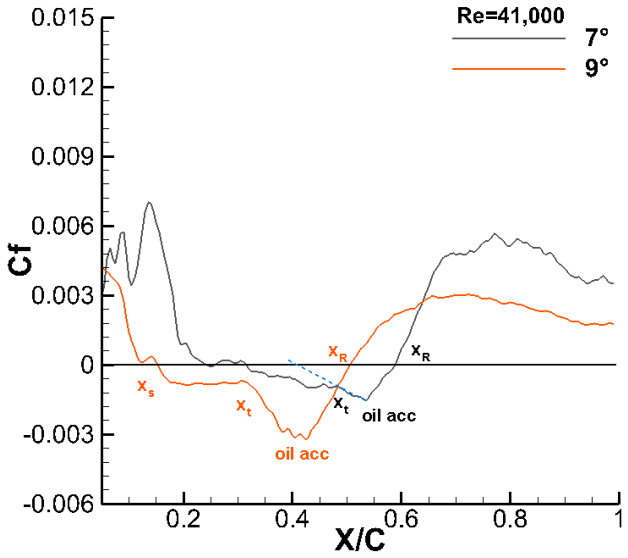

Figure 3.15: Skin friction Coefficient over SD7037 airfoil determined from velocity data, case Re=41,000 and AOA 7° and 9°

3.3.6 Shape of the LSB

Previous works show that LSB can be classified as a short or long bubble and each one affects the flow structures differently. The bubble shape can be extracted using BL flow velocity profiles. Although in forming a long bubble, separation occurs with a very narrow deflected shear layer. In this condition, velocity derivatives may provide more accurate data in detecting the separation points, Figure 3.16.

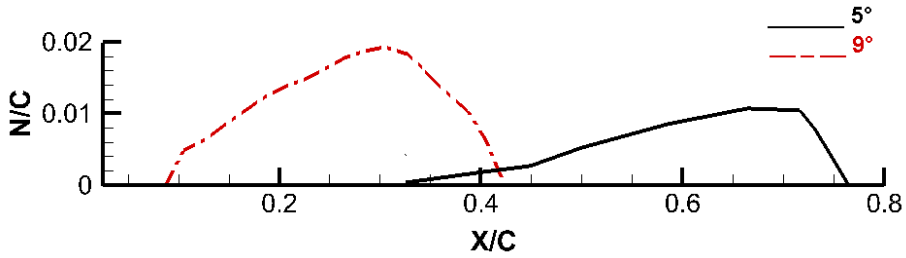

Figure 3.16: Profile of the LSB determined from flow velocity profiles at AOA=9° and 5°

3.3.7 Proper orthogonal decomposition(POD)

POD is a practical post-processing technique when it is not possible to follow a physical phenomenon in real time like identifying and tracking coherent structures. This technique reconstructs the PIV database and recovers lost time information. Reconstructed PIV data can be used to validate CFD codes too[68]. Proper Orthogonal Decomposition is a mathematical procedure to illustrate physical phenomena. It is an interesting tool when the physical phenomenon is statistically inhomogeneous such as turbulent flow, or near-wall flows. This method is based on the energy of the finite domain at various times so that extracting the dominant components of a multi-dimensional process and decrease the system's dimension. For the POD of PIV vector fields, the energy of n^{th} component of the velocity at the specific location(x) is the sum of the POD modes. POD modes are the energy relevant structures of the physical process that are extracted based on their energy contribution to the total energy of the physical phenomena at a limited time. Sirovich(1987) developed the method of snapshots for a limited sample size of PIV data that is used in this research. In his method:

- Each instantaneous PIV velocity field $u(x,t)$ is considered a snapshot of the flow.

- The average velocity at each location of the velocity field is calculated ($\bar{u}(x)$) and considered mode zero of the POD.
- The rest of the POD analysis is performed on the velocity fluctuation components matrix ($\acute{u}(x,t) = u(x,t) - \bar{u}(x)$). Forming the energy matrix shown in equation 3.8

$$C_{ki} = \frac{1}{N_t} \int_D \acute{u}(x,t_k).\acute{u}^*(x,t_i)dx \quad k = 1, ..., N_t \tag{3.8}$$

- Solve the eigenvalue problem ($C\Phi_i = \lambda_i \Phi_i$) for eigen vectors $C\Phi_i$ gives the POD modes (3.9) ordered by sizing the eigenvalues(λ_i)[3, 22, 49].

$$\varphi_i = \frac{\acute{U}\Phi_i}{\|\acute{U}\Phi_i\|} \quad i = 1, ..., N-1 \tag{3.9}$$

Legrand *et al.* [68, 69, 70] suggest a data reconstruction from the first three POD eigenvectors(POD coefficients) instead of POD modes to specify travelling coherent structures from stochastic turbulence in periodic or transient flows. Their method is based on four assumptions; first, the Taylor hypothesis is valid in the flow field. Second, the region of interest is larger than the typical structure sizes. Third, the flow is periodic. Fourth, there is not an extreme change in the average flow field velocity in the convection direction. Therefore, the periodicity of the flow field is the same as the contribution of eigenvectors to the first three POD modes. Validating the results showed that the ratio of the energy of the second POD mode (λ_1) to the total energy of all the modes ($\Lambda = \lambda_1 / \sum_{k=1}^{N} \lambda_k$) decreases with increases in the turbulence intensity, therefore, lower modes present larger-scale coherent structures and higher modes present small scale non-correlated structures of turbulent flow. When lower modes contribution to the flow energy decrease, temporal reconstruction may be compromised. They propose a 7% threshold of Λ for applicability of their method.

Coherent structures

There are different definitions of coherent structures in flows. In general, coherent structures are building blocks of turbulent flows that are coherent in time and space. In other words, they are coherent motions of eddies that can be recognized in flow visualization due to their repeating topological patterns. These structures have a substantial effect on mean flow behaviour[2, 49]. These coherent structures might be recognizable through the

velocity gradient tensor (vorticity, swirling strength, lambda-2, and 2nd invariant Q)[1] of the instantaneous flow fields regardless of their temporal development[49]. The POD analysis of PIV data can identify the coherent structures with substantial contribution to the turbulent kinetic energy. POD modes and coefficients can present spatial and temporal features of coherent structures[49].

3.3.8 Lift & Drag calculation based on control volume method

In general, understanding the flow behavior through experiments can be done by measuring velocity/pressure fields, force measurements, or flow visualization techniques, but combining a method to measure aerodynamic forces and flow visualization gives a complete understanding of flow condition and its effects that can provide further understandings of the phenomenon. Therefore in this study aerodynamic forces are calculated from the velocity field that is measured from FOV=2.5c. Here, the used methodology of calculating lift and drag based on the two dimensional incompressible control volume method that was used by Michel [89] is explained, see Figure 3.17. The conservation of the momentum is described by the following equation:

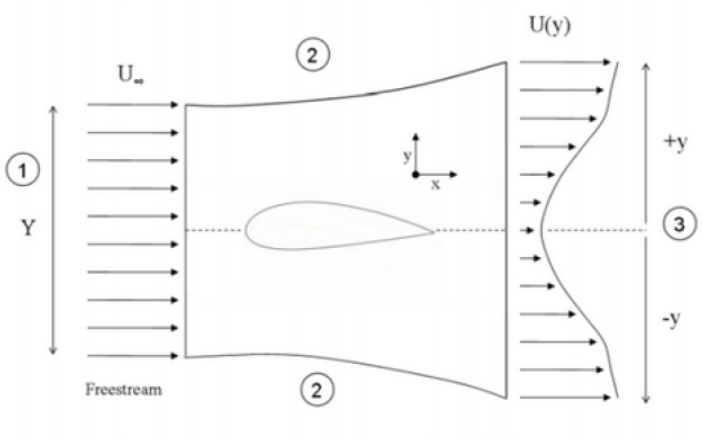

Figure 3.17: Schematic showing the control volume used for the 2D momentum theory[89]

[1]Swirling Strength: Imaginary part of the complex eigen value of the velocity gradient tensor,
Lambda-2: It is a criterion based on velocity gradient tensor for volumetric data,
2nd invariant Q for 2D data: $Q = (\frac{U}{x}\frac{V}{y} - \frac{V}{x}\frac{U}{y})$[22]

$$\sum \vec{F} = \frac{d}{dt}\int\int\int_V \rho\vec{V}dV + \int\int_A \rho\vec{V}(\vec{V}\cdot\vec{n})dA = \int\int_A -P\cdot\vec{n}dA + \int\int_A \tau\vec{n}dA - \vec{D} - \vec{L} = 0 \tag{3.10}$$

In the above equation the $\vec{D}$ is the drag force and $\vec{L}$ is the lift force. Assuming that the flow is in steady state (averaged velocity field), the unsteady term of the equation can be considered zero:

$$\frac{d}{dt}\int\int\int_V \rho\vec{V}dV = 0 \tag{3.11}$$

By choosing a clockwise direction for the contour of the control volume and considering a steady flow the total force $\vec{F}$ can be written as:

$$\vec{F} = \begin{bmatrix} d \\ l \end{bmatrix} = \rho\oint\begin{bmatrix} -uudy + uvdx \\ -uvdy + vvdx \end{bmatrix} - \oint\begin{bmatrix} Pdy \\ -Pdx \end{bmatrix} + \mu\oint\begin{bmatrix} 2\frac{\partial u}{\partial x}dy - (\frac{\partial u}{\partial y} + \frac{\partial v}{\partial x})dx \\ (\frac{\partial u}{\partial y} + \frac{\partial v}{\partial x})dy - 2\frac{\partial v}{\partial y}dx \end{bmatrix} + \rho\oint\begin{bmatrix} -\overline{u\prime u\prime}dy + -\overline{u\prime v\prime}dx \\ -\overline{u\prime v\prime}dy + -\overline{v\prime v\prime}dx \end{bmatrix} \tag{3.12}$$

As it can be seen, the equation above depends on the pressure term, however in the experiments which use PIV, only the velocity field is known and the pressure field needs to be indirectly calculated. To simplify the calculation of the pressure field for the control volume method, the pressure field is first calculated based on Bernoulli's equation over an area over the airfoil (black region of Figure 3.18).

For the wake region of the flow (red region in Figure 3.18), the following Navier Stokes equations (RANS equations) should be used to more accurately calculate the pressure:

$$\frac{\partial P}{\partial x} = -\rho\left(u\frac{\partial u}{\partial x} + v\frac{\partial u}{\partial y} + \frac{\partial\overline{u'u'}}{\partial x} + \frac{\partial\overline{u'v'}}{\partial y}\right) + \mu\left(\frac{\partial^2 u}{\partial x^2} + \frac{\partial^2 u}{\partial u^2}\right) = B1 \tag{3.13}$$

$$\frac{\partial P}{\partial y} = -\rho\left(u\frac{\partial v}{\partial x} + v\frac{\partial v}{\partial y} + \frac{\partial\overline{u'v'}}{\partial x} + \frac{\partial\overline{v'v'}}{\partial y}\right) + \mu\left(\frac{\partial^2 v}{\partial x^2} + \frac{\partial^2 v}{\partial u^2}\right) = B2 \tag{3.14}$$

In order to calculate pressure, the partial derivatives of pressure ($\frac{\partial P}{\partial x}$ and $\frac{\partial P}{\partial y}$) should be integrated for pressure to be calculated. There are two major approaches proposed in

the literature. The first approach uses spatial-marching algorithm to calculate the pressure [38, 39, 78, 131]. The other approach uses the Poisson equation to solve the following partial differential equation [31, 52]:

$$\bigtriangledown P = \Delta^2 P = \frac{\partial^2 P}{\partial x^2} + \frac{\partial^2 P}{\partial y^2} \tag{3.15}$$

$\frac{\partial^2 P}{\partial x^2}$ and $\frac{\partial^2 P}{\partial y^2}$ can be calculated using the central difference (finite difference method) of the $\frac{\partial P}{\partial x} = B1$ and $\frac{\partial P}{\partial y} = B2$ respectively. The relations obtained from the finite difference method create the matrix $[A]$. By using over defined least square method, the pressure field can be calculated by the following equation:

$$\{P\} = ([A]^T[A])^{-1}[A]^T \begin{pmatrix} \{B1\} \\ \{B2\} \end{pmatrix} \tag{3.16}$$

A Dirichlet boundary condition was used for the top and bottom lines of the wake region (lines AB and CD in Figure 3.18), the values for the boundary condition is taken from the pressure calculated based on the Bernoulli equation.

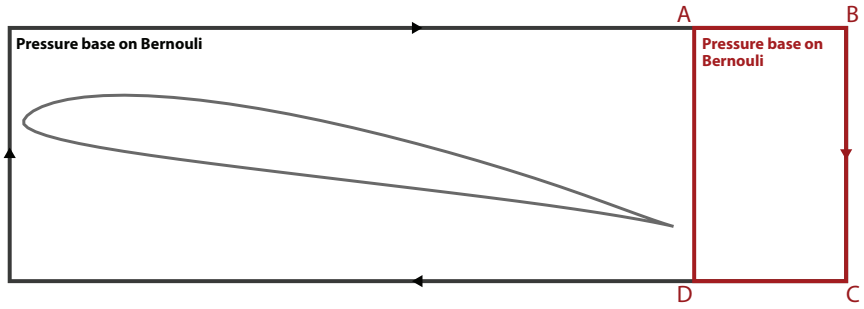

Figure 3.18: Schematic showing the two different methods the pressure field is calculated for the different regions of the flow.

Chapter 4

Static Results

4.1 Surface Oil Flow Visualization[1]

In this part to estimate the effects of airfoil manufacturing on the SOFV results two SD7037 airfoil models with the same size were manufactured/machined from aluminium. In the research, for one of the SD7037 airfoil models, the experiments were conducted for three chord Re, 32000, 38000, and 48000. For Re=48000 the experiment was repeated using the second SD7037 airfoil model. The angle of attack was increased from 1° to 11° in 1° steps.

In these tests, the maximum time running the wind tunnel to observe a formed LSB in the steady-state condition was less than 10 minutes. After turning off the wind tunnel, images were captured. For the first model of the SD7037 airfoil at $Re = 48000$ at all designated angles of attack, the experiment was repeated three or four times on different days to make sure that the results are repeatable. Repeating these tests allowed calculation of the uncertainty of the results due to the unsteadiness and measurement errors. The uncertainty of the experiments depends on the uncertainty in the measuring devices, repeatability, linearization, changes in density and viscosity due to temperature, position of the airfoil (adjustments with the servo motor), etc. Pressure changes in the wind tunnel have a negligible effect on Re. The uncertainty for the Re in this experiment is about 5.4%.

4.1.1 AOA effect

Figure 4.1 shows the results of SOFV determining separation and reattachment. The distance of separation (x_s) and reattachment (x_r) points from the leading edge are divided

[1]Presented at the 25th CANCAM Conference, London, Canada, May 31 - June 4, 2015

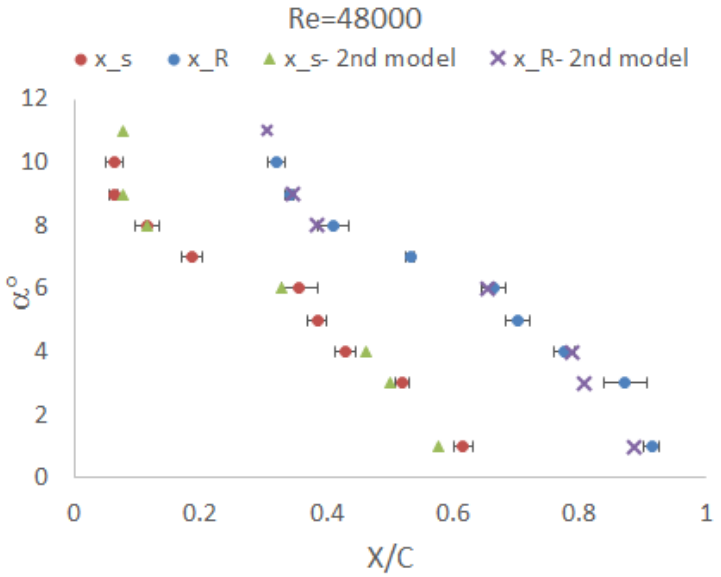

Figure 4.1: Position of separation and reattachment points with changing angle of attack at $Re = 48000$, x_s: separation point, x_R: reattachment point

by the chord (c). As can be seen in this graph the separation points move from 0.6c to 0.06c with increasing AOA. Along with the separation point, the reattachment point changes from 0.9c to 0.3c. Comparing these numbers simply indicates that the reattachment point moves faster toward the leading edge than the separation point therefore the length of the bubble is reduced by increasing the angle of attack. Also the results of the second airfoil model are compared with these results. Almost all the results of measured separation and reattachment points for the second model are found to be located very close to the same points of the first model. In the second model the separation point moves about 50% along the chord from 1° to 11° and the reattachment point moves about 60% toward the leading edge that causes a reduction in the length of the bubble by increasing the angle of attack similar to the first airfoil model. Error bars are calculated from the repeated tests measurements.

Figure 4.2 shows raw images of surface oil flow visualization that was performed in this study. By looking at these results movement of the separation and reattachment with increasing α is clear, but also there are more interesting features in these images. For $\alpha > 5°$ the difference between the accumulation line and the reattachment line is very clear. For $7° < \alpha < 10°$, the reattached flow at higher Re is turbulent and attached to the surface so that the streaklines were fully visible. For lower Re streaklines cannot be seen in spite of

the existence of the accumulation line and sounds the flow barely attaches to the surface. At $\alpha < 2^\circ$ laminar separation occurred at $Re = 32000$ but the disturbances were not strong enough, and flow did not reattach to the surface. On the other hand at $\alpha = 11^\circ$ for the lower Re, it seems that an unstable LSB was burst or in other words bursting the bubble defined in previous work as a sudden increase in the length of the bubble in the streamwise direction causing an intense change in pressure distribution over the surface of the airfoil. The location and size of the LSB has effects on the bubble bursting phenomenon [48] while in higher Re flow it was still attached.

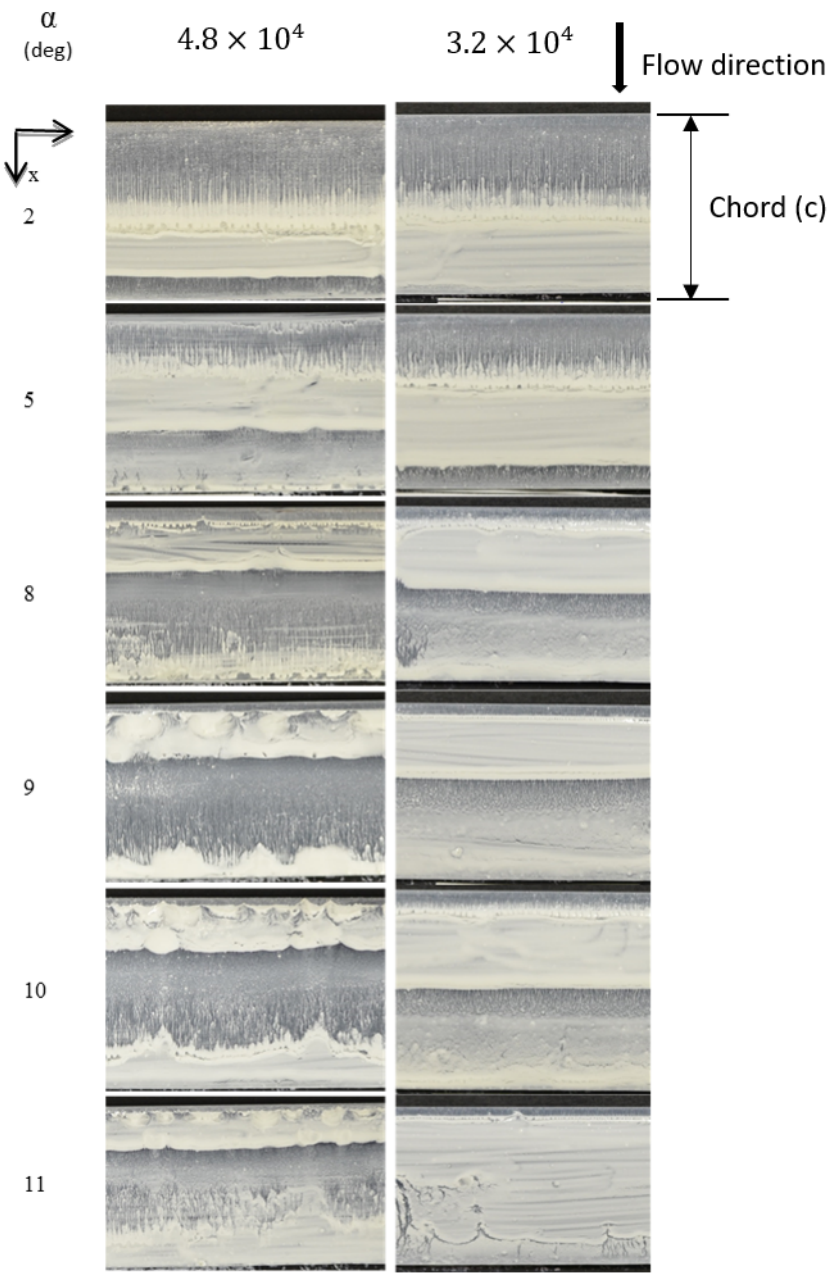

Figure 4.2: Images of oil flow visualization for $Re = 48000$ and 32000 at different AOAs

4.1.2 Re effect

In Figure 4.3 the characteristics of the LSB, and separation and reattachment points, for different Re are presented briefly. The major difference can be seen between $Re = 48000$ and 32000 while there is not a significant difference for $Re = 48000$ and 38000. The difference in the reattachment point for these Re are more visible than the separation point. This could be explained by the fact that the flows are laminar until the separation point, but in the reattachment point momentum transfer occurs due to turbulent mixing and higher Re will aid momentum transfer.

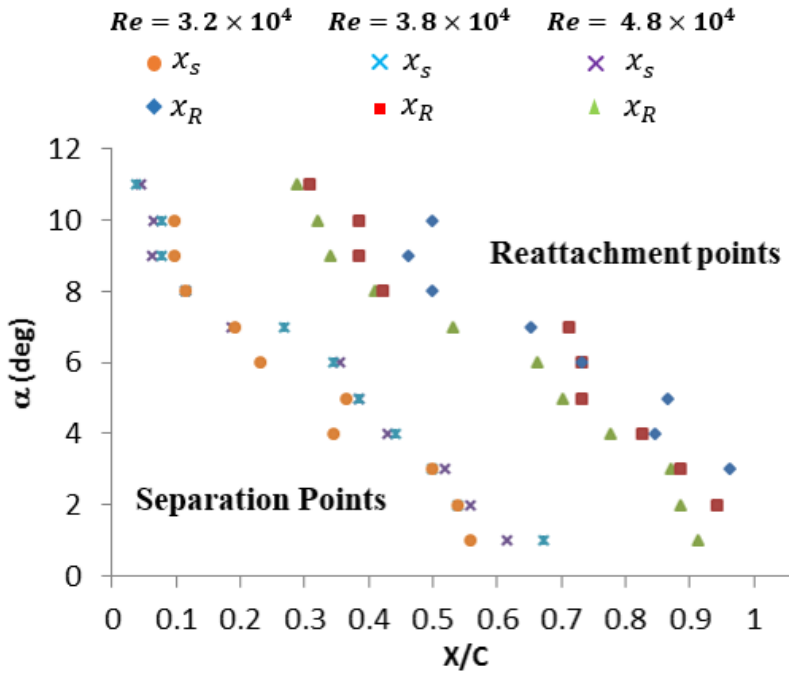

Figure 4.3: Position of separation and reattachment points on the surface of the airfoil by changing Re

Figure 4.4 summarizes the results of this SOFV study by presenting the changes in the length of the LSB at different α and Re. As can be seen for the lowest Re the difference between minimum lengths of LSB occurs at 9° and the maximum length of bubble is at 4° at 0.14c. But for the highest Re in the majority of α, the length is about 0.30c. In other words, for higher Re the rate of change of the length of the LSB is slower than the lower Re.

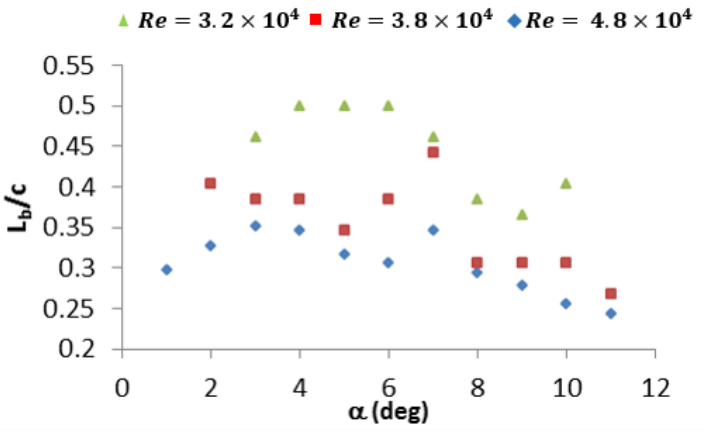

Figure 4.4: Changes of the length of the LSB by changing α and Re

4.2 IR Thermography[2]

In this section, the results of IR thermography are presented in comparison with SOFV. IR thermography tests were completed for constant Re = 48000, with the AOA changed from 0° to 13°. The number of data points varies by the heating methods, and it will be discussed for each method in the following results. Figures 4.5 and 4.6 present a set of results of the *third heating method*, utilizing the air heater, a passive heating technique on the 3D printed airfoil for a range of angles of attack (AOA) from 4° to 11°. For these results averages and fluctuations of temperature were calculated with 10 individual images in sequence while the standard deviation determined from a spanwise average of 100 pixels from each of the individual images. In figure 4.5, two AOA a) 4°, b) 7° and in figure 4.6, two AOA a) 10°, and b) 11° are presented. For all figures, the flow is from left to right (from LE to TE of the airfoil) as indicated at the base of each plot. For each AOA presented the top colour figure shows an IR image indicating the surface temperature variation from leading edge (LE) on the left side to the trailing edge (TE) on the right side that is scaled by chord length. The temperature legend presented above those figures indicate a sufficient range of temperature difference in using this method that is about $2°C$. The lower plot for each AOA shows the standard deviation of the temperature along the chord from the LE to the TE with the image of surface oil flow visualization (SOFV) results in the background of the plot obtained at the same AOA and Re. Text labels indicate where the flow separates and reattaches on the airfoil if appropriate. There is a significant amount of information

[2]Published at Journal of Physics: Conf. Series 1037 (2018)

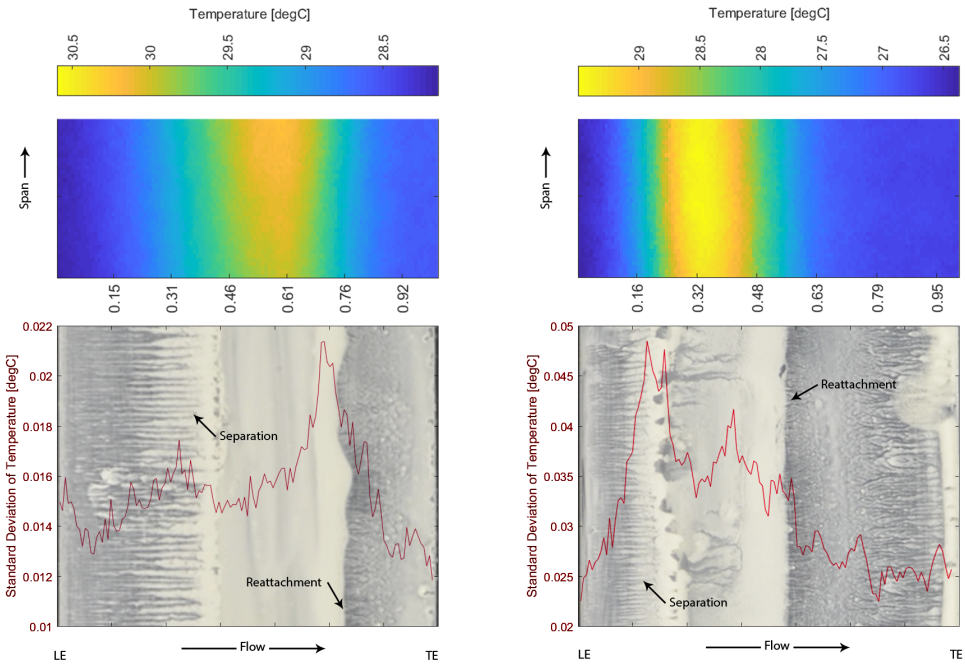

(a) 4° (b) 7°

Figure 4.5: Thermographic flow visualization with air heater (top image of each angle), and surface oil flow visualization in the background of temperature fluctuation graph (bottom image of each angle) for two AOA: a) 4°, b)7° at Re= 48,000, horizontal axis x/c.

revealed in the combined figure that will now be discussed. Firstly, it is evident that there is a close correspondence between the SOFV and the IR images regarding the separation and reattachment regions for all cases shown increasing confidence in the IR methodology. As can be seen, at separation and reattachment of the flow the temperature fluctuation as shown by the standard deviation increases considerably and that may be used to determine these points. After reattachment, the temperature fluctuations are much lower and may also be used to locate the reattachment point. Within the laminar separation bubble that forms there is a decrease in fluctuation in the core of the bubble. Another noticeable point on these plots is the change of the slope of the temperature standard deviation at the reattachment points which is correctly matched with the SOFV results. Although the results presented in these figures are for Re of 48,000 there is no reason that the techniques and results would not be applicable to a much larger surface or larger Re values such as full scale turbines. This is especially true in the passive heating technique presented here in that a small temperature difference could occur in a natural outdoor setting.

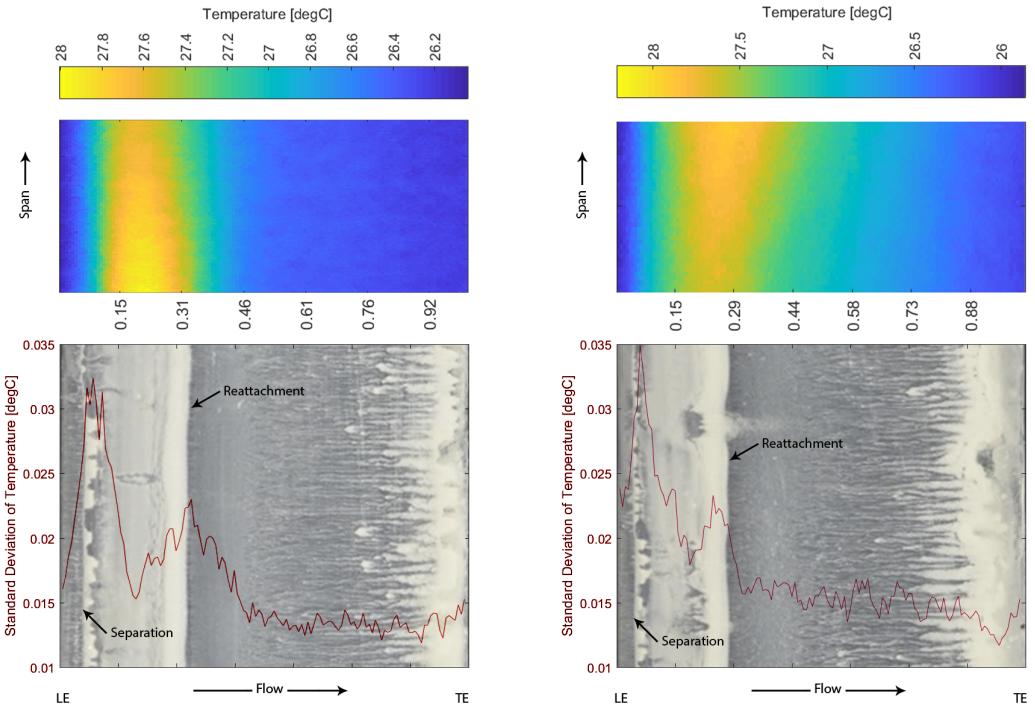

(a) 10° (b) 11°

Figure 4.6: Thermographic flow visualization with air heater (top image of each angle), and surface oil flow visualization in the background of temperature fluctuation graph (bottom image of each angle) for two AOA: a) 10°, and b) 11° at Re= 48,000, horizontal axis x/c.

Figure 4.7 presents plots of the temperature gradient along the non-dimensional chord of the airfoil with surface oil flow visualization SOFV results in the background for AOA: a) 4°, b) 7°, c) 10°, and d) 11°. In all the AOA, no matter if the LSB is long or short in length (the difference between separation and reattachment locations), there is a peak in separation and reattachment points and the temperature gradient decreases along the bubble. Looking at this figure it indicates the difference between the laminar (pre-LSB) and turbulent flow (post-LSB). The temperature gradient changes linearly in the laminar flow region before the separation points, but after reattachment, the temperature gradient is almost constant. This is clearer at higher angles where the turbulent flow after the LSB has higher fluctuation than lower angles. Therefore, either using standard deviation or gradient of temperature as a post-processing technique, the type of flow on the surface of the airfoil would be determinable through thermography results utilizing an air heater.

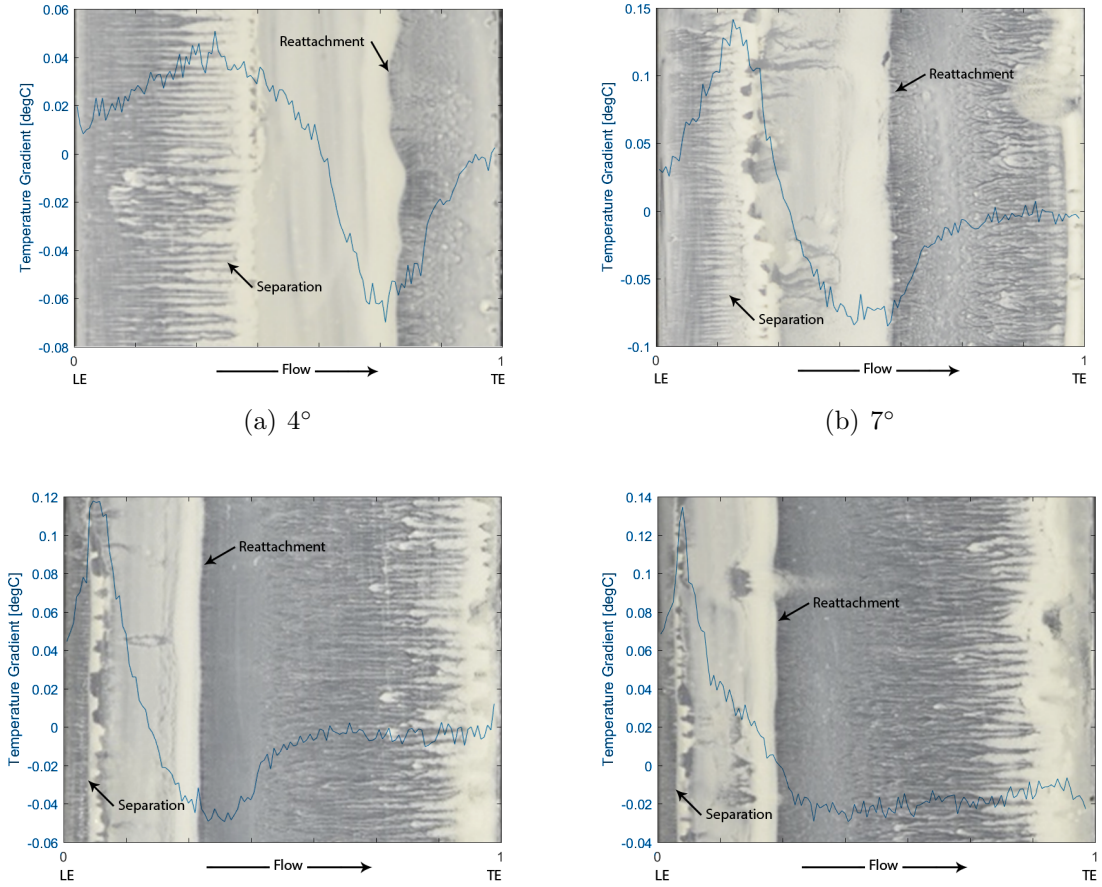

(a) 4° (b) 7°

(c) 10° (d) 11°

Figure 4.7: Temperature gradient (obtained from air heater method) along the non-dimensional chord of the airfoil (x/c) with surface oil flow visualization images in the background for four AOA: a) 10°, and b) 11° at Re= 48,000

The data post-processing technique of using temperature fluctuation (standard deviation of temperature in time) has also been used to extract data from raw images of thermographic flow visualization from the *second heating method*, electrically conductive paint on the 3D printed airfoil. Sample results can be seen on the left side of Figure 4.8. These results are calculated from 100 individual sequential images. Although separation and reattachment lines are visible in the raw data, keeping uniformity of the paint on the airfoil surface is a challenging task and small non-uniformity causes a large difference especially at lower AOA. Also, it should be mentioned that this technique requires a constant heating source

during the experiment, to keep the surface temperature in a reasonable range to provide usable results and not influence the flow. Since this heating method provides uniform data along the span, another post-processing technique was used so that in each chord position, temperature data are multiplied along the span (for the length of 100 pixels). This technique amplifies the temperature changes along the chord and the graph makes the separation and reattachment points reasonably clear. Sample results are presented on the right side of Figure 4.8.

Figure 4.9 presents the data using the resistive heating wire attached to the pressure side of the aluminum airfoil, the *first heating method*, for two AOA: a) 1°, b) 7°. In collecting the data for these results, the source of heating was turned off during the experiment to avoid excessive temperature. These data are the result of averaging the data over time for about 50 frames and 100 pixels span-wise correspondingly. In both sample angles that are presented in this figure, a sudden jump in temperature shows the separation and reattachment points. At 7° the flow structures are clear from both graphs of the average of temperature and surface oil flow visualization image. As can be seen at 1°, the separation point is a bit uncertain. In this method, the wire did not cover the whole pressure side of the airfoil and part of LE and TE of the airfoil was left with less heating coverage that may have caused less accurate data regarding the change of the angle of attack compared to the two other methods. Also from thermographic flow visualization graphs in this figure, it is clear that the range of temperature difference in using this method is less than $1°C$ which may increase the error.

Figures 4.10(a) and 4.10(b) show the measured location of the separation point (x/c) and reattachment point for both the SOFV and IT (resistive heating wire method) for varying AOA. Each data point represents 600 chordwise measurements for every one of the 200 IR images analysed. The linear relation found for both separation and reattachment is expected and has also been found using different techniques. The measured differences between separation and reattachment for different AOA predict that the bubble size decreases and moves toward the leading edge as AOA increases. In general, both methods show close agreement although the slope of the separation measured with IT is different than the SOFV. It could be due to the following reasons; first, the results for this graphs are obtained from preliminary IT tests that were acquired while transparent wind tunnel section walls were used. Using transparent walls increase the errors due to the reflection effects on the airfoil surface. Second, effects of the oil visualization materials on the airfoil surface[40].

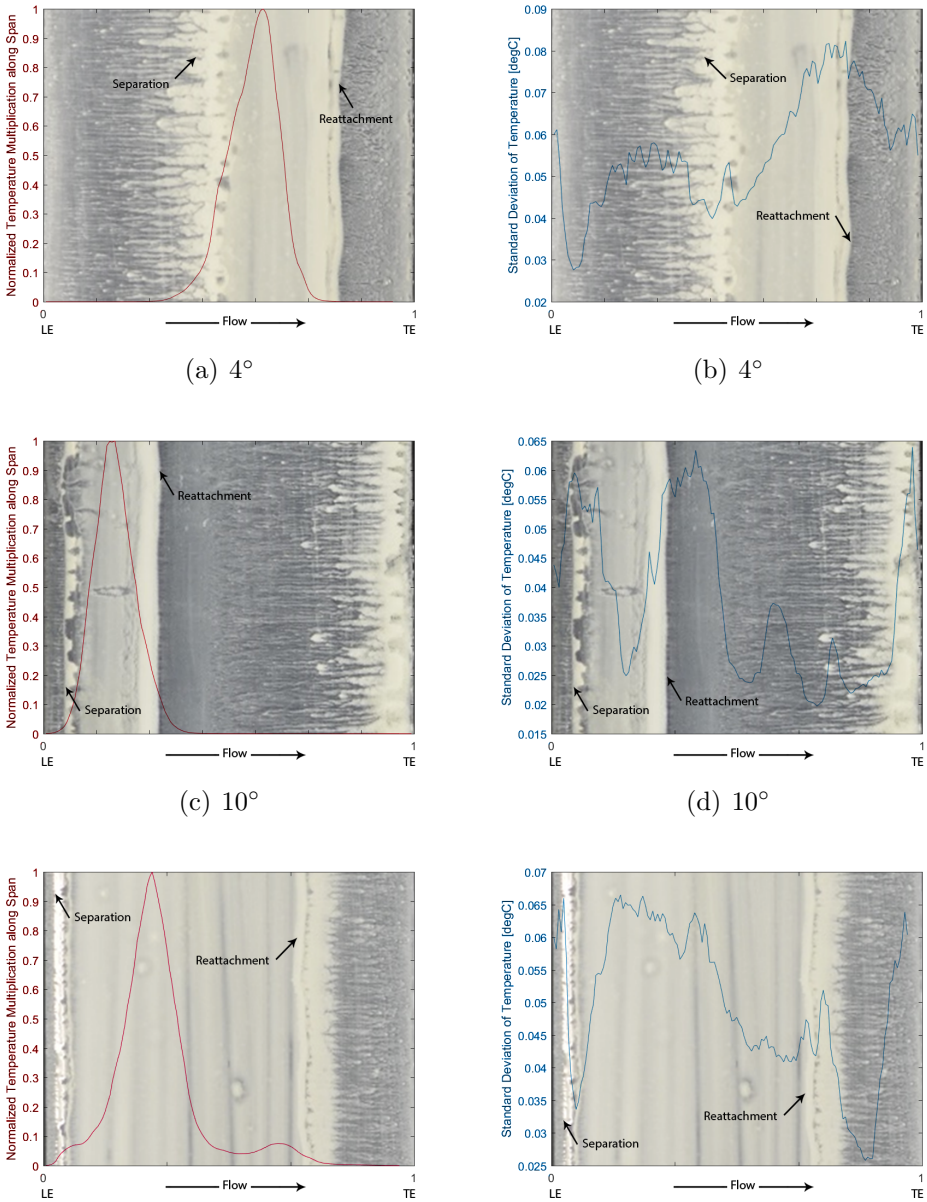

(a) 4° (b) 4°

(c) 10° (d) 10°

(e) 13° (f) 13°

Figure 4.8: Left side- Surface oil flow visualization and normalized multiplied temperature data along the span of the airfoil for a) 4°, c) 10°, and e) 13°). Right side- surface oil flow visualization and standard deviation of temperature for b) 4°, d) 10°, and f) 13°) at Re= 48,000 (results of Thermographic flow visualization with electrically conductive paint, second method)

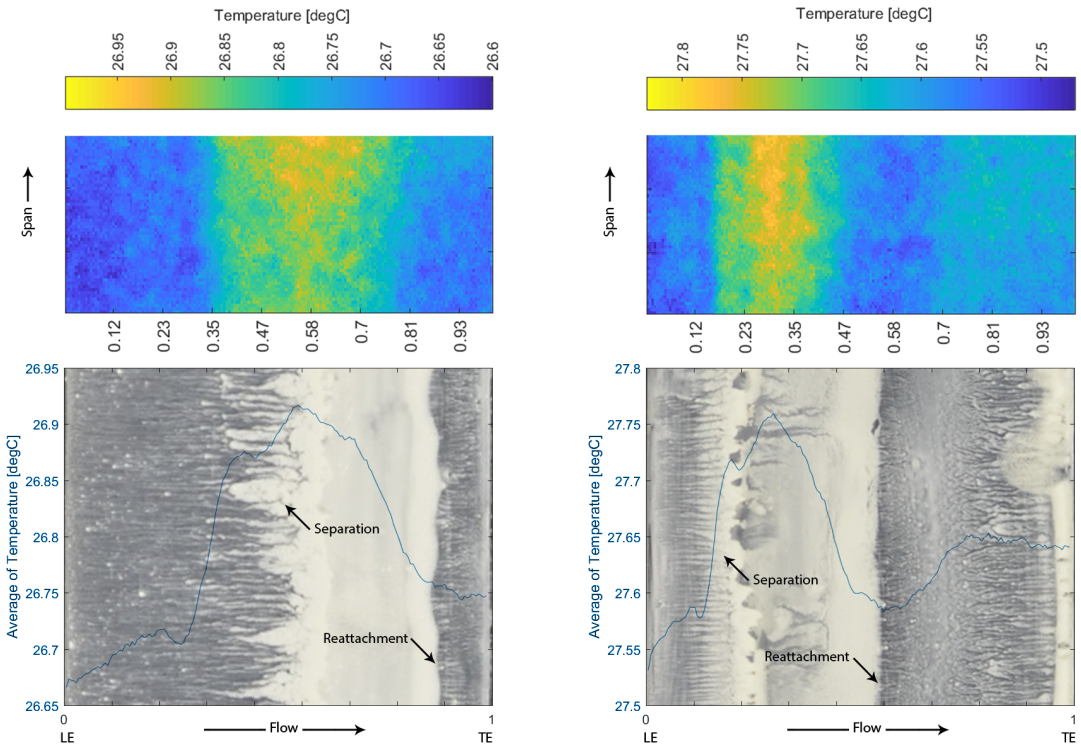

(a) 1°

(b) 7°

Figure 4.9: Thermographic flow visualization of first heating method (resistant heating wire method), surface oil flow visualization and the average of temperature over spanwise direction, a) 1°, b) 7° at Re= 48,000

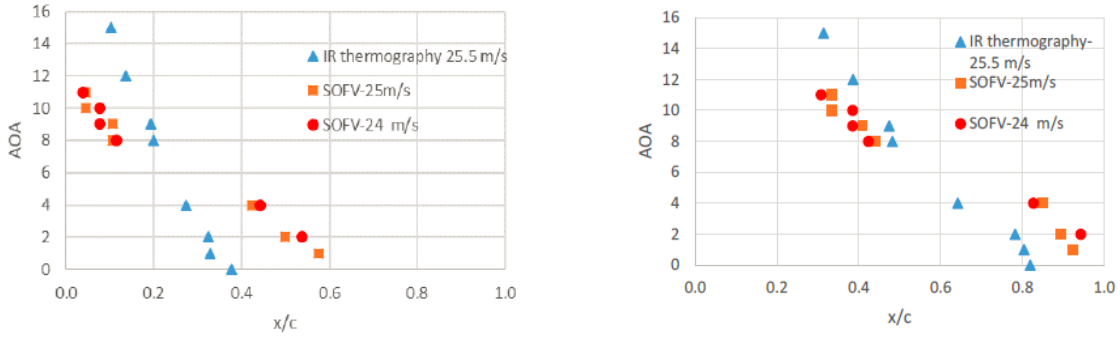

(a) (b)

Figure 4.10: a) Measured separation location for SOFV and IT methods, b) Measured reattachment location for SOFV and IT methods.

4.3 PIV- LSB Characteristics

Low Reynolds flow over the thin cambered airfoil is investigated using particle image velocimetry. As explained, a miniature airfoil model of an SD7037 airfoil has been used.

The original post-processed flow field data are calculated in x-y coordinates then the velocity field is transferred to the S-N coordinates (S: airfoil surface, N: Normal to the surface), Figure 4.11. Some features are measured from the x-y coordinates data, but S-N coordinates are used in integration calculations, such as BL features, pressure coefficient, and vorticity integration to minimize errors due to the curved geometry of the surface. As shown in figure 4.11, the tangent line at the surface of each point is calculated, and the line perpendicular to this line at each point is considered as the N direction.

4.3.1 Case studies

In this section effects of Reynolds number and AOA on the laminar separation bubble over the SD7037 airfoil in static conditions are investigated. Table 4.1 present a summary of the PIV experimental test plan for static case studies, As presented in table 4.1, five low Reynolds number are chosen. As explained before (see section 1), this range of Re is critical for airfoils. Also, due to the difficulty of performing experiments in low Re flows not enough data and information are available (see section 1.3.1).

The bubble characteristics are extracted from the velocity field data of 1.05C. The grid of 8×8 pixels has been used in post-processing PIV data, therefore, there is a vector (data

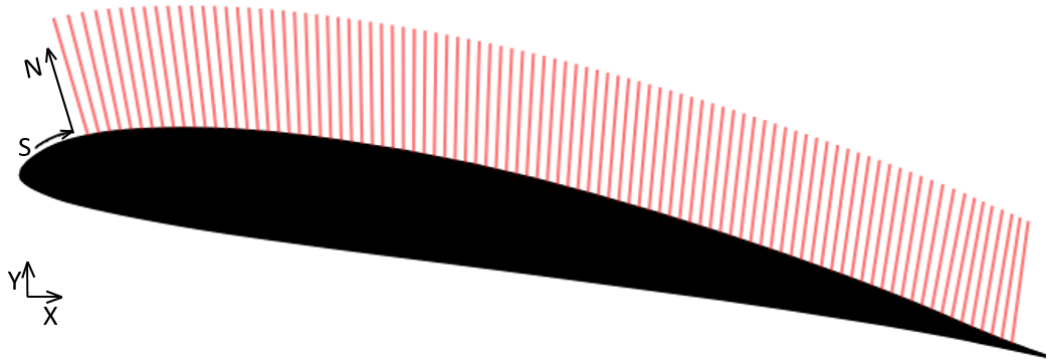

Figure 4.11: S-N coordinates over SD7037C airfoil

Table 4.1: Static case studies

Reynolds Number	$14500, 22500, 32000, 41000, 48000$
Angle of Attack	$1°$ - $10°$
Field of View	$\frac{x}{c} \approx \frac{y}{c} \approx 2.5C, 1.0C, 0.6C$

point) per $0.105mm$ of a $27mm$ flow field. In the processed PIV data including long and narrow bubbles, results may show late separation compared to the raw data. This is due to the BL thickness in laminar flow that could be less than the minimum distance (minimum grid size). Changing the grid size to 4×4 pixels, modifies the results and presents more accurate data for the separation point but with an increase in experimental uncertainty. Although the grid size has a important effect on the skin friction coefficient especially in long and narrow LSB (such as $7°$ in Re=48,000), decreasing the grid size increases the post-processing time considerably. Considering these points, the separation point can be detected from the pressure coefficient in comparison with the velocity contour and skin friction coefficient to avoid using smaller grid sizes. POD analysis has been done using a section of velocity filed data of FOV 1.05c and 0.6c. Although experiments have been completed for most AOA, results are presented for every other angle.

Table 4.2 presents a summary of the methods that were used to determine separation, transition, and reattachment points. A few points should be noted. Using velocity and its derivatives' profiles the airfoil BL would be detectable with high accuracy. The velocity profiles are in a good agreement with typical results as shown in figure 1.3.

The reattachment point found through the averaged velocity field is further downstream from the reattachment point from the instantaneous velocity field data. Instantaneous data

Table 4.2: Summary of various methods to characterize LSB used in this thesis

Separation point detection
- streamlines
- velocity field
- velocity and its derivatives' profiles
- BL thickness and BL momentum
- Skin friction coefficient

Transition point detection
- Pressure Coefficient (Cp)
- Reynolds shear stress
- TEM, Transition Exponential Method using Reynolds shear stress
- BL displacement thickness(δ^*), BL momentum thickness (θ),and shape Factor (H)
- Skin friction coefficient (C_f)
- POD

Turbulent reattachment point detection
- Pressure Coefficient (Cp)
- streamlines
- velocity field
- BL thickness and BL momentum
- Skin friction coefficient

or the projected velocity field from POD data can be used to determine the reattachment point as well as the transition point.

As explained in section 1.3.1 Russell theory [110] has been used here to identify LSB characteristics.The starting point of plateau pressure is the separation point, transition of laminar BL to turbulent BL is accompanied by a beginning of a rapid pressure rise. Therefore the endpoint of a constant pressure line is the transition point. The reattachment occurs after the transition, and the reattachment point is where the slope of Cp changed. The length of the LSB was divided into laminar and turbulent lengths; the laminar part of an LSB is where the surface pressure distribution is flat, and the turbulent length is the region with a high surface pressure gradient[53, 50].

4.3.2 Static results

First, to validate the results, the surface pressure coefficient measured from PIV data are compared with XFoil [26] and CFD [142] results of the SD7037 airfoil. In XFoil, free transition with $Ncrit = 9$ is considered, this is a standard number for average wind tunnels although Ncrit can vary from 10 to 12 for clean wind tunnels. Figure 4.12 shows the effect of transition number on the pressure distribution results obtained from XFoil at Re=41,000 and 48,000 and different AOA. The turbulence intensity has a clear effect on Cp_{min} at higher AOA and no/negligible effect at lower AOA on Cp_{min}. Also, effects of TI is more considerable in the lower Re. This behavior of Cp versus TI also observed for NACA0018 in the previous works[55].

There are no experimental data of pressure distribution for the SD7037 airfoil at low Re flows. Figure 4.13 shows the lift coefficients (C_l) for this airfoil at Re=60,000 including experimental results [118] and Xfoil results. As AOA increases from 5°, the difference between lift coefficient calculated from two methods increases. So that, the calculated lift from Xfoil shows higher values for higher AOA with a maximum difference at AOA= 9° and 10°. This could result from higher Cp value calculated from XFoil especially in AOA higher than 5° in comparison with experimental data, and we can expect this behavior when comparing our results with XFoil data. It is important to mention at Re=60,000, higher Ncrit (N=10) does not have any effect on results until AOA=10° as expected, and it is shown in Figure 4.12 at Re=48,000.

Surface pressure coefficient

Figures 4.14 and 4.15 show the pressure coefficient measured from PIV data in comparison with CFD[142] and XFoil results for Re=41,000 at $AOA = 1°$ and $AOA = 5°$. As can

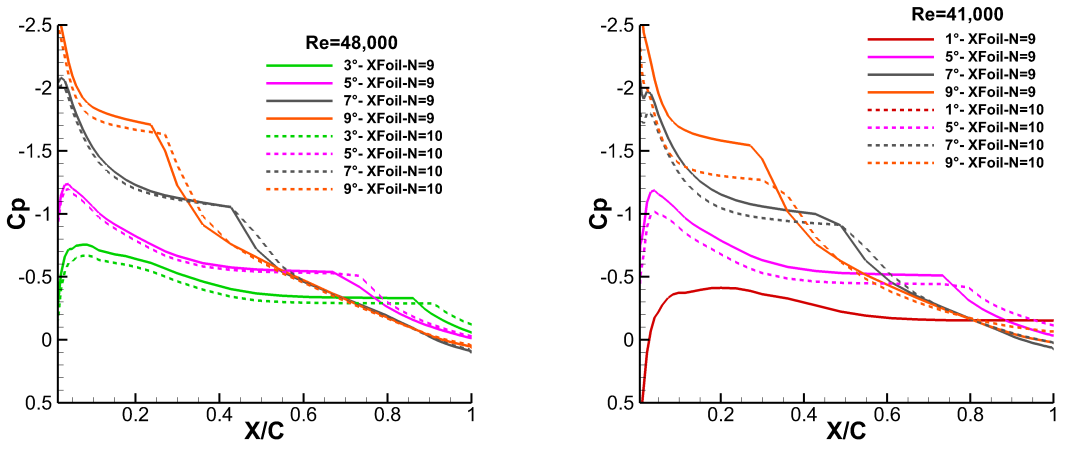

(a) (b)

Figure 4.12: Comparison of pressure distribution over SD7037 airfoil for different Ncrit in XFoil a) Re=48000, at AOA= 3°,5°, 7° and 9° , b) Re=41,000, at AOA= 1°, 5°, 7°, and 9°.

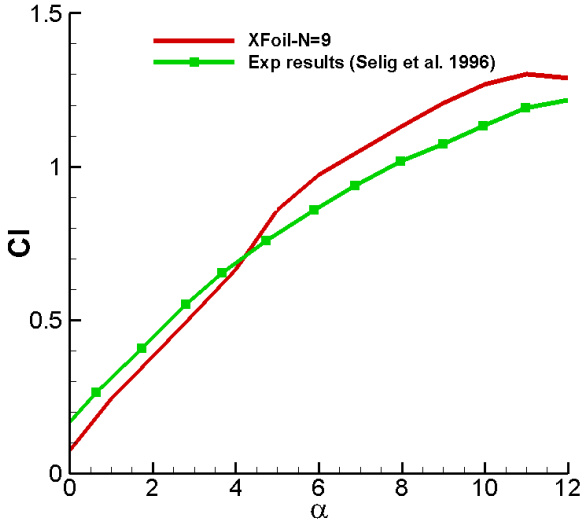

Figure 4.13: Lift coefficent (C_l) of SD7037 airfoil at Re=60,000, including experimental [118] and XFoil results

be seen, the experimental data are in excellent agreement with XFoil and CFD results. The slight difference between CFD and experimental results could be due to many reasons such as; the final profile of the built airfoil with CNC machine is slightly different from the perfect profile of the SD7037 airfoil especially in the LE and TE parts that have a notable effect on pressure distribution over the airfoil. The constant values that are used as air properties might slightly differ in different cases too. As can be seen the PIV results is slightly off at the peak Cp. This could be due to the flow acceleration in this region that is quite high and the thickness of the thin laminar BL that results in sharp velocity differences in this region. Also, as explained the data are transfered from x-y coordinates to S-N coordinates and there are not enough data normal to the chord close to the LE.

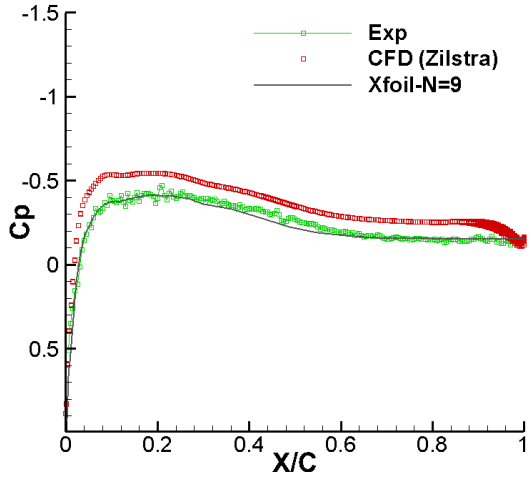

Figure 4.14: Pressure distribution over SD7037 airfoil including PIV experimental results, LES CFD simulation[142], and XFoil[26], case Re=40,000, $AOA = 1°$

Figure 4.16 shows the pressure distribution over the SD7037 airfoil at AOA= 1° to 9° at Re=41,000. As can be seen the effects of Ncrit are more considerable at higher AOA and lower Reynolds but the overall behavior of the pressure distribution stays the same, As expected for AOA higher than 6°, here showing 7° and 9° the difference can be seen between XFoil and experiments that is expected based on comparing the results at Re=60,000 that were mentioned above.

From the wind tunnel calibration data that has been collected a few times along with the experiments, turbulence intensity of the tunnel is minimum for Re=41,000. The TI of the tunnel is always less than 1%, but it slightly changes with Reynolds number as it is

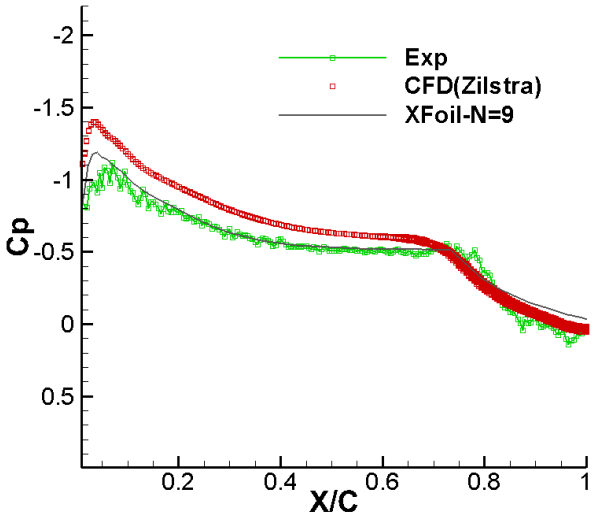

Figure 4.15: Pressure distribution over SD7037 airfoil including PIV experimental results, LES CFD simulation[142], and XFoil[26], case Re=40,000, $AOA = 5°$

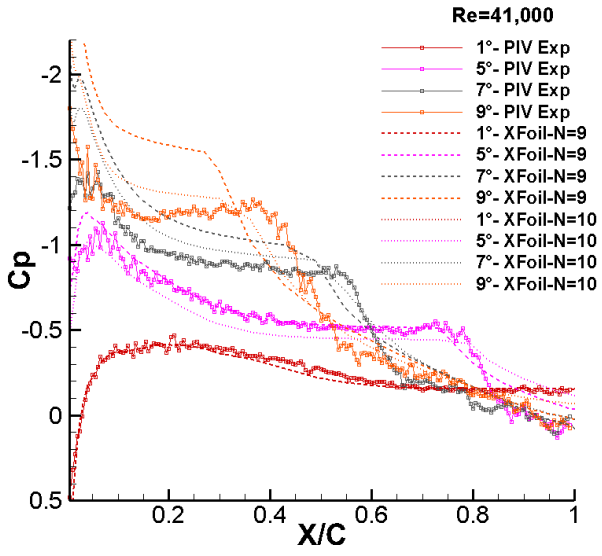

Figure 4.16: Comparison of pressure distribution over SD7037 airfoil including experimental results measured from PIV and XFoil, case Re=41,000, AOA=1° to 9°

higher in lower flow velocities. Therefore, based on experimental results of Cp at different AOA and Re, XFoil results with $Ncrit = 9$ have been used to compare with Cp from PIV experiment results. Figure 4.17 shows the pressure distribution over the SD7037 airfoil at AOA= 3°, 7° at Re=32,000 and 48,000. As can be seen, the results are in excellent agreement.

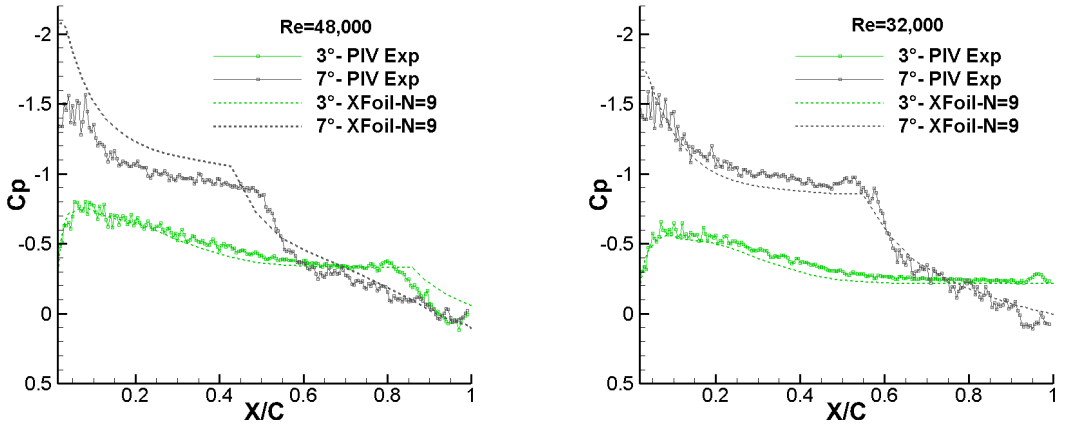

(a) (b)

Figure 4.17: Comparison of pressure distribution over SD7037 airfoil including experimental results measured from PIV and XFoil, a) case Re=48,000, AOA=3° and AOA=7° b) case Re=32,000, AOA=3° and AOA=7°

Figures 4.18 to 4.22 show the measured pressure distribution over the SD7037 airfoil (left side) and a sample of raw instantaneous PIV images at different AOA (right side) at Re=14,000 to Re=48,000. As can be seen in Figure 4.18 at Re=48000, there is a very narrow bubble from AOA=3° to AOA=9°. Cp gradually increases with increasing AOA as well. The same behavior can be seen for Re=41000 in Figure 4.19.Despite the small change in the length of the LSB, the height of the bubble clearly increases (later in this chapter, this will be discussed in detail). With decreasing Re to 32000 (Figure 4.20), stall will happen at AOA=9°. It is important that at Re=41000 and 48000, stall occurs after a short bubble close to the LE but at Re=32000 stall occurs at $AOA = 8°$, after the existence of a long bubble at AOA=7°. At Re=22000, Figure 4.21, the transition occurs close to the TE at AOA=5°. Flow separation moves toward the LE at AOA 7° and 9°. Looking at Cp shows that with increasing AOA the transition region moves toward the LE, similar to the separation point. This is the same for the lowest Re, Figure 4.22. But overall the Cp value is higher for AOA=7° and 9° compared to the two lower angles at Re=14000 while Cp at

AOA=5°, 7°, and 9° is almost the same at Re=22000. At Re=14000, except at AOA=9°, it is hard to identify the transition point from Cp. At Re=22000, pressure recovery is associated with pressure fluctuations at AOA= 5°,7°, and 9°. These fluctuations are also showing up at AOA=9° at Re=14000. These fluctuations occur due to the existence of vortical structures in the flow. The first fluctuation is the result of a formed vortex at the end of the bubble and shows the transition point. The flow reattached to the surface at about $x/c = 0.88$. Although the Cp behavior is different from higher Re and shows a rise to the second peak after the reattachment. This rise is due to the separated vortex following the LSB. From Cp, the reattachment point at Re=22000 and AOA=5° seems to be at the TE of the airfoil that is in agreement with time averaged velocity field illustrated in Figure 4.28.

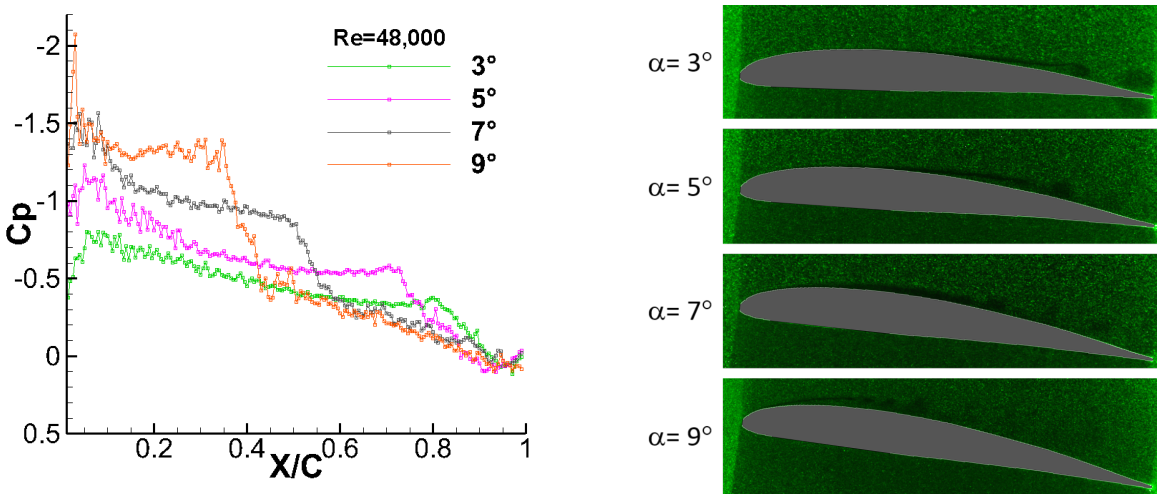

(a) Cp

(b) Sample instantaneous PIV Images

Figure 4.18: a) Pressure distribution over the suction side of the SD7037 airfoil b) Sample instantaneous PIV images at Re=48000

Table 4.3 presents separation, transition and reattachment points at different Re and AOA, determined from surface pressure coefficient graphs calculated and measured from PIV data as explained in section 3.3.4. From Cp plots, the transition point can be identified at the end of constant pressure region where fluctuation increases or at the beginning of the change in the slope of Cp. In XFoil data it occurs as a sharp edge at the end of the constant pressure region but PIV data provide more information that might reveal details about the flow in this region. In Table 4.3, the transition point is considered as the end of

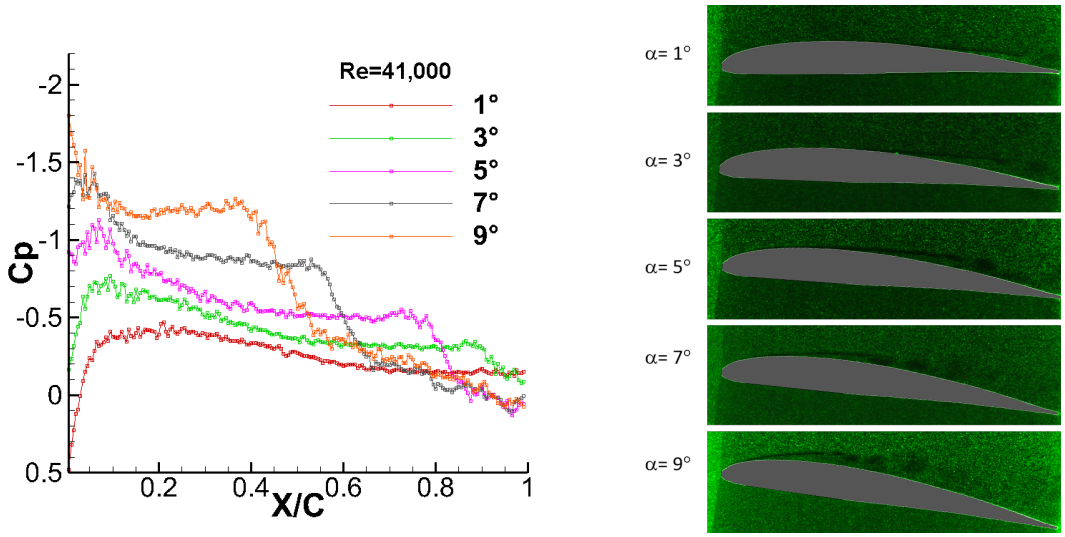

(a) Cp (b) Sample instantaneous PIV Images

Figure 4.19: a) Pressure distribution over the suction side of the SD7037 airfoil b) Sample instantaneous PIV images at Re=41000

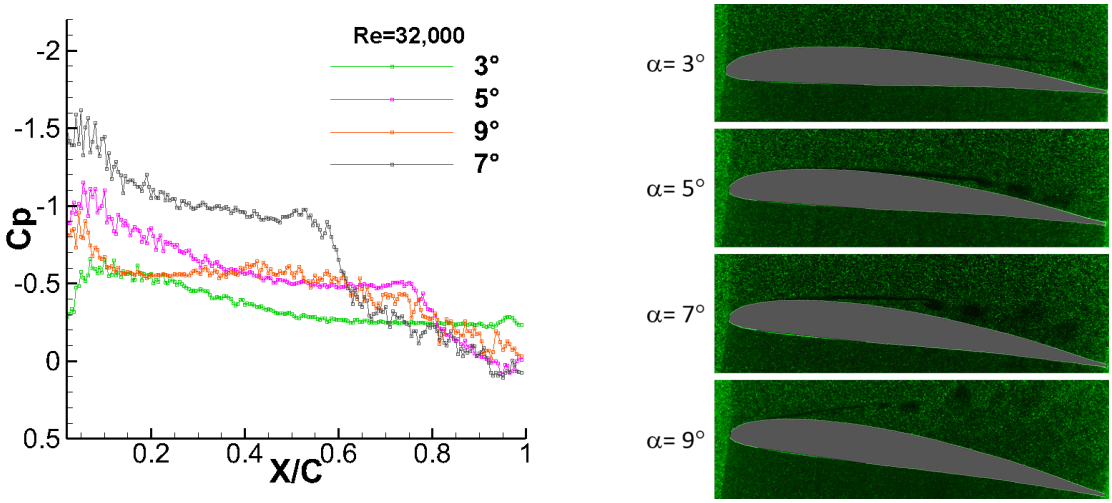

(a) Cp (b) Sample instantaneous PIV Images

Figure 4.20: a) Pressure distribution over the suction side of the SD7037 airfoil b) Sample instantaneous PIV images at Re=32000

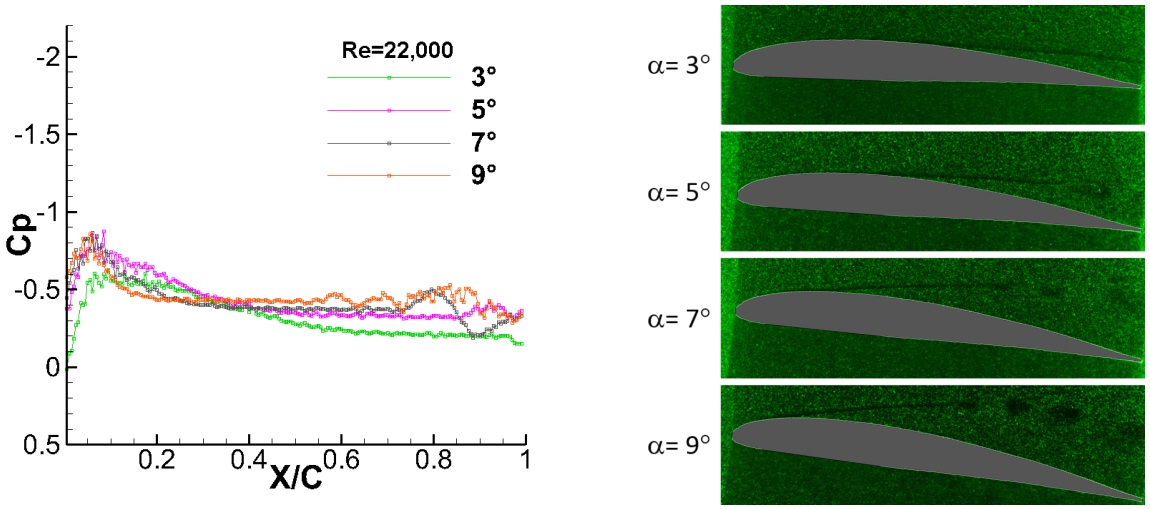

(a) Cp (b) Sample instantaneous PIV Images

Figure 4.21: a) Pressure distribution over the suction side of the SD7037 airfoil b) Sample instantaneous PIV images at Re=22000

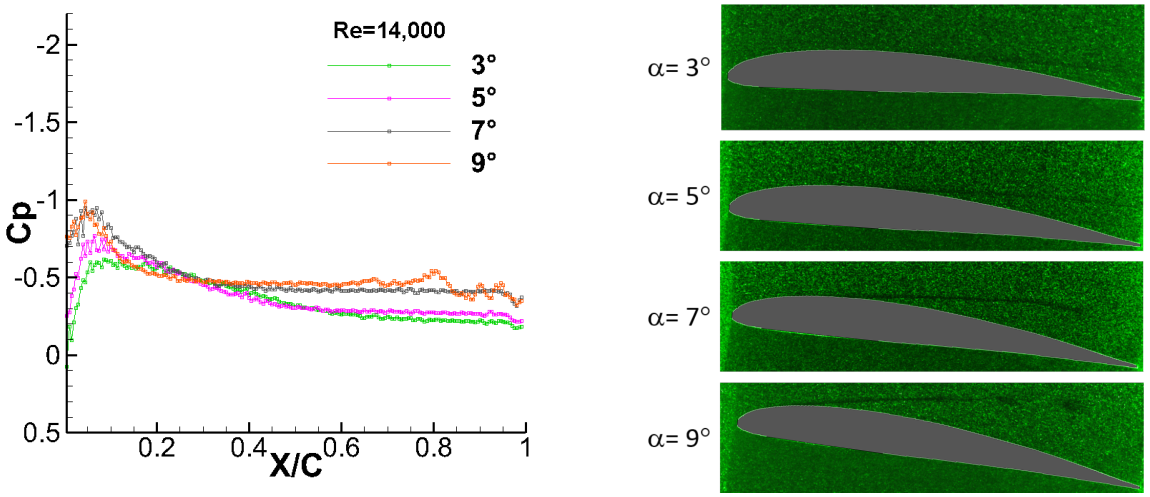

(a) Cp (b) Sample instantaneous PIV Images

Figure 4.22: a) Pressure distribution over the suction side of the SD7037 airfoil b) Sample instantaneous PIV images at Re=14000

Table 4.3: Laminar separation bubble parameters for investigated static cases

Re	AOA (°)	x_s/c	x_t/c	x_R/c
14000	No recognizable Bubble			
22000	5	0.41	0.83	0.92
	7	0.22	0.70	0.88
32000	3	0.56	0.90	-
	5	0.44	0.68	0.80
	7	0.20	0.50	0.70
	9	0.12	0.36	-
41000	1	0.60	0.88	-
	3	0.52	0.85	0.91
	5	0.41	0.70	0.83
	7	0.24	0.50	0.60
	8	0.12	0.39	0.50
	9	0.09	0.34	0.48
48000	3	0.52	0.75	0.87
	5	0.40	0.67	0.76
	7	0.17	0.42	0.55
	8	0.12	0.34	0.44
	9	0.09	0.27	0.40

the constant pressure region but it will be discussed in more detail later.

Figure 4.23 presents Cp for all investigated Re flows at AOA= 3° and 5° and Figure 4.24 presents Cp for all investigated Re at AOA= 7° and 9°. As can be seen with decreasing the Re, the length of short bubble increases until stall and the flow separates from the surface without reattachment (AOA=9°). Although there is a long bubble at 5°, the length of the bubble stays the same at the three highest Re. Unusually the pressure distribution over the suction side of the airfoil at Re=14,000 is higher than Re=22,000 except at AOA=5°. While there is no clear difference in Cp for these two cases, looking at Figure 4.21(b) shows the separated shear layer is breaking down close to the TE at Re=22000. Investigating the instantaneous velocity field reveals breaking down of the separated shear layer and formation of a vortex after closing the bubble. The separated vortex forms almost at the TE of the airfoil in most of time. Therefore it might be considered that the flow reattached to the surface but it does not reach fully turbulent flow conditions. Figures 4.25 and 4.26 show four random instantaneous velocity fields at Re=14000 and 22000. From the figures, cat-eye vortices can be seen at the TE of the airfoil at Re=22000. As mentioned, this is

the reason for the pressure jump at the TE of the airfoil at Re=22000 and higher pressure distributions over the airfoil (Figure 4.24).

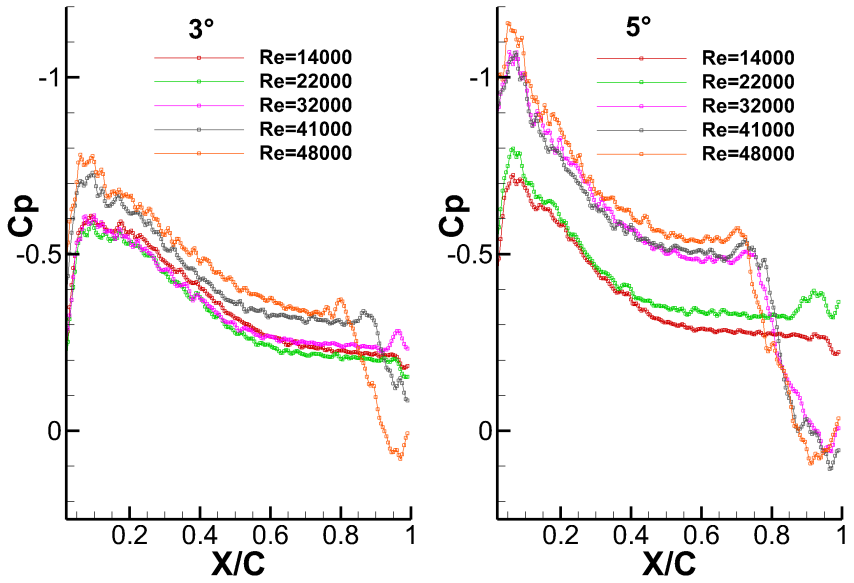

Figure 4.23: Surface pressure coefficient over SD7037 airfoil at AOA=3° and 5° at all investigated Re.

This difference also can be seen in the time averaged velocity vectors and velocity fields. Figures 4.27 and 4.28 show the averaged velocity field and velocity vectors at Re=14000 and 22000 at AOA=5° to compare with instantaneous plots shown in Figures 4.25 and 4.26. Although instead of two separate small vortices, the time averaged flow misleadingly shows only a larger vortex at the TE at Re=22000. Velocity vectors at Re=22000 show the existence of a strong vortex at the TE. At Re=22000 (Figure 4.28), the maximum reversed flow velocity is about $14\%U_\infty$ and averaged velocity vectors show a relatively large vortex at the TE while at Re=14000 (Figure 4.27), the maximum reversed flow velocity is only $4\%U_\infty$ and velocity vectors illustrate flow separation. The effect of the TE vortex and its reversed flow on the surface pressure distribution can be seen in the Cp plot (Figure 4.23). In the investigated Re range, changes of flow behavior with Re are more tangible at high angles compared to lower angles.

In discussion of different S series airfoil, Somers [126] discusses in designing the airfoil, a short region of slightly adverse pressure gradient called the "transition ramp" is developed where transition from laminar to turbulent flow occurs efficiently [126]. This region is shown in Figure 4.29. Here we use the same definition as Selig[115] for the transition ramp, the

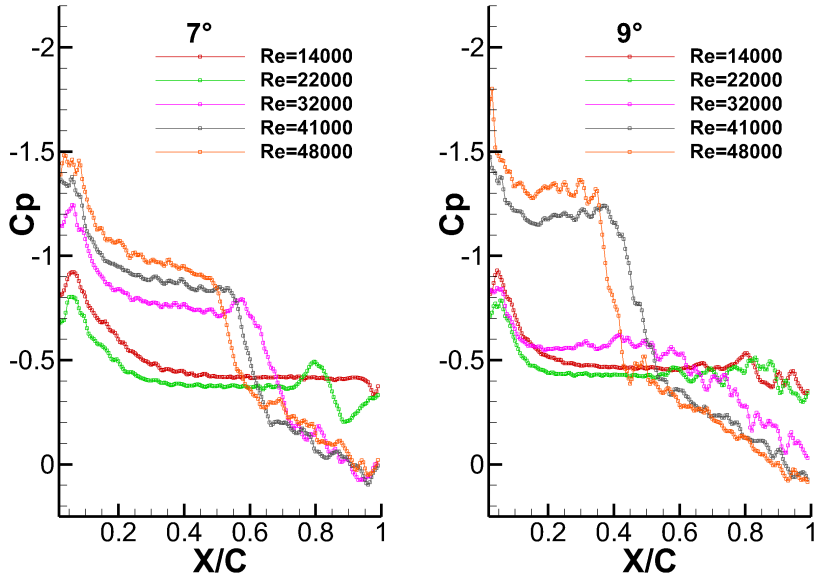

Figure 4.24: Surface pressure coefficient over SD7037 airfoil at AOA=7° and 9° at all investigated Re.

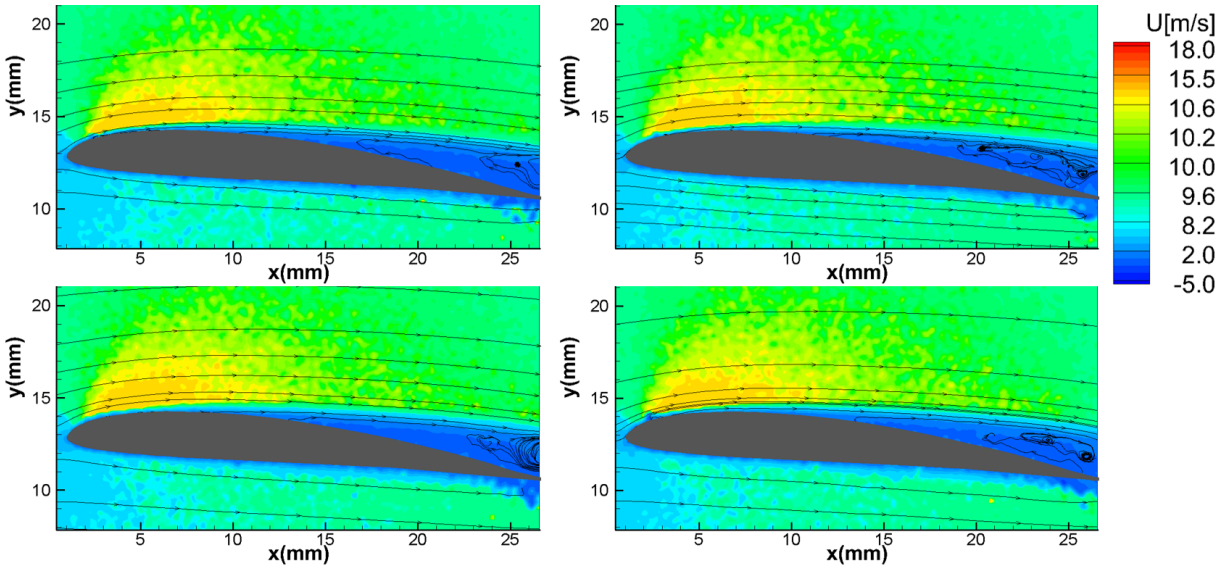

Figure 4.25: Random instantaneous velocity field, SD7037 airfoil, case Re=14000, AOA=5° with streamlines overlaid

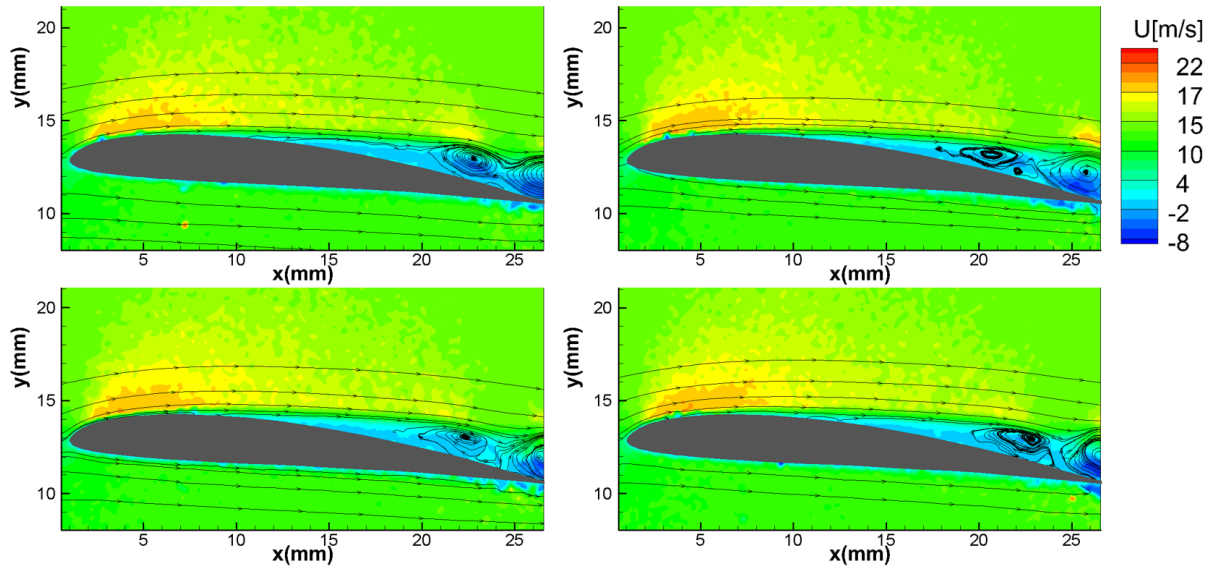

Figure 4.26: Random instantaneous velocity field, SD7037 airfoil, case Re=22000, AOA=5° with streamlines overlaid

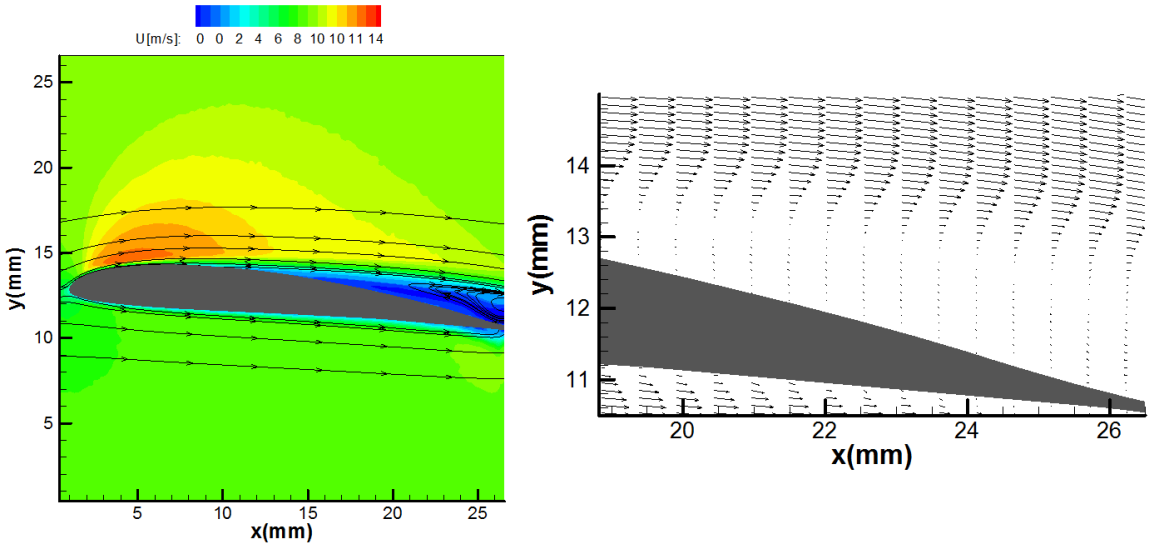

Figure 4.27: Time averaged velocity field and velocity vectors over SD7037 airfoil, case Re=14000, AOA=5°, right side zoomed in picture at second half of the chord

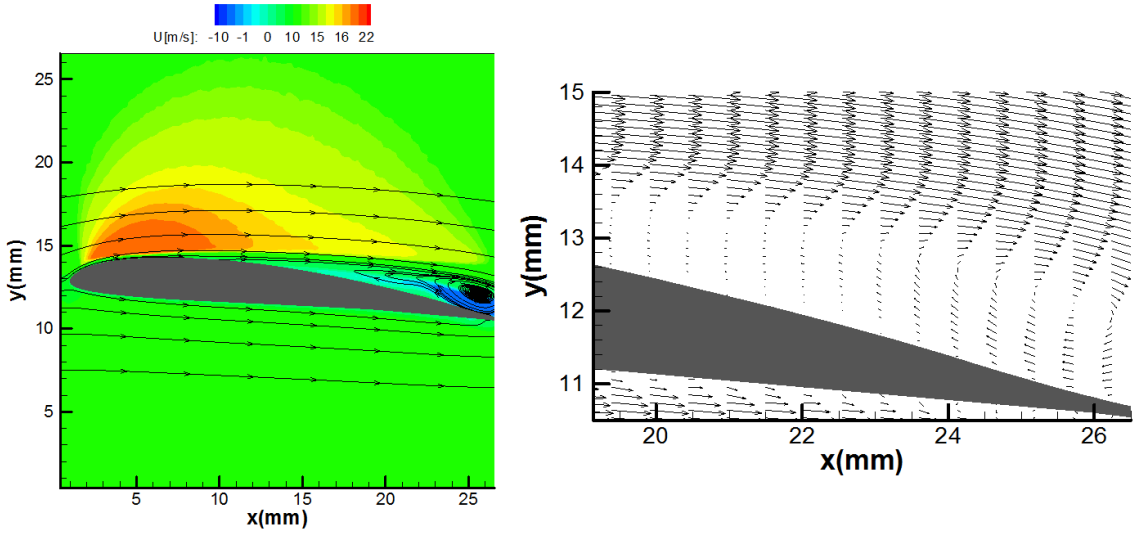

Figure 4.28: Time averaged velocity field and velocity vectors over SD7037 airfoil, case Re=22000, AOA=5°, right side zoomed in picture at second half of the chord

chord-wise distance where transition occurs. As can be seen in Figure 4.19(a) this transition ramp decreases with decreasing AOA [29]. The slope of the transition ramp is related to the LSB location and height[91] that can be used to identify the bubble parameters. This will be explained in detail later when investigating the thickness and length of an LSB. Selig[115] mentioned that even small changes in the shape of a transition ramp can have significant effects on the airfoil performance.

Figure 4.30 shows SOFV at Re=32,000 and AOA=9° and Figure 4.31 shows time averaged velocity vectors measured from PIV data for the same case study. In this picture two oil painted regions remain untouched while an oil accumulation line is at about X=0.44C. This behavior also can be seen at AOA=8° and 10° in Figure 4.2. Looking at the instantaneous PIV images of these three angles reveals that flow at the roll-up location is highly unsteady so that formed vortices close to the transition point are moving toward and away from the surface constantly. While at AOA=11°, the flow remains separated from the surface all the time. The averaged velocity field shows maximum reversed flow value at this region too. Therefore only considering the SOFV shows stable reattached turbulent flow just considering the oil accumulation line but PIV data shows that there is only unsteady behavior close to the location of the transition point that might push the oil on the surface toward the LE but overall the flow did not reattach to the surface and as SOFV shows the painted oil at the TE region of the airfoil stayed untouched too.

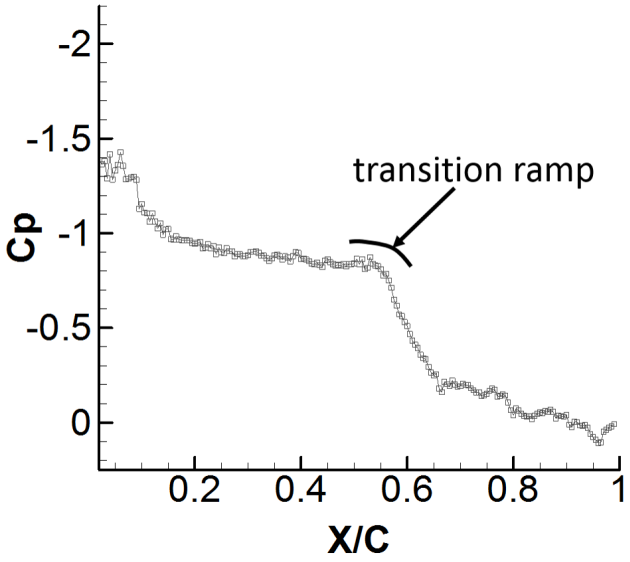

Figure 4.29: Transition ramp on SD7037 airfoil at Re=41000, AOA=7°

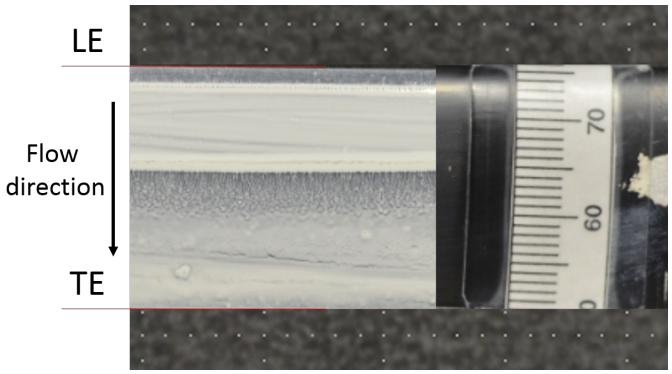

Figure 4.30: Surface oil flow visualization over SD7037 airfoil, Re=32000, AOA=9°

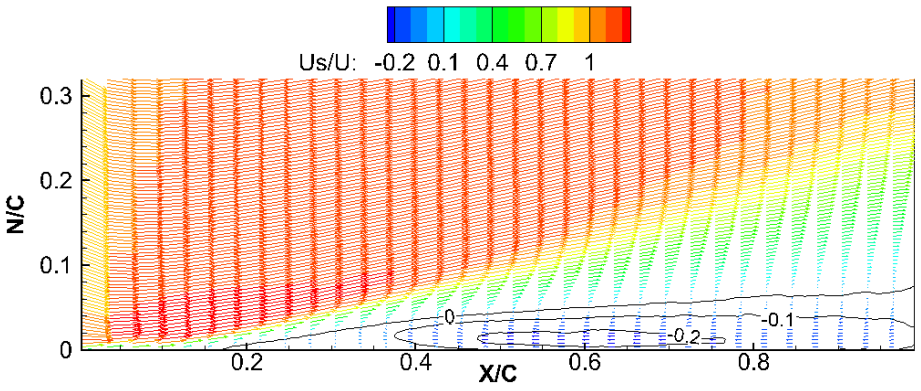

Figure 4.31: Time averaged velocity vectors ,SD7037 airfoil, case: Re=32000, AOA=9°, iso-contour lines of reversed flow are overlaid

Skin friction coefficient

As presented, laminar separation, transition and turbulent reattachment points can be identified through PIV velocity data and the determined pressure distribution. As explained in section 3.3.5, skin friction,C_f, can be used as well. In this research the zero crossing line of C_f vs X/C was used to determine the separation and reattachment points. The transition point is considered to be at the beginning of the negative spike in the C_f distribution that is somewhere between the transition onset as Walker *et al.* [133] defined and the location of maximum negative Cf where Singh and Sarkar [124] defined the transition length. Yuan *et al.* [139] mentioned the sudden decrease of Cf before reaching its negative peak indicated the transition. The oil accumulation line is slightly upstream of the flow reattachment. The oil is scrubbed forward by a roll up vortex until the surface tension of the oil pool equals the shear stress of the flow field and forms the oil accumulation line[80]. Figure 4.32 presents C_f over the SD7037 airfoil at Re=41000. With increasing AOA, the minimum C_f marked as the oil accumulation point decreases that is in accordance with the strength of the reversed flow results of LSB. The results are in good agreement with C_f presented results by Dorschner *et al.*[24] for a SD7003 airfoil at Re=60000 at AOA=4°.

The LSB parameters calculated from the skin friction coefficient are summarized in Table 4.4. The results are in good agreement with the data extracted from surface pressure (Table 4.3) although in most of the cases, the separation point is measured further downstream. This error is due to the thickness considered to calculate wall shear stress and it decreases with decreasing the AOA or Re when the thickness of the bubble increases.

Another point is that with increasing Re, the distance between the oil accumulation line

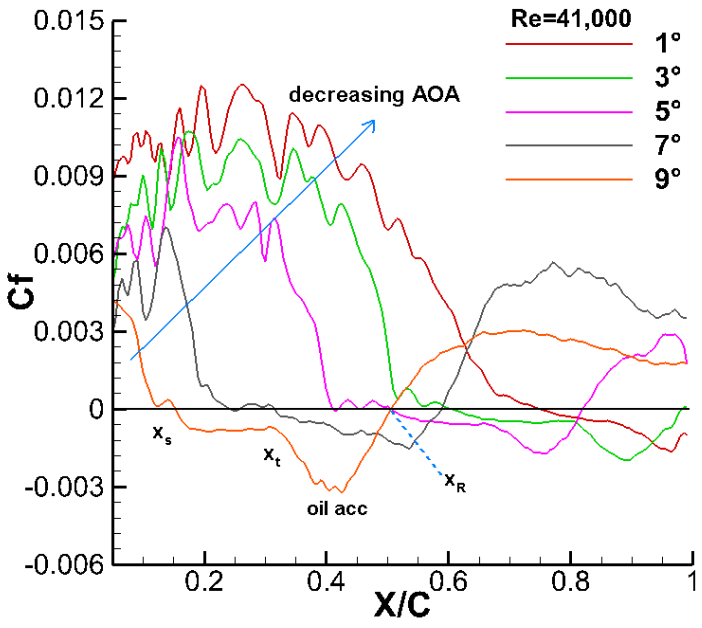

Figure 4.32: Skin friction coefficient distribution over the upper surface of SD7037 airfoil measured and calculated from PIV data

Table 4.4: Laminar separation bubble parameters for investigated static cases calculated from skin friction coefficient (for variable definitions see figure 4.32)

Re	AOA (°)	x_s/c	x_t/c	x_R/c	x_{oilacc}/c
32000	3	0.56	0.90	-	0.96
	5	0.44	0.67	0.82	0.76
	7	0.22	0.52	0.70	0.62
41000	1	0.68	0.89	-	0.97
	3	0.51	0.84	0.95	0.89
	5	0.41	0.70	0.82	0.76
	7	0.23	0.49	0.59	0.53
	8	0.14	0.38	0.51	0.44
	9	0.12	0.34	0.50	0.40
48000	3	0.57	0.75	-	0.80
	5	0.42	0.66	0.77	0.72
	7	0.24	0.40	0.49	0.46
	8	0.17	0.33	0.40	0.36
	9	0.13	0.28	0.37	0.34

and the reattachment point decreases. This behavior also can be seen in data measured by McGranahan *et al.* [85].

Figure 4.33 shows instantaneous and time-averaged normal to the airfoil surface velocity component. As can be seen the reattachment point due to the unsteady behavior of the shear layer roll-up at the end of the bubble moves a bit, and the averaged reattachment point is a bit further downstream than the instantaneous ones. Although the drifting vortices in the turbulent boundary layer that can be seen in instantaneous data (can be seen in the second from the left at the bottom of Figure 4.33) move along the chord and time averaging washes them out. In this figure, the typical cat-eye structures at the end of the bubble and vortex roll-up are observed. The cat-eye structures confirm the domination of Kelvin-Helmholtz instabilities in LSB transition that are also reported by Burgman and Schroder [15] and Nati *et al.* [93].

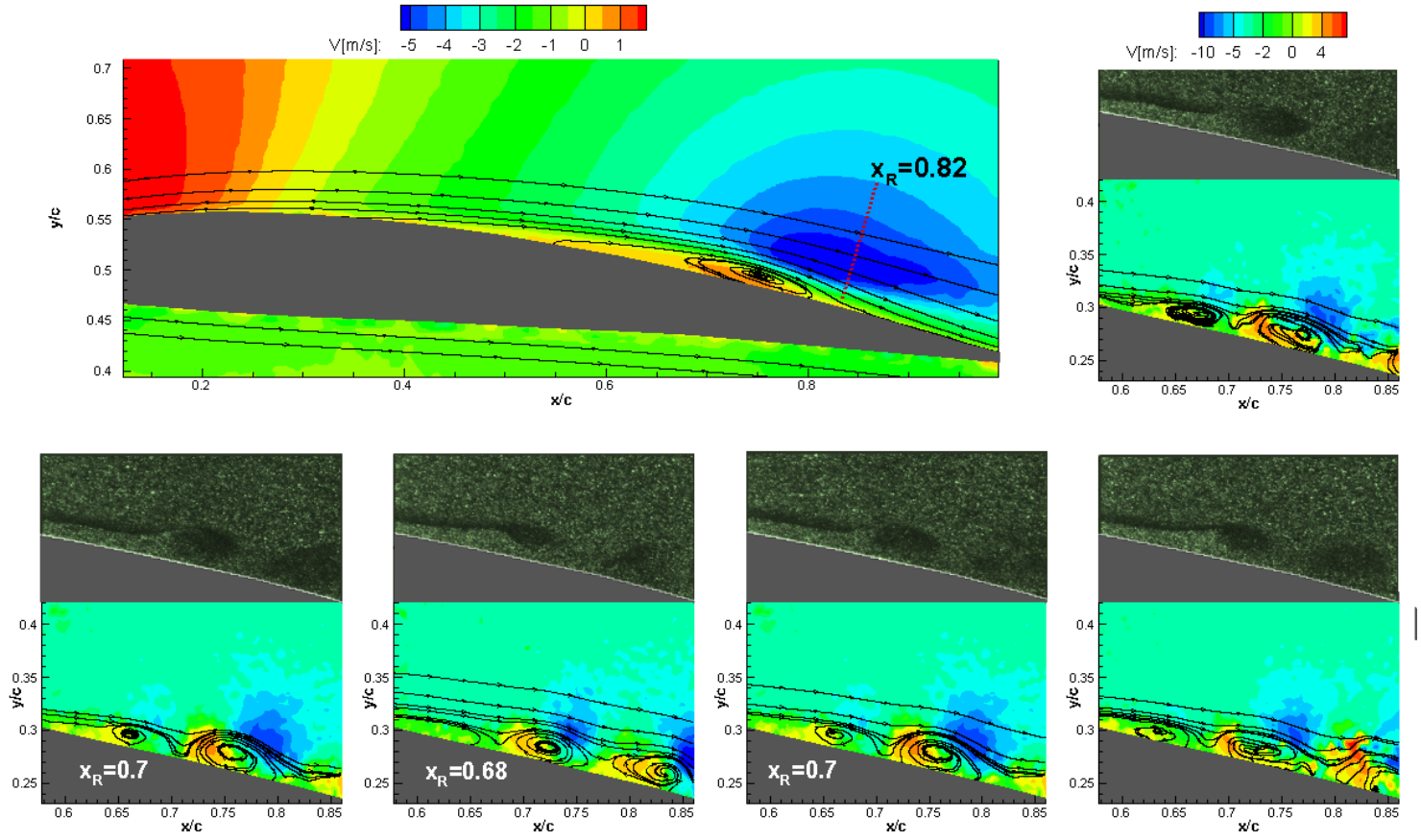

Figure 4.33: Instantaneous and time averaged normal velocity component contour over SD7037 airfoil, case Re=32000,$AOA = 5°$, streamlines are added to the velocity contours too, and the same velocity scale used for all instantaneous data

Integral boundary layer parameters

As mentioned in sections 3.3.2 and 3.3.1, velocity contours, streamlines and integral boundary layer features ((δ^*, θ, H) can be used to characterize LSB and BL parameters. Figure 4.34 shows the shape factor parameter for Re=48000 at different AOA. The location of maximum H is usually considered as the transition point shown in the figure. Shape factor H is highly dependent on momentum thickness θ. In the θ determination the thickness of the BL us assumed where $U_s = 0.99U_e$. This criteria is not 100% accurate in the experiments since velocity is increasing continuously. The better option is considering infinity as the upper limit for the integral BL features to estimate the BL thickness too. Both methods have been used in this research and results show that the location of maximum H stays constant but the numerical value of H slightly decreases in the second method. This is more noticeable where there is a stronger vortex or reverse flow due to the existence of a bubble. As can be seen the part of H after x_{tr} which represent turbulent flow is lower than the laminar part. McAuliffe and Yaras [84] reported H about 3 at the separation point over SD7003 airfoil at Re=40,000 and AOA= 4°, 8° that is in good agreement with this result. For the transition point they reported H_{max} about 8-9 calculated from PIV data that was higher than H they calculated from hot-film data that showed zero for velocity near the wall up to the transition location and means zero is considered for reversed velocity regions up to the transition point. There are not enough published PIV studies providing BL integral features with full information about BL flow. This lack of data is more noticeable for curved surfaces like an airfoil where the pressure gradient changes the shear layer shape. Most of the published work performed the experiment on a flat plate while forcing a pressure gradient on the surface.

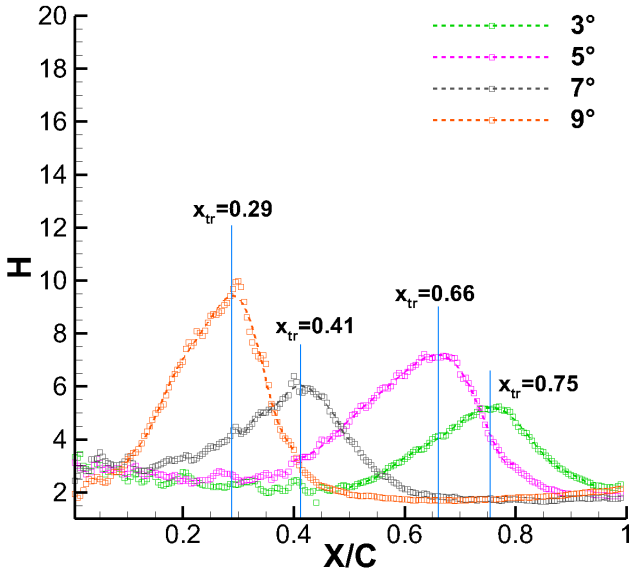

Figure 4.34: Shape Factor H versus X/C, SD7037 airfoil, case: Re=48000, AOA=3°, 5°, 7°, 9°

Figure 4.35(a) shows the shape factor H at Re=41000. As expected the location of maximum shape factor can be considered as the transition point. This point indicates a sharp increase in normal velocity fluctuation that is in agreement with results of Michelis *et al.*[90]. Maximum H location is upstream of the reattachment point and the value of H decreases after the transition point. If there is enough distance H will reach a value lower than $H_{laminar}$ that represents the turbulent flow region. As shown, H reached to values of 2 and 1.6 at AOA=5° and 7° respectively that is typical for turbulent flows[136]. Reaching fully turbulent flow might take several bubble lengths[90]. As explained before the value of H is in accordance with the thickness of the reversed flow region. Also, an increasing maximum H value with a decreasing Re indicates a decrease in the reversed flow value.

Figure 4.35(b) shows the comparison of H at Re=14,000, 22000, and 32000 at AOA=5°.As explained above the eye-cat structure can be seen at Re=22000 at AOA= 5° while looking at instantaneous data confirms flow reattachment close to the TE. From the shape factor flow transition and flow tendency to reattachment can be detected too. As expected the H factor is highly dependent on the size and strength of the reversed flow region, although the hypothetical boundary layer edge ($\delta_{0.99}$) has an important role in BL integration features especially in transition and turbulent regions where rate of change of velocity compared

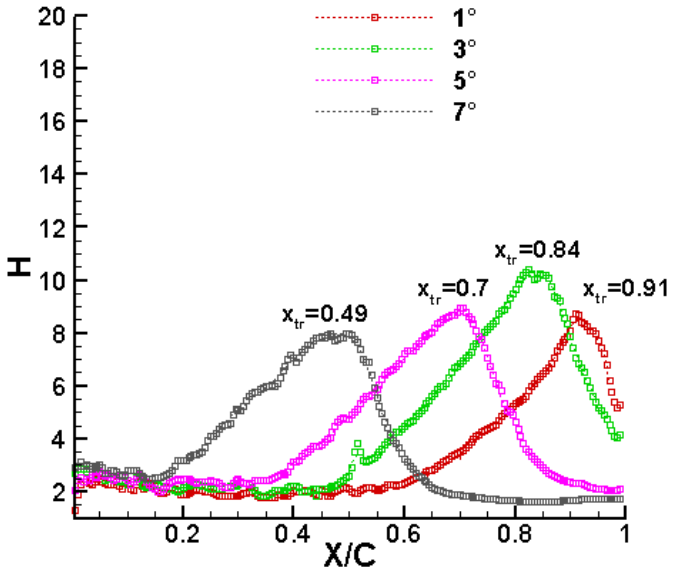

(a)

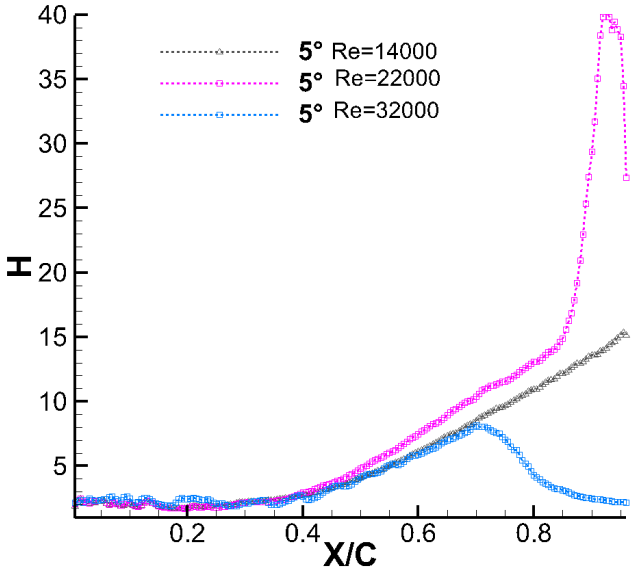

(b)

Figure 4.35: Shape factor H at different AOA a) Re=41000, b) Re=32000, 22000, 14000 at AOA=5°

to laminar flow decreases after the viscous sub-layer. In lower Re or high AOA (i.e. 9°) the vortical structures in the transition region of the flow are stronger, and the transition ramp represents a larger peak in Cp, Figure 4.21. As explained the beginning of this ramp was considered as the transition point in Cp. This point is in very good agreement with the location of the maximum shape factor at Re=48000 and 41000. Although at lower Re, Re=22000 and 32000, less agreement can be seen in the occurrence of two conditions; at AOA=5°,7° where there is a large separated vortex following the reattachment point and results in a large reversed flow therefore the location of maximum H slightly moves closer to the TE. In these cases with increasing the limitation of the BL integral to the end of data points, two peaks show up in the shape factor. The location of the first local peak is in good agreement with the measured transition point from Cp ($x_{tr,AOA=5^\circ} = 0.83c$ and $x_{tr,AOA=7^\circ} = 0.69c$) but after the first peak, the shape factor does not dramatically decreases and after a short distance it rises again due to the existence of the following large vortex at the TE.

As explained before, δ^* considerably increases during flow separation. Figure 4.36 shows detected separation points based on δ^* at Re=48,000. The maximum δ^* usually occurs downstream of the maximum shape factor and can be used in detecting the height of the bubble. Also since displacement thickness increases along the separation bubble it can be used in identifying the shape of the bubble or the angle of the separated streamline. Displacement thickness in the laminar region ahead of the separation slightly decreases with decreasing AOA that is in agreement with XFoil [26] results in the same study cases. As shown in section 3.3.1 and Figure 3.10, the inflection line lies on top of δ^* too. Separation points measured from δ^* are in good agreement with other methods used. The displacement thickness at the separation point decreases with increasing AOA that is consistent with the results of Burgmann and Schroder [15]. Figure 4.37 shows δ^* (top) and θ (bottom) at Re=41000. Although the behavior of δ^* and θ in the existence of a LSB is the same at both Re, the trend of these graphs after flow reattachment illustrate different types of turbulent flow. At Re=48000 almost at all AOA the BL flow reached fully turbulent conditions but at Re=41000 it only occurs at AOA= 7° and it is getting close to a fully turbulent BL at AOA= 5°. This is also recognizable from the shape factor (Figure 4.35). As expected θ stayed almost constant during separation and shows a spike at the onset of the transition region. The transition points measured from momentum thickness θ are in excellent agreement with the location of H_{max}. Also Re_θ is defined based on the momentum thickness at the separation point (Equation 3.5) and presented in Table 4.5.

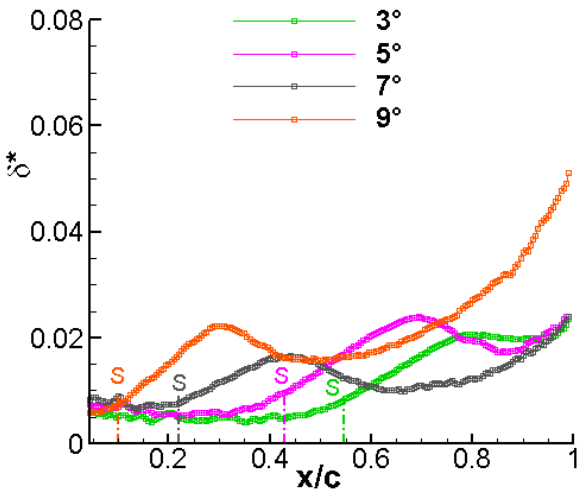

Figure 4.36: δ^* over SD7037 airfoil at Re=48,000 and AOA=3°, 5°, 7°, and 9°, S: separation point

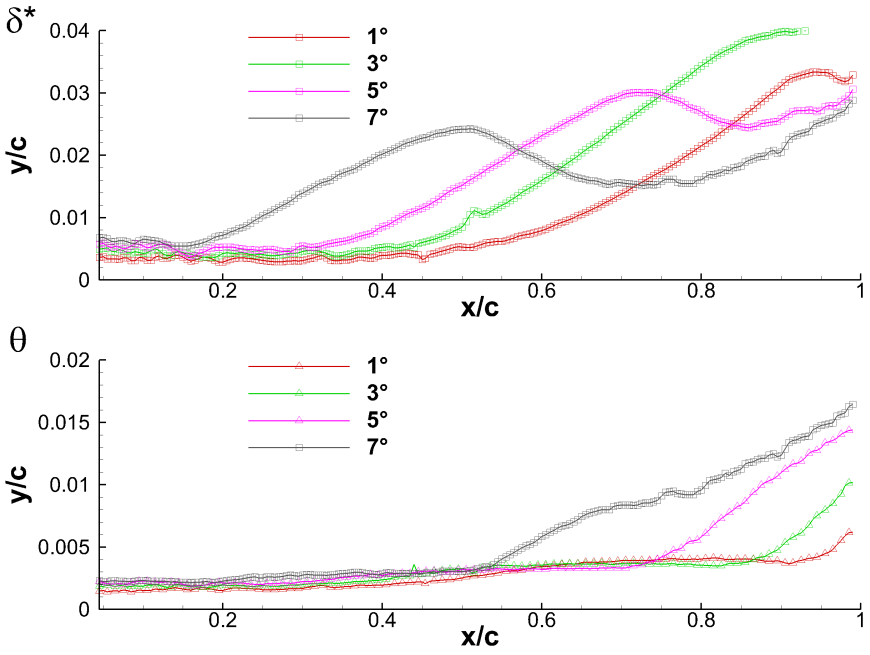

Figure 4.37: δ^* and θ versus X/C, SD7037 airfoil at Re=41,000 and AOA=1°, 3°, 5°, and 7°

LSB characteristics presented in Table 4.5 are examined from integral BL features. With increasing Re, the length and height of the bubble decreases that is consistent with previous works[14]. A reduction in the size of the bubble is more considerable with the existence of a short bubble (AOA= 9° at Re=41000, 48000). Re_θ increases with increasing Re and decreasing θ at a constant AOA, and decreases with increasing AOA at a constant Re that was also observed by McAuliffe and Yaras [84], and Pauley *et al.*[101]. Burgmann *et al.*[14] reports almost the same length at different AOA for SD7003 at Re=20,000 but the length of bubble is not constant and changes about 15%. At constant Re, the length of the bubble decreases with increasing AOA except for the lowest AOA where that bubble reattached to the surface close to the TE. This is also true of the height of the bubble. More study is required to confirm this condition because time averaged results are quite different from instantaneous results in this condition. Phase averaging of data can provide more detail about the bubble in this condition.

Table 4.5: Laminar separation bubble parameters for investigated static cases calculated from integral boundary layer features and velocity field contours

Re	AOA (°)	x_s/c	x_t/c	x_R/c	$x_{\delta^* max}/c$	l_b/c	h_b/c	δ^*_s/c	θ_s/c	$Re_{\theta,s}$
48000	3	0.51	0.75	0.85	0.80	0.34	0.0210	0.0064	0.0029	167
	5	0.40	0.66	0.75	0.70	0.35	0.024	0.0085	0.0026	163
	7	0.21	0.41	0.50	0.43	0.29	0.0164	0.0075	0.0023	158
	9	0.12	0.29	0.35	0.30	0.23	0.0222	0.0084	0.0024	166
41000	1	0.60	0.89	0.96	0.91	0.36	0.041	0.0079	0.0034	154
	3	0.50	0.84	0.92	0.87	0.42	0.039	0.0088	0.0033	155
	5	0.40	0.70	0.80	0.72	0.40	0.03	0.008	0.0028	139
	7	0.20	0.49	0.60	0.50	0.40	0.024	0.007	0.0023	126
	9	0.11	0.35	0.46	0.38	0.35	0.036	0.0091	0.0024	143
32000	3	0.50	0.89	-	0.95	-	0.057	0.0139	0.0038	142
	5	0.44	0.70	0.81	0.73	0.37	0.0322	0.0139	0.0032	136
	7	0.20	0.50	0.67	0.52	0.47	0.0241	0.0076	0.0025	117
22000	5	0.42	0.83	0.92	0.91	0.50	0.076	0.0127	.0040	104
	7	0.23	0.68	0.88	0.835	0.65	0.12	0.0081	.0031	83

Hu and Yang [53] found that for a GA (W)-1 airfoil at Re=70,000, the length of the LSB remains almost constant, 20% of chord length, by increasing the AOA from 8° to 12°. However, in these experiments at the two highest Re, the length of the bubble was almost constant at AOA=3° to 7° and it changed at 9° that is in agreement with results of Burgmann and Schroder [15] for presented results at AOA=4° and 6° and 8°

In the following time averaged velocity component fields are presented. Streamlines and iso contours are overlaid when it is necessary to show the mean dividing streamline, separation, transition and reattachment points. The height, length and shape of the bubble are shown also. The transition criteria of 0.001 (Equation 1.11) for the Reynolds shear stress used by others cannot be used because this number shows the momentum transfer at the edge of the BL that can present instabilities growing from separation points that lead the flow to transition to turbulent flow [14]. Figure 4.38 shows velocity contours at Re=41,000 and AOA= 9°. As can be seen the location of the maximum shape factor (H_{max}) is very close to the location of the maximum height of the bubble (maximum displacement thickness). Reverse flow under the bubble reached about $0.2U_\infty$ although it should be noted that the boundary layer edge velocity increases to $1.45U_\infty$ at this Re and AOA. As can be seen the bubble characteristics can be found from all these images. The separation point is considered where $\frac{\partial u_s}{\partial N}$ is close to zero. The first picture shows the tangential velocity component, iso-contour lines are added to mark the bubble region. The third picture illustrates the normal velocity component, and vortical structures at the end of the bubble where the shear layer breaks down and reattaches to the surface are clear that can be used to identify the reattachment point. The separation and reattachment points and shape of the bubble clearly can be identified using velocity vectors (last picture in Figure 4.38) that in this case they illustrate a short LSB.

As explained before, the transition process from laminar to turbulent flow begins with T-S waves upstream of the laminar separation point. These harmonic waves grow exponentially traveling downstream of the separation point until the instabilities grow so large that laminar structures break down to turbulence[139]. Figure 4.39 shows a schematic of the transition process through forming a LSB[139]. Yuan *et al.*[139] consider the final transition phase where flow breaks down to turbulence. In this stage, vortical structures in the flow increase and present a rise in the fluctuations of the normal velocity component as seen in the BL integral features above. Therefore transition can also be seen through u' and v' profiles.

Figure 4.40 shows (σ_u, σ_v) vectors for the case Re=48000, and $AOA = 7°$. As can be seen at about X/C=0.42 the shape of the profile in the N direction (normal to the surface) shows an increase that is different from laminar and turbulent flows, therefore the transition point can be between X/C=0.4 to X/C=0.42. Kim *et al.*[62] presented $\frac{\overline{u'}}{U_\infty^2}$ profiles in laminar, turbulent and transitional flows and results are in agreement.

Figure 4.41 shows velocity fluctuations at Re=41000 and AOA=9°. Zoomed vectors of each region of the bubble are shown. As can be seen the fluctuations reach their maximum at the edge of the separated shear layer or the edge of the bubble. Inside the bubble in the dead air region, the fluctuation vectors are almost constant from the wall to the edge of the

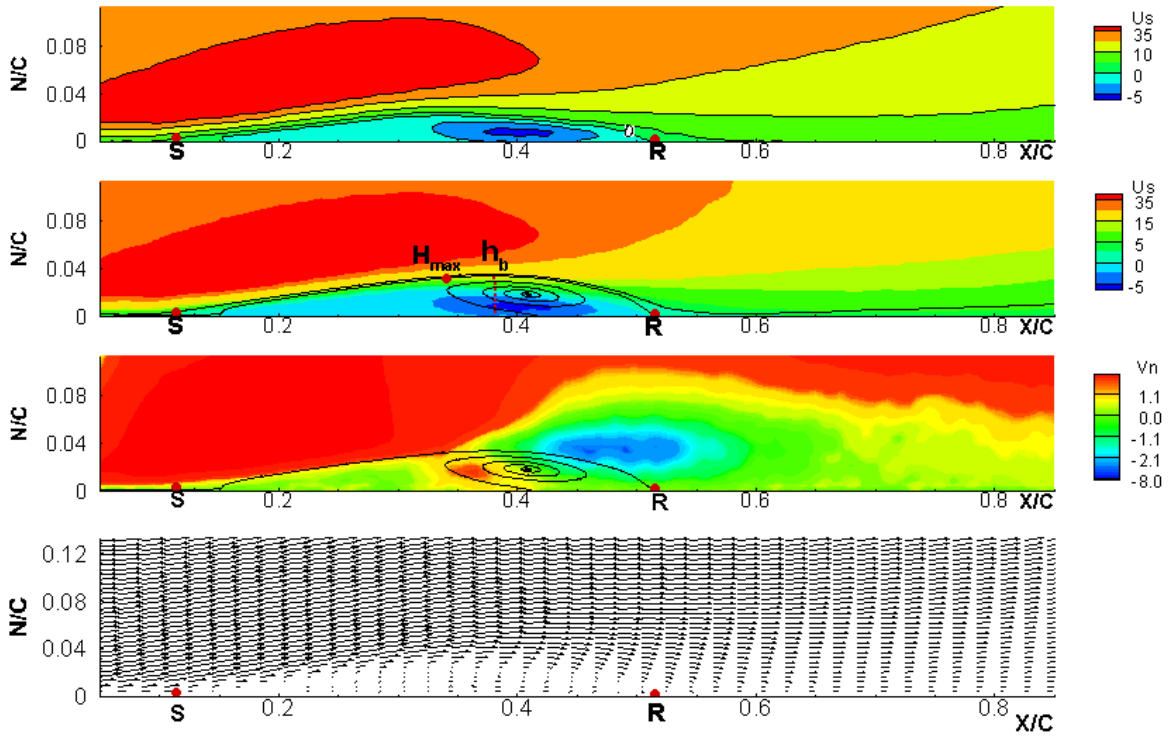

Figure 4.38: Velocity contours and velocity vectors versus X/C, SD7037 airfoil, case: Re=41000, AOA=9°, separation (S) and reattachment (R) points are marked. On the first image iso-contour U_s are added, streamlines are overlaid in the second and third images, the last image is velocity vectors

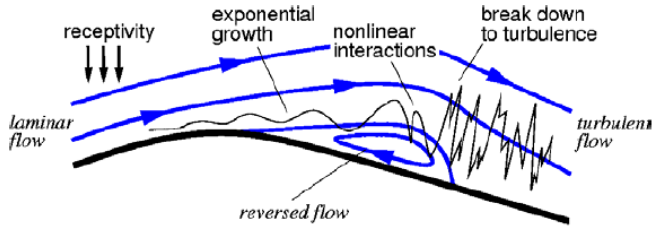

Figure 4.39: A schematic of the process of instabilities and transition from laminar to turbulent flow over the surface[139]

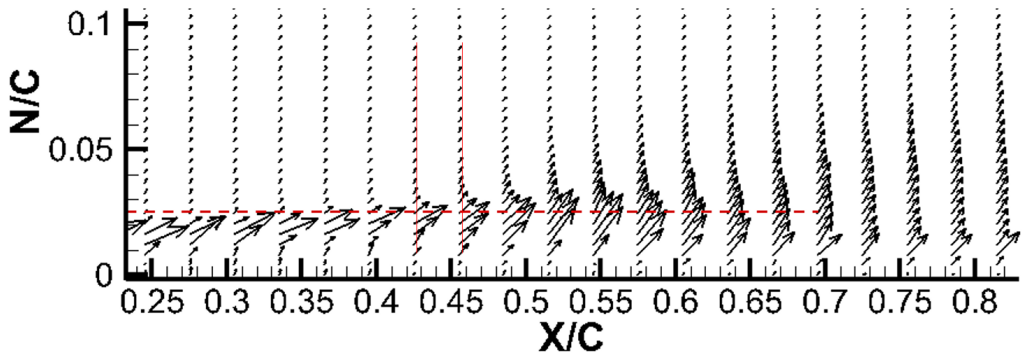

Figure 4.40: Velocity Fluctuation profiles versus X/C, SD7037 airfoil, case Re=48000,$AOA = 7°$, vertical red lines mark after the transition region

bubble. In the turbulent region, after the reattachment point, the rate of change of the vectors normal to the wall is constant. The only region where fluctuation increases from the wall to the edge of the shear layer is in the transition region where roll up vortices are formed. In the time averaged results, a strong vortex can be seen in the second half of the bubble that is also named the transition length of the bubble.

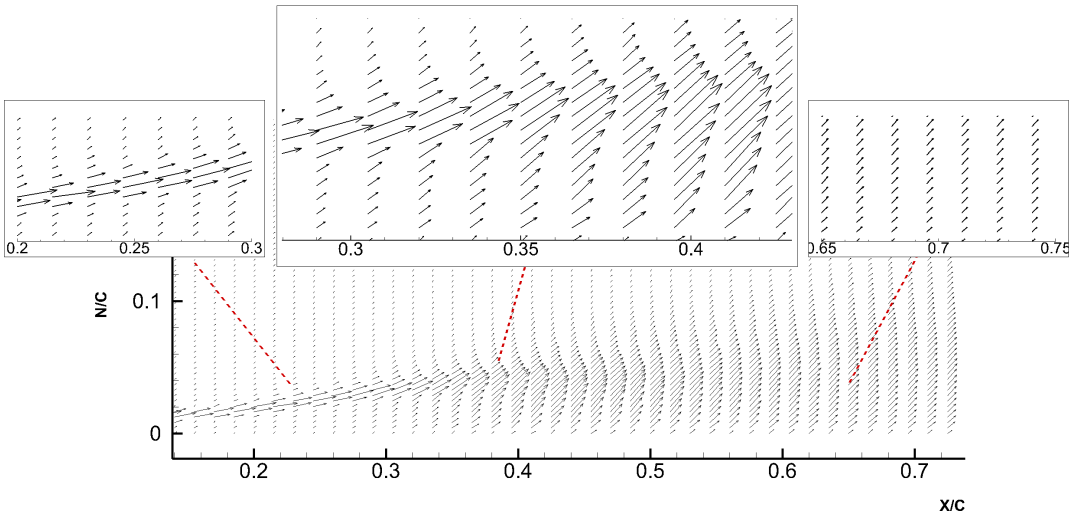

Figure 4.41: Velocity fluctuations vectors ($\frac{\sqrt{\overline{u'^2}}}{U^2_\infty}$, $\frac{\sqrt{\overline{v'^2}}}{U^2_\infty}$) over SD7037 airfoil, case: Re=41000, AOA=9°

Figures 4.42 and 4.43 show velocity contours for Re=22000 to 48000 at AOA=9° and AOA=5°. A long bubble can be seen at all Re at AOA=5° except Re=22000. Although the presented results of the instantaneous velocity field showed that the flow also reattached at Re=22000 at AOA=5° but it cannot be seen in the averaged velocity field. The height and length of the bubble decreases when increasing Re although the difference is larger between Re=41000 and Re=48000 (height of LSB decreases 20%, and the length of LSB decreases 10%) compared with Re=32000 and Re=41000 (height of LSB decreases 7%, and length of LSB decreases 5%). The maximum reverse flow velocity is about $5\%U_\infty$ at Re=48000, $7\%U_\infty$ at Re=41000, and $10\%U_\infty$ at Re=32000. So that by decreasing the height of the bubble, the maximum reverse flow velocity decreases too. If the flow is considered reattached at Re=22000, $h_{b,Re=22000} = 2.6h_{b,Re=32000}$ and the maximum reversed flow at Re=22000 is about $25\%U_\infty$ While at AOA=9° a short bubble only exists at the two higher Re and the flow is separated at the two lower Re. At AOA=9°, only a short bubble can be detected at Re=48000 and 41000. The height of the bubble at AOA=9° and Re=48000 is 40% less than h_b at Re=41000. The maximum reverse flow velocity is about 4.5% and 10% of the free stream velocity at Re=48000 and Re=41000 respectively.

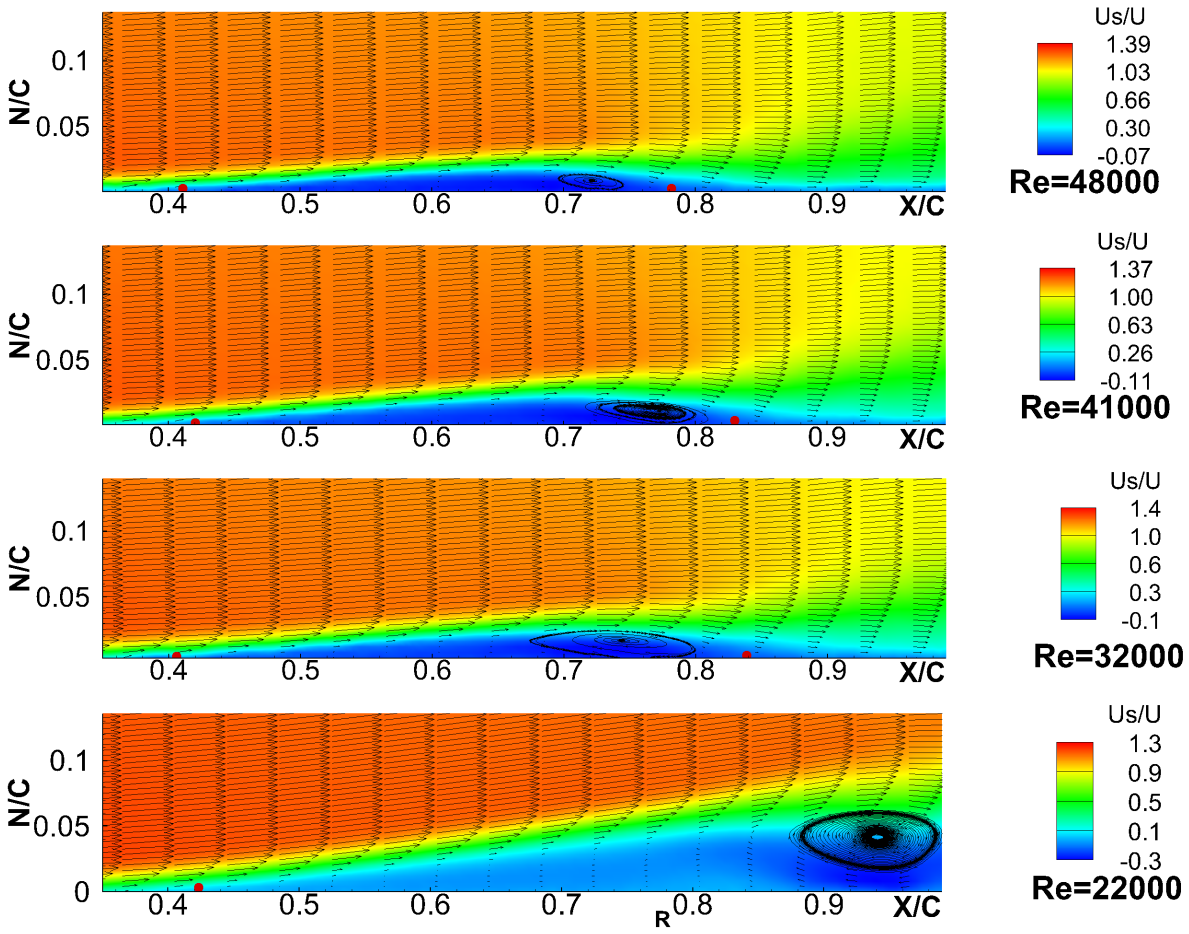

Figure 4.42: Time averaged velocity contour and velocity vectors at Re=22000 to 48000 at AOA=5° over SD7037 airfoil, stream lines of rear part of the bubble overlaid on the velocity contours and every other eight vectors are illustrated

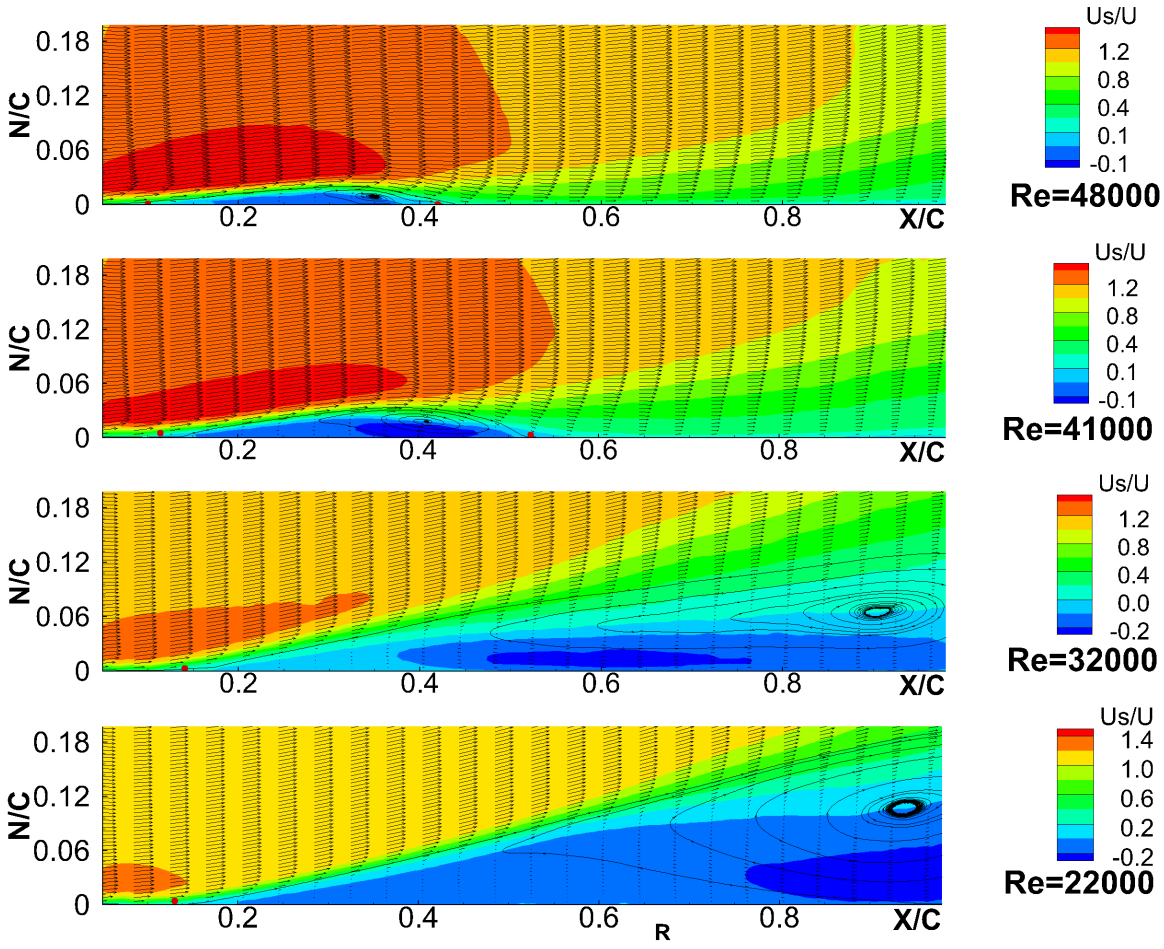

Figure 4.43: Time averaged velocity contour and velocity vectors at Re=22000 to 48000 at AOA=9° over SD7037 airfoil, stream lines of rear part of the bubble overlaid on the velocity contours and every other eight vectors are illustrated

Proper orthogonal decomposition

Figure 4.45 shows the instantaneous velocity field and streamlines over the airfoil at Re=41000 and AOA of 5°, as can be seen, the separation point is clearly identifiable through streamlines. Figure 4.46 shows streamlines of averaging of 300 analyzed images, as illustrated, the small turbulent vortices are not recognizable and it shows a long vortex. In other words, averaging the results will not give accurate information about the unsteady behaviour of the flow after the transition point. For this reason data is post-processed using Proper Orthogonal Decomposition (POD) and shear layer analysis to acquire more details at transition and reattachment points[3].

Acquired PIV images, Figures 4.44(a)and4.44(b) as examples, have been processed with the Adaptive PIV method over a 16 × 16 pixels interrogation area as explained before. Lengani *et al.*[74] showed that in LSB cases that the "first two POD modes are not necessarily coupled" but calculating the energy for separate components of velocity; streamwise and normal to the wall, will reveal coupled POD modes. They showed that PIV images can be sorted based on "phase-dependent vortex shedding phenomenon" using the POD method. Although POD usage has increased lately Lengani *et al.*[74] mention that there are not enough POD studies in LSB research. In this research, POD analysis, considering initially the FOV of x=y=c produced low energy levels of eigenvalues. As a result of this two solutions have been used, isolation of the transition and reattachment area from the PIV images and calculation of the energy levels from this localized velocity field such as Figure 4.44(a). Utilizing a specific area doubled the maximum level of the energy in the initial modes. A second approach, calculating the POD snapshot from the image with a FOV of 0.6c that covers the rear half of the airfoil, Figure 4.44(b), increased the first maximum energy level by a factor of three. To study the unsteady flow field following the formation of an LSB, a transition location is identified from the acquired PIV images for a FOV=c.

Figure 4.47(a), shows the covariance contour which is proportional to the Reynolds shear stress, for Re=32000 at AOA=5°. From this figure, the transition occurred at about 0.6c while using TEM and shape factor methods the transition point is detected at 0.7c, the skin friction coefficient and Cp show the transition point about $x_{tr} = 0.67c$. On the right side, Figure 4.47(b), from velocity streamlines, the location of flow reattachment to the surface of airfoil is recognizable at about 0.84c that is in agreement with previous results utilizing surface oil flow visualization[42],and time averaged velocity contours. Therefore, the distance from $x/c = 0.56$ to 0.87 would be the region of interest for the focused FOV

[3]Published and presented at the 19th International Symposium on the Application of Laser and Imaging Techniques to Fluid Mechanics, Lisbon, Portugal, JULY 16 19, 2018

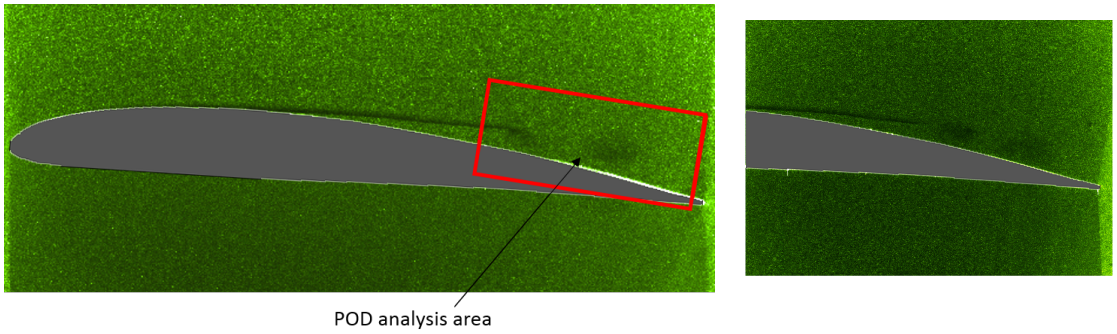

(a) (b)

Figure 4.44: a) Cropped PIV image at Re=41000 and AOA of 5°, airfoil outlined, FOV of x=y=c, b) Sample image of FOV of 0.6c, second half of the airfoil model

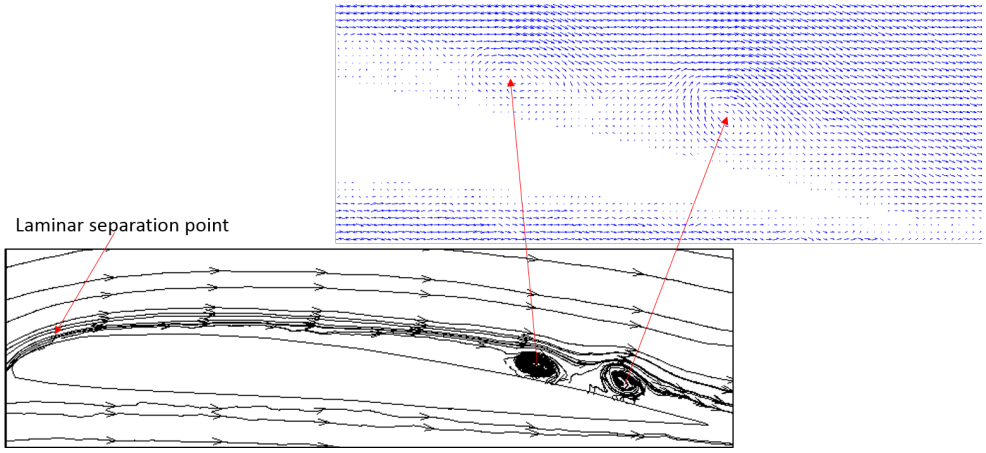

Figure 4.45: Instantaneous streamlines and velocity field over the airfoil at Re=41000 and AOA of 5°

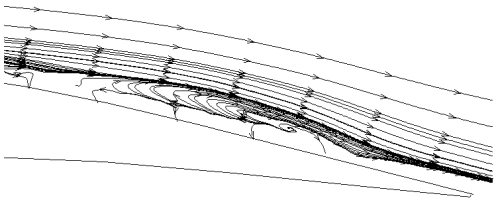

Figure 4.46: Streamlines of averaging of 300 analyzed pair images at Re=41000 and AOA of 5°

experiments ($FOV = 0.6c$) to study velocity fluctuation along the LSB at this condition. Regarding experimental setup limitations, the minimum possible FOV is about $0.58c$ ($15mm \times 15mm$) but only the region of 0.56c to 0.87c was post-processed to speed up the post-processing procedure. For all the experiments (different Re and AOA) the same strategy has been used to find the focused FOV for post processing and POD analysis. Figure 4.48 shows the average velocity field and covariance contour for Re=32000 and AOA 5° at the region of 0.56 to $0.87c$ acquired from focused FOV data. Comparing the results of two FOVs shows the accuracy and repeatability of the tests. In the left side of Figure 4.48, boundary layer (BL) velocity profiles perpendicular to the airfoil's surface, along the chord are presented. The clear trend of velocity profiles in the BL indicating measured regions of reverse flow (blue contour area just above airfoil) clarifies the shear layer region on the surface of the airfoil.

The first step to initiate POD analysis is an investigation of the required number of image pairs sample size. Based on a review of literature, the sample size could range from 100 to 1000. This number could depend on the complexity of the flow in the region of interest.

Figure 4.49(a) presents the results of the sensitivity of POD analysis to the size of sample size(N - number of images) for the case of Re=32000, AOA 5°. As can be seen, all graphs present similar behaviour and differences in energy level between 200 and 300 samples are negligible. Therefore the rest of the analysis has been done considering 200 samples. The quality of the PIV images also has a considerable effect on the required sample size. As mentioned before, the study of the modal energy distribution for velocity components separately can provide more useful data to reconstruct the flow field data. Figure 4.49(b) shows the modal energy distribution for velocity vectors (u,v), and two velocity components u and v, separately. Although, in this case, the 1st and 2nd modes are paired and have similar energy levels for all velocity maps, the first two modes of the v velocity component have the highest energy levels. Also, from this modal energy distribution, pair behaviour

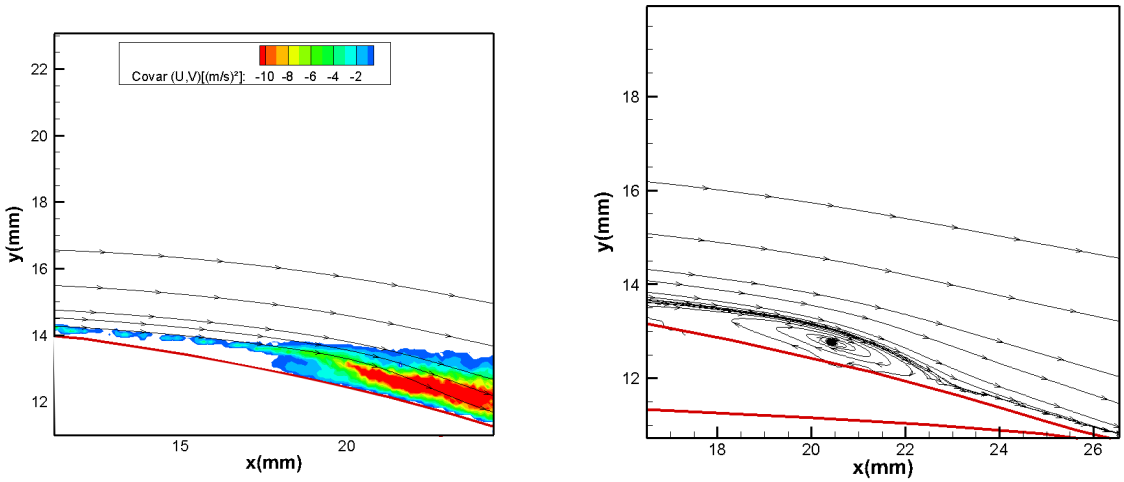

(a) Establishing transition location (b) Establishing turbulent reattachment location

Figure 4.47: a) Covariance (u,v) contour at Re=32000 and AOA 5°, and b) Velocity streamlines above the airfoil at Re=32000 and AOA 5° (airfoil outline in red).

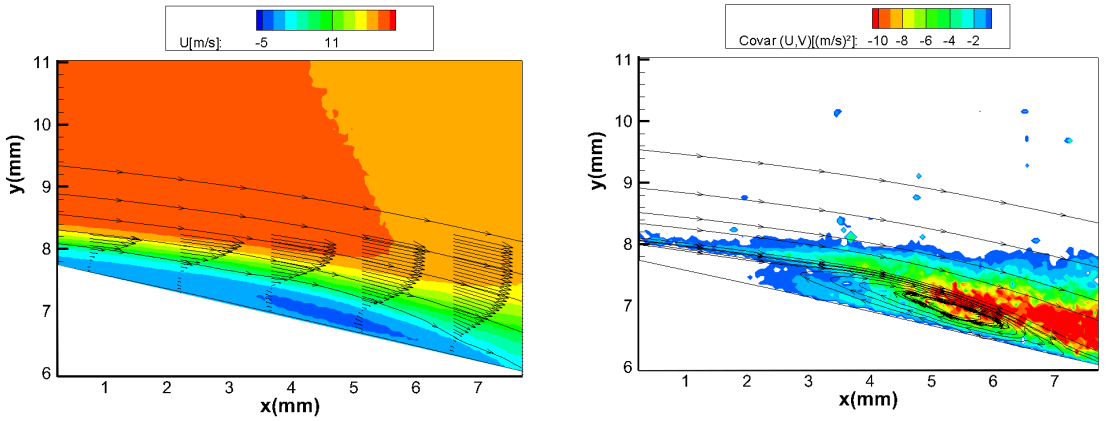

(a) (b)

Figure 4.48: a) Average of streamwise velocity component (u) along with boundary layer (BL) velocity profiles, b) contour of Covar (u,v) or Reynolds shear stress, acquired results from FOV= $0.6c$ at Re=32000 and AOA 5°.

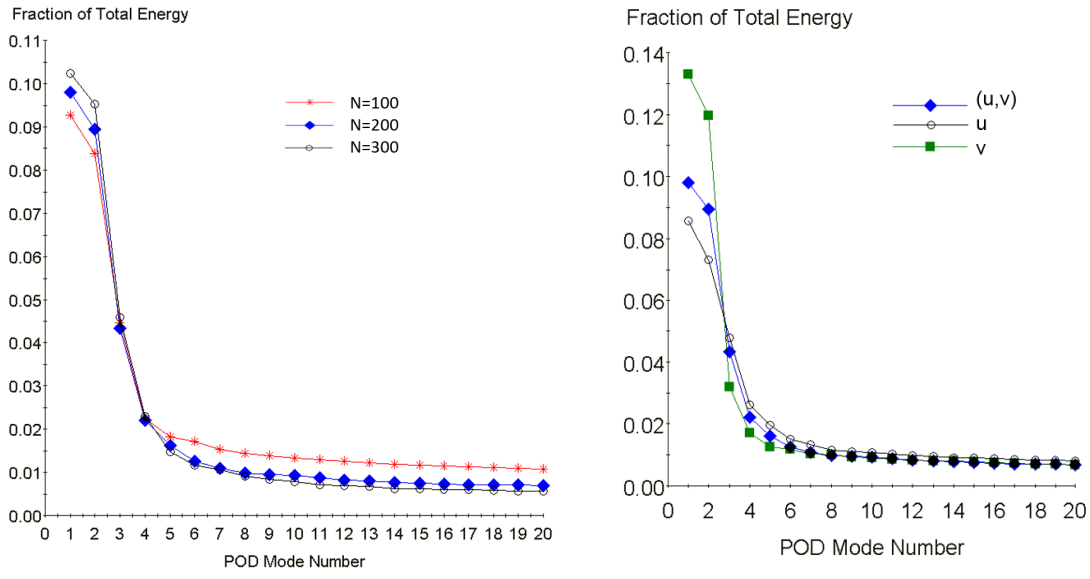

(a) (b)

Figure 4.49: a) Modal energy distribution of velocity vector *(u,v)* for different sample size for case study of Re=32000 and AOA 5° b) Modal energy distribution for velocity vector *(u,v)*, stream-wise velocity component, u, and normal to the wall velocity component, v at Re=32000 and AOA 5°.

can be seen between 5-6 and 7-8 modes of the v component while this behaviour is not as clear for the other two velocity maps.

Using the correct sample size and POD eigenvalues, Figure 4.50 presents the projection of first two POD modes on the mean v velocity component. As Lengani *et al.*[74] explained, the beginning of the shear layer roll up is detectable by finding the first local maximum and minimum values in the shear layer. As can be seen, from mode 1 (Figure 4.50), the local minimum occurs somewhere along 0.62c to 0.64c (mode 1) and the local maximum occurs about 0.66c (mode 2) that is close to the transition point where the shear layer roll up is expected. Another feature of vortex shedding is that mode 1 and 2 are related and similar values are found about $1/4\lambda$ separation from mode 1 to mode 2. To find the relation of mode 1 and mode 2, using the POD snapshot, the original vector/scalar map projects to POD modes. Figure 4.51(a) provides a time history of POD coefficient values for modes 1 and 2. Even though the data are not time resolved (10 Hz acquisition) it is clear that there is a relationship betwen mode 1 and 2. Figure 4.51(b) shows POD coefficients for modes 1 and 2 in a phase portrait clearly showing cyclic phenomena. Although the shape/amplitude

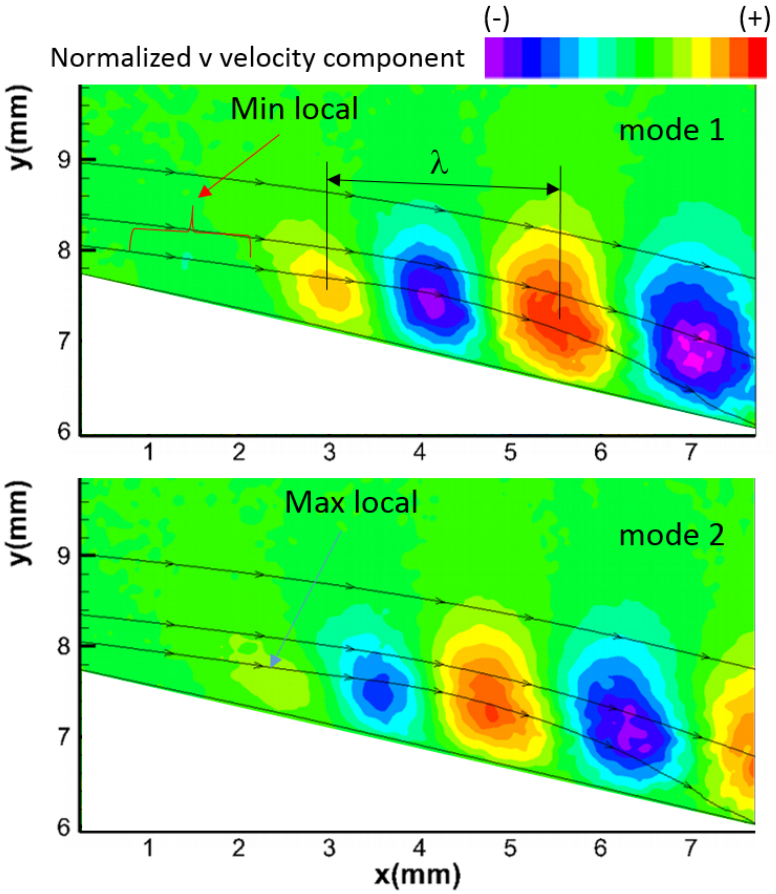

Figure 4.50: Projection of POD modes 1 and 2 of the velocity component of v (airfoil is white)

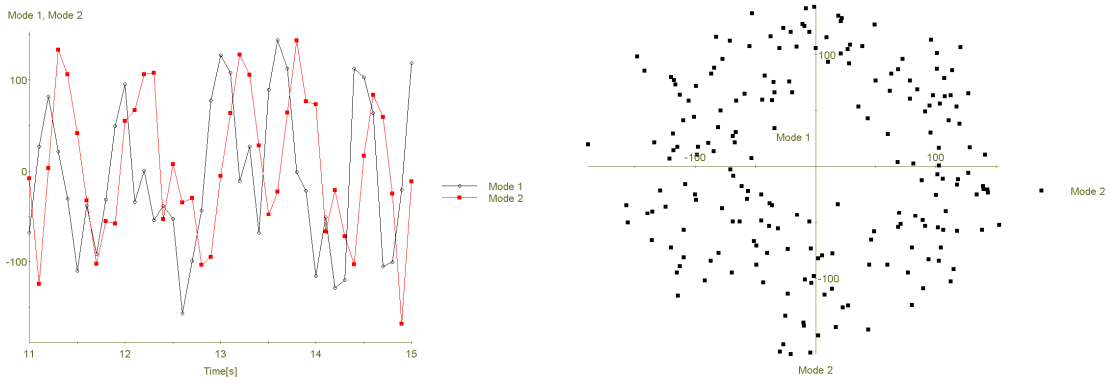

(a) (b)

Figure 4.51: a) A time history of POD coefficient values for modes 1 and 2, b) POD coefficients for modes 1 and 2 in a phase portrait at $Re = 3 \times 10^4$ and AOA 5°.

of the results are not perfect it can be seen clearly that these two modes are paired and may represent cyclical vortex shedding phenomenon.

In this case ($Re = 3 \times 10^4$ at AOA 5°), the energy level of the u component of the velocity was much lower than the energy level of the v component of the velocity for first two modes. Therefore, acquired results using the velocity vector's modal energy distribution are very close to POD results using the v component of velocity so that the wavelength was measurable through modes 1 and 2 using the energy distribution of both, v and u,v. Reconstruction of the vector map of PIV instantaneous data using the POD projection using 60% of the energy vector map (u,v) creates a smoother and more uniform vector map.

The next case study is at Re=41000, AOA=5° and a similar analysis strategy has been used. For this case, the results show the distance between 0.67c to 0.69c where the shear layer roll up is expected. This range is exactly upstream of the measured transition point from previous methods that is about 0.7c. Figure 4.52 provides the modal energy distribution for velocity vectors *(u,v)*, and individual velocity components u, and v. In this experiment, the same POD region (0.56c-0.87c) has been selected. As can be seen, only the energy distribution of v velocity component presents paired modes (1-2, 3-4, and 5-6) therefore the v velocity component should be considered for POD analysis and reconstruction of PIV data in order to study a vortex roll-up along the LSB. It is important to mention, selecting a proper region for POD analysis is crucial to avoid undesirable effects of unsteady behavior of turbulent flow that may decrease the level of energy for initial modes and affect the accuracy of reconstructed data. Although many other parameters such as Re of the flow, and the type of LSB can affect the region of vortex shedding.

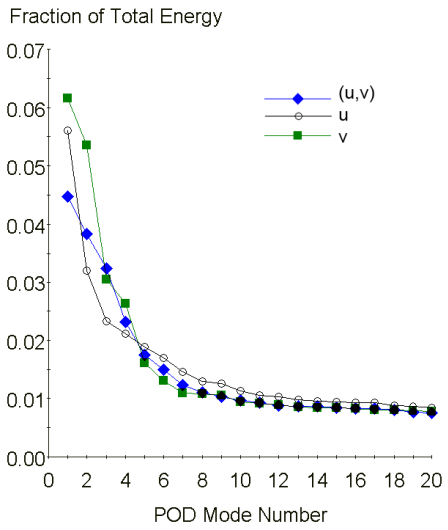

Figure 4.52: Modal energy distribution for velocity vector *(u,v)*, stream-wise velocity component, u, and normal to the wall velocity component, v, at Re=41000 and AOA 5°.

Figure 4.53 presents the first six POD modes calculated for velocity components u and v. As expected from modal energy distribution results, the first two POD modes of data acquired from velocity component v are paired and indicate shear layer roll-up while the first mode of velocity component u presents only a large negative value region. This mode is very similar to the average velocity field of the original PIV data where the reattachment location can be found. Clear paired behavior can be seen for Modes 3-4 and 5-6 of POD results of velocity component v, although paired behavior for modes with lower energy levels of velocity component u are also recognizable. Lengani *et al.*[74] mentioned that this behavior could be related to the Kelvin-Helmholtz vortex shedding. Therefore, more study of this case may be necessary.

In this study[43], keeping the same AOA and slightly changing the Re, the behavior of the flow changed considerably. To complete the study of flow field about the SD7037 airfoil, calculating the aerodynamic forces from the velocity domain including LSB effects is an obvious next step.

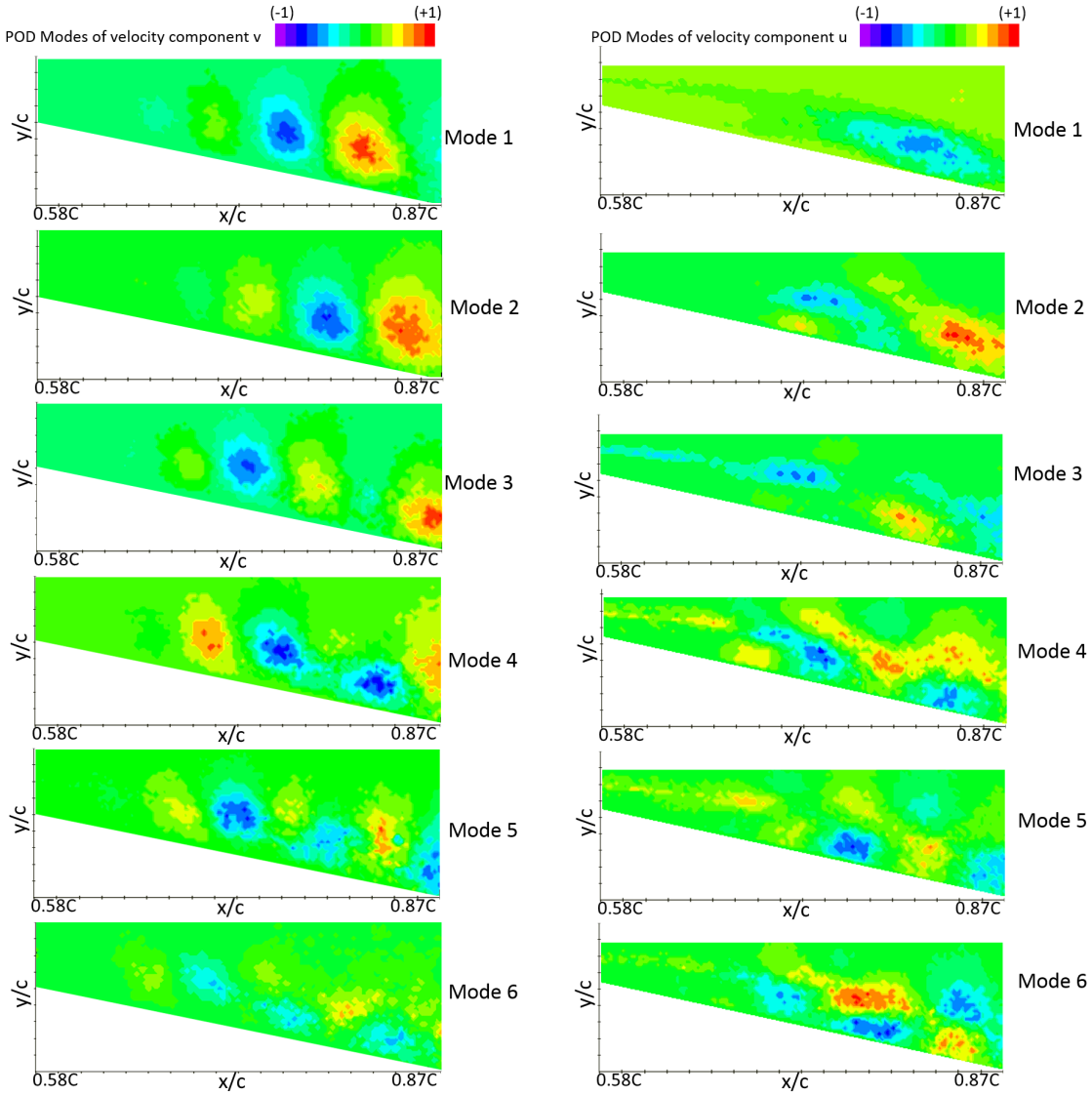

(a) (b)

Figure 4.53: a) First 6 modes of velocity component v, b) First 6 modes of velocity component u, Re=41000 and AOA 5°.

Chapter 5

Dynamic Results

5.1 Flow Behaviour and LSB Characteristics

In this section the flow behavior over the SD7037 airfoil in dynamic conditions is investigated. In comparison with static cases in upstroke pitch motion stronger moving vortices form after flow reattachment. The frequency of pitch motion adds extra unsteadiness so that the location of these vortices permanently changes with time. In this section effects of unsteadiness in addition to Re and AOA on flow behavior over the SD7037 airfoil are examined. Table 5.1 presents a summary of the completed PIV experimental test plan for dynamic case studies. Sinusoidal pitch oscillation, Equation 1.5 with $\alpha_{mean} = 8°$ and $\alpha_{amp} = 9°$ is considered. $\alpha_{mean} = 8°$ is about the static stall AOA for investigated Re flows. Based on the flow behavior over the airfoil in investigated static cases, three Re (22000, 32000, and 41000) are selected to be studied in dynamic conditions. Three reduced frequencies k=0.05, 0.08, and 0.1 have been used to study flow behavior over the SD7037 airfoil at quasi-steady and unsteady conditions. Similar to the static cases, the S-N coordinates are used to post-process the results and calculate integral BL features(see section 4.3). Same as the static cases, FOV=c has been used to study BL flow parameters. Also, aerodynamic force calculation has been done using velocity field of FOV=2.5c.

5.1.1 Surface pressure coefficient

The surface pressure coefficient was calculated from the time averaged velocity field of 450 sample images at a constant phase or AOA as explained in section 3.3.4. Figures 5.1 to 5.3 present the surface pressure coefficients (left) and sample instantaneous PIV images

Table 5.1: Dynamic case studies

Reynolds Number	22000, 32000, 41000
Angle of Attack	5° - 15°
Reduced Frequency	0.05, 0.08, 0.1
Field of View	$\frac{x}{c} \approx \frac{y}{c} \approx 2.5C, C, 0.6C$

(right) at Re=41000 in all investigated k. As it is clear from raw images, a LSB has not formed on the suction side of the airfoil until AOA=7° at Re=41000 and k=0.10 while in the static case there was a long thin bubble at AOA=7°. Similar to the static cases, the maximum negative Cp increases with increasing AOA until forming a short bubble at the LE. In other words, increasing the AOA decreases the effects of the surface on the free shear layer resulting in a more unstable BL. Increased turbulence in the flow accelerates the shear layer breakdown process and creates a shorter bubble consequently[76].

But unlike the static cases, immediately after the short LE bubble, a LEV develops. In the occurrence of a LEV, the surface pressure coefficient remain constant almost from the LE until the end of the LEV. Another difference in Cp in comparison with static cases is the appearance of noticeable fluctuation at or after the flow transition. Similar but weaker pressure fluctuations were observed at lower Re for the static cases where a fairly thick separated shear layer breaks down and reattached to the surface (i. e. AOA=7° at Re=22000). Comparing the surface pressure distribution in Figures 5.1 to 5.3 reveals Cp fluctuations after the transition region are higher for the low reduced frequency (k) than the Cp fluctuations in high k in the existence of a long bubble. These fluctuations are also reported in previous studies. In a study of flow behavior on a Eppler 387 airfoil at low Re by Lin and Pauley [76] show Cp fluctuations where there is a LSB (vortex). In their results, Cp from experimental and numerical results lie on top of each other but the trend of the fluctuations can be followed through numerical results. It can be concluded when measuring surface pressure at discrete points, some information could be lost and considering linear behavior between discrete points in Cp on the surface with a pressure gradient may not be true. These fluctuations are also observed in some static cases on the SD7037 airfoil that were presented in chapter 4 but the reversed flow regions in the dynamic case are much stronger in comparison with static cases and correspond to a stronger pressure gradient. This will be explained later in this chapter by illustrating a measured velocity field about the airfoil. Cp results are consistent with Cp calculated from a LES simulation over a bionic airfoil in the existence of LSB by Ge[33], see Figure 1.11. In addition to the static studies, recent numerical simulation of unsteady flow by Sharma and Visbal [119] also confirms Cp instabilities associated with the transition region and unstable surface pressure distribution after the reattachment point (Figure 1.10) similar to Cp fluctuations after reattachment on

SD7037 at Re=41000, k=0.08, and AOA=11°. Noticeable pressure fluctuations are also reported by Gharali[36] in pitch motion. Ge [33] also observed sharp peaks in Cp where there is a bubble and drifting vortex after the reattachment on a bionic airfoil[33].

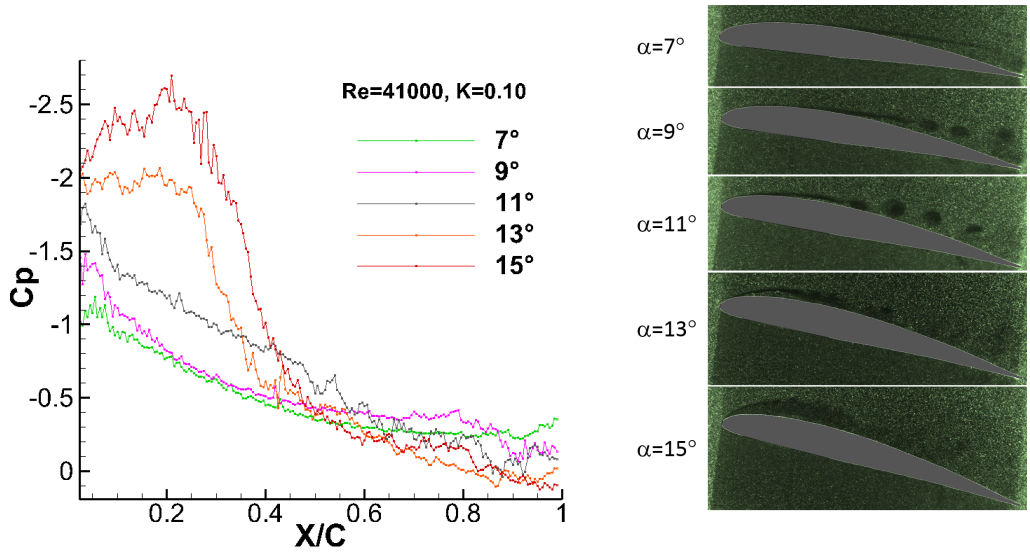

(a) Cp

(b) Sample instantaneous PIV Images

Figure 5.1: a) Pressure distribution over the suction side of SD7037 airfoil at Re=41000, k=0.1 measured from PIV data b) Sample instantaneous PIV images at Re=41000, k=0.1

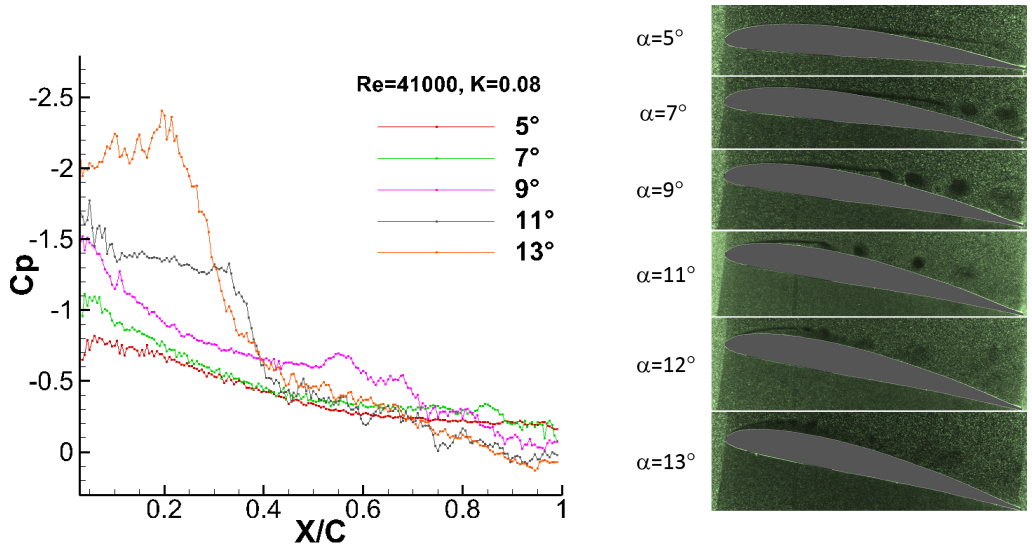

(a) Cp (b) Sample instantaneous PIV Images

Figure 5.2: a) Pressure distribution over the suction side of SD7037 airfoil at Re=41000, k=0.08 measured from PIV data b) Sample instantaneous PIV images at Re=41000, k=0.08

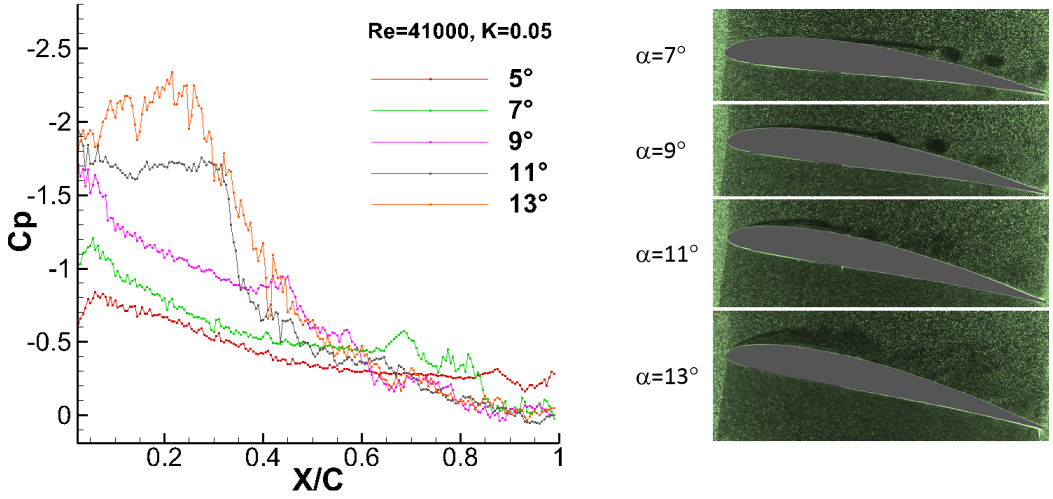

(a) Cp (b) Sample instantaneous PIV Images

Figure 5.3: a) Pressure distribution over the suction side of SD7037 airfoil at Re=41000, k=0.05 measured from PIV data b) Sample instantaneous PIV images at Re=41000, k=0.05

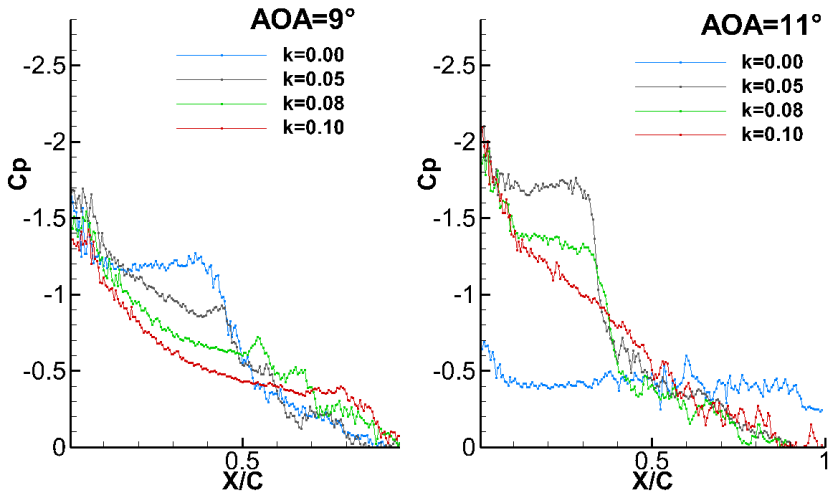

Figure 5.4: Effects of the reduced frequency on measured surface pressure distribution over SD7037 airfoil at Re=41,000, AOA=9° and 11°

To look closely, Figure 5.4 shows surface pressure distribution versus X/C over the SD7037 airfoil at AOA=9° and 11° for Re=41000 at different k. Cp decreases with increasing k, from the static case (k=0.0) to k=0.1 at AOA=9°. In other words, increasing k empowers the laminar BL and delays flow separation. As expected from the non stationary Bernoulli equation [93]:

$$\frac{dP_e}{d(x/c)} = \left(\frac{\partial P_e}{\partial(x/c)}\right)_{\alpha=0} - \left(\frac{\partial P_e}{\partial \alpha}\right)\left(\frac{c\dot{\alpha}}{U_e}\right) \tag{5.1}$$

Pitch up motion creates a favorable pressure gradient that delays separation for both 9° and 11°. This is even more favorable at 11° that prevents the stall condition with increasing k from 0 to 0.05 (Therefore k shows an increase in Cp). The thick LE bubble forms at AOA=11° at k=0.05, and increased pitch rate delays the occurrence of the LE bubble until AOA=13° at k=0.1. The LSB displaces the outer flow that mostly increases the pressure drag therefore the height of the bubble has an important role in the pressure drag [102]. These results are consistent with measured Cp of a pitching NACA0012 by Kim and Chang [61] that used pressure transducers to measure the surface pressure distribution. By changing the reduced frequency, the maximum negative Cp stayed almost the same and only the pressure recovery slope has changed. This behavior was also observed by Kim and Chang [61] at Re=48000 in upstroke motion. Ragni *et al.* [104] measured surface pressure using 2D PIV and pressure tabs over NACA0012-30 at high Re. They mentioned inaccurate

velocity data close to the surface due to the reflection that appeared in the increased scatter of the pressure data. Therefore, they considered the PIV velocity data 1%c higher above the surface and extrapolated the remaining velocity fields up to the surface. Their results show that calculating the surface pressure up to 1%c higher than the surface will decrease the maximum Cp, but generally, both methods show similar trends and are in a good agreement. Also inaccurate results in Cp close to the LE could be the result of a lack of data in the direction normal to the surface and a thin laminar BL that produces a large velocity gradient in this region. Usually the separation point is located after 0.05c that means possible errors in calculated Cp in the LE region that does not affect the results although it should be considered if using the pressure field to calculate aerodynamic forces.

Figures 5.5 and 5.6 show tangential and normal velocity contours at constant AOA= 9° and Re=41000, for k=0 to 0.1(k=0 represents the static case). As can be seen with increasing the reduced frequency to k=0.05 (quasi-steady condition) the thick and short bubble in the LE (in static case) transforms to a long thin bubble (k=0.05) and moves further downstream while when increasing the reduced frequency to k=0.08 and higher, the separation point moves toward the TE along with an increase in the height of the bubble. If the momentum transfer due to the growing turbulence is not enough, the flow cannot overcome the strong adverse pressure gradient to reattach to the surface and separation occurs without forming a long bubble. This separation can cause a drag increase and lift reduction[102]. Results of Gharali [38] for lift coefficient shows that increasing k slightly decreases the lift coefficient at constant AOA although the effect of the height of the bubble is more considerable on the drag.

The results shows that increasing k does not always have a similar effect on the pressure coefficient. The Cp behavior mostly depends on the type of the bubble that forms on the airfoil and it is highly dependent on Re and AOA although it always delays separation. As seen in Figures 5.4 and 5.5, Cp decreases by increasing k at Re=41000 and AOA=9° but this Cp behavior can be seen if there is no dynamic or static stall involved. For the test case with Re=41000 and AOA=11° that flow is fully separated in the static case, with increasing k to reach quasi steady condition a LSB forms in the LE, see Figure 5.7. Due to the formation of this LSB, Cp and consequently lift increases. Also friction drag drops dramatically. As can be seen in figures 5.5 and 5.6, increasing k (from 0.05 to 0.1) increased the size of the bubble.

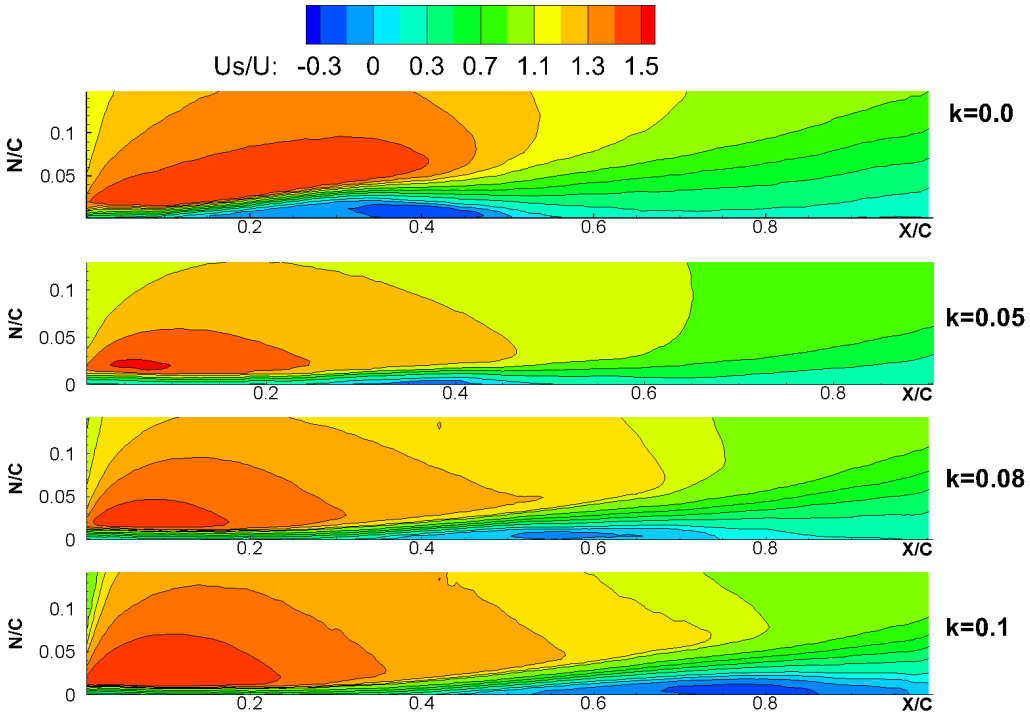

Figure 5.5: Tangential velocity component contour over SD7037 airfoil at Re=41,000, AOA=9° at K=0, 0.05,0.08, and 0.10, iso-contours added

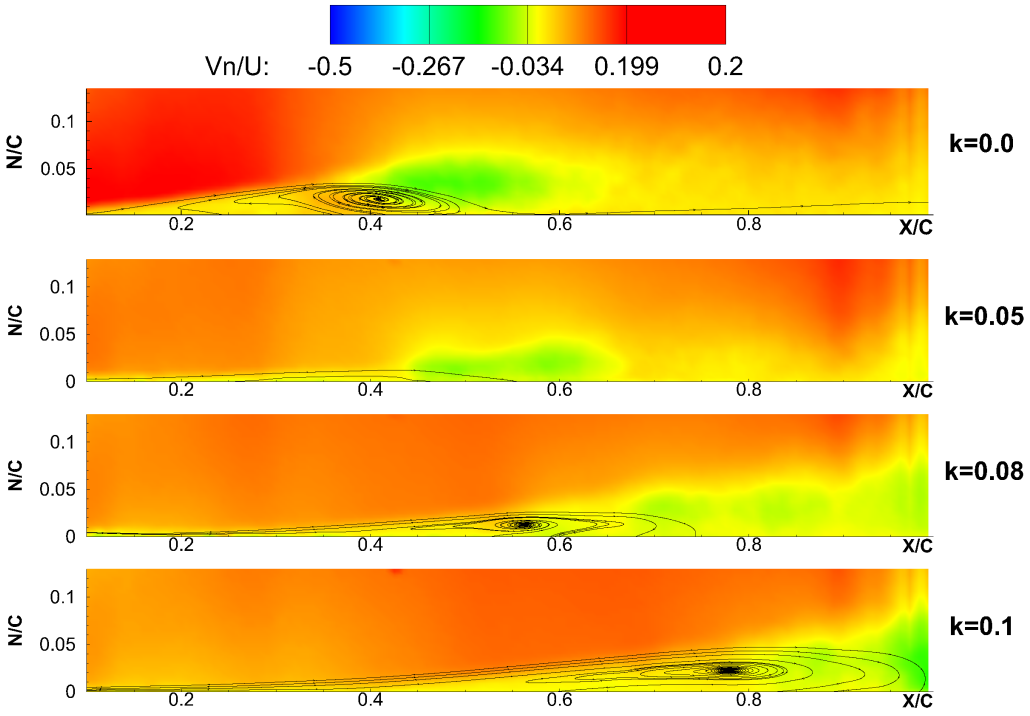

Figure 5.6: Normal velocity component contour over SD7037 airfoil at Re=41,000, AOA=9° at K=0, 0.05,0.08, and 0.10, streamlines overlaid

In comparison to AOA=9°, Figures 5.7 and 5.8 show the tangential and normal velocity field at AOA=11° and Re=41000 at k=0.1. As can be seen increasing the reduced frequency decreases the bubble height in this case. Velocity profiles (i.e. vectors) and normal velocity contours in Figure 5.8 clearly show a reduction in the normal velocity magnitude at the end of the bubble. With increasing reduced frequency from 0.05 to 0.1, the magnitude of tangential component of reversed flow under the bubble shows a 7% increase. It should be noted that a sharp rate of velocity differences in a small area about a thin bubble might increase the error in the PIV velocity calculation and overestimate the velocity but the small height difference in all three reduced frequency cases keeps the post processing condition the same so that results can be compared.

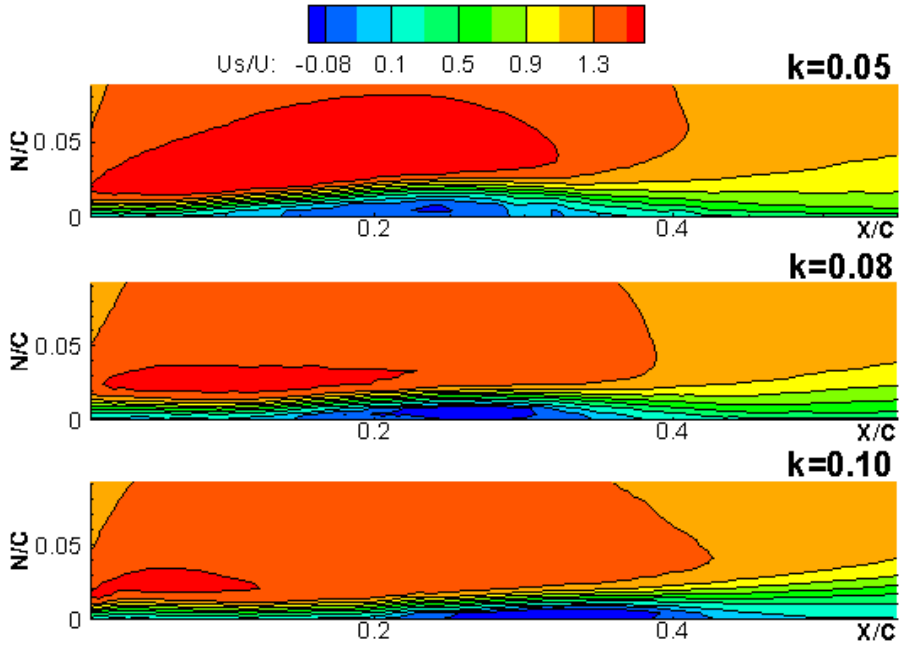

Figure 5.7: Tangential velocity component contour over SD7037 airfoil Case: Re=41,000, AOA=11°, k=0.05, 0.08, 0.10, iso-contours added

Figure 5.11(b) shows raw PIV images at AOA=12°, Re=22000, at k=0.08, and 0.1. As can be seen a thick LE bubble (i.e. initial Leading edge vortex, LEV) formed at AOA=12° and k=0.08 while an LSB with shorter height occurs at k=0.1. The LEV can increase the drag considerably [38] and drop the airfoil performance (L/D). Also a LEV can be seen at AOA=13° and k=0.1. From the BL integral parameters, the separation point moves from $x_s = 0.13c$ at 12° to $x_s = 0.07c$ at 13°, and the transition point moves from $x_t = 0.45c$ to $x_t = 0.34c$ respectively. The maximum height of the LEV, considered the

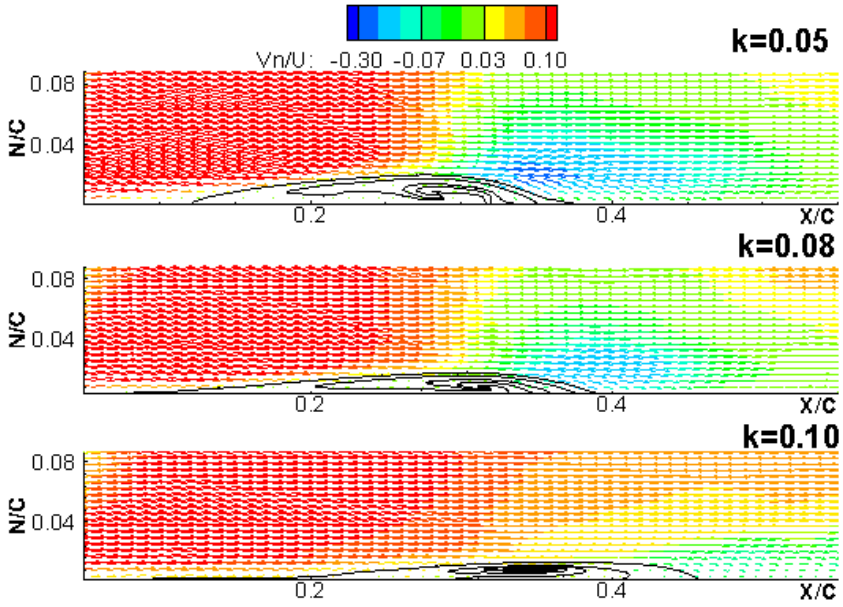

Figure 5.8: Normal velocity component contour over SD7037 airfoil Case: Re=41,000, AOA=11°, k=0.05, 0.08, 0.10, streamlines overlaid

maximum displacement thickness, occurs downstream of the transition point. This line lies on the inflection line (see section 1.2.1) with good agreement and shows a maximum height(h_b) of about 0.063c at $x = 0.42c$ for 13°. The BL displacement thickness shows a continuous increase until $x/c = 0.66$ and a change in the slope at about $x/c = 0.5c$ at AOA=12°. Matching displacement thickness with the inflection line and velocity profiles confirms $h_b = 0.05c$ at $x/c = 0.5$. Instantaneous velocity field and the angle of a separated streamline are studied to reveal more information about the bubble at AOA=12°. Figure 5.9 shows a sample instantaneous velocity field and their PIV images at AOA=12°, Re=22000, and k=0.1. As can be seen the instantaneous reattachment point moves mostly between $x/c = 0.5$ to $x/c = 0.55$. The second formed vortex has not always completely separated from the end of the bubble (i.e. 2^{nd} picture from top). Therefore, time averaging the velocity fields results in merging of the drifting vortices into the bubble so that $x_R = 0.88c$. This merging results could be in misleading in the determination of the height and length of the bubble. From instantaneous data the maximum height and its location is in agreement with what it is determined from time averaged data. The h_b and its location that is measured from time averaged data is in agreement with the location and height of the formed vortex at the end of the bubble in sample instantaneous data. The inflection line (solid red line) is added to the instantaneous velocity field to mark the behavior of velocity profiles and the

bubble. In this figure, picture one and four show a small vortex between the end of the bubble and drifting vortices in the opposite direction. This pattern was also observed by Kim and Chang [60] for a pitching airfoil through smoke visualization, that showed a smoke streak was broken down over the airfoil surface in this condition. The pressure distribution in Figure 5.11 shows $x_s = 0.11c$, $x_t = 0.42c$, and $x_R = 0.55c$ that is in good agreement with these results but Cp provides a better estimation for the reattachment point. The reattachment point that is considered where the slope of Cp changes after the transition point for the first time. The reason is that vortical structures in the flow result in pressure fluctuation. In the case of large vortices like this case, the effects of fluctuations can clearly be seen in the Cp plot.

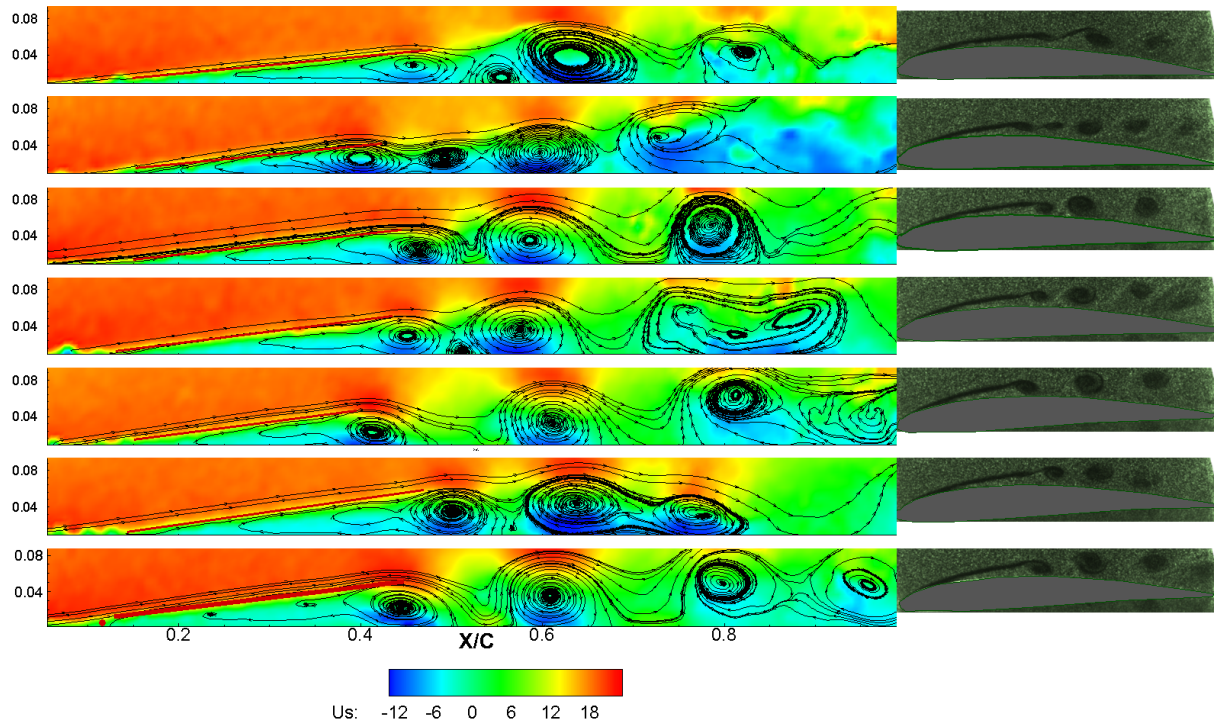

Figure 5.9: Tangential velocity component contour over SD7037 airfoil with streamlines overlaid, case: Re=22,000, AOA=12°, k=0.10

It is important to mention the leading edge bubble includes a strong vortex that moves close to the LE therefore averaging the results does not change the separation and reattachment points considerably. But in the case of LSB, the large shedding vortices along with drifting vortices are highly unsteady and move along the chord therefore the reattachment point may be detected from instantaneous results or Cp instead of velocity

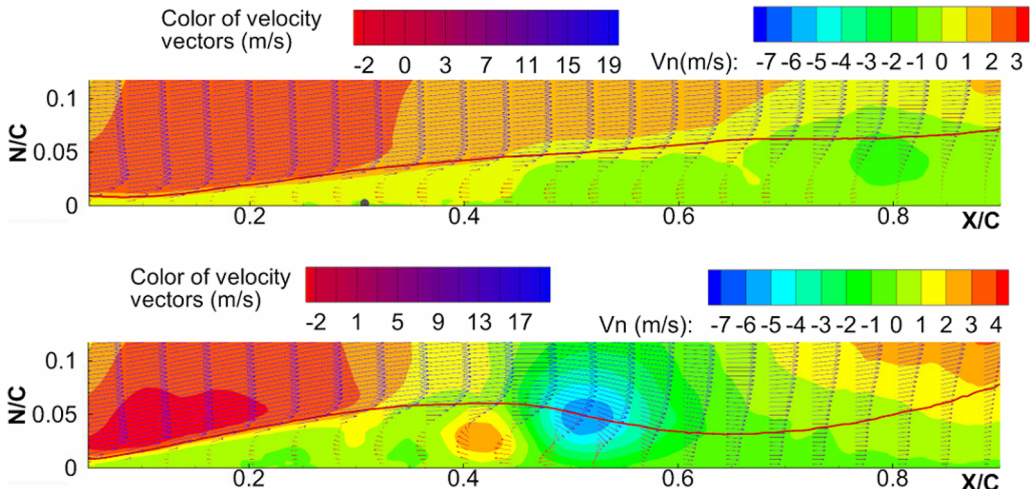

Figure 5.10: Normal velocity component contour versus X/C, SD7037 airfoil with velocity vectors overlaid, case: Re=22,000, AOA=12° (top), 13° (bottom), k=0.1

vectors. The laminar flow separates from the surface with an angle of 15° at AOA=13° and with an angle of 10° at AOA=12° that considering the length of the separated region, a long laminar separation bubble was formed at AOA=12° and a short thick bubble was formed at AOA=13°. Figure 5.10 shows time averaged velocity vectors and normal velocity contour at AOA= 12° and 13° at Re=22000 and k=0.10. As can be seen a strong vortical structure forms at the end of the LEV while a long bubble with a weaker shedding vortex forms at 12°. To compare these two cases more information on their lift and drag forces seems necessary. In these cases friction and pressure drag both play an important role in total drag that should be considered.

Figure 5.11 shows Cp at different AOA for k=0.05. Static results revealed that the energy of growing turbulence at Re=22000 was not high enough to overcome the adverse pressure gradient and close the laminar separation. At this Re, increasing k to 0.05 empowers the BL flow and delays flow separation. An LSB forms at about AOA= 9° and remains until 11°. Compared to higher Re flows, the energy of the flow is too low and the flow fully separates from the surface at 13° without creating a LEV or a short bubble. At k=0.08, a LEV forms on the suction side of the airfoil at 12° while there is a thick bubble with large shedding vortices at AOA=12° and k=0.1 that was discussed above.

Figure 5.12 shows vorticity ($\frac{\omega_z c}{U_\infty}$) and $u'v'(m/s)^2$ fields. Cp is added to both contours to highlight the surface pressure behavior with the existence of a LEV. The transition point is marked on the Cp line and where $u'v'(m/s)^2$ reaches $0.001{U_\infty}^2$. As can be seen, the

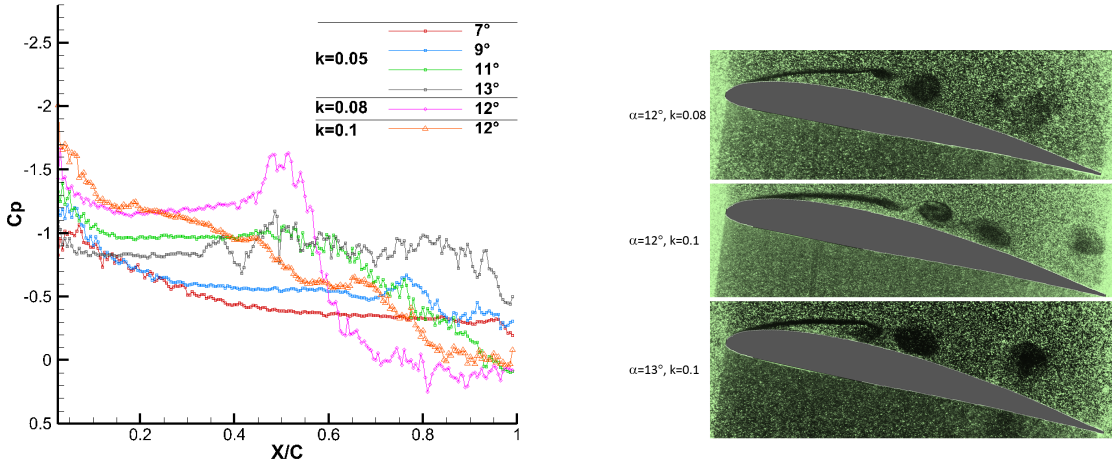

(a) Cp

(b) Sample instantaneous PIV Images

Figure 5.11: a) Pressure distribution over the suction side of SD7037 airfoil at Re=22000, k=0.05 measured from PIV data b) Sample instantaneous PIV images at Re=22000, AOA=12° and 13° at k=0.08 and k=0.1

transition point acquired from TTM is closer to the LE. The criteria of 0.001 cannot be used as an absolute condition to detect the transition point [93, 15]. This number highly depends on u' and v' that define momentum transfer into the boundary layer ([139, 15]) that can be varied in different test conditions. Therefore, the transition point was considered where there was a clear growth in Reynolds shear stress. There is not a firm definition for the transition point so that some researchers used the beginning of the logarithmic growth of Reynolds shear stress as the transition point and others defined the transition point where the growth rate of Reynolds shear stress deviates from the exponential growth [15, 93]. The results showed that Reynolds shear stress is highly dependent on the height of the bubble and boundary layer thickness. Where the BL thickness is too close to the surface, this number increases noticeably. Although the criteria used by McAuliffe and Yaras [84] that defines the transition point where the growth rate of shear stress deviates from exponential growth is more in agreement with presented results, here Cp was used to detect the transition point from time averaged PIV data. Also skin friction coefficient and integral BL parameters have been used in detecting the transition point that will be explained in the following sections.

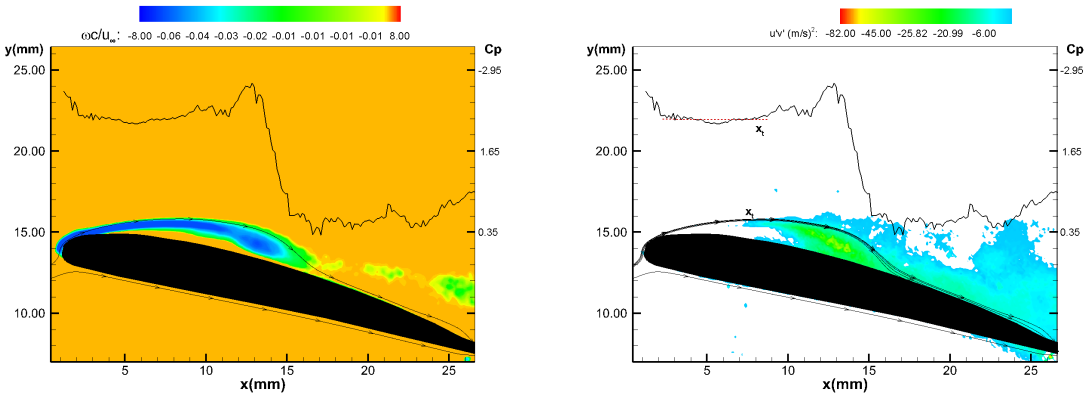

(a) ω_z (b) $u'v'(m/s)^2$

Figure 5.12: a) vorticity (ω_z) field and b) $u'v'(m/s)^2$ field about SD7037 airfoil at Re=22000, k=0.1 measured from PIV data, black line: Cp

5.1.2 Skin friction coefficient

As explained in the static results, skin friction coefficient (C_f) can also be used to determine the bubble characteristics. This criteria cannot solely be used to determine the unsteady separation and reattachment points [60]. In unsteady flow, the separation point is considered where $u_w = 0$ and $(\frac{du}{dn})_w = 0$ that is named the MRS criterion[111]. Here to calculate the skin friction coefficient, forward and central difference approximation has been used to calculate $\frac{\partial u}{\partial y}|_{wall}$ then C_f was used in comparison with other methods to find the proper criteria in finding the LSB parameters. The transition point was considered where there was a sharp drop in C_f, similar to the static case.

To study shear stress behavior in the existence of a LSB it is necessary to look at instantaneous and average velocity fields. As is clear from sample instantaneous images (see Figures 5.1 to 5.11), following the LSB, small vortices form. Although general behavior of the flow in the existence of a LSB at dynamic flow is similar to static cases but in dynamic conditions these vortices are larger and have a stronger structure so that in spite of time averaging of the data, a shedding vortex is visible especially at lower Re that flow have larger vortical structures, Figure 5.11 at AOA=12°. This is in agreement with the results of Kim and Chang [60] using a NACA0012 airfoil at k=0.1 who defined the turbulent reattachment point immediately ahead of the beginning of the shedding vortex.

Figure 5.13 shows the instantaneous and time averaged velocity contours. As can be seen the reattachment point that is the same as the static cases moves and the averaged

reattachment point is about 20% further downstream. Also eye-cat structures can be observed in instantaneous data. As it has been shown the time averaging washed out the drifting vortices in the turbulent BL as also happens in the static cases but decreasing the Re to 32000, Figure 5.14 shows different results. Time averaging the data did not remove the turbulent vortices instead showing two attached strong vortices at the TE. This could be due to many reasons including the shedding frequency of the drifting vortices, the size and strength of the drifting vortices compared to the outer BL flow. Therefore more study is needed to define these reasons. Certainly, Re and AOA have a major impact on the BL phenomena but the effects are more considerable with decreasing Re. As explained in previous sections these vortical structures affect Cp and the reattachment point can be identified from Cp. From the time averaged velocity field in Figure 5.14, it is clear that after the flow reattachment the tangential velocity stayed negative, representing the reversed flow results of the second vortex.

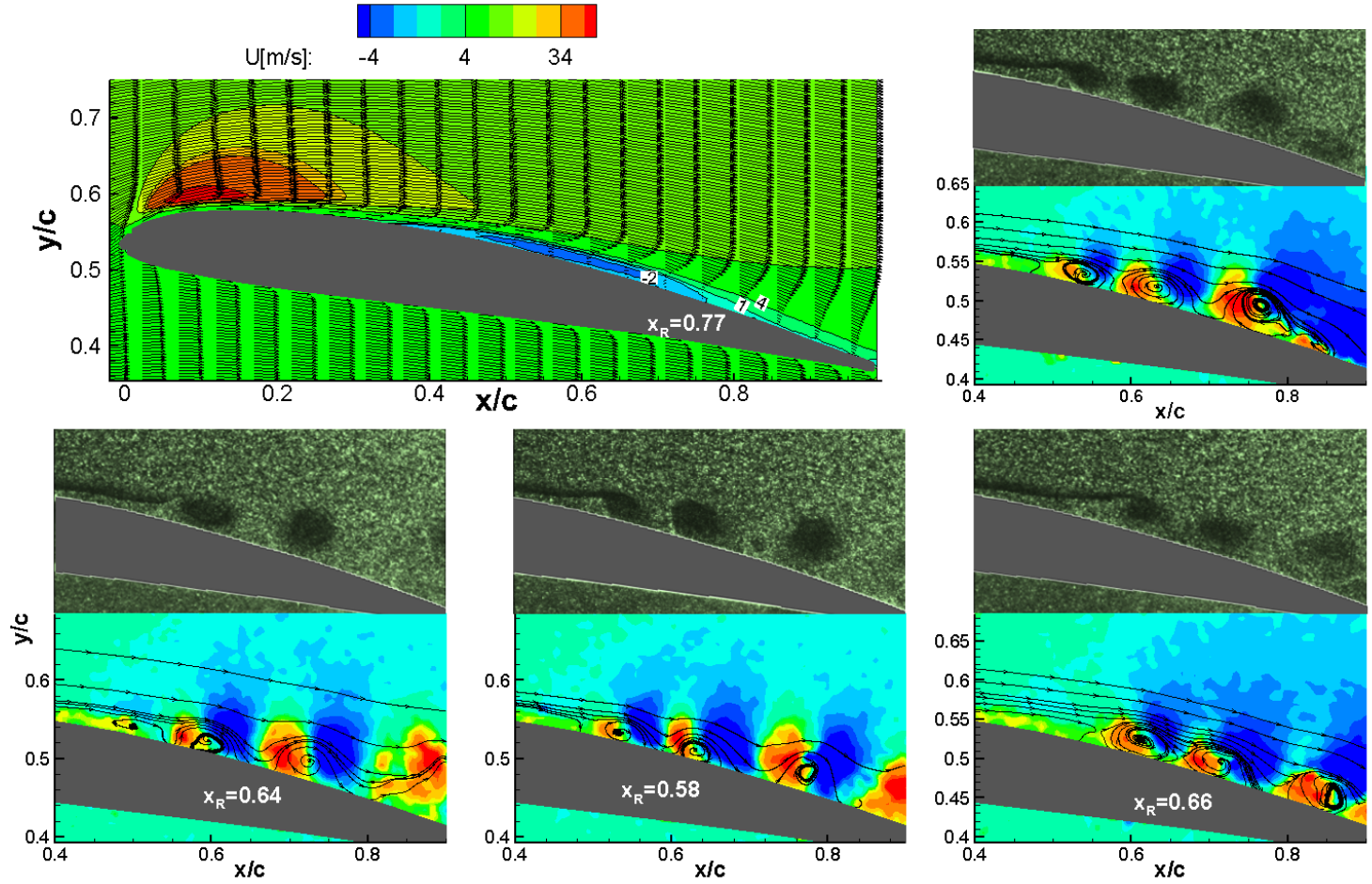

Figure 5.13: top left) Time averaged U_s velocity component contour versus X/C, SD7037 airfoil with iso-contour lines of 0 m/s, 1 m/s and 4 m/s, only every 15 velocity vectors are shown for clarity. Smaller figures present raw images and their instantaneous v_n component contours, case: Re=41000, k=0.08, $AOA = 9°$

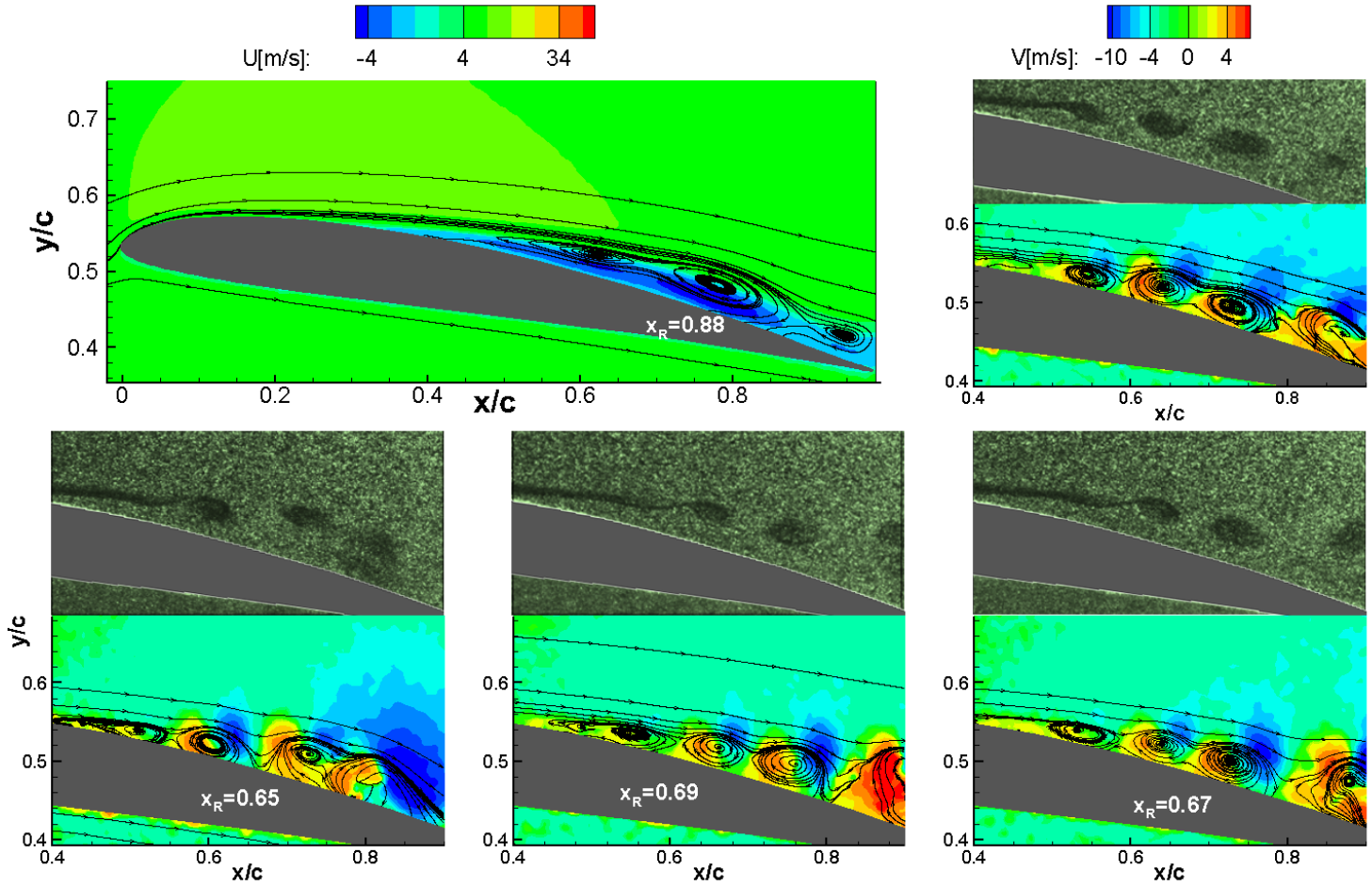

Figure 5.14: top left) Time averaged U_s velocity component contour versus X/C, SD7037 airfoil. Smaller figures present raw images and their instantaneous v_n component contours, case: Re=32000, k=0.08, $AOA = 9°$

Figure 5.15 shows the skin friction coefficient measured from PIV data at Re=32000 and k=0.08. To define the separation point, Figure 5.16 and 5.17 show the $\frac{\partial u}{\partial y}$ field at AOA=7° and 9°. The iso-contour of zero U_s is added to these figures. Only every four velocity vectors are shown for clarity. As can be seen the separation occurs between 0.5c to 0.52c, at AOA= 7° and about 0.32c at AOA= 9°. Comparing these results with C_f in Figure 5.17 shows that the zero crossing line can be used to detect the separation point, the zero crossing line method gives $x_s = 0.51c$ at AOA=7° and $x_s = 0.33c$ at AOA=9°. Therefore this line can provide a good estimation of the separation point in dynamic cases similar to the static cases. Onset of the transition region is where a sharp reduction in C_f occurs. But looking at C_f at AOA=9° reveals the appearance of three distinct troughs in C_f after the transition point. Comparing C_f with the velocity and pressure distribution confirms that these fluctuations present vortical structures in the flow as a result of drifting vortices. Considering the reattachment point where the rate of increasing C_f changed provided the results that are in agreement with instantaneous velocity fields and pressure coefficient. With this assumption, the reattachment point measured at $x_R = 0.66c$ is consistent with the reattachment points measured from instantaneous results in Figure 5.14.

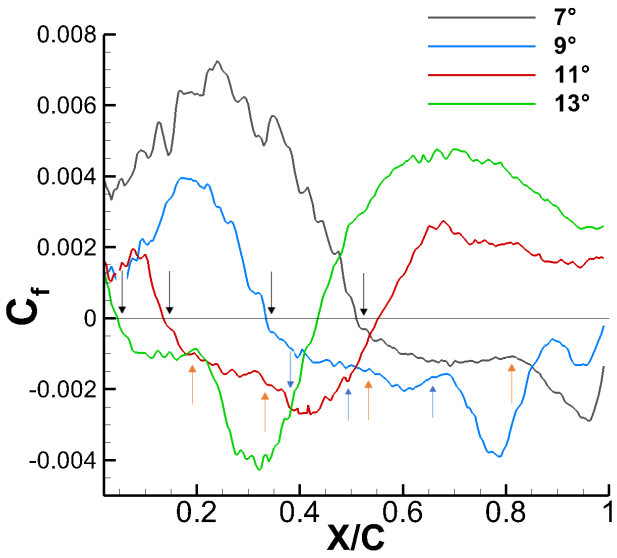

Figure 5.15: Skin friction coefficient distribution, SD7037 airfoil, case: Re=32000, k=0.08, black arrow: separation point, orange arrow: transition point, blue arrow: reattachment point

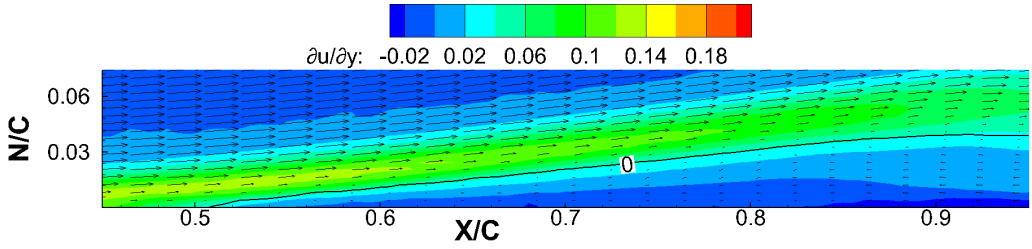

Figure 5.16: $\frac{\partial u_s}{\partial y}$ versus X/C, SD7037 airfoil, case: Re=32000, k=0.08, AOA=7°

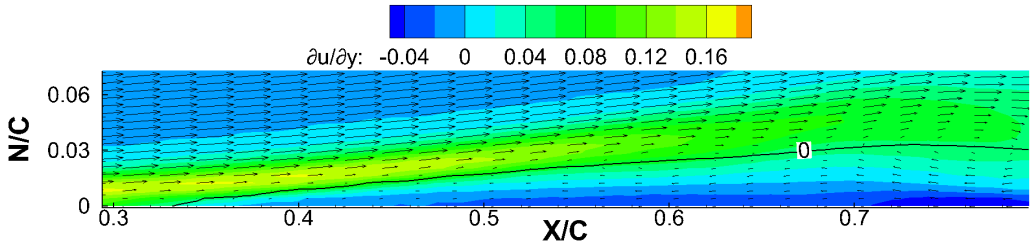

Figure 5.17: $\frac{\partial u_s}{\partial y}$ versus X/C, SD7037 airfoil, case: Re=32000, k=0.08, AOA=9°

5.1.3 Integral boundary layer parameters

As explained before, the BL edge can be defined as $\delta_{0.99}$ where $u = 0.99U_{local\,free\,stream}$. In practice, detecting the BL thickness through this criteria is not a precise method especially in experiments and this is an arbitrary condition especially in the existence of turbulent vortices or an unsteady flow field therefore displacement thickness and momentum thickness can provide more accurate information about the BL characteristics[17]. Yanase and Pentti [138] extend the integral limit to where the tangential velocity reached its maximum in calculating integral BL parameters. Also as mentioned before, in PIV where there is a large velocity gradient in a small distance, there is velocity overestimation [57] that could affect the results. This maximum likely occurs in the vicinity of the surface especially in a laminar BL where the velocity gradient is high or in the existence of vortices. Radespiel *et al.* [102] calculate U_e from wall pressure and the Bernoulli equation and then used $0.99U_e$ criteria to define the BL thickness. Where the velocity did not reach this number, they consider the location of the maximum velocity as the BL edge. Van Ingen and Boermans [91] measured a large value of about 60 for the shape factor (H) and they explained this high value is due to the large region with reversed flow that caused a noticeable increase in δ^*.

In the calculation of boundary layer parameters in unsteady conditions where there are relatively large drifting vortices in the turbulent reattached flow the criteria of $u = 0.99U_{local\,free\,stream}$ was not always applied and alternative explained solutions were used, such as extending the upper limit point of integral parameters as Burr *et al.* noted the upper point for the integral quantities of BL is where beyond that point the integrand is negligible[17].

Figure 5.18 and 5.19 illustrate δ^* and θ^* versus X/C at Re=41000 and k=0.05, respectively. Static results added to these figures show the effects of unsteadiness on the BL flow behavior. Vertical arrows in H show the location of H_{max} that is equivalent to the transition point. As explained in section 3.3.1, h_b considered to be the same as the maximum displacement thickness. Similar to the static cases δ^*_{max} is located downstream of H_{max}. As can be seen in Figure 5.18, when the transition point for a dynamic condition occurs at the same X/C as a static case (AOA=9° at k=0.05, and AOA=9° static), H shows lower values in laminar and turbulent flow regions but it takes longer in comparison to the static case for the BL to reach the relaxation state (constant H). Measured H values are 2-2.2 in the laminar region and 1.4-1.7 in the turbulent region. Table 5.2 summarizes the results at Re=41000 and k=0.05 and shows the separation, transition and reattachment locations, in addition to the length and height of LSB. Measured results were in excellent agreement with the results extracted from Cp. The reattachment point in Cp was considered where the slope of Cp changed for the first time after the transition point. The rest of the points are measured as explained in chapter 3. If the reattachment points extracted from time averaged velocity vectors are far from the instantaneous reattachment point then this method has not been used. The separation point from velocity contours, velocity vectors, and Cp are in good agreement. The separation and reattachment points measured from the (σ_u, σ_v) field also confirm the results as was used by Lou and Hourmouziadis [79].

Table 5.2: Laminar separation bubble parameters at Re=41000 and k=0.05 measured from pressure distribution, velocity field, and integral BL parameters

Re	AOA (°)	x_s/c	x_t/c	x_R/c	h_b/c	l_b/c	δ^*_s/c	θ_s/c	Re_θ
41000	5	0.55	0.87	0.92	0.040	0.37	0.012	0.003	161
	7	0.42	0.68	0.72	0.032	0.30	0.007	0.003	144
	9	0.17	0.38	0.46	0.013	0.29	0.005	0.002	116
	11	0.08	0.24	0.34	0.021	0.26	0.008	0.002	143
	13	0.04	0.17	0.51	0.051	0.47	0.011	0.003	155

It was discussed that changes in the LSB size are highly dependent on Re and AOA while pitch motion affects pressure gradient and delays separation. Increasing turbulence

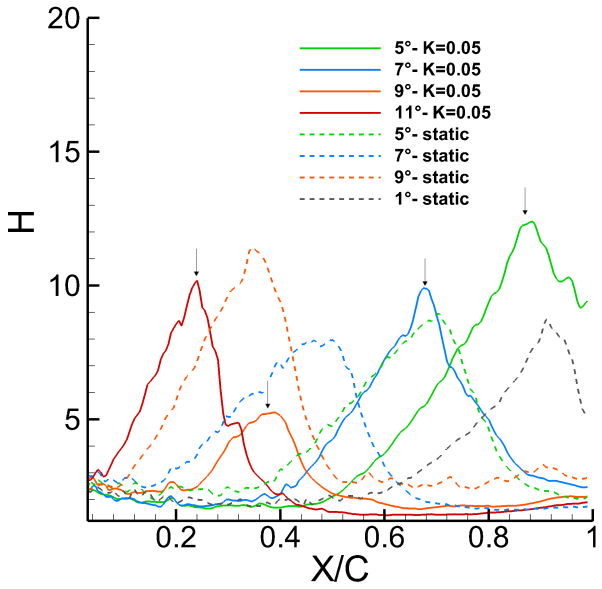

Figure 5.18: Shape Factor H versus X/C, SD7037 airfoil, Case: k=0.05, Re=41000, AOA=5°-11°

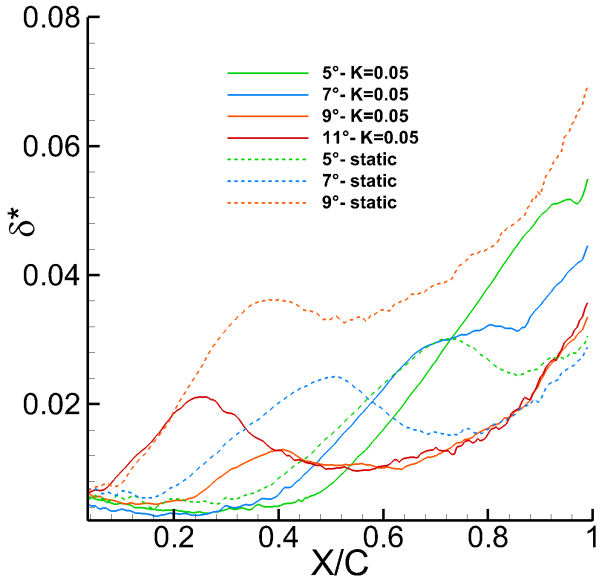

Figure 5.19: δ^* versus X/C, SD7037 airfoil, Case: k=0.05, Re=41000, AOA=5°-11°

could considerably affect flow transition as momentum transfer normal to the shear layer rises in the existence of turbulence[102]. Effects of reduced frequency on the transition point at Re=41000 at different reduced frequencies presented in Figure 5.20 (Only AOA with a LSB are presented). As expected transition is delayed with increasing reduced frequency. The transition point shows a minimum difference at AOA=11° at the two lowest k where a LEV was observed at AOA=13° for either of them.

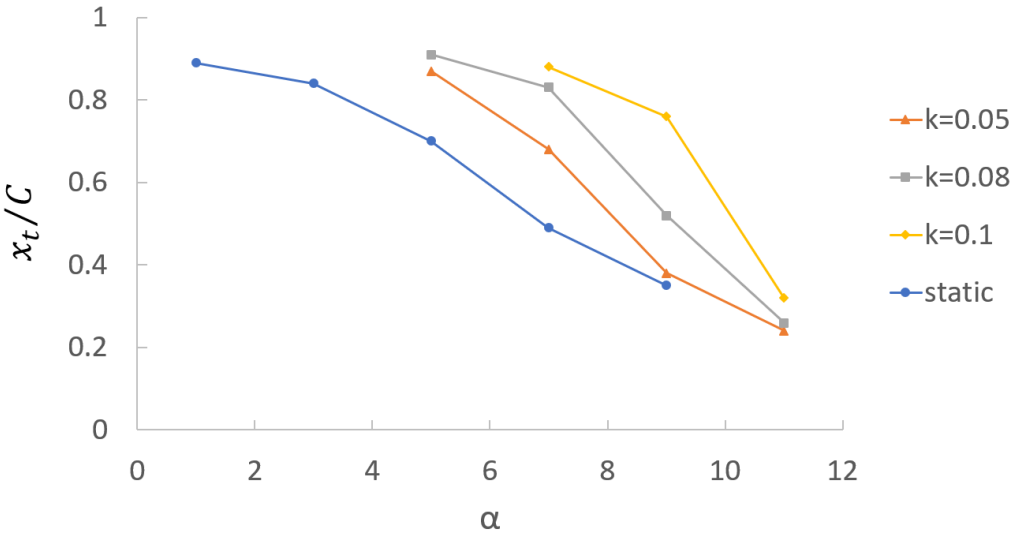

Figure 5.20: Transition point location versus X/C, SD7037 airfoil, Case: k=0.05, Re=41000, AOA=5°-11°

The results shows that with increasing reduced frequency, the overall size of the bubble decreased so that the height of a long bubble decreased about 45% for k=0.05 in comparison with the static case with the same Re. These changes also can be seen in the length of the bubble. The length of the long bubble decreased about 25% in the same case study. A similar trend can be seen in the size of a short bubble. Therefore increasing the reduced frequency can considerably impact the drag force caused by a LSB and improve the airfoil's aerodynamic performance [93, 79, 137]. Results are consistent with results of Lou and Hourmouziadis[79] in that the overall structure of laminar separation, transition, and reattachment is the same for steady and unsteady flows. In unsteady flow, separation remains the same, but there is a strong relation between the transition and reattachment points with oscillatory flow parameters.

5.1.4 Aerodynamic loads

Lift and drag were calculated as explained in section 3.3.8 from 450 samples using velocity field of FOV=2.5c in static and pitching motion. Figure 5.21 shows static results in comparison with XFoil[26] and Gharali[36] at Re=41000. The overall results are in good agreement, the difference could be due to the different size of the window where the pressure field was calculated and using the Bernoulli equation in the pressure calculation instead of the N-S equations. As can be seen in Figure 5.21, all results represent a reduction in drag from 5° to 7°. As explained in Chapter 4.3, the length of the bubble in these two AOA is almost the same ($l_b = 0.4c$) but the height of the bubble h_b at AOA=7° is 20% less than h_b at AOA=5°. The h_b increased at AOA=9°, $h_{b,9^\circ} = 1.5h_{b,7^\circ}$ that shows a jump in the drag coefficient despite a reduction in the length of the bubble.

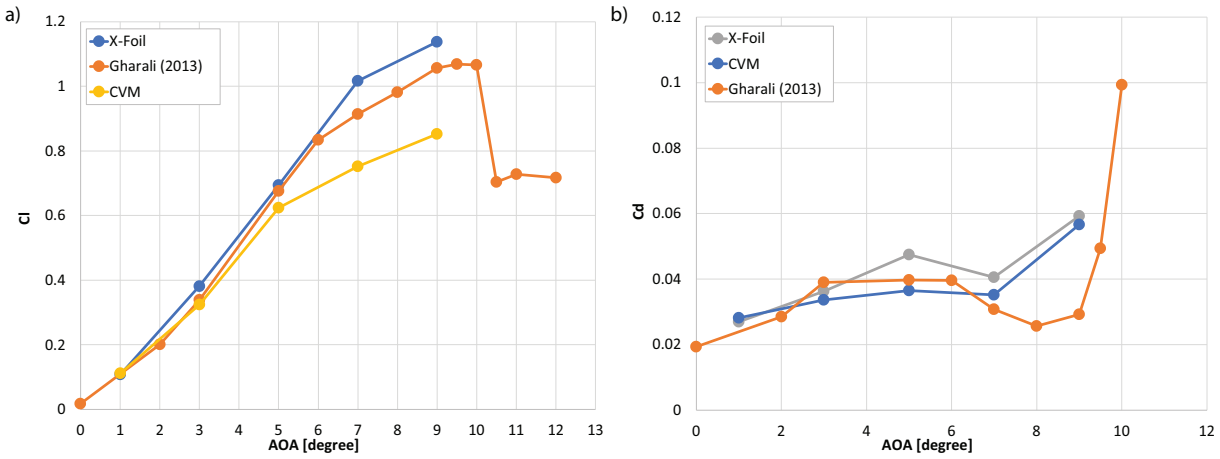

Figure 5.21: a) Lift coefficient versus AOA b) Drag coefficient versus AOA, on SD7037 airfoil at Re=41000 measured from PIV data using CVM in comparison with XFoil, and previous work by Gharali[36]

Figure 5.22 illustrates the lift coefficient versus AOA at Re=41000 and k=0.05, 0.08, and 0.10. Figure 5.22a shows Gharali[36] results at Re=40000 and high amplitude pitch motion so that airfoil reached dynamic stall AOA at all reduced frequencies. As can be seen the lift coefficient is almost constant at all reduced frequencies. Figure 5.22b presents the lift coefficient calculated from PIV data at Re=41000 with pitch motion ($\alpha_{mean} = 8^\circ$ and $\alpha_{amp} = 9^\circ$). The difference between the lift coefficients is more noticeable between k=0.05 and higher reduced frequencies. Previous results show that the SD7037 airfoil at k=0.05 and Re=40000 reached dynamic stall at AOA about 17° while at higher k, it did not not reach the dynamic stall AOA. Therefore, the flow was not affected by large LE

and TE vortices that are the result of the dynamic stall condition. The results of this can be seen as a considerable difference between lift coefficient at lower (k=0.05) and higher reduced frequencies (k=0.08, 0.10).

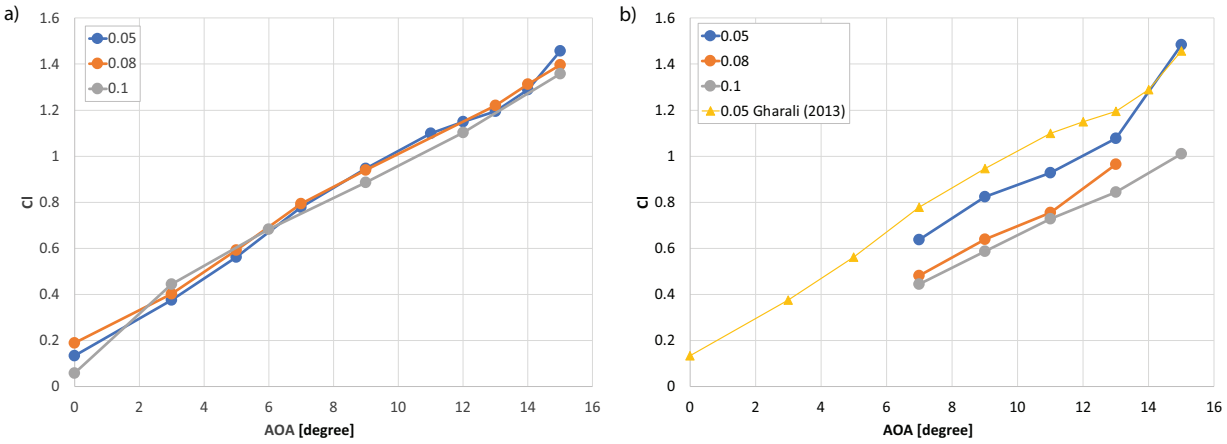

Figure 5.22: a) Lift coefficient versus AOA at k=0.05, 0.08, 0.12 [36] b) Lift coefficient versus AOA calculated from PIV data at k=0.05, 0.08, 0.10

Chapter 6

Conclusion and Future Work

6.1 Summary and Conclusion

The scale of BL flow and laminar separation bubble phenomenon, in addition to the low Re flows has limited the experimental studies in this field. In the following, the main findings are summarized.

Applying three non-intrusive experimental methods (SOFV, IR thermography and PIV) confirms the possibility of reducing the scale of experiments while maintaining accuracy to overcome the lack of experimental data for low Re airfoils.

SOFV provided surface visualization that could be used to study the flow qualitatively and quantitatively. The results show that the rate of increasing the length of the bubble increases with decreasing Re. Also at higher Re, the length of the long bubble stays almost constant with changing AOA. Although in lower Re where there are large vortical structures in the flow, SOFV might show an oil accumulation line while the flow was separated and could be misleadingly considered as a reattached flow. No other SOFV has been reported at this size in studying low Re BL flows that the author is aware of.

Acquired data from IR-Thermography show that this method can provide LSB details including separation and reattachment points in good agreement with the other techniques providing the experiments are performed at low temperature differences.

A high-resolution PIV study of three FOV= 0.6c, 1.0c and 2.5c and five low Re in a steady flow and at three low Re and three reduced frequencies in high amplitude pitch motion gave more insight into the boundary layer flow and laminar separation bubble than has been reported before. Effects of the LSB on the suction side of the airfoil were studied

using pressure distribution coefficient, skin friction coefficient, and integral BL parameters, in addition to velocity contours and velocity vectors. High-resolution PIV captured vortical structures in the turbulent reattachment region in static and dynamic flow.

The surface pressure coefficient was estimated from the time-averaged velocity field measured from PIV data at FOV=1.0c. Measured Cp from PIV data revealed vortical structure effects as low-pressure waves. These vortical structures are more considerable in low Re flow with dynamic motion. Also, Cp was used to determine LSB characteristics.

Measuring the skin friction coefficient of extremely low magnitude was one of the experimental challenges. The skin friction coefficient in low shear regions on the SD7037 airfoil was calculated from PIV data. The skin friction coefficient increased with reducing Re and lowering Re increased the rate of increase. A sharp drop in C_f was observed after the transition at Re lower than 22000. There is no other literature on skin friction over a SD7037 airfoil at these Re. Therefore the results were compared with the only available source, XFoil model results that show the magnitude of the results was in agreement with this source.

Integral boundary layer features such as displacement thickness, momentum thickness and shape factor were calculated from the velocity field in steady and pitching motion conditions and provided in-depth information regarding LSB characteristics. BL thickness increased dramatically at lower Re at constant AOA that results in the formation of a bubble with higher height in lower Re. Later the measured aerodynamic force shows the effect of the height of the bubble on increasing the drag. Integral BL features were also estimated from instantaneous data and confirm the results and accuracy of the individual velocity fields. BL flow and reversed flow under the separated bubble were captured precisely while the FOV covers the whole airfoil and results were confirmed by acquired data using finer spatial resolution.

Averaged transition and reattachment points can be identified from time-averaged data although the reattachment point measured from averaged data is quite far downstream of the instantaneous reattachment point. The accuracy of the averaged reattachment point decreases with lowering Re when vortical structures are large and unstable. An estimation of the instantaneous reattachment point can be defined considering the appearance of the instabilities in pressure and skin friction coefficient due to vortical structures of the flow. These structures are larger in lower Re and in dynamic conditions. Pitching affects BL flow such that it takes longer for the BL flow to reach the relaxation state but it decreases H in comparison to the static case.

The POD method provided more details of the behavior of vortices. The estimated location of the shear layer rollup measured from the POD method is close to the measured

transition point. Therefore using POD revealed more information regarding transition and reattachment.

Results showed that LSB characteristics mainly depend on Re and AOA, therefore, increased pitching can have different effects on the height and length of the bubble at a specific Re and AOA although it delays separation. But if considering the same type of the bubble (short, or long), it could be said that the overall height of the bubble decreases by increasing pitching.

Increasing the reduced frequency decreases the strength of vortical structures in most of the studied cases.

The height of the bubble has a considerable effect on moving the streamlines and changes the drag force. A higher spatial resolution can provide more accurate results of the laminar BL region and detecting the separation point, especially where there is a thin and long LSB when the BL thickness is thin and the rate of velocity changes are high.

6.2 Future Work and Recommendations

For future studies, further research in different aspects regarding experimental setup, data post-processing and new experiments can be recommended. Suggested topics are outlined below.

An advanced PIV setup in small-scale experiments could increase the accuracy of the experiment and decrease the required time of the experiment. Therefore, a design including a controller system for the laser, optics and camera is highly suggested.

Develop image processing to phase average PIV images (velocity fields) to determine the location of drifting vortices in the turbulent region.

Develop the applied image processing methods on a graphics processing unit (GPU) to accelerate image processing considerably.

Also, design and completion of the following experiments are recommended:

Using high speed IR thermography in a study of pitching low Re flow, this method with low cost can provide reliable results.

Design an experiment to combine IR thermography (electrically conductive paint) and 2D PIV. This provides the ability to study the boundary layer flow in spanwise and chordwise directions simultaneously.

Design a virtual family of SD7037 airfoils by changing specific geometry parameters (such as camber, location of maximum camber, maximum thickness, and location of maximum

thickness) to study effects of airfoil geometry on an LSB, fully. The experiment can be done using 3D printed models and IR thermography.

Design a miniature airfoil applying smart memory alloys to vary airfoil geometry. This model can be used as an experimental model that can extend the number of case studies or be used as an active controller to control flow separation and LSBs.

Moreover, a combination of some of the listed projects can provide a smaller scale experimental facility with an advanced PIV setup and the ability to solve complex flow fields in no time while using smart airfoils with controllable geometry that can be used in designing optimized airfoils.

These topics have the potential to further the knowledge of flow behavior around static and pitching airfoils.

References

[1] R. J.Adrian, K. T.Christensen, and Z.-C.Liu. Analysis and interpretation of instantaneous turbulent velocity fields. *Experiments in Fluids*, 29(3):275–290, 2000.

[2] R. J.Adrian, I.Marusic, and I. A.Fulton. Coherent structures in flow over hydraulic engineering surfaces. *Journal of Hydraulic Research*, 50(5):451–464, 2012.

[3] R. J.Adrian and J.Westerweel. *Particle Image Velocimetry*. Cambridge University Press, 2011.

[4] J.Aholt and F.Finaish. Active Flow Control Strategy of Laminar Separation Bubbles Developed over Subsonic Airfoils at Low Reynolds Numbers. In *49th AIAA Aerospace Sciences Meeting including the New Horizons Forum and Aerospace Exposition- 4- 7 January*, Orlando, Florida, 2011. American Institute of Aeronautics and Astronautics.

[5] N. A.Andersen. Camera Technology and Advanced Imaging Applications. Technical report, Dantec Dynamics, 2007.

[6] K.Angele and B.Muhammad-Klingmann. PIV measurements in a weakly separating and reattaching turbulent boundary layer. *European Journal of Mechanics B/Fluids*, 25:204–222, 2006.

[7] T.Astarita, G.Cardone, G. M.Carlomagno, and C.Meola. A survey on infrared thermography for convective heat transfer measurements. *Optics & Laser Technology*, 32(7):593–610, 2000.

[8] AZoM.com. Float Glass, Properties and Applications, 2001.

[9] J. B.Barlow, W. H.Rae, Jr., and A.Pope. *Low Speed Wind Tunnel Testing*. John Wiley & Sons. Interscience publication, USA, third edition, 1999.

[10] L. H.Benedict and R. D.Gould. Towards better uncertainty estimates for turbulence statistics. *Experiments in Fluids*, 22(2):129–136, dec 1996.

[11] D. M.Bremmer, F. V.Hutcheson, and D. J.Stead. Methodology for the Elimination of Reflection and System Vibration Effects in Particle Image Velocimetry Data Processing. Technical Report February, NASA Langley Research Center Hampton, VA 23681-2199, 2005.

[12] J. R.Brinkerhoff and M. I.Yaras. Interaction of viscous and inviscid instability modes in separation-bubble transition. *Physics of Fluids*, 23:124102, 2011.

[13] S.Burgmann, C.Brücker, and W.Schröder. Scanning PIV measurements of a laminar separation bubble. *Experiments in Fluids*, 41(2):319–326, 2006.

[14] S.Burgmann, J.Dannemann, and W.Schröder. Time-resolved and volumetric PIV measurements of a transitional separation bubble on an SD7003 airfoil. *Experiments in Fluids*, 44(4):609–622, 2008.

[15] S.Burgmann and W.Schröder. Investigation of the vortex induced unsteadiness of a separation bubble via time-resolved and scanning PIV measurements. *Experiments in Fluids*, 45(4):675–691, 2008.

[16] S.Burgmann, M.Klaas, and W.Schröder. VORTEX DETECTION VIA SCANNING PIV MEASUREMENTS. In *Lasermethoden in der Strömungsmesstechnik*, Braunschweig VORTEX, 2006.

[17] K. P.Burr, T. R.Akylas, and C. C.Mei. Two-Dimensional Laminar Boundary Layer. In *High Reynolds number flows*, chapter two. web.mit.edu, two edition.

[18] B. J.Cantwell. Chapter 8. In *Fundamentals of compressible flow (course material for AA210A)*, chapter 8. Department of Aeronautics and Astronautics Stanford University, Stanford California, 2015.

[19] G. M.Carlomagno and G.Cardone. Infrared thermography for convective heat transfer measurements. *Experiments in Fluids*, 49(6):1187–1218, dec 2010.

[20] M.Costantini, U.Fey, U.Henne, and C.Klein. Nonadiabatic Surface Effects on Transition Measurements Using Temperature-Sensitive Paints. *AIAA Journal*, 53(5):1172–1187, 2015.

[21] D.Dabiri. Cross-Correlation Digital Particle Image Velocimetry-A Review. *Turbulência, Ed., Freire, AS, Iiha, A., Breidenthal, B., ...*, pages 1–54, 2006.

[22] Dantec Dynamics A/S. *DynamicStudio User's Guide*. Dantec Dynamics A/S, Skovlunde, Denmark, 2013.

[23] C.Dollinger, N.Balaresque, A. P.Schaffarczyk, and A.Fischer. Thermographic Detection of separated Flow. *J. Phys.: Conf. Ser- The Science of Making Torque from Wind (TORQUE 2016)*, 753, 2016.

[24] B.Dorschner, S. S.Chikatamarla, and I. V.Karlin. Transitional flows with the entropic lattice Boltzmann method. *Journal of Fluid Mechanics*, 824(August):388–412, 2017.

[25] H.-S.Dou. Viscous flow instability of inflectional velocity profile. In *Fourth International Conference on Fluid Mechanics, July 20-23*, Dalian, China, 2004.

[26] M.Drela. XFOIL, Subsonic Airfoil Development System.

[27] M.Drela. XFOIL: An Analysis and Design System for Low Reynolds Number Airfoils. Technical report, MIT Dept. of Aeronautics and Astronautics, Cambridge, Massachusetts, 1989.

[28] Z.Duan, B.He, and Y.Duan. Sphere Drag and Heat Transfer. *Scientific reports*, 5:12304, 2015.

[29] R.Eppler. SOME NEW AIRFOILS. Technical report, Universitat Stuttgart, Stuttgart, West Germany.

[30] T. M.Faure, L.Hétru, and O.Montagnier. Vortex dynamics resulting from the interaction between two NACA 23 012 airfoils. In *50h 3AF International Conference on Applied Aerodynamics, 29 March- 1 April*, Toulouse - France, 2015.

[31] N.Fujisawa, S.Tanahashi, and K.Srinivas. Evaluation of pressure field and fluid forces on a circular cylinder with and without rotational oscillation using velocity data from PIV measurement. *Measurement Science and Technology*, 16(4):989–996, 2005.

[32] M.Gaster. The Structure and Behaviour of Separation Bubbles. Technical Report 3595, Queen Mary College, London University, 1969.

[33] C.Ge. Noise Generation of a Bionic Airfoil Based on Owl Wings. In *MATEC Web of Conferences*, 2017.

[34] M. S.Genç, I.Karasu, H. H.Açikel, and M. T.Akpolat. Low Reynolds number flows and transition. In *Low Reynolds Number Aerodynamics and Transition*, chapter 1, pages 1–28. InTech, Rijeka, 2012.

[35] M. S.Genç, I.Karasu, and H.Hakan Açikel. An experimental study on aerodynamics of NACA2415 aerofoil at low Re numbers. *Experimental Thermal and Fluid Science*, 39:252–264, 2012.

[36] K.Gharali. *Pitching airfoil study and freestream effects for wind turbine applications*. PhD thesis, University of Waterloo, 2013.

[37] K.Gharali and D.Johnson. Reduced frequency effects on Laminar Separation Bubbles. In *10th International Symposium on Particle Image Velocimetry, July 1-3*, Delft, Netherlands, 2013.

[38] K.Gharali and D. A.Johnson. Dynamic stall simulation of a pitching airfoil under unsteady freestream velocity. *Journal of Fluids and Structures*, 42:228–244, 2013.

[39] K.Gharali, N.Tam, and D. A.Johnson. A PIV load and flow structure study of a serrated dynamic airfoil. *17th International Symposium on Applications of Laser Techniques to Fluid Mechanics*, 2014.

[40] F.Ghorbanishohrat and D. A.Johnson. Evaluating airfoil behaviour such as laminar separation bubbles with visualization and IR thermography methods. *J. Phys.: Conf. Ser*, 1037(052037), 2018.

[41] F.Ghorbanishohrat and D.Johnson. Effects of the Laminar Separation Bubble on the Performance of Small Wind Turbine Blade. In *1000 Island Energy Research Forum, 2014*, Ottawa, 2014.

[42] F.Ghorbanishohrat and D. A.Johnson. Oil Flow Visualization of the Laminar Separation Bubble on a SD 7037 Airfoil. In *25th CANCAM*, London, Ontario, Canada, 2015.

[43] F.Ghorbanishohrat and D. A.Johnson. Investigation of Laminar Separation Bubble using Particle Image Velocimetry and Proper Orthogonal Decomposition (POD). In *19th International Symposium on the Application of Laser and Imaging Techniques to Fluid Mechanics, 16-19 July*, Lisbon, 2018.

[44] F.Ghorbanishohrat, F.Samara, and D. A.Johnson. Investigation of laminar separation bubble behavior under unsteady flows using PIV and Thermal Imaging Methods. In *18th International Symposium on the Application of Laser and Imaging Techniques to Fluid Mechanics, 4-7 July*, Lisbon, jul 2016.

[45] P.Giguere and M. S.Selig. New Airfoils for Small Horizontal Axis Wind Turbines. *Journal of Solar Energy Engineering*, 120(2):108, 1998.

[46] P.Giguere and M. S.Selig. Low Reynolds Number Airfoils for Small Horizontal Axis Wind Thrbines. *Wind Engineering*, 21(6):367–380, 1997.

[47] M.Grawunder, R.Reß, and C.Breitsamter. Thermographic Transition Detection for Low-Speed Wind-Tunnel Experiments. *AIAA Journal*, 54(6):1–5, 2016.

[48] C.Häggmark. Investigations of disturbances developing in a laminar separation bubble flow. Technical report, Department of Mechanics, Royal Institute of Technology, Stockholm, Sweden, 2000.

[49] J.Higham. *The application of modal decomposition techniques for the analysis of environmental flows*. PhD thesis, University of Sheffield, 2017.

[50] H. P.Horton. *Laminar Separation Bubbles in Two and Three Dimentional Incompressible Flow*. PhD thesis, University of London, 1968.

[51] H. P.Horton. A semi-empirical theory for the growth and bursting of laminar separation bubbles. Technical Report 1073, Ministry of Technology, Aeronautical Research Council, London, 1969.

[52] S.Hosokawa, S.Moriyama, A.Tomiyama, and N.Takada. PIV measurement of pressure distributions about single bubbles. *Journal of Nuclear Science and Technology*, 40(10):754–762, 2003.

[53] H.Hu and Z.Yang. An Experimental Study of the Laminar Flow Separation on a Low-Reynolds-Number Airfoil. *Journal of Fluids Engineering*, 130(5):051101, 2008.

[54] ILWIS. Image Processing. In *ILWIS 3.0 User's guide*, pages 209–276. 2001.

[55] M. S.Istvan, J. W.Kurelek, and S.Yarusevych. Turbulence Intensity Effects on Laminar Separation Bubbles Formed over an Airfoil. *AIAA Journal*, 56(4):1335–1347, apr 2018.

[56] M.Jahanmiri. Laminar Separation Bubble : Its Structure , Dynamics and Control. *Chalmers University of Technology*, pages 1–24, 2011.

[57] S.Junqi, P.Chong, and W.Jinjun. Accurate measurement of wall skin friction by single-pixel ensemble correlation. *SCIENCE CHINA Physics, Mechanics & Astronomy*, 57(7):1352–1362, 2014.

[58] C. J.Kahler. High resolution measurements by long-range micro-PIV Proc. In *VKI Lecture Series on Recent Advances in Particle Image Velocimetry*, pages 26–30, Rhode Saint Genese, Belgium, 2009.

[59] D.-H.Kim and J.-W.Chang. Measurement of an unsteady boundary layer of an oscillating airfoil at a low Reynolds number. *Journal of the Korean Society for Aeronautical & Space Sciences*, 34(12):9–17, 2006.

[60] D. H.Kim and J. W.Chang. Unsteady boundary layer for a pitching airfoil at low Reynolds numbers. *Journal of Mechanical Science and Technology*, 24(1):429–440, 2010.

[61] D.-H.Kim and J.-W.Chang. Low-Reynolds-number effect on the aerodynamic characteristics of a pitching NACA0012 airfoil. *Aerospace Science and Technology*, 32(1):162–168, jan 2014.

[62] J.Kim, T. W.Simon, and M.Kestoras. Fluid Mechanics and Heat Transfer Measurements in Transitional Boundary Layers Conditionally Sampled on Intermittency. *Journal of Turbomachinery*, 116(3):405, jul 1994.

[63] A. R.Lambert. *Vortex Dynamics within the Laminar Separation Bubble over a NACA 0018 Airfoil at Low Reynolds Numbers*. PhD thesis, University of Waterloo, 2015.

[64] M.Lang, U.Rist, and S.Wagner. Investigations on controlled transition development in a laminar separation bubble by means of LDA and PIV. *Experiments in Fluids*, 36(1):43–52, 2004.

[65] T.Lee and S.Basu. Measurement of unsteady boundary layer developed on an oscillating airfoil using multiple hot-film sensors. *Experiments in Fluids*, 25(2):108–117, 1998.

[66] T.Lee and P.Gerontakos. Investigation of flow over an oscillating airfoil. *Journal of Fluid Mechanics*, 512:313–341, 2004.

[67] T.Lee, G.Petrakis, F.Mokhtarian, and F.Kafyeke. Boundry-Layer Transition, Seperation, and Reattachment on an Oscillating Airfoil. *Journal of Aircraft*, pages 356–360, 1999.

[68] M.Legrand, J.Nogueira, and A.Lecuona. Flow temporal reconstruction from non-time-resolved data part I: mathematic fundamentals. *Exp Fluids*, 51:1047–1055, 2011.

[69] M.Legrand, J.Nogueira, T.Shigeru, A.Lecuona, and S.Nauri. Flow temporal reconstruction from non time-resolved data part II: practical implementation, methodology validation, and applications. *Exp Fluids*, 51:861–870, 2011.

[70] M.Legrand, S.Tachibana, J.Nogueira, A.Lecuona, S.Nauri, and P. A.Rodríguez. Flow temporal reconstruction from non time-resolved data. In *5th Int Symp on Applications of Laser Techniques to Fluid Mechanics , 05-08 July*, Lisbon, Portugal, 2010.

[71] J. G.Leishman. Challenges in Modeling the Unsteady Aerodynamics of Wind Turbines. *American Institute of Aeronauticy and Astronautics*, 37:1–28, 2002.

[72] J. G.Leishman. *Principles of helicopter aerodynamics*. Cambridge University Press, 2nd ed. edition, 2006.

[73] D.Lengani and D.Simoni. Recognition of coherent structures in the boundary layer of a low-pressure-turbine blade for different free-stream turbulence intensity levels. *International Journal of Heat and Fluid Flow*, 54, 2015.

[74] D.Lengani, D.Simoni, M.Ubaldi, and P.Zunino. POD analysis of the unsteady behavior of a laminar separation bubble. *Experimental Thermal and Fluid Science*, 58:70–79, 2014.

[75] D.Lengani, D.Simoni, M.Ubaldi, P.Zunino, and F.Bertini. Analysis of the Reynolds stress component production in a laminar separation bubble. *International Journal of Heat and Fluid Flow*, 64:112–119, 2017.

[76] J. C. M.Lin and L. L.Pauley. Low-Reynolds-number separation on an airfoil. *AIAA Journal*, 34(8):1570–1577, 1996.

[77] P. B. S.Lissaman. Low-Reynolds-Number Airfoils. *Annual Review of Fluid Mechanics*, 15(1):223–239, 1983.

[78] X.Liu and J.Katz. Instantaneous pressure and material acceleration measurements using a four-exposure PIV system. *Experiments in Fluids*, 41(2):227–240, 2006.

[79] W.Lou and J.Hourmouziadis. Separation Bubbles Under Steady and Periodic-Unsteady Main Flow Conditions. *Journal of Turbomachinery*, 122:634–643, oct 2000.

[80] C.Lyon, M.Selig, and A.Broeren. Boundary Layer Trips on Airfoils at Low Reynolds Numbers. In *35th Aerospace Sciences Meeting & Exhibit, January 6 - 10*, Reno, NV, 1997. AIAA.

[81] S.Mangalam, J. F.Meyers, J. R.Dagenhart, and W. D.Harvey. A Study of Laminar Separation Bubble in the Concave Region of an Airfoil Using Laser Velocimetry. *Symposium A Quarterly Journal In Modern Foreign Literatures*, 1985.

[82] R. E.Mayle. The Role of Laminar-Turbulent Transition in Gas Turbine Engines. *Journal of Turbomachinery*, 113(October 1991):509, 1991.

[83] J.McArthur. *Aerodynamics of wings at low reynolds numbers*. PhD thesis, University Of Southern California, 2007.

[84] B. R.McAuliffe and M. I.Yaras. Separation-Bubble-Transition Measurements on a Low-Re Airfoil Using Particle Image Velocimetry. *Volume 3: Turbo Expo 2005, Parts A and B*, pages 1029–1038, 2005.

[85] B. D.McGranahan and M. S.Selig. Surface Oil Flow Measurements on Several Airfoils at Low Reynolds Numbers. In *21st AIAA Applied Aerodynamics Conference, June 23-26*, Orlando, FL, 2003. AIAA.

[86] J. H.McMasters and M. L.Henderson. Low Speed Single Element Airfoil Synthesis. In *Langley Research Center The Sci. and Technol. of Low Speed and Motorless Flight, Pt. 1 Hampton*, pages 1–31, Virginia, 1979.

[87] S.McTavish, D.Feszty, and F.Nitzsche. Evaluating Reynolds number effects in small-scale wind turbine experiments. *J. WindEng.Ind.Aerodyn.*, 120:81–90, 2013.

[88] R.Meynart. Instantaneous velocity field measurements in unsteady gas flow by speckle velocimetry. *Appl. Opt.*, 22(4):535–540, 1983.

[89] G.Michel. Lift and drag on an airfoil calculation from PIV results. Technical report, Institut National Des Sciences Appliquees, 2016.

[90] T.Michelis, S.Yarusevych, and M.Kotsonis. Response of a laminar separation bubble to impulsive forcing. *J. Fluid Mech*, 820:633–666, 2018.

[91] T. J.Mueller, editor. *Proceedings of the Conference on Low Reynolds Number Airfoil Aerodynamics*. 1985.

[92] T. J.Mueller and J. D.Delaurier. Aerodynamics of small vehicles. *Annu. Rev. Fluid Mech*, 35:89–111, 2003.

[93] A.Nati, R.de Kat, F.Scarano, and B. W.van Oudheusden. Dynamic pitching effect on a laminar separation bubble. *Experiments in Fluids*, 56(9):1–17, 2015.

[94] New Wave Research. *Operator's Manual New Wave Research, Inc. Tempest and Gemini PIV Nd: YAG Lasers*. New Wave Research, Inc., Fremont CA, 2000.

[95] W.Nitsche and C.Dobriloff. *Imaging Measurement Methods for Flow Analysis*. Notes on Numerical Fluid Mechanics and Multidisciplinary Design. Springer Berlin Heidelberg, 2009.

[96] M. V.Ol. Unsteady Low Reynolds Number Aerodynamics For Micro Air Vehicles (MAVs). Technical report, Air Force Research Laboratory Air, 2010.

[97] M. V.Ol, B. R.McCauliffe, E. S.Hanff, U.Scholz, and C.Kähler. Comparison of Laminar Separation Bubble Measurements on a Low Reynolds Number Airfoil in Three Facilities. In *Proceedings of the 35th AIAA˜Fluid Dynamics Conference and Exhibit*, pages 1–11, Toronto, Ontario, Canada, 2005.

[98] M.O'Meara and T.Mueller. Laminar Separation Bubble Characteristics on an Airfoil at Low Reynolds Numbers. *AIAA*, 25(8):1033–1041, 1987.

[99] S. M.Orlando. *Laser Doppler Anemometry and Acoustic Measurements of an S822 Airfoil at Low Reynolds Numbers*. Master of applied science in mechanical engineering waterloo,, University of Waterloo, 2011.

[100] M.Pascazio, J.Autric, D.Favier, and C.Maresca. Unsteady boundary-layer measurement on oscillating airfoils - Transition and separation phenomena in pitching motion. In *34th Aerospace Sciences Meeting and Exhibit*, Reston, Virigina, jan 1996. American Institute of Aeronautics and Astronautics.

[101] A. L.Pauley, P.Moinz, and W. C.Reynolds. The structure of two-dimensional separation. *J. Fluid Mech*, 220:397–411, 1990.

[102] R. E.Radespiel, J.Windte, and U.Scholz. Numerical and Experimental Flow Analysis of Moving Airfoils with Laminar Separation Bubbles. *AIAA Journal*, 45(6):1346–1356, 2007.

[103] M.Raffel, C. B.Merz, T.Schwermer, and K.Richter. Differential infrared thermography for boundary layer transition detection on pitching rotor blade models. *Experiments in Fluids*, 56(2):1–13, 2015.

[104] D.Ragni, A.Ashok, B. W.van Oudheusden, and F.Scarano. Surface pressure and aerodynamic loads determination of a transonic airfoil based on particle image velocimetry. *Measurement Science and Technology*, 20(7):074005, jul 2009.

[105] H.Rhoads, S. S.Schwartz, K.Zarowny, T.Weis, S.Whittaker, M.Gluckman, and M.French. Small Wind Turbine Purchasing Guide. Technical report, Pembina Institute, 2008.

[106] R.Ricci and S.Montelpare. A quantitative IR thermographic method to study the laminar separation bubble phenomenon. *International Journal of Thermal Sciences*, 44(8):709–719, 2005.

[107] F.Richez, I.Mary, V.Gleize, and C.Basdevant. Simulation and Modelling of a Laminar Separation Bubble on Airfoils. In *IUTAM Symposium on Unsteady Separated Flows and their Control, IUTAM Bookseries 14*, volume 14, pages 457–469, 2007.

[108] W. B.Roberts. Calculation of Laminar Separation Bubbles and Their Effect on Airfoil Performance. *AIAA*, 18(1):25–31, 1980.

[109] D.Rudmin, A.Benaissa, and D.Poirel. Detection of Laminar Flow Separation and Transition on a NACA-0012 Airfoil Using Surface Hot-Films. *Journal of Fluids Engineering*, 135(10):101104, 2013.

[110] J. M.Russell. Length and Bursting of Separation Bubbles: A Physical Interpretation. 1979.

[111] H.Schlichting and K.Gersten. *Boundary-Layer Theory*. Springer-Verlag Berlin Heidelberg 2017, 9th edition, 2017.

[112] E. J.Schroeder. Low Reynolds Number Flow Validation Using Computational Fluid Dynamics with Application to Micro Air Vehicles. 2005.

[113] A.Sciacchitano and F.Scarano. Elimination of PIV light reflections via a temporal high pass filter. *Measurement Science and Technology*, 25(8):084009, 2014.

[114] M. S.Selig, J. F.Donovan, and D. B.Fraser. *Airfoils at Low Speeds*. H. A. Stokely, Virginia Beach, Virginia 23451 USA, 1989.

[115] M. S.Selig. Low Reynolds Number Airfoil Design Lecture Notes. Technical report, Department of Aerospace Engineering, University of Illinois, 2003.

[116] M. S.Selig and B. D.McGranahan. Wind Tunnel Aerodynamic Tests of Six Airfoils for Use on Small Wind Turbines. *Journal of Solar Energy Engineering*, 126(4):986, 2004.

[117] M.Selig, J. J.Guglielmo, A. P.Broeren, and P.Giguere. *Summary of Low-Speed Airfoil Data Summary of Low-Speed Airfoil Data*, volume 1. SoarTech Publications, Virginia Beach, Virginia, 1995.

[118] M.Selig, J. J.Guglielmo, A. P.Broeren, and P.Giguere. *Summary of Low-Speed Airfoil Data*, volume 2. SoarTech Publications, Virginia Beach, Virginia 23451 USA, 1996.

[119] A.Sharma and M.Visbal. Numerical Investigation of the Effect of Airfoil Thickness on Onset of Dynamic Stall. *ArXiv e-prints [physics.flu-dyn]*, 1705.00230:31, 2017.

[120] W.Shyy, Y.Lian, J.Tang, D.Viieru, and H.Liu. *Aerodynamics of Low Reynolds Number Flyers*. Cambridge University Press, New York, USA, 2008.

[121] M. P.Simens and A. G.Gungor. The Effect of Surface Roughness on Laminar Separated Boundary Layers. *Journal of Turbomachinery*, 136(3):031014, 2013.

[122] B.Simon, A.Filius, C.Tropea, and S.Grundmann. IR thermography for dynamic detection of laminar-turbulent transition. In *18th International Symposium on the Application of Laser and Imaging Techniques to Fluid Mechanics, July 4 - 7*, Lisbon, Portugal, 2016.

[123] D.Simoni, D.Lengani, M.Ubaldi, P.Zunino, and M.Dellacasagrande. Inspection of the dynamic properties of laminar separation bubbles: freestream turbulence intensity effects for different Reynolds numbers. *Exp Fluids*, 58(66), 2017.

[124] N. K.Singh and S.Sarkar. DNS of a Laminar Separation Bubble. *World Academy of Science, Engineering and Technology 57*, 57:439–443, 2011.

[125] R. K.Singh, M. R.Ahmed, M. A.Zullah, and Y.-H.Lee. Design of a low Reynolds number airfoil for small horizontal axis wind turbines. *Renewable Energy*, 42:66–76, 2012.

[126] D. M.Somers. Design and Experimental Results for S805 Airfoil. Technical report, National Renewable Energy Laboratory, 1997.

[127] B.Sperandei. *The application of Particle Image Velocimetry in a small scale wind tunnel*. Masc, University of Waterloo, 2002.

[128] H.Tanaka. Flow Visualization and PIV Measurements of Laminar Separation Bubble Oscillating at Low Frequency on an Airfoil Near Stall. In *24th International Congress of the Aeronautical Sciences*, 2004.

[129] I.Tani. Low-speed flows involving bubble separations. *Progress in Aerospace Sciences*, 5:70–103, 1964.

[130] O.Uzol, Y. C. Y.-C.Chow, J.Katz, and C.Meneveau. Unobstructed PIV measurements within an axial turbo-pump using liquid and blades with matched refractive indices. *4th International Symposium on Particle Image Velocimetry*, 33(Sep 17-19):909–919, 2001.

[131] B. W.Van Oudheusden. Principles and application of velocimetry-based planar pressure imaging in compressible flows with shocks. *Experiments in Fluids*, 45(4):657–674, 2008.

[132] R.Wahidi, W.Lai, J. P.Hubner, and A.Lang. Time-averaged and time-resolved volumetric velocimetry measurements of a laminar separation bubble on an airfoil. *European Journal of Mechanics, B/Fluids*, 41:46–59, 2013.

[133] G. J.Walker, P. H.Subroto, and M. F.Platzzer. Transition Modeling Effects on Viscous/Inviscid Interaction Analysis of Low Reynolds Number Airfoil Flow Involving Laminar Separation Bubbles. In *Gas Turbine and Aeroengine Congress, June 6 - 9*, Amsterdam, Netherlands, 1988. ASME.

[134] F.White. *Viscous Fluid Flow*. McGraw-Hill, New York, 1974.

[135] C. E.Willert and M.Gharib. Digital Particle image Velocimetry. *Experiments in Fluids*, 10:181–193, 1991.

[136] J. G.Wissink and W.Rodi. DNS of a Laminar Separation Bubble in the Presence of Oscillating External Flow. *Flow, Turbulence and Combustion*, 71:311–331, 2003.

[137] J.Wissink and W.Rodi. DNS of a Laminar Separation Bubble Affected by Free-Stream Disturbances. In *Direct and Large-Eddy Simulation V*, pages 213–220. Kluwer Academic Publishers, 2004.

[138] K.Yanase and P.Saarenrinne. Boundary layer control by a fish: Unsteady laminar boundary layers of rainbow trout swimming in turbulent flows. *Biology Open*, 2016.

[139] W.Yuan, M.Khalid, J.Windte, U.Scholz, and R.Radespiel. An Investigation of Low-Reynolds-number Flows past Airfoils. In *23rd AIAA Applied Aerodynamics Conference, July 2015*, pages 1–19, Toronto, 2005.

[140] W.Zhang, R.Hain, and C. J.Kähler. Scanning PIV investigation of the laminar separation bubble on a SD7003 airfoil. *Experiments in Fluids*, 45(4):725–743, 2008.

[141] Y.Zhou and Z. J.Wang. A Low-Frequency Instability/Oscillation near the Airfoil Leading-Edge at Low Reynolds Numbers and Moderate Incidences. In *20th AIAA Computational Fluid Dynamics Conference*, Honolulu, Hawaii, 2011.

[142] A.Zilstra. *Computational Aeroacoustic Noise Prediction for Wind Turbine Applications*. Msc, University of Waterloo, 2018.

APPENDICES

Appendix A

Drawing of the SD7037 airfoil model